SANDIA REPORT
SAND2017-3657
Unlimited Release
Printed April 2017

Reflection and Transmission of Plane Electromagnetic Waves by a Geologic Layer

David F. Aldridge

Prepared by
Sandia National Laboratories
Albuquerque, New Mexico 87185 and Livermore, California 94550

Sandia National Laboratories is a multi-mission laboratory managed and operated by Sandia Corporation, a wholly owned subsidiary of Lockheed Martin Corporation, for the U.S. Department of Energy's National Nuclear Security Administration under contract DE-AC04-94AL85000.

Issued by Sandia National Laboratories, operated for the United States Department of Energy by Sandia Corporation.

Available to DOE and DOE contractors from
U.S. Department of Energy
Office of Scientific and Technical Information
P.O. Box 62
Oak Ridge, TN 37831

Telephone: (865) 576-8401
Facsimile: (865) 576-5728
E-Mail: reports@adonis.osti.gov
Online ordering: http://www.osti.gov/bridge

Available to the public from
U.S. Department of Commerce
National Technical Information Service
5285 Port Royal Rd.
Springfield, VA 22161

Telephone: (800) 553-6847
Facsimile: (703) 605-6900
E-Mail: orders@ntis.fedworld.gov
Online order: http://www.ntis.gov/help/ordermethods.asp?loc=7-4-0#online

SAND2017-3657
Unlimited Release
Printed April 2017

REFLECTION and TRANSMISSION of PLANE ELECTROMAGNETIC WAVES by a GEOLOGIC LAYER

David F. Aldridge
Geophysics Department
Sandia National Laboratories
Albuquerque, New Mexico, USA, 87185-0750

ABSTRACT

Electric field and magnetic field reflection and transmission responses generated by a plane wave normally incident onto a finite-thickness geologic layer are mathematically derived and numerically evaluated. A thin layer with enhanced electric current conductivity and/or magnetic permeability is a reasonable geophysical representation of a hydraulic fracture injected with a high-contrast proppant pack. Both theory and numerics indicate that backward- and forward-scattered electromagnetic wavefields are potentially observable in a field experiment, despite the extreme thinness of a fracture compared to a typical low-frequency electromagnetic wavelength. The First Born Approximation (FBA) representation of layer scattering, significant for inversion studies, is shown to be accurate for a thin layer with mild medium parameter (i.e., conductivity, permeability, and permittivity) contrasts with the surrounding homogeneous wholespace. However, FBA scattering theory breaks down for thick layers and strong parameter contrasts.

ACKNOWLEDGEMENTS

Sandia National Laboratories is a multi-mission laboratory managed and operated by Sandia Corporation, a wholly owned subsidiary of Lockheed Martin Corporation, for the US Department of Energy's National Nuclear Security Administration under contract DE-AC04-94AL85000.

This research is conducted under the auspices of CRADA (Cooperative Research and Development Agreement) SC11/01780.00 between Carbo Ceramics Inc. and Sandia National Laboratories. The author acknowledges former Carbo R&D Vice-President Mr. Chad Cannan and former SNL Geophysics Department manager Ms. Amy Halloran for their interest in and support of this work. Technical discussions with Project Manager and Principal Investigator Dr. Chester J. Weiss of the SNL Geophysics Department greatly benefited this work. Dr. Lewis C. Bartel, formerly with SNL and presently a consultant to Carbo Ceramics, provided many useful and intuitive insights, and is acknowledged as the originator of the concept underpinning a recent patent grant (Aldridge and Bartel, 2016) involving electromagnetic wave scattering.

CONTENTS

1.0 INTRODUCTION

In seismic reflection exploration, a *thin* geologic layer in defined as one with thickness less than about one-fourth wavelength of an incident plane wave (Widess, 1957-58; 1973). In this case, distinct reflection arrivals from top and bottom bed boundaries are difficult to recognize. Information regarding layer thickness and material properties is encoded in the amplitude of the composite (reflected and/or transmitted) response. Due to the significantly larger wavelength of a diffusing electromagnetic (EM) wave, virtually all geologic layers would be considered extremely thin via this definition. This is particularly true for a single hydraulic fracture (~1 cm width) or even a fracture zone (~meters width).

Seismic and (low-frequency) EM wavelengths are given by

$$\lambda(f)\big|_{\text{SEIS}} = \frac{c}{f}, \qquad \lambda(f)\big|_{\text{EM}} = \frac{c(f)}{f} \approx \sqrt{\frac{4\pi}{\sigma\mu f}},$$

where c is phase speed, f is frequency, and σ and μ are current conductivity and magnetic permeability. For example, the wavelength of a 30 Hz sinusoid propagating with a seismic velocity of 3000 m/s in an elastic medium is 100 m, whereas the analogous EM signal diffusing through a conductive body of 0.1 S/m (clayey shale) has wavelength 1826 m. This larger wavelength has implications for the resolution capabilities of the EM prospecting method.

In this investigation, we restrict consideration to a normally-incident plane EM wave, and calculate reflection and transmission responses of a uniform-thickness layer embedded between two (possibly dissimilar) homogeneous and isotropic halfspaces. Exact frequency-domain expressions for the electric vector **E** and magnetic vector **B** are obtained via two mathematical methodologies: 1) summing primaries and all intrabed multiples (the SEIS way), and 2) solving a boundary value problem by imposing wavefield continuity at the interfaces (the EM way). The equivalence between the two approaches is rigorously established in Appendix C. Time-domain responses are subsequently obtained by inverse numerical Fourier transformation.

Our synthetic calculations predict observable **E** and **B** field responses, in both reflection and transmission, from layers that are several orders of magnitude smaller than the incident dominant wavelength. Large conductivity or permeability contrast of the layer, as with a hydraulic fracture injected with a suitable EM detection agent, enhances response amplitude. Contrary to LaBrecque et al. (2016), we find that permittivity contrast exerts negligible influence at the low frequencies typically used in EM geophysical exploration. Interestingly, responses appear to be insensitive to the fixed (parameter × thickness) product, a result that agrees with First Born Approximation scattering theory.

A significant portion of the present work involves developing the First Born Approximation (FBA) scattering representation of a thin geologic layer. Scattering of seismic waves by small-spatial-scale heterogeneities within Earth's crust and mantle has long been examined via the Born approximation (see Hudson and Heritage (1981) and the references cited therein for early work in this area). However, application of the FBA to electromagnetic wavefield scattering appears to be less common in the frequency band of interest in geophysics. The FBA involves replacing a perturbation in material properties (i.e., current conductivity σ, magnetic permeability μ, and/or dielectric permittivity ε) by an equivalent body source of EM waves. A particular advantage of the present model (a geologic layer with plane parallel interfaces, subject to a normally-incident plane EM wave) is that FBA scattered responses (in backward/forward directions) generated by these effective body sources can be calculated *exactly*. Comparison with the previously-developed reflection/transmission responses of the layer then establishes conditions for accuracy of the Born approximation. In particular, if the layer is thin (with respect to a wavelength of the incident EM wave) and has mild medium parameter contrasts with the surrounding wholespace, then FBA and actual responses agree well. Very strong parameter contrasts, as with a

hydraulic fracture injected with highly conductive and/or magnetic proppant particles, lead to Born scattering amplitudes that greatly exceed the actual scattering amplitudes.

In addition to providing a simple theoretical framework for understanding and analysing wavefield scattering, the FBA has practical utility for numerical algorithms used in simulating wave propagation through three-dimensional (3D) earth models. A small-scale heterogeneity (say, a steel borehole casing with thickness ~1 cm) is difficult to accurately represent on a numerical grid. Replacing this material parameter perturbation by an equivalent body source of waves (as in Aldridge, et al., 2015) may constitute a more feasible simulation approach. Finally, the FBA underlies a recently patented process (Aldridge and Bartel, 2016) for imaging a subsurface hydraulic fracture injected with electrically conducting proppant. The method had been applied to field-acquired EM data with some limited success (Palisch *et al*., 2016; 2017). The theoretical evaluation of FBA accuracy contained herein will assist in understanding the limitations of this new imaging approach.

An obvious extension of the present investigation involves a non-normal incident plane wave, which offers the intriguing possibility of Electromagnetic Amplitude vs. Offset (EMAVO) analysis, analogous to the well-known seismic counterpart.

In the following report, certain more mathematical and foundational topics (like plane EM wave propagation, reflection/transmission coefficients, First Born Approximation theory, and pulse-sequence mathematics) are reserved for the Appendices. Interestingly, in the course of the development, we have "discovered" (or perhaps "rediscovered") that the normal incidence plane wave reflection coefficient can be made to vanish (i.e., equal *zero*) by a suitable choice of the parameter contrast ratios for conductivity, permeability, and permittivity (see the development in Appendix B). This result does not appear to be well-known in electromagnetic geophysics. Perhaps the result may suggest an initial pathway toward developing a "reflectionless" or "transparent" material for EM waves.

2.0 PROBLEM DEFINITION

2.1 Geologic Layer Earth Model

Consider a one-dimensional (1D) electromagnetic (EM) earth model composed of three homogeneous and isotropic media. Figure 2.1 depicts overburden, layer, and substratum, each characterized by the triad of isotropic EM parameters electric permittivity ε, magnetic permeability μ, and current conductivity σ.

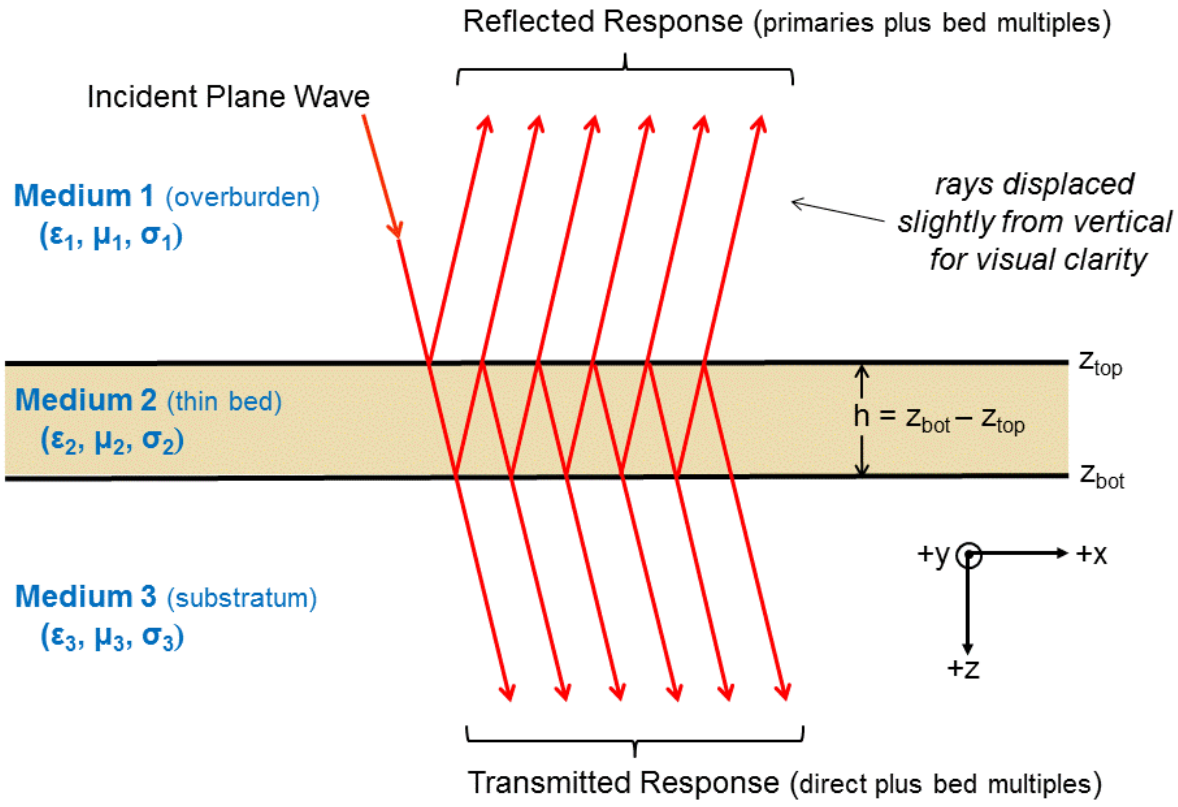

Figure 2.1. Geometric setup of the geologic layer reflection / transmission problem.

The layer is bounded by upper and lower plane horizontal interfaces located at $z = z_{top}$ and $z = z_{bot}$, respectively.

Next, consider a downward propagating plane EM wave normally incident on the geologic layer from above. The wave will reflect from both the top and bottom interfaces, as well as reflect internally multiple times within the layer. The totality of arrivals that return to a receiver $z_r < z_{top}$ constitute the layer *reflection response*. Similarly, the layer *transmission response* is composed of the direct (i.e., through-going) arrival and all trailing intrabed multiples sensed by a receiver at $z_r > z_{bot}$. In Figure 2.1, the raypaths associated with these many arrivals are displaced slightly from vertical for visual clarity. In actuality, all rays are normal to the interfaces.

2.2 Incident Plane Wave

The basic mathematics describing plane electromagnetic wave propagation within a homogeneous and isotropic body is developed in Appendix A. In the frequency-domain, the *x*-component of a downward-propagating electric vector within the upper medium #1 of Figure 2.1 is given by

$$E_{inc}(z,\omega) = E_{inc}(z_s,\omega)\exp\left[+iK_1(\omega)(z-z_s)\right], \tag{2.1}$$

where $E_{inc}(z_s,\omega)$ is the value at the source level $z = z_s$, and $K_1(\omega)$ is the *complex wavenumber* associated with medium #1 parameters. The positive sign within the exponent corresponds to +*z*-direction propagation. Generally, an electromagnetic complex wavenumber is given by

$$K(\omega) = \frac{1}{c_\infty}\left[\frac{\omega}{s(\omega/\omega_t)} + i\frac{\omega_t s(\omega/\omega_t)}{2}\right], \tag{2.2}$$

where the dimensionless function $s(w)$ is defined as

$$s(w) \equiv \sqrt{2|w|}\left[\sqrt{1+w^2} - |w|\right]^{+1/2}. \tag{2.3}$$

$s(w)$ is a positive and even function that approaches zero and unity as $w \to 0$ and $w \to \pm\infty$, respectively. The *infinite-frequency phase speed* c_∞ and transition frequency ω_t in equation (2.2) are defined by

$$c_\infty = \frac{1}{\sqrt{\varepsilon\mu}}, \qquad \omega_t = \frac{\sigma}{\varepsilon}, \tag{2.4a,b}$$

respectively. The transition frequency separates (roughly) the frequency ranges for electromagnetic wave diffusion ($|\omega| << \omega_t$) and electromagnetic wave propagation ($|\omega| >> \omega_t$).

A low-frequency approximation to the complex wavenumber is

$$\begin{aligned} K(\omega) &\approx \frac{\omega_t}{c_\infty}\sqrt{\frac{|\omega|}{\omega_t}}\left[\frac{\mathrm{sgn}(\omega) + i(1-\delta_0(\omega))}{\sqrt{2}}\right] = \sqrt{\sigma\mu|\omega|}\left[\frac{\mathrm{sgn}(\omega) + i(1-\delta_0(\omega))}{\sqrt{2}}\right], \\ &= \sqrt{\frac{\sigma\mu|\omega|}{2}}\,\mathrm{sgn}(\omega)e^{+i\frac{\pi}{4}\mathrm{sgn}(\omega)}, \end{aligned} \tag{2.5}$$

where $\mathrm{sgn}(\omega)$ is the sign function (= $\omega/|\omega|$ for $\omega \neq 0$, zero otherwise) and $\delta_0(\omega)$ is the null function (= 0 for $\omega \neq 0$, one otherwise) (Bracewell, 1965). The low-frequency approximation is independent of the electric permittivity ε. A high-frequency approximation to the complex wavenumber is

$$K(\omega) \approx \frac{\omega}{c_\infty} + i\alpha_\infty = \sqrt{\varepsilon\mu}\left(\omega + i\frac{\sigma}{2\varepsilon}\right), \tag{2.6}$$

where

$$\alpha_\infty = \omega_t/2c_\infty = (\sigma/2)\sqrt{\mu/\varepsilon}, \tag{2.4c}$$

is the *infinite-frequency attenuation factor*. Retaining a non-zero imaginary part enables attenuation of a propagating high-frequency EM wave. Otherwise, vanishing conductivity $\sigma = 0$ implies the complex wavenumber is $K(\omega) = \omega/c_\infty$ (i.e., pure real) appropriate for wave propagation without attenuation and dispersion.

2.3 Reflection and Transmission Coefficients

Frequency-domain expressions for normal incidence plane wave reflection and transmission coefficients are developed in Appendix B. The physical boundary conditions imposed on the EM wavefields are continuity of the tangential components of both the electric vector $\mathbf{E}(\mathbf{x},\omega)$ and the magnetic vector $\mathbf{H}(\mathbf{x},\omega)$ at an interface. At the top and the bottom interfaces bounding the embedded layer illustrated in Figure 2.1, plane wave reflection coefficients are given by

$$R_{top}(\omega) = \frac{K_1(\omega)/\mu_1 - K_2(\omega)/\mu_2}{K_1(\omega)/\mu_1 + K_2(\omega)/\mu_2}, \qquad R_{bot}(\omega) = \frac{K_2(\omega)/\mu_2 - K_3(\omega)/\mu_3}{K_2(\omega)/\mu_2 + K_3(\omega)/\mu_3}, \tag{2.7a,b}$$

respectively. These forms correspond to a wave incident on an interface from *above*; for a wave incident on the upper interface from *below*, the corresponding reflection coefficient is $-R_{top}(\omega)$. Downward and upward transmission coefficients at the top interface z_{top} are

$$T_{12}(\omega) = \frac{2K_1(\omega)/\mu_1}{K_1(\omega)/\mu_1 + K_2(\omega)/\mu_2}, \qquad T_{21}(\omega) = \frac{2K_2(\omega)/\mu_2}{K_2(\omega)/\mu_2 + K_1(\omega)/\mu_1}, \tag{2.8a,b}$$

respectively. Straightforward algebra yields the well-known relation $T_{12}(\omega) = 1 + R_{top}(\omega)$ (and correspondingly for the lower interface).

The (downward × upward) transmission coefficient product $T_{12}(\omega)T_{21}(\omega)$ arises in the derivation of the total reflection response of the embedded geologic layer below. From equations (2.8a and b), we have $T_{21}(\omega) = \left(\mu_1 K_2(\omega)/\mu_2 K_1(\omega)\right) T_{12}(\omega)$. Also, from expression (2.7a) we have the relation $\left(\mu_1 K_2(\omega)/\mu_2 K_1(\omega)\right) = \left(1 - R_{top}(\omega)\right)/\left(1 + R_{top}(\omega)\right)$. Combining these yields the interesting expression

$$T_{12}(\omega)T_{21}(\omega) = \left(\frac{1 - R_{top}(\omega)}{1 + R_{top}(\omega)}\right)\left(1 + R_{top}(\omega)\right)^2 = \left(1 - R_{top}(\omega)\right)\left(1 + R_{top}(\omega)\right) = 1 - R_{top}(\omega)^2. \tag{2.9}$$

So, for a small reflection coefficient $R_{top}(\omega)$, two-way transmission loss through the upper interface is negligible.

3.0 LAYER REFLECTION RESPONSE

3.1 Electric Field

The *reflection response* of the geologic layer is observed by a receiver placed on the same side of the layer as the source level: $z_r < z_{top}$. Working directly with Figure 2.1, the total reflection response may be built up by summing the many arrivals indicated by the (deviated) raypaths. Recall that $R_{top}(\omega)$ and $R_{bot}(\omega)$ are the normal incidence reflection coefficients (for a *downward* propagating plane wave) at the top and bottom interfaces bounding the bed. The reflection coefficient for an *upward* propagating plane wave encountering the upper interface is just $-R_{top}(\omega)$. Finally, $T_{12}(\omega)$ and $T_{21}(\omega)$ are downward and upward normal incidence transmission coefficients at the interface z_{top}. The reflection response sum is

$$\begin{aligned}\mathcal{R}(z_s,z_r,\omega) = E_{inc}(z_s,\omega)e^{+iK_1(\omega)(z_{top}-z_s)}\Big\{ & R_{top}(\omega) \\ & + T_{12}(\omega)R_{bot}(\omega)T_{21}(\omega)e^{+iK_2(\omega)2h} \\ & + T_{12}(\omega)R_{bot}(\omega)^2\left(-R_{top}(\omega)\right)T_{21}(\omega)e^{+iK_2(\omega)4h} \\ & + T_{12}(\omega)R_{bot}(\omega)^3\left(-R_{top}(\omega)\right)^2 T_{21}(\omega)e^{+iK_2(\omega)6h} \\ & +\cdots+ T_{12}(\omega)R_{bot}(\omega)^n\left(-R_{top}(\omega)\right)^{n-1}T_{21}(\omega)e^{+iK_2(\omega)2nh} \\ & +\cdots+ T_{12}(\omega)R_{bot}(\omega)^N\left(-R_{top}(\omega)\right)^{N-1}T_{21}(\omega)e^{+iK_2(\omega)2Nh}\Big\}e^{+iK_1(\omega)(z_{top}-z_r)},\end{aligned} \tag{3.1}$$

where the sum is terminated at N terms for convenience. We will let $N \to \infty$ shortly. The first term within braces {} corresponds to the primary reflection from the upper interface. The next term is the primary reflection from the lower interface, which includes two-way transmission loss through the upper interface. Subsequent terms in the sum correspond to so-called "intrabed multiples". [The term with exponent n on $R_{bot}(\omega)$ is actually the $(n-1)^{th}$ intrabed multiple, with $(n-1)$ downward reflections at z_{top} and $2n$ crossings of the bed.] The two complex exponentials outside of the braces { } carry the electromagnetic wavefield from the source level z_s down to the top interface z_{top} and from there back up to the receiver level z_r.

In more compact notation, the reflection response sum is

$$\begin{aligned}\mathcal{R}(z_s,z_r,\omega) = E_{inc}(z_s,\omega)e^{+iK_1(\omega)(2z_{top}-z_s-z_r)} \times \\ \left\{ R_{top}(\omega) + T_{12}(\omega)T_{21}(\omega)\sum_{n=1}^{N} R_{bot}(\omega)^n\left(-R_{top}(\omega)\right)^{n-1}e^{+iK_2(\omega)2nh}\right\},\end{aligned}$$

which is easily expressed as

$$\begin{aligned}\mathcal{R}(z_s,z_r,\omega) = E_{inc}(z_s,\omega)e^{+iK_1(\omega)(2z_{top}-z_s-z_r)} \times \\ \left\{ R_{top}(\omega) - \frac{T_{12}(\omega)T_{21}(\omega)}{R_{top}(\omega)}\sum_{n=1}^{N}\left(-R_{bot}(\omega)R_{top}(\omega)e^{+iK_2(\omega)2h}\right)^n\right\}.\end{aligned} \tag{3.2}$$

The sum may be evaluated via the famous geometric progression formula $\sum_{n=1}^{N} x^{n-1} = \left(1-x^N\right)/\left(1-x\right)$, to obtain

$$\Re\left(z_s, z_r, \omega\right) = E_{inc}(z_s, \omega) e^{+iK_1(\omega)\left(2z_{top}-z_s-z_r\right)} \times$$

$$\left\{ R_{top}(\omega) - \frac{T_{12}(\omega)T_{21}(\omega)}{R_{top}(\omega)} \left(-R_{bot}(\omega)R_{top}(\omega)e^{+iK_2(\omega)2h}\right) \left[\frac{1-\left(-R_{bot}(\omega)R_{top}(\omega)e^{+iK_2(\omega)2h}\right)^N}{1-\left(-R_{bot}(\omega)R_{top}(\omega)e^{+iK_2(\omega)2h}\right)} \right] \right\}.$$

Using $T_{12}(\omega)T_{21}(\omega) = 1 - R_{top}(\omega)^2$ from equation (2.9) finally yields

$$\Re\left(z_s, z_r, \omega\right) = E_{inc}(z_s, \omega) e^{+iK_1(\omega)\left(2z_{top}-z_s-z_r\right)} \times$$

$$\left\{ R_{top}(\omega) + \left(1-R_{top}(\omega)^2\right) R_{bot}(\omega) e^{+iK_2(\omega)2h} \left[\frac{1-\left(-R_{bot}(\omega)R_{top}(\omega)e^{+iK_2(\omega)2h}\right)^N}{1+R_{bot}(\omega)R_{top}(\omega)e^{+iK_2(\omega)2h}} \right] \right\}. \qquad (3.3)$$

Equation (3.3) is an expression for layer reflection response for the case of a finite number (N–1) of intrabed multiples. If the modulus of the reflection coefficient product $\left\|R_{bot}(\omega)R_{top}(\omega)\right\| < 1$, then as integer $N \to \infty$ this reduces to

$$\Re\left(z_s, z_r, \omega\right) = E_{inc}(z_s, \omega) e^{+iK_1(\omega)\left(2z_{top}-z_s-z_r\right)} \times$$

$$\left\{ R_{top}(\omega) + \left(1-R_{top}(\omega)^2\right) R_{bot}(\omega) e^{+iK_2(\omega)2h} \left[\frac{1}{1+R_{bot}(\omega)R_{top}(\omega)e^{+iK_2(\omega)2h}} \right] \right\}, \qquad (3.4a)$$

which is equivalent to

$$\Re\left(z_s, z_r, \omega\right) = E_{inc}(z_s, \omega) e^{+iK_1(\omega)\left(2z_{top}-z_s-z_r\right)} \left\{ \frac{R_{top}(\omega) + R_{bot}(\omega)e^{+iK_2(\omega)2h}}{1+R_{top}(\omega)R_{bot}(\omega)e^{+iK_2(\omega)2h}} \right\}. \qquad (3.4b)$$

Appendix B demonstrates that the inequality condition $\left\|R_{top}(\omega)R_{bot}(\omega)\right\| < 1$ is indeed true. Hence, the passage from (3.3) (with finite N) to (3.4a and b) (with $N \to \infty$) is valid.

Equation (3.4b) is the final expression for the reflection response of a geologic layer, where all intrabed multiples are accounted for! If the modulus of the reflection coefficient product is *very* small (i.e., $\left\|R_{bot}(\omega)R_{top}(\omega)\right\| << 1$) then the denominator may be approximated as unity, yielding the form

$$\Re\left(z_s, z_r, \omega\right) \approx E_{inc}(z_s, \omega) e^{+iK_1(\omega)\left(2z_{top}-z_s-z_r\right)} \left\{ R_{top}(\omega) + R_{bot}(\omega)e^{+iK_2(\omega)2h} \right\}. \qquad (3.5)$$

The interpretation of this expression is clear: it includes only the *primary* reflections from the top and bottom interfaces bounding the bed. The bottom-bed reflection is delayed in time and attenuated (via the medium parameters of the intervening layer) relative to the top-bed reflection. Moreover, the approximation neglects two-way transmission through the top interface. Hence, the more complicated denominator in equation (3.4b) compactly accounts for all intrabed multiples and interface transmission effects.

An interesting and common special case occurs when medium #3 is identical to medium #1. This implies $R_{bot}(\omega) = -R_{top}(\omega)$. Assuming $z_s = z_r = 0$ we obtain

$$\Re(0,0,\omega) = E_{inc}(0,\omega)e^{+iK_1(\omega)2z_{top}} R_{top}(\omega) \left\{ \frac{1-e^{+iK_2(\omega)2h}}{1-R_{top}(\omega)^2 e^{+iK_2(\omega)2h}} \right\}. \tag{3.6}$$

The quantity in braces { } is a frequency-dependent filter that modifies the top-bed primary reflection response. Note that if bed thickness h vanishes, then $\Re(0,0,\omega) = 0$ as expected.

In the limit of vanishing bed thickness $h \to 0$ (and top interface coordinate z_{top} remaining fixed), the general reflection response expression (3.4b) reduces to

$$\Re(z_s, z_r, \omega) = E_{inc}(z_s,\omega)e^{+iK_1(\omega)(2z_{top}-z_s-z_r)} \left\{ \frac{R_{top}(\omega)+R_{bot}(\omega)}{1+R_{top}(\omega)R_{bot}(\omega)} \right\}. \tag{3.7}$$

However, from the reflection coefficient formulae (2.7a and b), it can be demonstrated that the quantity in braces { } is just the reflection coefficient for medium #1 overlying medium #3:

$$R_{13}(\omega) = \frac{K_1(\omega)/\mu_1 - K_3(\omega)/\mu_3}{K_1(\omega)/\mu_1 + K_3(\omega)/\mu_3}. \tag{3.8}$$

Thus, the reflection response of a geologic "layer" of infinitesimal thickness is

$$\Re(z_s, z_r, \omega)\big|_{h=0} = E_{inc}(z_s,\omega)e^{+iK_1(\omega)(2z_{top}-z_s-z_r)} R_{13}(\omega), \tag{3.9}$$

which is, of course, a reflection from a single plane horizontal interface located at $z = z_{top}$ separating media #1 and #3. More generally, expanding the exact reflection response formula (3.4b) to first order in the assumed small quantity $\|iK_2(\omega)2h\|$ yields the approximate electromagnetic reflection response of a thin geologic bed as

$$\Re(z_s, z_r, \omega)\big|_{\|K_2(\omega)2h\|<<1} \approx E_{inc}(z_s,\omega)e^{+iK_1(\omega)(2z_{top}-z_s-z_r)} \times \left\{ R_{13}(\omega) + \frac{R_{bot}(\omega)\left[1-R_{top}(\omega)^2\right]}{\left[1+R_{top}(\omega)R_{bot}(\omega)\right]^2}\, iK_2(\omega)2h \right\}. \tag{3.10}$$

Clearly, (3.10) approaches (3.9) as bed thickness $h \to 0$. Moreover, for medium #1 = medium #3, we have $R_{13}(\omega) = 0$ and $R_{bot}(\omega) = -R_{top}(\omega)$, implying expression (3.10) reduces to

$$\Re(z_s, z_r, \omega)\Big|_{\|K_2(\omega)2h\|<<1} \approx E_{inc}(z_s, \omega) e^{+iK_1(\omega)(2z_{top}-z_s-z_r)} \left[\frac{-R_{top}(\omega)}{1-R_{top}(\omega)^2} \; iK_2(\omega)2h \right]. \tag{3.11}$$

This can also be obtained directly from equation (3.6) by expanding to first order in the small quantity $\|iK_2(\omega)2h\|$. If in addition medium parameter contrasts are small, so that squared reflection coefficients may be neglected, then equations (3.10) and (3.11) reduce to

$$\Re(z_s, z_r, \omega)\Big|_{\|K_2(\omega)2h\|<<1} \approx E_{inc}(z_s, \omega) e^{+iK_1(\omega)(2z_{top}-z_s-z_r)} \left[R_{13}(\omega) + R_{bot}(\omega)\, iK_2(\omega)2h \right], \tag{3.12a}$$

and

$$\Re(z_s, z_r, \omega)\Big|_{\|K_2(\omega)2h\|<<1} \approx E_{inc}(z_s, \omega) e^{+iK_1(\omega)(2z_{top}-z_s-z_r)} R_{top}(\omega) \left[-iK_2(\omega)2h \right], \tag{3.12b}$$

respectively. The second expression has an interesting interpretation: insertion of a thin low-contrast geologic bed into a homogeneous electromagnetic wholespace generates a "single-interface" top-bed reflection response, but altered by the multiplicative frequency-domain filter $\left[-iK_2(\omega)2h \right]$.

Finally, it is worth noting that the *total* electromagnetic plane wave response observed within medium #1 is the sum of the downgoing incident wave plus the upgoing reflection response:

$$E_{tot}(z_s, z_r, \omega) = E_{inc}(z_s, z_r, \omega) + \Re(z_s, z_r, \omega).$$

Using equation (2.1) for the incident wave and equation (3.4b) for the reflection response yields the interesting form

$$E_{tot}(z_s, z_r, \omega) = E_{inc}(z_s, \omega) e^{+iK_1(\omega)(z_r - z_s)} \left\{ 1 + \left[\frac{R_{top}(\omega) + R_{bot}(\omega) e^{+iK_2(\omega)2h}}{1 + R_{top}(\omega) R_{bot}(\omega) e^{+iK_2(\omega)2h}} \right] e^{+iK_1(\omega)2(z_{top}-z_r)} \right\}. \tag{3.13}$$

The unit factor "1" within braces { } accounts for the downgoing incident wave.

3.2 Magnetic Field

The reflected *magnetic* response (i.e., $\mathbf{H}(\mathbf{x},\omega)$ vector with SI unit (A/m)/Hz) is obtained from Faraday's law via

$$\mathbf{H}(z, \omega) = \frac{1}{i\omega\mu} \mathbf{curl}\, \mathbf{E}(z, \omega) = \mathbf{e}_y \frac{1}{i\omega\mu} \frac{\partial E_x(z, \omega)}{\partial z}. \tag{3.14}$$

Hence, the reflected *y*-component of the magnetic induction vector is

$$B_y(z_s, z_r, \omega)\Big|_{ref} = \mu_1 H_y(z_s, z_r, \omega)\Big|_{ref} = E_{inc}(z_s, \omega) e^{+iK_1(\omega)(2z_{top}-z_s-z_r)} \times \left[\frac{R_{top}(\omega) + R_{bot}(\omega) e^{+iK_2(\omega)2h}}{1 + R_{top}(\omega) R_{bot}(\omega) e^{+iK_2(\omega)2h}} \right] \left[\frac{-K_1(\omega)}{\omega} \right], \tag{3.15a}$$

or

$$B_y(z_s, z_r, \omega)\Big|_{ref} = E_x(z_s, z_r, \omega)\Big|_{ref}\left[\frac{-K_1(\omega)}{\omega}\right]. \qquad (3.15b)$$

Hence, the magnetic field reflection response is obtained merely by multiplying the electric reflection response by the ratio $-K_1(\omega)/\omega$. This could present some numerical problems for DC frequency.

4.0 LAYER TRANSMISSION RESPONSE

4.1 Electric Field

The electromagnetic wave transmitted *through* the geologic layer to a receiver at level $z_r > z_{bot}$ may be built up in exactly the same manner by summing N+1 distinct arrivals as depicted in Figure 2.1. We have

$$\mathcal{I}(z_s, z_r, \omega) = E_{inc}(z_s, \omega) e^{+iK_1(\omega)(z_{top} - z_s)}\ e^{+iK_2(\omega)h}\ e^{+iK_3(\omega)(z_r - z_{bot})}\ T_{12}(\omega) T_{23}(\omega)$$

$$\times \left\{ 1 + \sum_{n=1}^{N} \left(- R_{top}(\omega) R_{bot}(\omega) e^{+iK_2(\omega)2h} \right)^n \right\}. \qquad (4.1)$$

The first major term is the direct arrival propagating from the source level z_s to the receiver level z_r through the layer of thickness h. $T_{12}(\omega)$ and $T_{23}(\omega)$ are plane wave transmission coefficients at the top and bottom interfaces, respectively. The second major term accounts for all of the trailing intrabed multiples. The finite sum is easily evaluated via the geometric progression formula to obtain

$$\mathcal{I}(z_s, z_r, \omega) = E_{inc}(z_s, \omega) e^{+iK_1(\omega)(z_{top} - z_s)}\ e^{+iK_2(\omega)h}\ e^{+iK_3(\omega)(z_r - z_{bot})}\ T_{12}(\omega) T_{23}(\omega)$$

$$\times \left\{ 1 + \left(- R_{top}(\omega) R_{bot}(\omega) e^{+iK_2(\omega)2h} \right) \left[\frac{1 - \left(- R_{top}(\omega) R_{bot}(\omega) e^{+iK_2(\omega)2h} \right)^N}{1 + R_{top}(\omega) R_{bot}(\omega) e^{+iK_2(\omega)2h}} \right] \right\}, \qquad (4.2)$$

which is appropriate for a finite number N of intrabed multiples. Assuming the modulus of the reflection coefficient product $\|R_{top}(\omega)\ R_{bot}(\omega)\| < 1$ (which is indeed always true, as demonstrated in Appendix B) the limit as $N \to \infty$ yields

$$\mathcal{I}(z_s, z_r, \omega) = E_{inc}(z_s, \omega) e^{+iK_1(\omega)(z_{top} - z_s)}\ e^{+iK_2(\omega)h}\ e^{+iK_3(\omega)(z_r - z_{bot})}\ T_{12}(\omega) T_{23}(\omega)$$

$$\times \left[1 - \frac{R_{top}(\omega) R_{bot}(\omega) e^{+iK_2(\omega)2h}}{1 + R_{top}(\omega) R_{bot}(\omega) e^{+iK_2(\omega)2h}} \right],$$

which is equivalent to

$$\mathcal{I}(z_s, z_r, \omega) = E_{inc}(z_s, \omega) e^{+iK_1(\omega)(z_{top} - z_s)}\ e^{+iK_2(\omega)h}\ e^{+iK_3(\omega)(z_r - z_{bot})}\ T_{12}(\omega) T_{23}(\omega)$$

$$\times \left[\frac{1}{1 + R_{top}(\omega) R_{bot}(\omega) e^{+iK_2(\omega)2h}} \right]. \qquad (4.3a)$$

Since $T_{12}(\omega) T_{23}(\omega) = \left(1 + R_{top}(\omega)\right)\left(1 + R_{bot}(\omega)\right)$ we have the equivalent form (next page):

$$\mathcal{I}(z_s, z_r, \omega) = E_{inc}(z_s, \omega) e^{+iK_1(\omega)(z_{top} - z_s)}\ e^{+iK_3(\omega)(z_r - z_{bot})}$$

$$\times \left[\frac{\left(1 + R_{top}(\omega)\right)\left(1 + R_{bot}(\omega)\right) e^{+iK_2(\omega)h}}{1 + R_{top}(\omega) R_{bot}(\omega) e^{+iK_2(\omega)2h}} \right]. \qquad (4.3b)$$

The denominator has the same form as in the reflection response equation (3.4a). Note that if $R_{top}(\omega) = 0$ (say, because media #1 and #2 are identical), then this response reduces to

$$\mathcal{I}(z_s, z_r, \omega) = E_{inc}(z_s, \omega) e^{+iK_1(\omega)(z_{bot} - z_s)}\ e^{+iK_3(\omega)(z_r - z_{bot})}\ \left(1 + R_{bot}(\omega)\right),$$

(because in this case $K_2(\omega) = K_1(\omega)$ and $z_{top} + h = z_{bot}$). This is just a plane wave transmitted through the single interface (between media #2 and #3) at $z = z_{bot}$. Similarly, if $R_{bot}(\omega) = 0$ (say, because media #2 and #3 are identical), we have

$$\mathcal{I}(z_s, z_r, \omega) = E_{inc}(z_s, \omega) e^{+iK_1(\omega)(z_{top} - z_s)}\ e^{+iK_2(\omega)(z_r - z_{top})}\ \left(1 + R_{top}(\omega)\right),$$

which corresponds to a plane wave transmitted through the single interface located at $z = z_{top}$.

If media #1 and #3 are identical, then $R_{bot}(\omega) = -R_{top}(\omega)$ yields the simplified form

$$\mathcal{I}(z_s, z_r, \omega) = E_{inc}(z_s, \omega) e^{+iK_1(\omega)(z_r - z_s - h)} \left[\frac{\left(1 - R_{top}(\omega)^2\right) e^{+iK_2(\omega)h}}{1 - R_{top}(\omega)^2 e^{+iK_2(\omega)2h}} \right]. \qquad (4.4)$$

In this particular case, if $R_{top}(\omega) = 0$ (say, because all three media are identical) we have

$$\mathcal{I}(z_s, z_r, \omega) = E_{inc}(z_s, \omega) e^{+iK_1(\omega)(z_r - z_s)},$$

which is just the source plane wave propagating through a homogeneous (but still attenuating and dispersing) medium from level z_s to level z_r.

Expanding the exact transmission response formula (4.3b) to first order in the assumed small quantity $\left\| iK_2(\omega)2h \right\|$ yields the approximate electromagnetic transmission response of a thin bed as

$$\mathcal{I}(z_s, z_r, \omega)\Big|_{\|K_2(\omega)2h\| << 1} \approx E_{inc}(z_s, \omega) e^{+iK_1(\omega)(z_{top} - z_s)} e^{+iK_3(\omega)(z_r - z_{bot})} \times$$

$$\left[1 + R_{13}(\omega)\right] \left\{ 1 + \frac{1}{2} \left[\frac{1 - R_{top}(\omega) R_{bot}(\omega)}{1 + R_{top}(\omega) R_{bot}(\omega)} \right] iK_2(\omega)2h \right\}, \qquad (4.5a)$$

where $1 + R_{13}(\omega) = T_{13}(\omega)$ is the transmission coefficient from medium #1 to medium #3. In the limit of vanishing bed thickness h, the direct plane wave transmission from #1 to #3 is recovered. However, for all three media identical, expression (4.5a) reduces to the curious form

$$\mathcal{I}(z_s, z_r, \omega)\Big|_{\|K_2(\omega)2h\| << 1} \approx E_{inc}(z_s, \omega) e^{+iK_1(\omega)(z_r - z_s)} e^{-iK_1(\omega)h} \left\{ 1 + iK_2(\omega)h \right\},$$

which does *not* appear to be a plane wave propagating within homogeneous medium #1! However, adopt the approximation

$$e^{-iK_3(\omega)h} = e^{-iK_2(\omega)2h[K_3(\omega)/2K_2(\omega)]} = \left[e^{-iK_2(\omega)2h}\right]^{[K_3(\omega)/2K_2(\omega)]}$$

$$\approx \left[1-iK_2(\omega)2h\right]^{[K_3(\omega)/2K_2(\omega)]} \approx 1-\left[iK_2(\omega)2h\right]\left[K_3(\omega)/2K_2(\omega)\right] = 1-iK_3(\omega)h\,.$$

Then, equation (4.5a) is re-written to first order in *h* as

$$\mathcal{I}(z_s,z_r,\omega)\Big|_{\|K_2(\omega)2h\|<<1} \approx E_{inc}(z_s,\omega)e^{+iK_1(\omega)(z_{top}-z_s)}e^{+iK_3(\omega)(z_r-z_{top})} \times$$
$$\left[1+R_{13}(\omega)\right]\left\{1+\frac{1}{2}\left[\frac{1-R_{top}(\omega)R_{bot}(\omega)}{1+R_{top}(\omega)R_{bot}(\omega)}-\frac{K_3(\omega)}{K_2(\omega)}\right]iK_2(\omega)2h\right\}. \qquad (4.5b)$$

Clearly, if all three media are identical, this approximation approaches the proper limit corresponding to uni-directional plane wave propagation in a homogeneous wholespace. Utilizing equation (2.7b) for the bottom interface reflection coefficient, the ratio of complex wavenumbers $K_3(\omega)/K_2(\omega)$ can be replaced by

$$\frac{K_3(\omega)}{K_2(\omega)} = \frac{\mu_3}{\mu_2}\frac{1-R_{bot}(\omega)}{1+R_{bot}(\omega)}\,.$$

Rather than substitute this form into (4.5b), we immediately specialize to the low-contrast situation where products of reflection coefficients may be ignored. Moreover, take $\mu_3/\mu_2 \approx 1$, consistent with a low-contrast assumption. Expression (4.5b) simplifies to

$$\mathcal{I}(z_s,z_r,\omega)\Big|_{\|K_2(\omega)2h\|<<1} \approx E_{inc}(z_s,\omega)e^{+iK_1(\omega)(z_{top}-z_s)}e^{+iK_3(\omega)(z_r-z_{top})}\,T_{13}(\omega)\left[1+\frac{R_{bot}}{1+R_{bot}}iK_2(\omega)2h\right]. \quad (4.5c)$$

Next, assume medium #1 is identical to medium #3 (implying transmission coefficient $T_{13}(\omega) = 1$) to obtain

$$\mathcal{I}(z_s,z_r,\omega)\Big|_{\|K_2(\omega)2h\|<<1} \approx E_{inc}(z_s,\omega)e^{+iK_1(\omega)(z_r-z_s)}\left[1+\frac{R_{bot}}{1+R_{bot}}iK_2(\omega)2h\right]. \qquad (4.5d)$$

Hence, insertion of a thin low-contrast geologic bed into a homogeneous electromagnetic wholespace generates a transmitted plane wave with an *effective* transmission coefficient given in (4.5d).

4.2 Magnetic Field

The transmitted *magnetic* response (i.e., $\mathbf{H}(\mathbf{x},\omega)$ vector with SI unit (A/m)/Hz) is obtained from Faraday's law via

$$\mathbf{H}(z,\omega) = \frac{1}{i\omega\mu}\mathbf{curl}\,\mathbf{E}(z,\omega) = \mathbf{e}_y\frac{1}{i\omega\mu}\frac{\partial E_x(z,\omega)}{\partial z}\,. \qquad (3.11 \text{ again})$$

Hence, the transmitted *y*-component of the magnetic induction vector is

$$B_y(z_s,z_r,\omega)\big|_{trn} = \mu_3 H_y(z_s,z_r,\omega)\big|_{trn} = E_{inc}(z_s,\omega)e^{+iK_1(\omega)(z_{top}-z_s)}e^{+iK_2(\omega)h}e^{+iK_3(\omega)(z_r-z_{bot})} \times \left[\frac{\big(1+R_{top}(\omega)\big)\big(1+R_{bot}(\omega)\big)}{1+R_{top}(\omega)R_{bot}(\omega)e^{+iK_2(\omega)2h}}\right]\left[\frac{K_3(\omega)}{\omega}\right], \quad (4.6a)$$

or

$$B_y(z_s,z_r,\omega)\big|_{trn} = E_x(z_s,z_r,\omega)\big|_{trn}\left[\frac{K_3(\omega)}{\omega}\right]. \quad (4.6b)$$

Similar to the magnetic reflection response, the transmission response is obtained by multiplying the electric transmission response by a ratio $+K_3(\omega)/\omega$, again presenting some numerical problems for DC frequency.

4.3 Reflection / Transmission Relationship

The mathematical expressions for the layer reflection (equation (3.4b)) and layer transmission (equation (4.3b)) responses enable an investigation into their interrelation. Evaluating the *total* electric field (3.13) with a receiver located at the *top* of the bed $z_r = z_{top}$ yields

$$\begin{aligned}
E_{tot}(z_s,z_{top},\omega) &= E_{inc}(z_s,\omega)e^{+iK_1(\omega)(z_{top}-z_s)}\left[1+\frac{R_{top}(\omega)+R_{bot}(\omega)e^{+iK_2(\omega)2h}}{1+R_{top}(\omega)R_{bot}(\omega)e^{+iK_2(\omega)2h}}\right] \\
&= E_{inc}(z_s,\omega)e^{+iK_1(\omega)(z_{top}-z_s)}\left[\frac{\big(1+R_{top}(\omega)\big)\big(1+R_{bot}(\omega)e^{+iK_2(\omega)2h}\big)}{1+R_{top}(\omega)R_{bot}(\omega)e^{+iK_2(\omega)2h}}\right] \\
&= E_{inc}(z_s,\omega)e^{+iK_1(\omega)(z_{top}-z_s)}\left[\frac{\big(1+R_{top}(\omega)\big)\big(1+R_{bot}(\omega)\big)}{1+R_{top}(\omega)R_{bot}(\omega)e^{+iK_2(\omega)2h}}\right]\left[\frac{1+R_{bot}(\omega)e^{+iK_2(\omega)2h}}{1+R_{bot}(\omega)}\right] \\
&= E_{inc}(z_s,\omega)e^{+iK_1(\omega)(z_{top}-z_s)}\left[\frac{\big(1+R_{top}(\omega)\big)\big(1+R_{bot}(\omega)\big)}{1+R_{top}(\omega)R_{bot}(\omega)e^{+iK_2(\omega)2h}}\right]e^{+iK_2(\omega)h} \times \\
&\qquad \left[\frac{e^{-iK_2(\omega)h}+R_{bot}(\omega)e^{+iK_2(\omega)h}}{1+R_{bot}(\omega)}\right] \\
&= \mathcal{I}\big(z_s,z_{bot},\omega\big)\left[\frac{e^{-iK_2(\omega)h}+R_{bot}(\omega)e^{+iK_2(\omega)h}}{1+R_{bot}(\omega)}\right],
\end{aligned}$$

where equation (4.3b) is used to evaluate the transmission response for a receiver located at the *bottom* of the thin geologic bed $z_r = z_{bot}$. Since the total field is the sum of the incident and reflected fields, this becomes

$$E_{inc}(z_{top},\omega)+\Re(z_s,z_{top},\omega)=\Im(z_s,z_{bot},\omega)\left[\frac{e^{-iK_2(\omega)h}+R_{bot}(\omega)e^{+iK_2(\omega)h}}{1+R_{bot}(\omega)}\right]. \quad (4.7)$$

The reflection response at the top of the bed is linked to the transmission response at the bottom of the bed. However, the relationship is not as simple as $1+R(\omega)=T(\omega)$ for a single reflecting/transmitting horizon. In the limit as bed thickness $h \rightarrow 0$, expression (4.7) reduces to $1+R_{13}(\omega)=T_{13}(\omega)$, where the subscripts refer to media #1 and #3.

5.0 SCATTERED WAVEFIELDS

The normal-incidence EM plane wave *reflected response* $\mathcal{R}(z_s, z_r, \omega)$ and *transmitted response* $\mathcal{T}(z_s, z_r, \omega)$ generated by a geologic layer of thickness *h* embedded between two homogeneous and isotropic halfspaces are derived in the previous sections. In this section, we consider the analogous *scattered* EM wavefield responses. In the present context, a scattered response is loosely described as the wavefield directly attributable to a layer "inserted" into a suitably chosen background or reference earth model. If the layer were not present, there would be no scattered response. In a wordy style, a scattered response is defined as

Scattered Response = Actual model response *minus* Reference model response.

Obviously, there is rather wide latitude in obtaining a scattered response, because it depends on an arbitrarily specified "reference model" response. A judicious choice for the reference model is helpful for calculating and interpreting scattered wavefields. An obvious choice appropriate for the particular problem at hand is described below.

5.1 Reference Earth Model

Consider a reference model consisting of a single plane horizontal interface, located at the midpoint coordinate $z_{mid} = 0.5(z_{top} + z_{bot})$ between top and bottom interfaces of the embedded layer. Upper and lower halfspaces are assigned EM parameters associated with medium #1 (overburden) and medium #3 (substratum) of the actual earth model, respectively. Figure 5.1 depicts the reflected and transmitted wavefields. Clearly, there is only a *single* plane reflected wave, and a *single* plane transmitted wave.

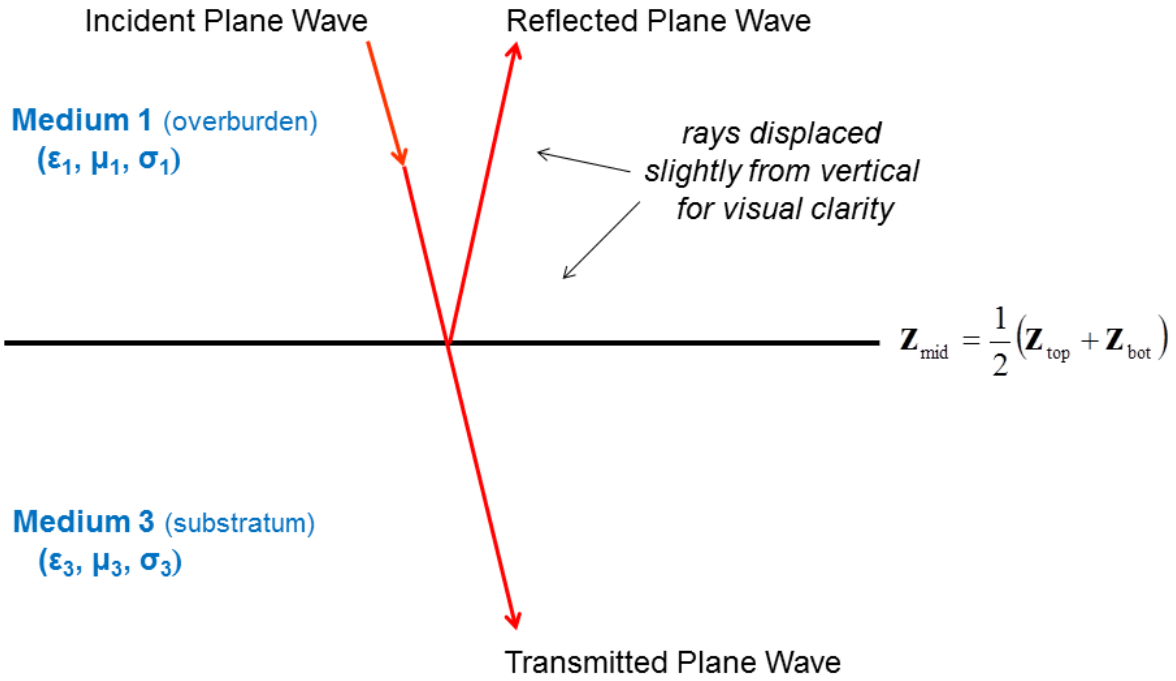

Figure 5.1. Reference or background model consisting of a single plane horizontal interface separating two (possibly dissimilar) upper and lower halfspaces.

The exact reflected and transmitted responses of a finite-thickness layer embedded between upper and lower halfspaces (with different EM parameters) are given by

$$\mathcal{R}(z_s, z_r, \omega) = E_{inc}(z_s, \omega) e^{+iK_1(\omega)(2z_{top} - z_s - z_r)} \left\{ \frac{R_{top}(\omega) + R_{bot}(\omega) e^{+iK_2(\omega)2h}}{1 + R_{bot}(\omega) R_{top}(\omega) e^{+iK_2(\omega)2h}} \right\}, \qquad \text{(3.4b again)}$$

and

$$\mathcal{T}(z_s, z_r, \omega) = E_{inc}(z_s, \omega) e^{+iK_1(\omega)(z_{top} - z_s)} \; e^{+iK_2(\omega)h} \; e^{+iK_3(\omega)(z_r - z_{bot})} \times \left[\frac{\left(1 + R_{top}(\omega)\right)\left(1 + R_{bot}(\omega)\right)}{1 + R_{top}(\omega) R_{bot}(\omega) e^{+iK_2(\omega)2h}} \right], \qquad \text{(4.3b again)}$$

respectively. Reflected and transmitted wavefields generated by the single plane interface reference model are

$$E_{inc}(z_s, \omega) e^{+iK_1(\omega)(z_{mid} - z_s)} R_{mid}(\omega) e^{+iK_1(\omega)(z_{mid} - z_r)}, \qquad \text{(5.1a)}$$

and

$$E_{inc}(z_s, \omega) e^{+iK_1(\omega)(z_{mid} - z_s)} T_{mid}(\omega) e^{+iK_3(\omega)(z_r - z_{mid})}, \qquad \text{(5.1b)}$$

respectively. Here $R_{mid}(\omega)$ and $T_{mid}(\omega)$ are normal-incidence plane wave reflection and transmission coefficients between media #1 and #3. Expressions (5.1a and b) are upward- and downward-propagating plane EM waves, respectively. An important special case occurs when the EM parameters of media #1 and #3 are identical. In this case there is no material property contrast, implying reflection coefficient $R_{mid}(\omega) = 0$ and transmission coefficient $T_{mid}(\omega) = 1$. Reference model reflected/transmitted responses become

$$0, \qquad \text{(5.2a)}$$

and

$$E_{inc}(z_r, \omega), \qquad \text{(5.2b)}$$

respectively. No reflection is generated, and the downward wave transmitted into medium #2 is identical to the incident wave. This realistic and common situation will be considered in detail in the sequel.

5.2 Thin Layer Criteria

Many geologic layers are considerably thinner than a wavelength of a typical propagating/diffusing electromagnetic (EM) disturbance. The exact scattered responses (both reflected or back-scattered and transmitted or fore-scattered) developed below will be expanded to first order in the layer thickness *h*. These expansions yield mathematical expressions that are reasonably accurate, as well as clearly exhibiting dependencies on the various parameters of the problem (i.e., layer thickness, EM material property contrasts). In this section, the specific mathematical conditions for layer "thinness" are defined, for both low-frequency and high-frequency ranges.

Equation (3.4b) for the reflection or back-scattering problem contains the complex exponential factor $\exp\left[iK_2(\omega)2h\right]$, where $K_2(\omega)$ is the complex wavenumber evaluated with the layer (i.e., medium #2) parameters. Hence, we define a thin *reflective* layer as one that satisfies the inequality

$$\left\|iK_2(\omega)2h\right\| << 1. \tag{5.3}$$

In turn, this implies

$$\frac{\lambda_2(\omega)}{2h} >> 2\pi\sqrt{1+\gamma_2(\omega)^2},$$

where $\lambda_2(\omega) = 2\pi c_2(\omega)/\omega$ is the wavelength calculated with the phase speed $c_2(\omega)$ of the thin bed, and a dimensionless frequency-dependent parameter is defined as $\gamma_2(\omega) \equiv \alpha_2(\omega)c_2(\omega)/\omega$. Recall that $\alpha_2(\omega)$ is the attenuation parameter of the layer. Hence, we have the thin layer reflection condition

$$\frac{h}{\lambda_2(\omega)} << \frac{1}{4\pi\sqrt{1+\gamma_2(\omega)^2}}. \tag{5.4}$$

For the transmission or forward-scattering, problem, equation (4.3b) contains the two factors $\exp\left[iK_2(\omega)h\right]$ and $\exp\left[iK_2(\omega)2h\right]$. Hence, condition (5.3) ensures that the arguments of both complex exponentials are small. Equation (5.4) is now safely interpreted as both a thin layer *reflection* and *transmission* criterion.

At low-frequency (i.e., $\omega << \omega_t = \sigma/\varepsilon$), phase speed $c(\omega) \approx \sqrt{\frac{2|\omega|}{\sigma\mu}}$ and attenuation parameter $\alpha(\omega) \approx \sqrt{\frac{\sigma\mu|\omega|}{2}}$, implying $\sqrt{1+\gamma_2(\omega)^2} = \sqrt{1+1} = \sqrt{2}$. Hence, the low-frequency thin-bed condition becomes

$$\frac{h}{\lambda_2(\omega)} << \frac{1}{4\pi\sqrt{2}} \approx 0.056. \tag{5.5}$$

A thin layer is one with thickness less than ~6% of a wavelength, calculated with the low-frequency layer phase speed.

At high-frequency (i.e., $\omega >> \omega_t$) phase speed $c(\omega) \approx c_\infty = \dfrac{1}{\sqrt{\varepsilon\mu}}$ and attenuation parameter $\alpha(\omega) \approx \alpha_\infty = \dfrac{\sigma}{2}\sqrt{\dfrac{\mu}{\varepsilon}}$, implying $\sqrt{1+\gamma_2(\omega)^2} = \sqrt{1+\left(\sigma_2/2\varepsilon_2\omega\right)^2}$, Hence, a high-frequency thin-bed condition is

$$\frac{h}{\lambda_2(\omega)} << \frac{1}{4\pi\sqrt{1+\left(\sigma_2/2\varepsilon_2\omega\right)^2}}. \tag{5.6a}$$

Dependence on layer conductivity σ_2 and permittivity ε_2 is evident. However, at infinite frequency (or $\sigma_2 = 0$) this criterion reduces to

$$\frac{h}{\lambda_2(\omega)} << \frac{1}{4\pi\sqrt{1}} \approx 0.080. \tag{5.6b}$$

The very-high-frequency criterion for a reflective thin bed is thickness h less than about ~8% of wavelength (again calculated with the phase speed of the layer). However, the high-frequency wavelength is $\lambda_2(\omega) = 2\pi c_2(\omega)/\omega \approx 2\pi/\sqrt{\varepsilon_2\mu_2}\,\omega$, and this vanishes in the limit of infinite frequency. So, the notion of a high-frequency thin-bed criterion is somewhat problematical. Nevertheless, we believe that the low-frequency thin-bed condition (5.5) commonly holds in typical EM geophysical exploration practice. Thus, *low-frequency* backward- and forward-scattering is emphasized and examined in the sequel.

Utilizing the low-frequency approximation for phase speed $c(\omega) \approx \sqrt{2|\omega|/\sigma\mu}$, we obtain an analogous approximation for wavelength (expressed in terms of temporal frequency $f = \omega/2\pi$) as

$$\lambda(f,\sigma,\mu) \equiv \frac{c(f)}{f} \approx \sqrt{\frac{4\pi}{\sigma\mu f}},$$

where f is assumed to be positive. Introducing reference values for the various dimensioned quantities into this expression yields the non-dimensional form

$$\frac{\lambda(f,\sigma,\mu)}{\lambda_{ref}} = \sqrt{\frac{4\pi}{\sigma_{ref}\mu_{ref}f_{ref}\lambda_{ref}^2}}\ \frac{1}{\sqrt{(\sigma/\sigma_{ref})(\mu/\mu_{ref})(f/f_{ref})}}. \tag{5.7}$$

Taking the base-10 logarithm of each side gives

$$\log_{10}\left[\frac{\lambda(f,\sigma,\mu)}{\lambda_{ref}}\right] = \frac{1}{2}\log_{10}\left(\frac{4\pi}{\sigma_{ref}\mu_{ref}f_{ref}\lambda_{ref}^2}\right) - \frac{1}{2}\left[\log_{10}\left(\sigma/\sigma_{ref}\right) + \log_{10}\left(\mu/\mu_{ref}\right) + \log_{10}\left(f/f_{ref}\right)\right]. \tag{5.8a}$$

Next, assigning numerical values to these reference quantities as

$$\lambda_{ref} = 1\,\text{m}, \qquad \sigma_{ref} = 1\,\text{S/m}, \qquad \mu_{ref} = \mu_0 = 4\pi\times10^{-7}\ \text{H/m}, \qquad f_{ref} = 1\,\text{Hz},$$

yields the logarithmic relation

$$\log_{10}\left[\frac{\lambda(f,\sigma,\mu)}{\lambda_{ref}}\right]=\frac{1}{2}\left[7-\log_{10}\left(f/f_{ref}\right)-\log_{10}\left(\sigma/\sigma_{ref}\right)-\log_{10}\left(\mu/\mu_{ref}\right)\right]. \qquad (5.8b)$$

There are three independent variables (the logarithms of the dimensionless ratios) on the right-hand-side. We fix the frequency ratio, and calculate the logarithmic wavelength as a function of the logarithmic conductivity and permeability ratios. The following three panels illustrate the results for values of frequency of f = 1 Hz, 10 Hz, and 100 Hz.

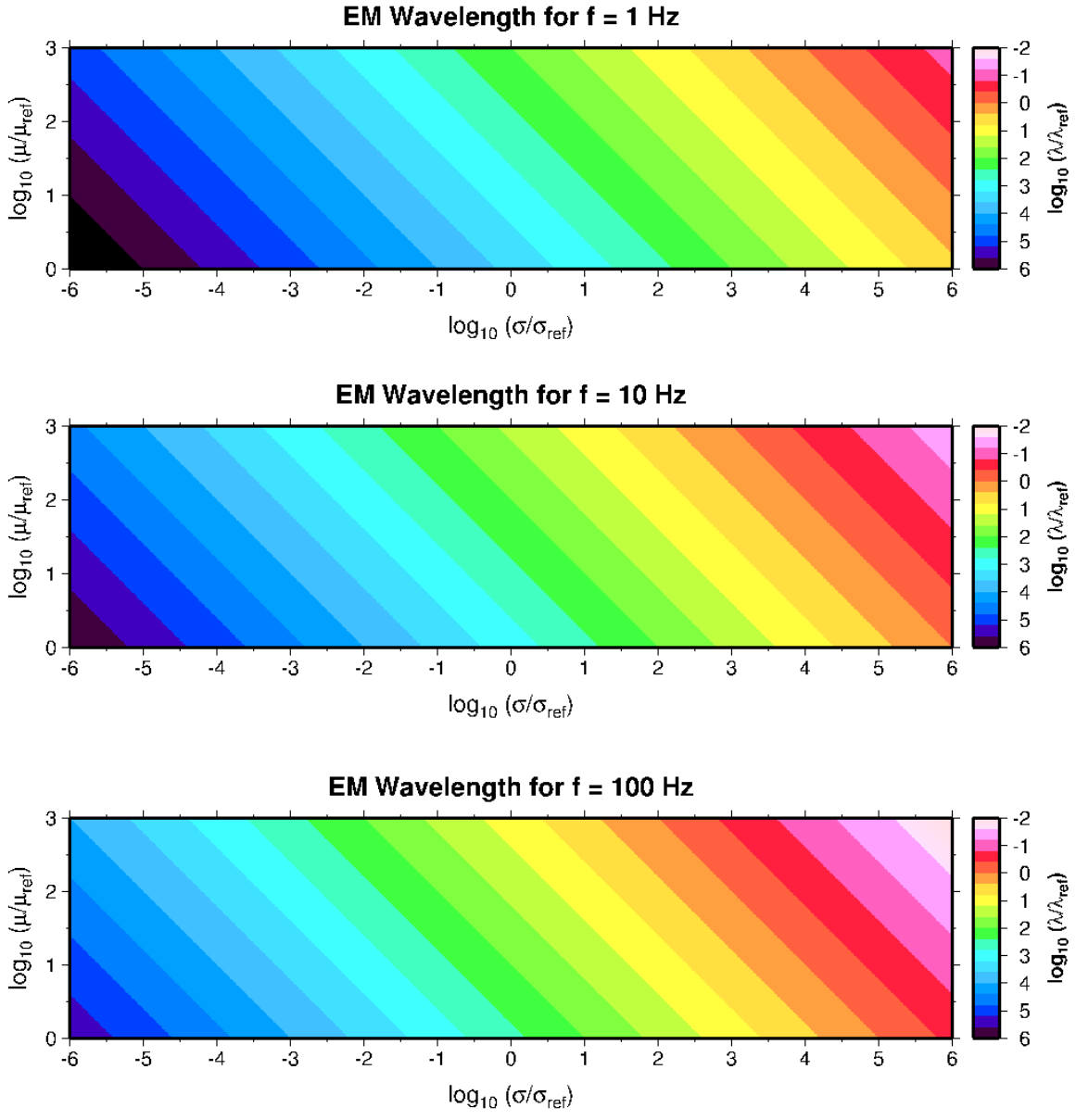

Figure 5.2. Logarithm of electromagnetic wavelength *vs*. logarithmic conductivity and logarithmic permeability, for frequency f = 1 Hz (top), f = 10 Hz (middle), and f = 100 Hz (bottom).

Current conductivity on the horizontal axis ranges from 10^{-6} S/m (extremely resistive) to 10^{+6} S/m (extremely conductive). Magnetic permeability on the vertical axis ranges from μ_0 (vacuum) to 10^3 μ_0 (highly magnetic). Thus, the lower left corner, with extremely long wavelengths, approaches vacuum whereas the upper right corner, with short wavelengths, approaches pure metal. Contours of fixed wavelength are straight lines with slope –1. As frequency increases, the color banding pattern shifts to the left.

The plots in Figure 5.2 are calculated using the low-frequency approximation to the EM phase speed. This approximation is valid provided frequency f is much less than the transition frequency $f_t = \sigma/2\pi\varepsilon$. The smallest transition frequency in Figure 5.2 is about 1800 Hz, corresponding to $\sigma = 10^{-6}$ S/m and $\varepsilon = 10\ \varepsilon_0$ with vacuum electric permittivity given by $\varepsilon_0 = 8.854\times10^{-12}$ F/m. So, the next frequency decade of f = 1000 Hz would not satisfy the low-frequency condition. This motivates developing an exact formula for EM wavelength, without requiring a low-frequency approximation. The exact phase speed, appropriate for the full frequency band, is given in Appendix A as

$$\frac{c(f)}{c_\infty} = \sqrt{\frac{2|f|}{f_t}}\left[\sqrt{1+\left(\frac{f}{f_t}\right)^2} - \frac{|f|}{f_t}\right]^{1/2}, \qquad \text{(A4.10a again)}$$

where $c_\infty = 1/\sqrt{\varepsilon\mu}$ is the infinite-frequency phase speed. The EM wavelength formula becomes

$$\frac{\lambda(f,\sigma,\mu,\varepsilon)}{\lambda_{ref}} = \sqrt{\frac{4\pi}{\sigma_{ref}\mu_{ref}f_{ref}\lambda_{ref}^2}}\ \frac{1}{\sqrt{(\sigma/\sigma_{ref})(\mu/\mu_{ref})(f/f_{ref})}}\ \times$$

$$\sqrt{\sqrt{1+\left(\frac{2\pi f_{ref}\varepsilon_{ref}}{\sigma_{ref}}\right)^2\left[\frac{(f/f_{ref})(\varepsilon/\varepsilon_{ref})}{(\sigma/\sigma_{ref})}\right]^2} - \left(\frac{2\pi f_{ref}\varepsilon_{ref}}{\sigma_{ref}}\right)\left[\frac{(f/f_{ref})(\varepsilon/\varepsilon_{ref})}{(\sigma/\sigma_{ref})}\right]}. \qquad (5.9)$$

The first factor on the right-hand-side, containing only medium parameters σ and μ, is identical to equation (5.7); the second factor containing σ and ε represents a multiplicative correction to account for higher frequencies. Taking the logarithm yields

$$\log_{10}\left[\frac{\lambda(f,\sigma,\mu,\varepsilon)}{\lambda_{ref}}\right] = \frac{1}{2}\log_{10}\left(\frac{4\pi}{\sigma_{ref}\mu_{ref}f_{ref}\lambda_{ref}^2}\right) - \frac{1}{2}\left[\log_{10}(\sigma/\sigma_{ref}) + \log_{10}(\mu/\mu_{ref}) + \log_{10}(f/f_{ref})\right]$$

$$+\frac{1}{2}\log_{10}\left\{\sqrt{1+\left(\frac{2\pi f_{ref}\varepsilon_{ref}}{\sigma_{ref}}\right)^2\left[\frac{(f/f_{ref})(\varepsilon/\varepsilon_{ref})}{10^{\log_{10}(\sigma/\sigma_{ref})}}\right]^2} - \left(\frac{2\pi f_{ref}\varepsilon_{ref}}{\sigma_{ref}}\right)\left[\frac{(f/f_{ref})(\varepsilon/\varepsilon_{ref})}{10^{\log_{10}(\sigma/\sigma_{ref})}}\right]\right\}. \qquad (5.10)$$

A logical choice for the reference value of electric permittivity is the vacuum value $\varepsilon_{ref} = \varepsilon_0 = 8.854\times10^{-12}$ F/m. Once again, the first two terms on the right-hand-side are appropriate for low-frequencies. The third term is an additive correction accounting for high-frequencies.

Top and middle panels of the following Figure 5.3 depict logarithmic EM wavelength calculated via the approximate (i.e., low-frequency) formula (5.8a) and the exact formula (5.10), for frequency f = 1000 Hz, respectively. The exact calculation leads to a slight curvature in the contours at very small conductivity values; at high conductivities there is no apparent difference between the panels. The linear contour distortion is accentuated at even higher frequency f = 10,000 Hz, as indicated in the bottom panel.

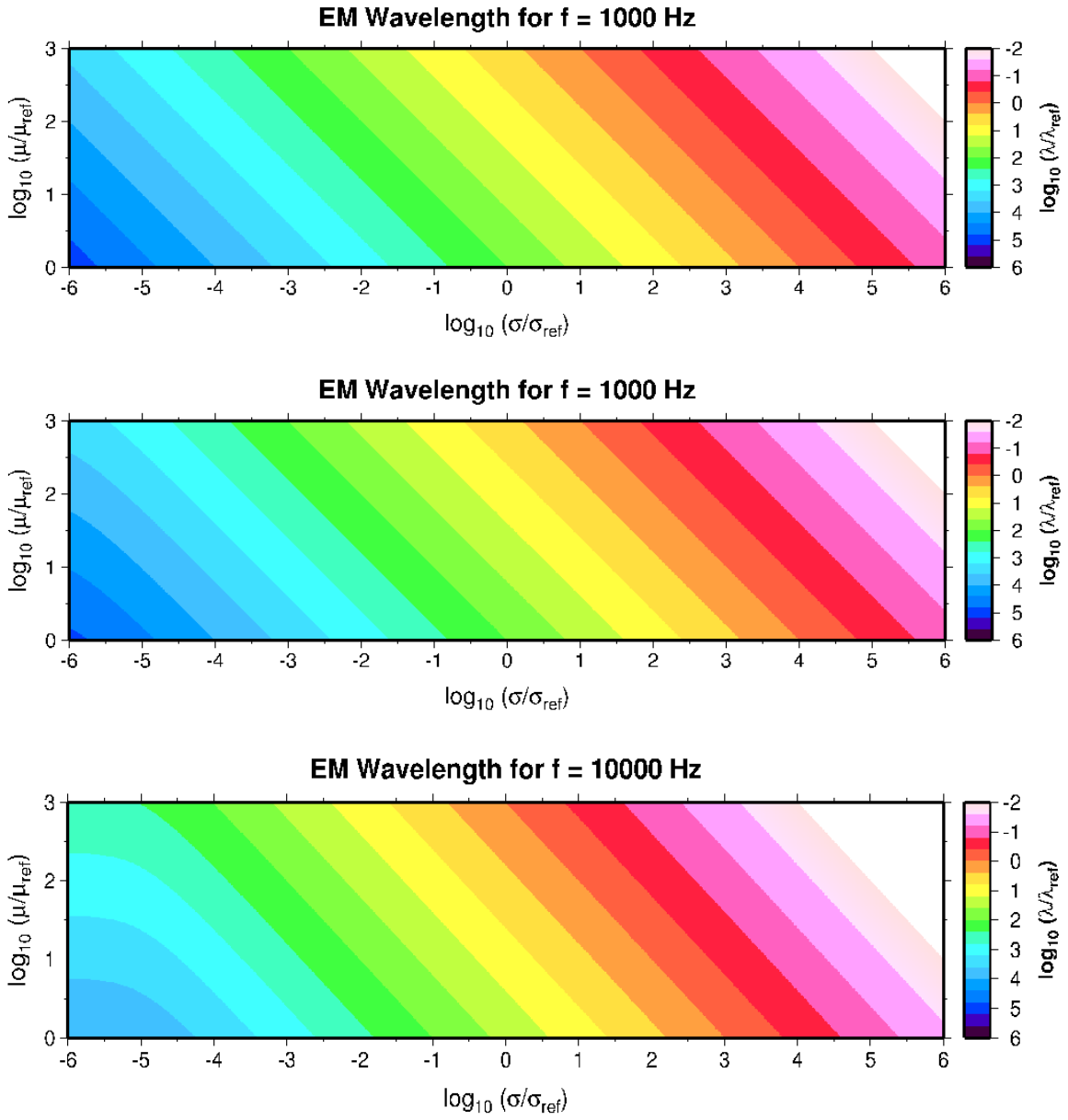

Figure 5.3. Logarithm of electromagnetic wavelength *vs*. logarithmic conductivity and logarithmic permeability. Top and middle panels are calculated with approximate (i.e., low-frequency) and exact formulae for frequency f = 1000 Hz, respectively. Bottom panel is exact calculation for f = 10,000 Hz. Electric permittivity $\varepsilon = 10\ \varepsilon_0$ is used for the calculations.

However, it is unlikely that such a high frequency would be utilized in a deep-target geophysical exploration context. On the other hand, ground penetrating radar (GPR) is used for shallow subsurface EM investigations (say, on the order of tens of meters). Hence, in Figure 5.4 below we extend the wavelength calculations to f = 100,000 Hz and f = 1,000,000 Hz in order to visualize the high-frequency effect.

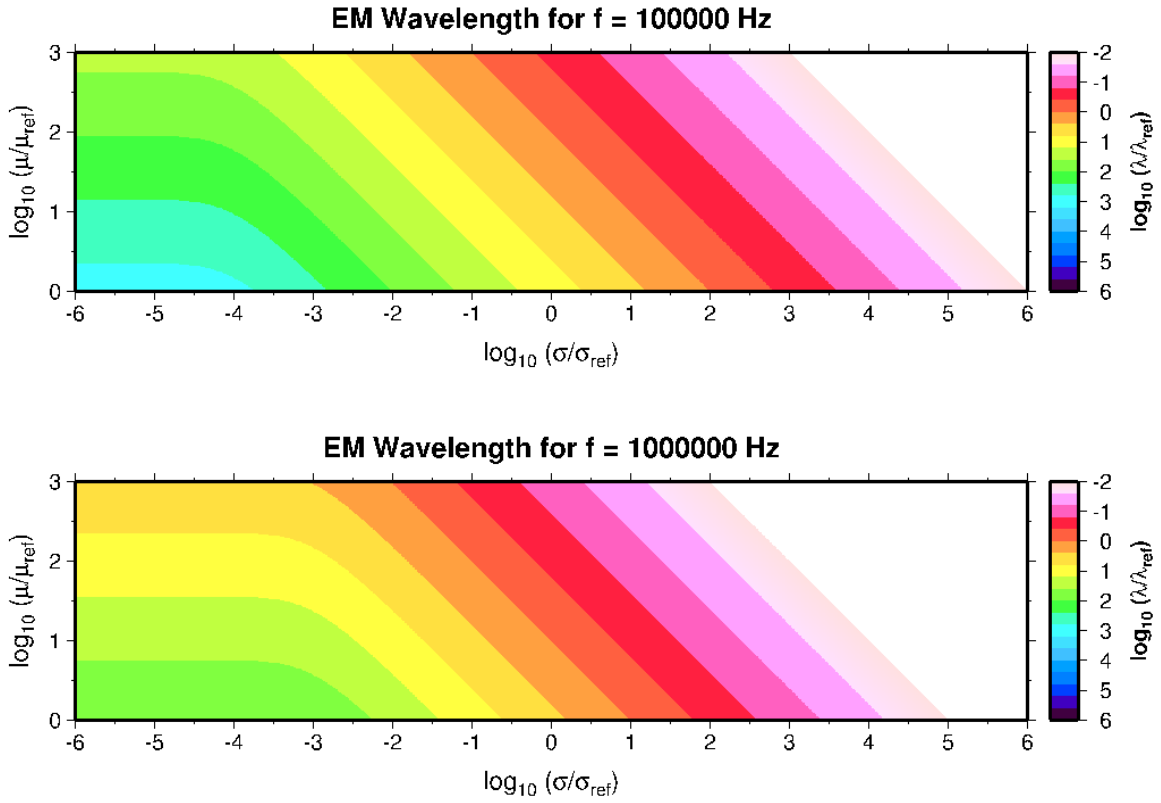

Figure 5.4. Logarithm of electromagnetic wavelength *vs*. logarithmic conductivity and logarithmic permeability, calculated with exact formula for frequency f = 100,000 Hz (top), and f = 1,000,000 Hz (bottom). Electric permittivity $\varepsilon = 10\ \varepsilon_0$ is used for the calculations.

As frequency increases, EM wavelength becomes independent of current conductivity and depends only on magnetic permeability (and the assumed electric permittivity). This evident on the left-hand-side of the panels for small conductivity values. Consider the high-frequency approximation for wavelength

$$\frac{\lambda(f,\mu,\varepsilon)}{\lambda_{ref}} \approx \left(\frac{c_\infty}{f_{ref}\lambda_{ref}}\right) \frac{1}{\sqrt{(\varepsilon/\varepsilon_{ref})(\mu/\mu_{ref})}} \frac{1}{(f/f_{ref})},$$

where infinite-frequency phase speed is $c_\infty = 1/\sqrt{\varepsilon\mu}$. In logarithmic form

$$\log_{10}\left[\frac{\lambda(f,\mu,\varepsilon)}{\lambda_{ref}}\right] \approx \log_{10}\left(\frac{c_\infty}{f_{ref}\lambda_{ref}}\right) - \frac{1}{2}\left[\log_{10}(\varepsilon/\varepsilon_0) + \log_{10}(\mu/\mu_0) + 2\log_{10}(f/f_{ref})\right],$$

where medium parameter reference values are taken as $\varepsilon_{ref} = \varepsilon_0$ and $\mu_{ref} = \mu_0$. So, in the high-frequency approximation, a better graphic approach is to contour logarithmic wavelength *vs*. logarithmic permittivity and logarithmic permeability, holding logarithmic frequency fixed.

An alternative way of examining the material parameter dependence of the thin bed criterion $\|iK_2(\omega)2h\| << 1$ is to substitute in the expression for the low-frequency complex wavenumber $K_2(\omega) \approx \sqrt{\sigma_2 \mu_2 \omega / 2}\,(1+i)$. After converting to temporal frequency $f = \omega/2\pi$, this yields the condition

$$\sqrt{8\pi\sigma_2\mu_2 f h^2} << 1, \tag{5.11a}$$

or after squaring

$$8\pi\sigma_2\mu_2 f h^2 <<< 1. \tag{5.11b}$$

In non-dimensional form:

$$\left(8\pi\sigma_{ref}\mu_{ref} f_{ref} h^2\right)\left(\sigma_2/\sigma_{ref}\right)\left(\mu_2/\mu_{ref}\right)\left(f/f_{ref}\right) <<< 1. \tag{5.11c}$$

Adopting the usual reference values

$$\sigma_{ref} = 1\,\text{S/m}, \qquad \mu_{ref} = \mu_0 = 4\pi\times 10^{-7}\ \text{H/m}, \qquad f_{ref} = 1\,\text{Hz},$$

yields the numerical form

$$\left(32\pi^2\times 10^{-7}\,\text{m}^{-2}\right)h^2\left(\sigma_2/\sigma_{ref}\right)\left(\mu_2/\mu_0\right)\left(f/f_{ref}\right) <<< 1, \tag{5.11d}$$

with bed thickness h measured in the SI unit m. Hence, the thin bed condition requires small relative conductivity, small relative permeability, and small relative frequency, in addition to small thickness. These appear to be rather severe restrictions, which must hold simultaneously! For example, consider a hydraulic fracture injected with electrically conductive proppant with $\sigma_2/\sigma_{ref} \sim 10^{+6}$ and $\mu_2/\mu_0 \sim 10^{+2}$ (~steel) and interrogated with an EM plane wave signal with frequency f = 1 Hz. For thinness, the bed thickness must then satisfy $h << 1/8\pi\sqrt{5} \approx 0.018\,\text{m} = 1.8\,\text{cm}$. Hence, a fracture of width h = 1 mm (about 20 times less than the limit) might be considered adequately thin.

This quantitative development of the multiple criteria constituting a thin geologic layer is important for understanding the First Born Approximation (FBA) scattering theory developed in the subsequent Section 6.0. Briefly, Born scattering is a reasonably accurate approximation to exact scattering if the layer is i) thin, ii) has low conductivity, iii) has low permeability, and iv) is illuminated with a low-frequency EM signal.

5.3 Backward Scattering

The *back-scattered* electric vector component, observed at a receiver position z_r on the same side of the geologic layer as the source position z_s, is defined as the difference

$$E_{bak}(z_s, z_r, \omega) \equiv \{ E_{inc}(z_s, z_r, \omega) + \Re(z_s, z_r, \omega) \}$$

$$- \{ E_{inc}(z_s, z_r, \omega) + E_{inc}(z_s, \omega) e^{+iK_1(\omega)(z_{mid} - z_s)} R_{mid}(\omega) e^{+iK_1(\omega)(z_{mid} - z_r)} \}. \qquad (5.12)$$

That is, the back-scattered response is the actual reflection response of the layer *minus* the reflection response of the single plane interface located at the layer midpoint. [We include the incident wavefield in equation (5.12) as a formality; clearly it cancels out by subtraction.] Substituting the reflection response $\Re(z_s, z_r, \omega)$ from equation (3.4b) and simplifying yields the form

$$E_{bak}(z_s, z_r, \omega) = E_{inc}(z_s, \omega) e^{+iK_1(\omega)(2z_{mid} - z_s - z_r)}$$

$$\times \left\{ \frac{R_{top}(\omega) + R_{bot}(\omega) e^{+iK_2(\omega)2h}}{1 + R_{top}(\omega) R_{bot}(\omega) e^{+iK_2(\omega)2h}} e^{-iK_1(\omega)h} - R_{mid}(\omega) \right\}, \qquad (5.13)$$

where $R_{top}(\omega)$ and $R_{bot}(\omega)$ are the top-interface and bottom-interface reflection coefficients.

In the important special case where medium #3 is identical to medium #1, we have $K_3(\omega) = K_1(\omega)$, $R_{bot}(\omega) = -R_{top}(\omega)$, and $R_{mid}(\omega) = 0$. Then, the exact back-scattered electric field (5.13) reduces to the simpler form

$$E_{bak}(z_s, z_r, \omega) = E_{inc}(z_s, \omega) e^{+iK_1(\omega)(2z_{mid} - z_s - z_r)} \; R_{top}(\omega) \left\{ \frac{1 - e^{+iK_2(\omega)2h}}{1 - R_{top}(\omega)^2 e^{+iK_2(\omega)2h}} \right\} e^{-iK_1(\omega)h}. \qquad (5.14a)$$

Of course, this is identical to the *actual* reflected response of the layer (say, from equation (3.6) above), because the homogeneous reference medium does not generate any reflected energy. Alternately, in terms of the incident electric field at the midpoint of the layer

$$E_{bak}(z_s, z_r, \omega) = E_{inc}(z_{mid}, \omega) e^{+iK_1(\omega)(z_{mid} - z_r)} R_{top}(\omega) \; \left\{ \frac{1 - e^{+iK_2(\omega)2h}}{1 - R_{top}(\omega)^2 e^{+iK_2(\omega)2h}} \right\} e^{-iK_1(\omega)h}. \qquad (5.14b)$$

The back-scattered response is directly proportional to the incident EM wavefield at the midpoint z_{mid}. However, a third version that we will subsequently utilize is

$$E_{bak}(z_s, z_r, \omega) = E_{inc}(2z_{mid} - z_r, \omega) \, R_{top}(\omega) \left\{ \frac{1 - e^{+iK_2(\omega)2h}}{1 - R_{top}(\omega)^2 e^{+iK_2(\omega)2h}} \right\} e^{-iK_1(\omega)h}. \qquad (5.14c)$$

In this version, the back-scattered wavefield is proportional to the incident wavefield at the coordinate $2z_{mid} - z_r$. Often, the midpoint coordinate z_{mid} is taken to be zero, implying that $-z_r$ is a *positive* number.

This field is multiplied by a frequency-dependent filter (which depends on the layer thickness and EM parameters).

We now expand the back-scattered response of (5.14c) to first order in the dimensionless quantity $iK_2(\omega)2h$:

$$E_{bak}(z_s, z_r, \omega) \approx E_{inc}(2z_{mid} - z_r, \omega)\left[\frac{-R_{top}(\omega)}{1-R_{top}(\omega)^2}\right](iK_2(\omega)2h). \tag{5.15}$$

[Exponential $e^{-iK(\omega)h}$ approximates as unity.] From equation (B9a) of Appendix B, the top-interface reflection coefficient may be expressed in terms of dimensionless ratios of wavenumbers and permeabilities as

$$R_{top}(\omega) = \frac{1-\left(\hat{K}(\omega)/\hat{\mu}\right)}{1+\left(\hat{K}(\omega)/\hat{\mu}\right)}, \tag{5.16}$$

with

$$\hat{K}(\omega) \equiv \frac{K_2(\omega)}{K_1(\omega)}, \qquad \hat{\mu} \equiv \frac{\mu_2}{\mu_1}. \tag{5.17a,b}$$

These dimensionless ratios are constructed as "layer parameters" divided by "incident medium parameters". The first-order approximate back-scattered response becomes

$$E_{bak}(z_s, z_r, \omega) \approx E_{inc}(2z_{mid} - z_r, \omega)\frac{1}{4}\left[\frac{\hat{K}(\omega)}{\hat{\mu}} - \frac{\hat{\mu}}{\hat{K}(\omega)}\right](iK_2(\omega)2h), \tag{5.18a}$$

or expressed in terms of the complex wavenumber of the incident medium:

$$E_{bak}(z_s, z_r, \omega) \approx E_{inc}(2z_{mid} - z_r, \omega)\frac{h}{2}\left[\frac{\hat{K}(\omega)^2}{\hat{\mu}} - \hat{\mu}\right] iK_1(\omega). \tag{5.18b}$$

We now examine the low-frequency regime for the above thin-bed back-scattered response. From equation (A4.15) of Appendix A, the low-frequency approximation to the complex wavenumber is

$$K(\omega) \approx \sqrt{\sigma\mu|\omega|}\,\mathrm{sgn}(\omega)e^{+i\,\mathrm{sgn}(\omega)(\pi/4)}. \tag{A4.15}$$

The dimensionless wavenumber ratio becomes $\hat{K}(\omega) = K_2(\omega)/K_1(\omega) = \sqrt{\hat{\sigma}\hat{\mu}}$, where a dimensionless conductivity ratio is similarly defined as

$$\hat{\sigma} \equiv \frac{\sigma_2}{\sigma_1}. \tag{5.17c}$$

Then, the low-frequency backscattered field is:

$$E_{bak}(z_s, z_r, \omega)\big|_{lo} \approx E_{inc}(2z_{mid} - z_r, \omega)\frac{h}{2}(\hat{\sigma} - \hat{\mu})\sqrt{\sigma_1 \mu_1 |\omega|}\left[i\,\mathrm{sgn}(\omega) e^{+i\,\mathrm{sgn}(\omega)(\pi/4)}\right].$$

But $i\,\mathrm{sgn}(\omega) e^{+i\,\mathrm{sgn}(\omega)(\pi/4)} = e^{+i\,\mathrm{sgn}(\omega)(3\pi/4)}$, yielding the (perhaps simpler) form

$$E_{bak}(z_s, z_r, \omega)\big|_{lo} \approx \frac{h}{2}(\hat{\sigma} - \hat{\mu})\sqrt{\sigma_1 \mu_1}\ \left[E_{inc}(2z_{mid} - z_r, \omega)\sqrt{|\omega|} e^{+i\,\mathrm{sgn}(\omega)(3\pi/4)}\right]. \tag{5.19}$$

Note that this expression embodies the several approximations of previous inequality condition (5.11d): thin layer, low-frequency, and "small" layer parameters σ_2 and μ_2. The low-frequency back-scattered EM wavefield is directly proportional to:

1) The layer half thickness $h/2$,
2) The difference in parameter contrast ratios $(\hat{\sigma} - \hat{\mu})$.

Interestingly, if both parameter contrast ratios are identical, then the back-scattered wavefield vanishes! This is a particular manifestation of the general conditions for vanishing normal incidence reflection coefficient outlined in Appendix B; if all three parameters of medium #2 are obtained by scaling the corresponding parameters of medium #1, then the reflection coefficient equals zero (at all frequencies). Also, note that conductivity enhancement acts in an opposite manner than permeability enhancement. That is, if $\hat{\sigma} > 1$ and $\hat{\mu} = 1$ then $(\hat{\sigma} - \hat{\mu}) > 0$ (positive), whereas if $\hat{\mu} > 1$ and $\hat{\sigma} = 1$ then $(\hat{\sigma} - \hat{\mu}) < 0$ (negative). This realization might be exploited in a back-scattering data acquisition experiment to distinguish the (unknown) scattering properties of a layer.

Finally, in the space-time domain, the low-frequency back-scattered field is expressed as

$$e_{bak}(z_s, z_r, t)\big|_{lo} \approx \frac{h}{2}(\hat{\sigma} - \hat{\mu})\sqrt{\sigma_1 \mu_1}\ \ e_{inc}(2z_{mid} - z_r, t) * \mathrm{F}^{-1}\left\{\sqrt{|\omega|} e^{+i\,\mathrm{sgn}(\omega)(3\pi/4)}\right\}, \tag{5.20}$$

where the asterisk denotes convolution and $\mathrm{F}^{-1}\{\ \}$ indicates inverse Fourier transformation. The inverse transform in (5.20) does not exist in the conventional sense. However, analysis on the complex-valued plane (draw a picture!) reveals the correspondence

$$\sqrt{|\omega|} e^{+i\,\mathrm{sgn}(\omega)(3\pi/4)} \leftrightarrow (-i\omega)^{1/2}.$$

Fractional derivative calculus (i.e, Bracewell, 1965, page 119) then implies that the inverse Fourier transform equals the half-integer differentiation operator: $F^{-1}\left\{\sqrt{|\omega|} e^{+i\,\mathrm{sgn}(\omega)(3\pi/4)}\right\} = d^{1/2}/dt^{1/2}$. Time-domain equation (5.20) becomes

$$e_{bak}(z_s, z_r, t)\big|_{lo} \approx \frac{h}{2}(\hat{\sigma} - \hat{\mu})\sqrt{\sigma_1 \mu_1}\ \ \frac{\partial^{1/2} e_{inc}(2z_{mid} - z_r, t)}{\partial t^{1/2}}. \tag{5.21}$$

The low-frequency back-scattered wavefield is proportional to the half-integer time-derivative of the incident plane wave EM wavefield at location $2z_{mid} - z_r$. So, in the common case where $z_{mid} = 0$, the EM wavefield is evaluated at the *positive* coordinate $-z_r$, on the opposite (i.e., fore-scattered) side of the bed from the back-scattered response. This properly accounts for plane wave dispersion/attenuation over the complete back-scattered travel path from source z_s to receiver z_r.

5.4 Forward Scattering

The *forward-scattered* electromagnetic wavefield, observed at a receiver position z_r on the opposite side of the geologic layer as the source position z_s, is defined as the difference

$$E_{for}(z_s, z_r, \omega) \equiv \mathcal{I}(z_s, z_r, \omega) - E_{inc}(z_s, \omega) e^{+iK_1(\omega)(z_{mid} - z_s)} T_{13}(\omega) e^{+iK_3(\omega)(z_r - z_{mid})}. \tag{5.22}$$

That is, the forward-scattered response is the actual transmission response of the layer *minus* the EM wavefield transmitted through a single plane interface located at the layer midpoint. Substituting expression (4.3b) for the transmitted response and simplifying yields

$$E_{for}(z_s, z_r, \omega) = E_{inc}(z_s, \omega) e^{+iK_1(\omega)(z_{top} - z_s)} \; e^{+iK_3(\omega)(z_r - z_{bot})}$$

$$\times \left\{ \frac{\left(1 + R_{top}(\omega)\right)\left(1 + R_{bot}(\omega)\right) e^{+iK_2(\omega)h}}{1 + R_{top}(\omega) R_{bot}(\omega) e^{+iK_2(\omega)2h}} - \left(1 + R_{mid}(\omega)\right) e^{+i0.5(K_1(\omega) + K_3(\omega))h} \right\}, \tag{5.23}$$

where $T_{13}(\omega) = 1 + R_{mid}(\omega)$ is used.

In the particular case where medium #3 identical to medium #1, we again have $K_3(\omega) = K_1(\omega)$, $R_{bot}(\omega) = -R_{top}(\omega)$, and $R_{mid}(\omega) = 0$. Then, the exact forward-scattered electric field (5.23) reduces to

$$E_{for}(z_s, z_r, \omega) = E_{inc}(z_s, \omega) e^{+iK_1(\omega)(z_r - z_s)} \quad \left\{ \frac{\left[1 - R_{top}(\omega)^2\right] e^{+i[K_2(\omega) - K_1(\omega)]h}}{1 - R_{top}(\omega)^2 e^{+iK_2(\omega)2h}} - 1 \right\}, \tag{5.24a}$$

which is the same as

$$E_{for}(z_s, z_r, \omega) = E_{inc}(z_r, \omega) \; \left\{ \frac{\left[1 - R_{top}(\omega)^2\right] e^{+i[K_2(\omega) - K_1(\omega)]h}}{1 - R_{top}(\omega)^2 e^{+iK_2(\omega)2h}} - 1 \right\}. \tag{5.24b}$$

Analogous to the back-scattering situation, the forward-scattered response depends on the incident wavefield at the receiver location z_r. This incident wavefield is multiplied by a frequency-dependent filter (the braces { } in expression (5.24b)).

Expanding to first-order in $iK_2(\omega)2h$ (equivalent to first-order in the bed thickness h) gives

$$E_{for}(z_s, z_r, \omega) \approx E_{inc}(z_r, \omega) \left[\frac{1 + R_{top}(\omega)^2}{1 - R_{top}(\omega)^2} - \frac{K_1(\omega)}{K_2(\omega)} \right] \left(iK_2(\omega)h\right). \tag{5.25}$$

Utilizing $R_{top}(\omega) = \dfrac{1 - \left(\hat{K}(\omega)/\hat{\mu}\right)}{1 + \left(\hat{K}(\omega)/\hat{\mu}\right)}$ with $\hat{K}(\omega) \equiv \dfrac{K_2(\omega)}{K_1(\omega)}$ and $\hat{\mu} \equiv \dfrac{\mu_2}{\mu_1}$ yields:

$$E_{for}(z_s, z_r, \omega) \approx E_{inc}(z_r, \omega)\ \frac{1}{2}\left[\frac{\hat{K}(\omega)}{\hat{\mu}} + \frac{(\hat{\mu}-2)}{\hat{K}(\omega)}\right](iK_2(\omega)h)$$

$$= E_{inc}(z_r, \omega)\ \frac{h}{2}\left[\frac{\hat{K}(\omega)^2}{\hat{\mu}} + \hat{\mu} - 2\right] iK_1(\omega)\,. \qquad (5.26)$$

This has a remarkable similarity to the EM wavefield (5.18b) back-scattered from a thin layer, although the incident plane wave is evaluated at positive coordinate z_r. The low-frequency approximation for forward scattering is now developed.

Substituting in the low-frequency approximation (A4.15) for the complex wavenumber gives

$$E_{for}(z_r, z_s, \omega)\Big|_{lo} \approx \frac{h}{2}(\hat{\sigma} + \hat{\mu} - 2)\sqrt{\sigma_1 \mu_1}\ \left[E_{inc}(z_r, \omega)\sqrt{|\omega|}e^{+i\,\mathrm{sgn}(\omega)(3\pi/4)}\right]. \qquad (5.27)$$

Inverting this to the space-time domain yields

$$e_{for}(z_r, z_s, t)\Big|_{lo} \approx \frac{h}{2}(\hat{\sigma} + \hat{\mu} - 2)\sqrt{\sigma_1 \mu_1}\ \ e_{inc}(z_r, t) * F^{-1}\left\{\sqrt{|\omega|}e^{+i\,\mathrm{sgn}(\omega)(3\pi/4)}\right\}$$

$$= \frac{h}{2}(\hat{\sigma} + \hat{\mu} - 2)\sqrt{\sigma_1 \mu_1}\ \ \frac{\partial^{1/2} e_{inc}(z_r, t)}{\partial t^{1/2}}\,. \qquad (5.28)$$

This exhibits the same half-integer time-derivative dependence as the low-frequency back-scattered response (5.21). However, in contrast to the back-scattering situation, conductivity enhancement and permeability enhancement have the *same* algebraic sign effect here. Of course, $\hat{\sigma} = \hat{\mu} = 1$ implies the forward-scattered wavefield vanishes. But $\hat{\sigma} = \hat{\mu} = (\text{say})10$ implies that the fore-scattering multiplier is 18, whereas the back-scattering multiplier is 0.

In order to facilitate a visual comparison of the various time-domain approximations for the scattered electric field responses, we construct the following table appropriate for a *thin* geologic bed within a homogeneous background medium (i.e., medium #1 = medium #3). In addition to the low-frequency responses derived above, we exhibit very-high-frequency (i.e., in the limit $\omega \to \infty$) responses obtained by using the a high-frequency approximation to the complex wavenumber. These particular responses are not derived here.

Thin Bed (h << λ) Time Domain Scattered Responses

	Low-Frequency	Very-High-Frequency
Backward Scattering	$\approx \frac{h}{2}(\hat{\sigma}-\hat{\mu})\sqrt{\sigma_1\mu_1}\ \frac{\partial^{1/2} e_{inc}(2z_{mid}-z_r,t)}{\partial t^{1/2}}$	$\approx \frac{h}{2}(\hat{\mu}-\hat{\varepsilon})\sqrt{\varepsilon_1\mu_1}\ \frac{\partial e_{inc}(2z_{mid}-z_r,t)}{\partial t}$
Forward Scattering	$\approx \frac{h}{2}(\hat{\sigma}+\hat{\mu}-2)\sqrt{\sigma_1\mu_1}\ \frac{\partial^{1/2} e_{inc}(z_r,t)}{\partial t^{1/2}}$	$\approx \frac{h}{2}(2-\hat{\mu}-\hat{\varepsilon})\sqrt{\varepsilon_1\mu_1}\ \frac{\partial e_{inc}(z_r,t)}{\partial t}$

Table 5.1. Thin-bed time-domain scattering formulae.

All four responses are directly proportional to the bed half thickness *h*/2. Low- and high-frequency responses are proportional to one-half and unity time derivatives of the incident plane electric field $e_{inc}(z,t)$, respectively. Symbols subscripted by "1" (i.e., $\varepsilon_1, \mu_1, \sigma_1$) are the EM medium parameters characterizing the reference (or background) wholespace. Symbols with a superposed "hat" (i.e., $\hat{\varepsilon}=\varepsilon_2/\varepsilon_1, \hat{\mu}=\mu_2/\mu_1, \hat{\sigma}=\sigma_2/\sigma_1$) are dimensionless ratios of the layer parameters to the surrounding wholespace parameters. Low- and high-frequency scattering are independent of permittivity contrast $\hat{\varepsilon}$ and conductivity contrast $\hat{\sigma}$, respectively. Once again, note that the condition $\hat{\varepsilon}=\hat{\mu}=\hat{\sigma}=r$ (where ratio *r* need not equal unity) implies zero backward scattering and enhanced forward scattering.

The analogous table of approximate thin bed frequency-domain response filters is:

Thin Bed (h << λ) Frequency-Domain Scattering Filters

	Low-Frequency	Very-High-Frequency
Backward Scattering	$\approx \frac{h}{2}(\hat{\sigma}-\hat{\mu})\sqrt{\sigma_1\mu_1}\left(\sqrt{\lvert\omega\rvert}e^{+i\,\mathrm{sgn}(\omega)(3\pi/4)}\right)$	$\approx \frac{h}{2}(\hat{\mu}-\hat{\varepsilon})\sqrt{\varepsilon_1\mu_1}\,(-i\omega)$
Forward Scattering	$\approx \frac{h}{2}(\hat{\sigma}+\hat{\mu}-2)\sqrt{\sigma_1\mu_1}\left(\sqrt{\lvert\omega\rvert}e^{+i\,\mathrm{sgn}(\omega)(3\pi/4)}\right)$	$\approx \frac{h}{2}(2-\hat{\mu}-\hat{\varepsilon})\sqrt{\varepsilon_1\mu_1}\,(-i\omega)$

Table 5.2. Thin-bed frequency-domain scattering formulae.

Back-scattering filters multiple the Fourier-transformed incident plane wave electric vector component $E_{inc}(2z_{mid}-z_r,\omega)$, whereas fore-scattering filters multiply $E_{inc}(z_r,\omega)$. Interestingly, for z_{mid} = 0, this is the *same* location in space.

5.5 Scattering Ratio

The (complex-valued) ratio of the backward-scattered wavefield to the forward-scattered wavefield may be a useful quantity for optimizing experiment design. In order to formulate this quantity, substitute equation (5.16) for the top-interface normal-incidence reflection coefficient

$$R_{top}(\omega) = \frac{1-\left(\hat{K}(\omega)/\hat{\mu}\right)}{1+\left(\hat{K}(\omega)/\hat{\mu}\right)}, \qquad \text{(5.16 again)}$$

into the previously-derived expressions for the scattered wavefields. Here $\hat{K}(\omega) = K_2(\omega)/K_1(\omega)$ and $\hat{\mu} = \mu_2/\mu_1$ are dimensionless ratios of complex wavenumbers and magnetic permeabilities, respectively. We specialize to the important case where medium #3 is identical to medium #1. From equation (5.14c), the back-scattered electric vector *x*-component is

$$E_{bak}(z,\omega) = E_{inc}(2z_{mid} - z_r, \omega)\left\{\frac{\frac{1}{2}\left[\frac{\hat{K}(\omega)}{\hat{\mu}} - \frac{\hat{\mu}}{\hat{K}(\omega)}\right]\tanh\left[iK_2(\omega)h\right]}{1-\frac{1}{2}\left[\frac{\hat{K}(\omega)}{\hat{\mu}} + \frac{\hat{\mu}}{\hat{K}(\omega)}\right]\tanh\left[iK_2(\omega)h\right]}\right\} e^{-iK_1(\omega)h}. \qquad \text{(5.29a)}$$

From equation (5.24b), the analogous forward-scattered wavefield is

$$E_{for}(z_r,\omega) = E_{inc}(z_r,\omega)\left\{\frac{\operatorname{sech}\left[iK_2(\omega)h\right]e^{-iK_1(\omega)h}}{1-\frac{1}{2}\left[\frac{\hat{K}(\omega)}{\hat{\mu}} + \frac{\hat{\mu}}{\hat{K}(\omega)}\right]\tanh\left[iK_2(\omega)h\right]} - 1\right\}. \qquad \text{(5.29b)}$$

Here $\tanh(z) \equiv \frac{\sinh(z)}{\cosh(z)} \approx z - \frac{z^3}{3}$ and $\operatorname{sech}(z) \equiv \frac{1}{\cosh(z)} \approx 1 - \frac{z^2}{2}$ where $z = x+iy$ is a complex number. With $K_2(\omega) = \hat{K}(\omega)K_1(\omega)$ these expressions become

$$E_{bak}(z_r,\omega) = E_{inc}(2z_{mid} - z_r, \omega)\left\{\frac{\frac{1}{2}\left[\frac{\hat{K}(\omega)}{\hat{\mu}} - \frac{\hat{\mu}}{\hat{K}(\omega)}\right]\tanh\left[\hat{K}(\omega)iK_1(\omega)h\right]}{1-\frac{1}{2}\left[\frac{\hat{K}(\omega)}{\hat{\mu}} + \frac{\hat{\mu}}{\hat{K}(\omega)}\right]\tanh\left[\hat{K}(\omega)iK_1(\omega)h\right]}\right\} e^{-iK_1(\omega)h}, \qquad \text{(5.30a)}$$

and

$$E_{for}(z_r,\omega) = E_{inc}(z_r,\omega)\left\{\frac{\operatorname{sech}\left[\hat{K}(\omega)iK_1(\omega)h\right]e^{-iK_1(\omega)h}}{1-\frac{1}{2}\left[\frac{\hat{K}(\omega)}{\hat{\mu}} + \frac{\hat{\mu}}{\hat{K}(\omega)}\right]\tanh\left[\hat{K}(\omega)iK_1(\omega)h\right]} - 1\right\}. \qquad \text{(5.30b)}$$

At low-frequencies, the complex wavenumber is $K(\omega) \approx \sqrt{\sigma\mu|\omega|}\,\mathrm{sgn}(\omega)e^{+i\,\mathrm{sgn}(\omega)(\pi/4)}$, implying $\hat{K}(\omega) = \sqrt{\hat{\sigma}\hat{\mu}}$. Also, $i\,\mathrm{sgn}(\omega)e^{+i\,\mathrm{sgn}(\omega)(\pi/4)} = e^{+i\,\mathrm{sgn}(\omega)(3\pi/4)}$ and $\sqrt{|\omega|}e^{+i\,\mathrm{sgn}(\omega)(3\pi/4)} = (-i\omega)^{1/2}$. Hence

$$iK_1(\omega)h = \sqrt{\sigma_1\mu_1|\omega|}\; e^{+i\,\mathrm{sgn}(\omega)(3\pi/4)}h = \sqrt{\sigma_1\mu_1}\,\sqrt{-i\omega}\;h = \sqrt{-i\omega\sigma_1\mu_1}\,h\,.$$

Substituting this into the above scattering expressions gives the forms

$$E_{bak}(z_r,\omega) = E_{inc}(2z_{mid} - z_r,\omega)\left\{\frac{\frac{1}{2}\left[\sqrt{\frac{\hat{\sigma}}{\hat{\mu}}} - \sqrt{\frac{\hat{\mu}}{\hat{\sigma}}}\right]\tanh\left[\sqrt{\hat{\sigma}\hat{\mu}}\sqrt{-i\omega\sigma_1\mu_1}h\right]}{1-\frac{1}{2}\left[\sqrt{\frac{\hat{\sigma}}{\hat{\mu}}} + \sqrt{\frac{\hat{\mu}}{\hat{\sigma}}}\right]\tanh\left[\sqrt{\hat{\sigma}\hat{\mu}}\sqrt{-i\omega\sigma_1\mu_1}h\right]}\right\}e^{-\sqrt{-i\omega\sigma_1\mu_1}h}, \qquad (5.31a)$$

and

$$E_{for}(z_r,\omega) = E_{inc}(z_r,\omega)\left\{\frac{\mathrm{sech}\left[\sqrt{\hat{\sigma}\hat{\mu}}\sqrt{-i\omega\sigma_1\mu_1}h\right]e^{-\sqrt{-i\omega\sigma_1\mu_1}h}}{1-\frac{1}{2}\left[\sqrt{\frac{\hat{\sigma}}{\hat{\mu}}} + \sqrt{\frac{\hat{\mu}}{\hat{\sigma}}}\right]\tanh\left[\sqrt{\hat{\sigma}\hat{\mu}}\sqrt{-i\omega\sigma_1\mu_1}h\right]} - 1\right\}. \qquad (5.31b)$$

Next, the low-frequency wavelength of an EM wave propagating in medium #1 (the incident medium) is

$$\lambda_1(\omega) \approx 2\pi\sqrt{\frac{2}{\sigma_1\mu_1\omega}} \quad \text{which implies} \quad \sqrt{-i\omega\sigma_1\mu_1}h = \frac{2\pi(1-i)h}{\lambda_1(\omega)}\,.$$

Then, the above scattering formulae are recast as

$$E_{bak}(z_r,\omega) = E_{inc}(2z_{mid} - z_r,\omega)\left\{\frac{\frac{1}{2}\left[\sqrt{\frac{\hat{\sigma}}{\hat{\mu}}} - \sqrt{\frac{\hat{\mu}}{\hat{\sigma}}}\right]\tanh\left[2\pi(1-i)\sqrt{\hat{\sigma}\hat{\mu}}\,(h/\lambda_1(\omega))\right]}{1-\frac{1}{2}\left[\sqrt{\frac{\hat{\sigma}}{\hat{\mu}}} + \sqrt{\frac{\hat{\mu}}{\hat{\sigma}}}\right]\tanh\left[2\pi(1-i)\sqrt{\hat{\sigma}\hat{\mu}}\,(h/\lambda_1(\omega))\right]}\right\}e^{-2\pi(1-i)(h/\lambda_1(\omega))}, \qquad (5.32a)$$

and

$$E_{for}(z_r,\omega) = E_{inc}(z_r,\omega)\left\{\frac{\mathrm{sech}\left[2\pi(1-i)\sqrt{\hat{\sigma}\hat{\mu}}\,(h/\lambda_1(\omega))\right]e^{-2\pi(1-i)(h/\lambda_1(\omega))}}{1-\frac{1}{2}\left[\sqrt{\frac{\hat{\sigma}}{\hat{\mu}}} + \sqrt{\frac{\hat{\mu}}{\hat{\sigma}}}\right]\tanh\left[2\pi(1-i)\sqrt{\hat{\sigma}\hat{\mu}}\,(h/\lambda_1(\omega))\right]} - 1\right\}. \qquad (5.32b)$$

These are our working expressions for the backward- and forward-scattered wavefields. The ratio of these two wavefields is easily put into the form

$$SR(\omega) \equiv \frac{E_{bak}(z_r,\omega)}{E_{for}(z_r,\omega)} = \left[\frac{E_{inc}(2z_{mid} - z_r(<z_{top}),\omega)}{E_{inc}(z_r(>z_{bot}),\omega)}\right] \times$$

$$\left\{\frac{\left[\sqrt{\frac{\hat{\sigma}}{\hat{\mu}}} - \sqrt{\frac{\hat{\mu}}{\hat{\sigma}}}\right]\sinh\left[\sqrt{\hat{\sigma}\hat{\mu}}\ \beta_1(\omega)\right]e^{-\beta_1(\omega)}}{\left[\sqrt{\frac{\hat{\sigma}}{\hat{\mu}}} + \sqrt{\frac{\hat{\mu}}{\hat{\sigma}}}\right]\sinh\left[\sqrt{\hat{\sigma}\hat{\mu}}\ \beta_1(\omega)\right] - 2\cosh\left[\sqrt{\hat{\sigma}\hat{\mu}}\ \beta_1(\omega)\right] + 2e^{-\beta_1(\omega)}}\right\}, \qquad (5.33)$$

with dimensionless parameter $\beta_1(\omega) \equiv 2\pi(1-i)\left(h/\lambda_1(\omega)\right)$. Dependence on the two receiver position coordinates z_r is contained in the first major term (in square braces [ ]) on the right-hand-side. It is logical to choose the receiver coordinates so that this factor equals unity. In turn, this means that the back-scattered and fore-scattered EM fields are measured at the *same* distance from the layer midpoint z_{mid}. The scattering ratio reduces to

$$SR(\omega) = \frac{\left[\sqrt{\frac{\hat{\sigma}}{\hat{\mu}}} - \sqrt{\frac{\hat{\mu}}{\hat{\sigma}}}\right]\sinh\left[\sqrt{\hat{\sigma}\hat{\mu}}\ \beta_1(\omega)\right]e^{-\beta_1(\omega)}}{\left[\sqrt{\frac{\hat{\sigma}}{\hat{\mu}}} + \sqrt{\frac{\hat{\mu}}{\hat{\sigma}}}\right]\sinh\left[\sqrt{\hat{\sigma}\hat{\mu}}\ \beta_1(\omega)\right] - 2\cosh\left[\sqrt{\hat{\sigma}\hat{\mu}}\ \beta_1(\omega)\right] + 2e^{-\beta_1(\omega)}}. \qquad (5.34)$$

The ratio depends on the two dimensionless parameter ratios $\hat{\sigma} = \sigma_2/\sigma_1$ and $\hat{\mu} = \mu_2/\mu_1$, as well as $\beta_1(\omega)$, which in turn depends on the homogeneous background medium parameters, layer thickness, and angular frequency. The wavelength of the incident EM wave is readily expressed as

$$\lambda_1(\omega) \approx 2\pi\sqrt{\frac{2}{\sigma_{ref}\mu_{ref}\omega_{ref}}}\ \frac{1}{\sqrt{(\sigma_1/\sigma_{ref})(\mu_1/\mu_{ref})(\omega/\omega_{ref})}}, \qquad \text{(variant of (5.7))}$$

where suitable reference values are selected. Hence we have

$$\beta_1(\omega) = (1-i)\sqrt{\frac{\sigma_{ref}\mu_{ref}\omega_{ref}h_{ref}^2}{2}}\ \sqrt{(\sigma_1/\sigma_{ref})(\mu_1/\mu_{ref})(\omega/\omega_{ref})(h/h_{ref})^2}, \qquad (5.35)$$

where h_{ref} is a reference value for layer thickness (typically 1 m).

Equations (5.34) and (5.35) constitute a pair of expressions for evaluating the backward-to-forward scattering ratio, as follows:

1) Select background medium conductivity σ_1 and magnetic permeability μ_1, layer thickness h, and frequency $f = \omega/2\pi$. This fixes quantity $\beta_1(\omega)$.
2) Evaluate and display the scattering ratio SR(ω) as a function of the two independent dimensionless ratios $\hat{\sigma}$ and $\hat{\mu}$.

The panels in the following Figure 5.5 depict the scattering ratio on a logarithmic scale for three decades of frequency (f = 0.1, 1, and 10 Hz). Layer thickness is h = 1 cm. Homogeneous background medium current conductivity and magnetic permeability are $\sigma_1 = 0.1\,\text{S/m}$ and $\mu_1 = \mu_0$, respectively.

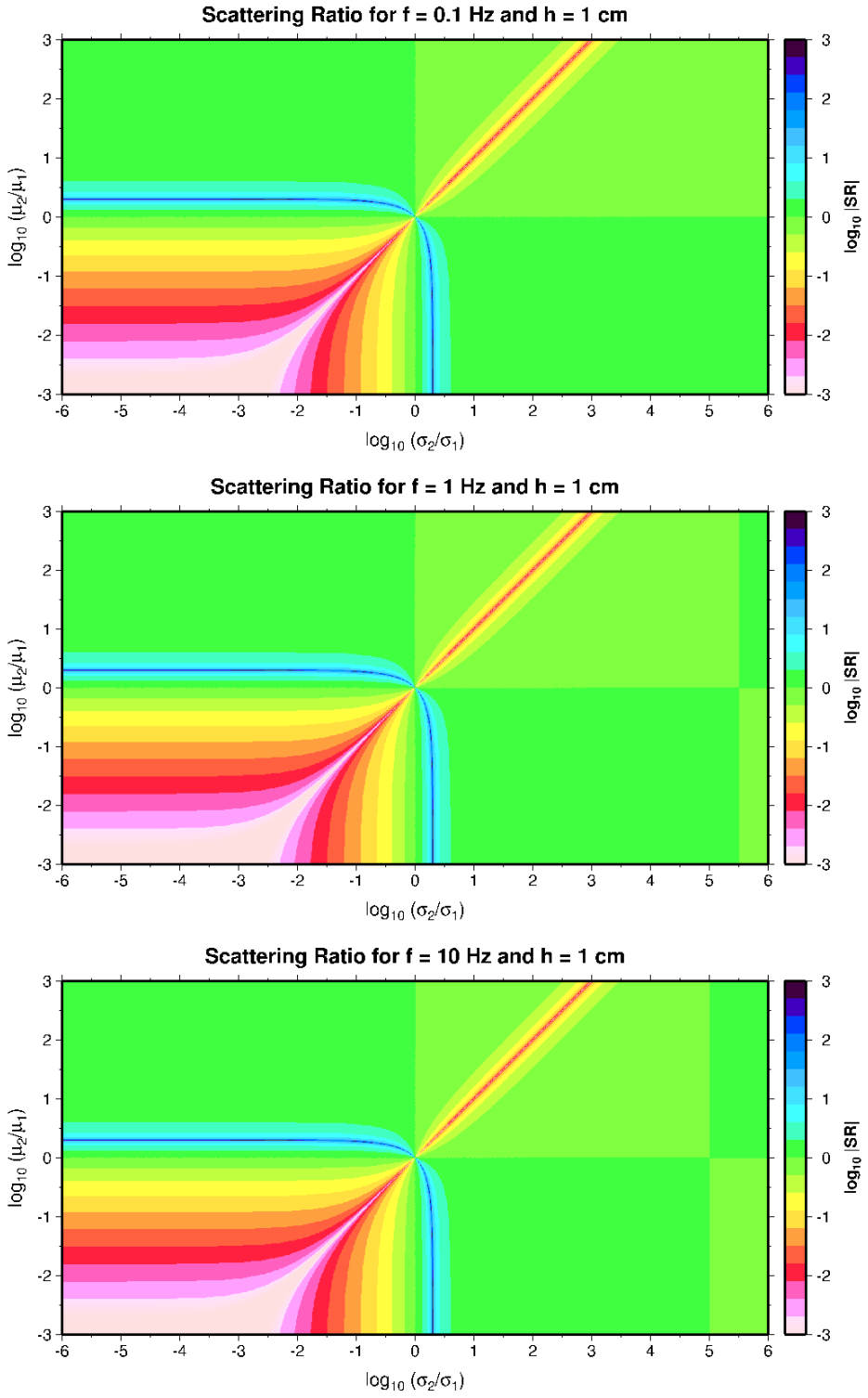

Figure 5.5. Logarithmic amplitude ratio of back-scattered to fore-scattered electric field for a thin (h = 1 cm) layer, at frequencies f = 0.1 Hz (top), f = 1 Hz (middle), and f = 10 Hz (bottom). Scattering ratio is plotted *vs*. logarithmic conductivity contrast ratio σ_2/σ_1 and logarithmic permeability contrast ratio μ_2/μ_1.

Very little difference is discernable in the three panels, with most of the zone colored light **green** indicating nearly equal backward- and forward-scattering amplitudes (~10^0 = 1). The logarithmic ratio along the slanting line $\hat{\mu} = \hat{\sigma}$ is theoretically $-\infty$, because SR(ω) vanishes by equation (5.34). [However, the origin appears to be a singular point. By L'Hopital's rule $\lim \mathrm{SR}(\omega) \to \pm \sinh(\beta_1)/\beta_1$, with + meaning $\hat{\sigma} \to 1$ and – meaning $\mu \to 1$.] The lower left quadrant is a broader zone of diminished back-scattering. Curiously, there is a ridge-like locus of enhanced back-scattering (~10^2) indicated by the thin curving **blue** line; this was unanticipated.

For thoroughness, we illustrate the same logarithmic scattering ratio for frequencies f = 100 Hz and f = 1000 Hz below. The only detectable difference appears to be a slightly shifting pattern in the **green** zone of nearly equal back- and fore-scattering.

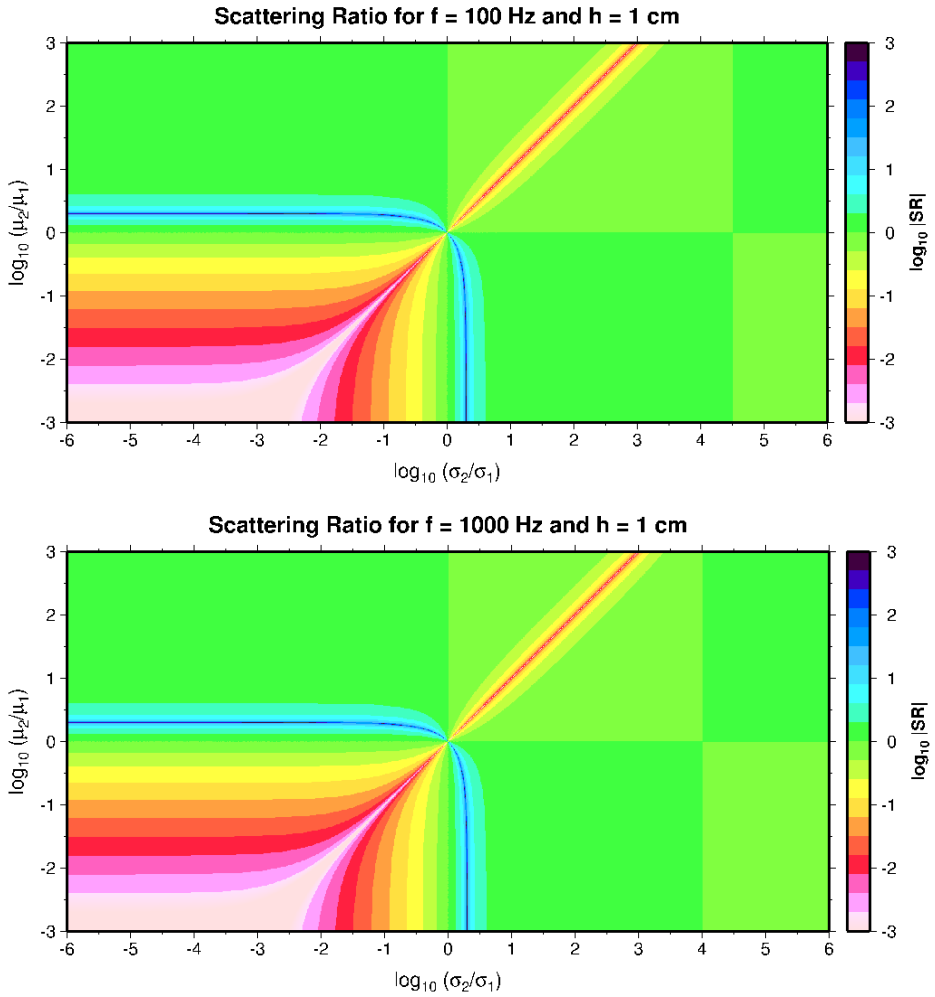

Figure 5.6. Logarithmic amplitude ratio of back-scattered to fore-scattered electric field for the layer in Figure 5.5, at higher frequencies f = 100 Hz (top) and f = 1000 Hz (bottom).

In this case with background permeability $\mu_1 = \mu_0$, the lower half of the plots where $\log_{10}(\mu_2/\mu_1) < 0$ might be challenged on theoretical grounds (e.g., can a magnetic permeability be less than the vacuum value?). However, we include this zone in the plots for symmetry purposes. Tests indicate that this zone remains with larger values of background permeability.

The backward-to-forward scattering logarithmic amplitude ratio is illustrated for a thicker layer (h = 10 m) in Figure 5.7 below. All other parameters remain the same.

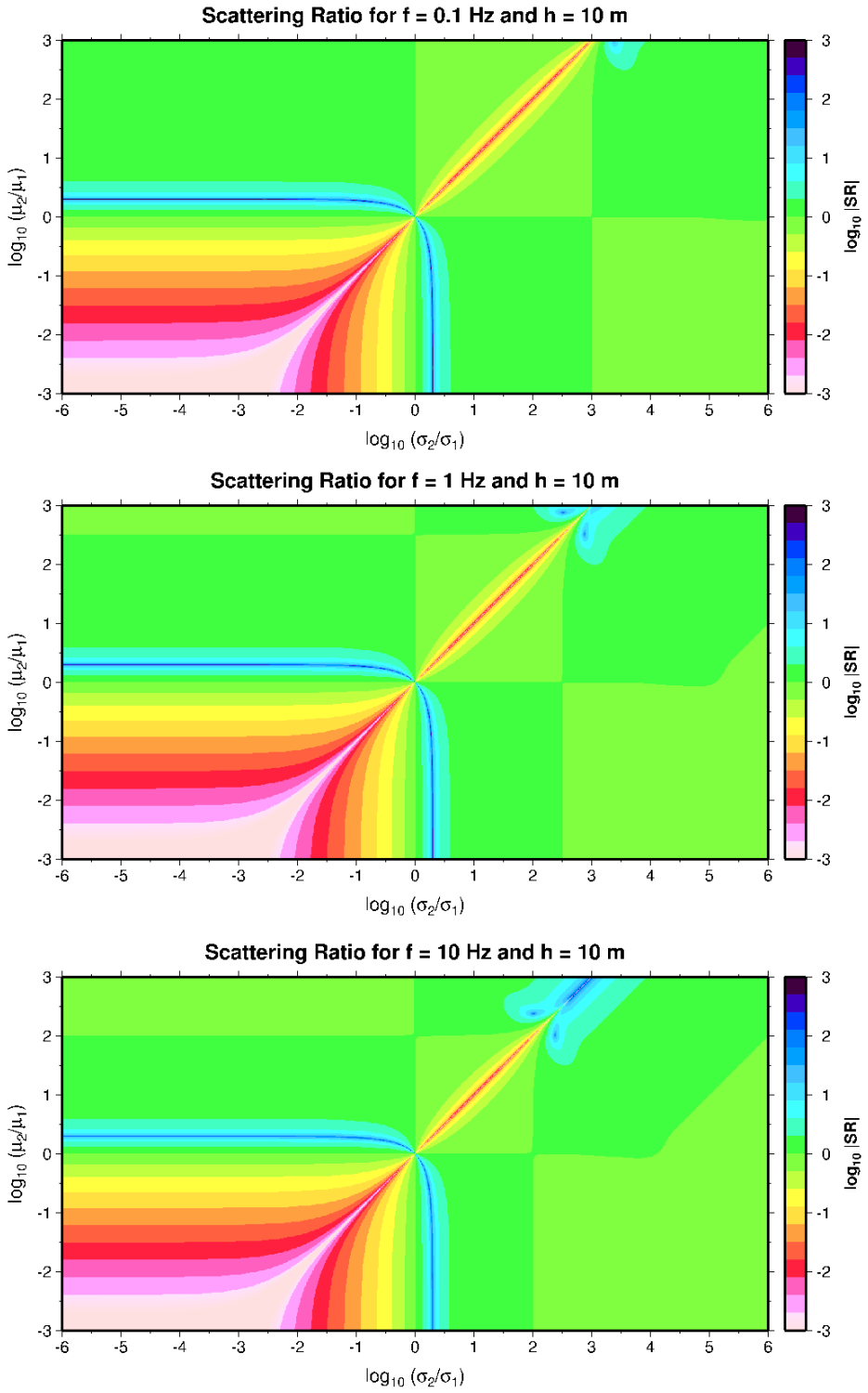

Figure 5.7. Same as Figure 5.5, except the scattering layer is relatively thicker (h = 10 m). Top, middle, and bottom panels correspond to frequency f = 0.1 Hz, f = 1 Hz, and f = 10 Hz, respectively.

A curious artifact (**blue** color) develops around the upper reaches of the line $\hat{\mu} = \hat{\sigma}$. This artifact appears to grow, and a zone of NANs (= not a number) develops in the upper right corner area, at higher frequencies (Figure 5.8 below). This leads us to suspect that numerical precision is low in this zone.

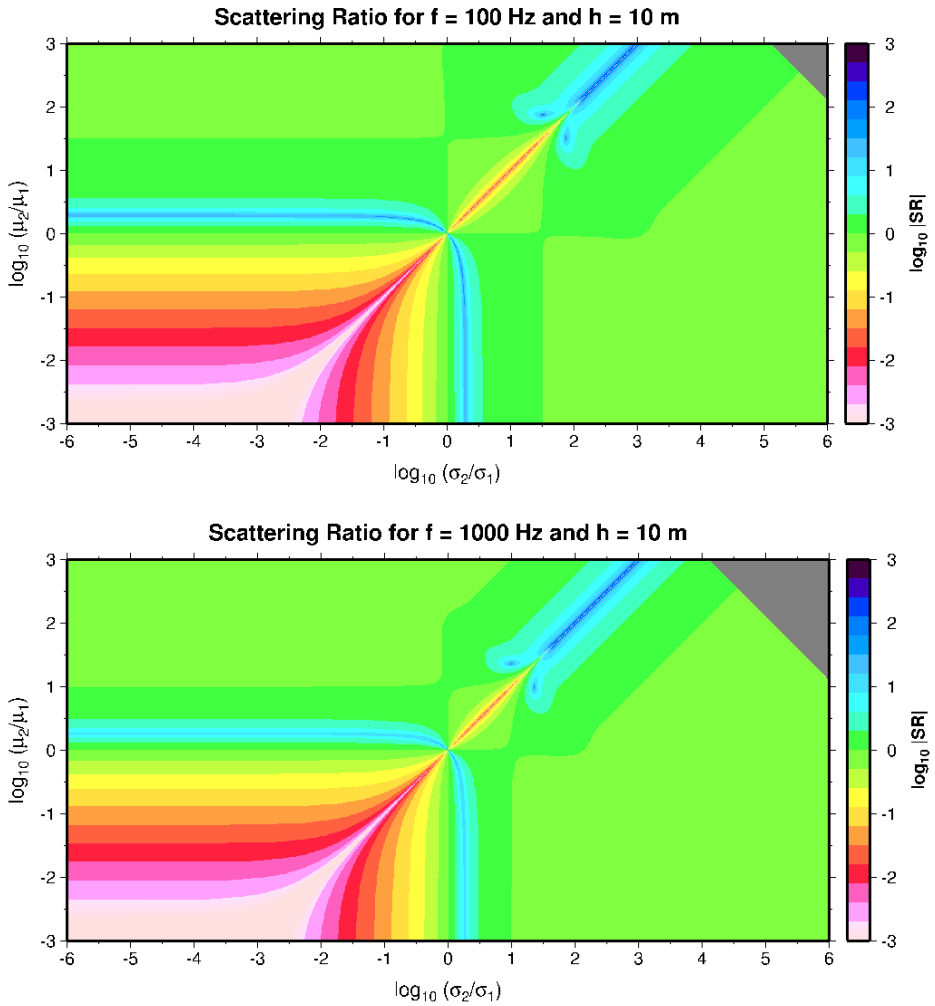

Figure 5.8. Same as Figure 5.6, except the scattering layer is relatively thicker (h = 10 m). Logarithmic amplitude ratio of back-scattered to fore-scattered electric field, at higher frequencies f = 100 Hz (top) and f = 1000 Hz (bottom).

The general conclusion from this study is that, for most of the dimensionless parameter ratio space (i.e., the **green** zones in the above figures), backward-scattered amplitudes are approximately the same as forward-scattered amplitudes. For example, $\log_{10}|SR(\omega)| \approx -0.25$ implies $SR(\omega) = 0.56$; back-scattering is about half as large as fore-scattering.

Finally, it is emphasized that equation (5.34) and the above figures give the amplitude *ratio*, at a fixed frequency, of the back-scattered to the fore-scattered signals measured at equal distances from the bed center. The actual physical values of the two signals could be quite small. For example, consider a 1 cm thick layer situated in a uniform background medium with $\sigma_1 = 0.1\,\text{S/m}$ and $\mu_1 = \mu_0$, and interrogated

by a f = 1 Hz (period P = 1 s) sinusoidal waveform. The middle panel of Figure 5.5 above depicts the relevant logarithmic scattering amplitude ratio. Next, the layer is assigned parameters $\sigma_2 = 0.001\,\text{S/m}$ and $\mu_2 = 1.995\mu_0$, which roughly corresponds to a point on the thin blue ridge (i.e., $\log_{10}(\sigma_2/\sigma_1) = -2$ and $\log_{10}(\mu_2/\mu_1) = +0.3$). So this is a relatively resistive and diamagnetic layer compared to the background. We place a source (of amplitude 1 V/m) and receivers only 5 m from the midpoint of the thin bed. Figure 5.9 below displays four periods of the back-scattered (**red** trace) and fore-scattered (**green** trace) electric fields, after gaining each by the factor 114,167 (this plots the red trace at about full scale on the panel). The sinusoidal variation in the forward-scattered trace is just barely perceptible at this plot scale. The ratio of the red-to-green maximum amplitudes is about 2212, which is roughly consistent with the selected point in Figure 5.5, middle panel (i.e., , or dark blue) $\log_{10}(2212) = 3.34$)

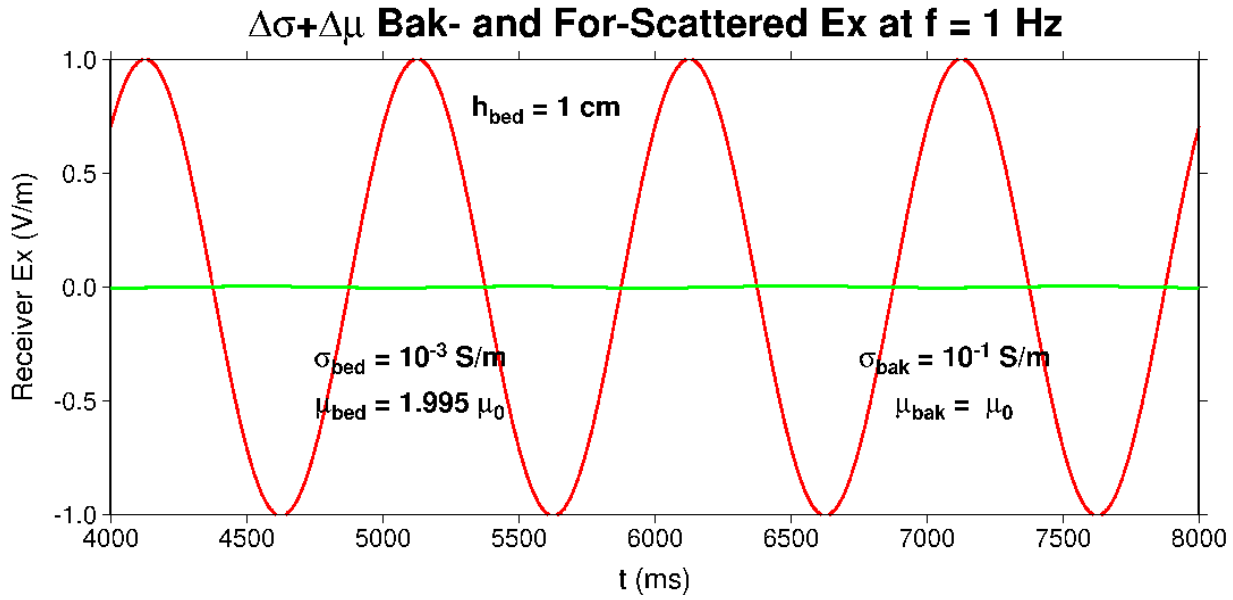

Figure 5.9. Back-scattered (**red** trace) and fore-scattered (**green** trace) sinusoidal waveforms (period P = 1 s) generated by a thin layer (h = 1 cm) possessing both conductivity and permeability contrasts with a uniform background medium. Amplitude ratio of the two signals is ~2212.

6.0 NUMERICAL EXAMPLES OF SCATTERING

Algorithm THEMBED has been developed to calculate normal incidence reflected and transmitted plane wave electric field responses by evaluating the frequency-domain formulae (3.4b) and (4.3b), respectively. [Intrabed responses, where a receiver is located *within* the geologic layer $z_{top} < z_r < z_{bot}$ are also available via equation (C9b) of Appendix C.] The associated magnetic field responses are calculated via equation (3.15b) (for reflection) and equation (4.6b) (for transmission). Time-domain responses are subsequently obtained by inverse numerical Fourier transformation.

THEMBED is a standalone program written in the Fortran programming language. Source code structure is similar to that of the Green function forward modeling program EMHOLE (Aldridge, 2013). A short list of source wavelets (e.g., Gaussian, Ricker, rectangular, sinusoidal, triangular, etc.) is available for selection by the program user. Alternately, a preferred source wavelet may be imported into THEMBED.

6.1 Backward / Forward Scattering

We present below several examples of normal-incidence plane EM wave scattering by geological layers with various thicknesses and material parameters. The layer is situated between two homogeneous and isotropic halfspaces with identical properties. In the context of Figure 2.1, the three parameters $(\varepsilon_3, \mu_3, \sigma_3)$ characterizing medium #3 (substratum) are taken to be the same as $(\varepsilon_1, \mu_1, \sigma_1)$ representing medium #1 (overburden). Parameter numerical values are

$$(\varepsilon_1, \mu_1, \sigma_1) = (\varepsilon_3, \mu_3, \sigma_3) = (10\varepsilon_0, \mu_0, 0.02\ \mathrm{S/m}),$$

where $\varepsilon_0 = 8.854 \times 10^{-12}$ F/m and $\mu_0 = 4\pi \times 10^{-7}$ H/m are vacuum (or free space) values of dielectric permittivity and magnetic permeability, respectively. This specialization to two identical halfspaces is particularly relevant to the problem of a hydraulic fracture generated within a uniform geologic formation.

For this situation, the natural reference model used to define backward- and forward-scattered responses is a homogeneous wholespace with parameters $(\varepsilon_1, \mu_1, \sigma_1)$. Hence, in the context of Figure 5.1, the reflected plane wave from a material contrast interface at $z = z_{mid}$ does not exist (as in equation (5.2a)). The transmitted plane wave is identical to the incident (or direct) wave propagating downward in homogeneous medium #1 (= medium #3) (as in equation (5.2b)). Thus, back-scattered responses depicted in the following figures are identical to the reflected responses from the layer; fore-scattered responses are identical to the transmitted responses *minus* the direct wave. These scattered responses are generated by program THEMBED via user-selectable option.

The center coordinate of the geologic layer in the following examples is $z_{mid} = (z_{top} + z_{bot})/2 = 0.0$ m, with the electric vector plane wave source located at z_s = –100 m. Source current waveform is an alternating polarity square pulse sequence with period P = 4 s and duty cycle d = 50% (implying 1 s on +, 1 s off, 1 s on –, and 1 s off), and run for 25 full periods (or 100 s). The frequency spectrum of this type of source waveform is developed and analyzed in Appendix E. Square pulse amplitude is 1 V/m. The receivers recording back/for-scattered responses are located at $z_r = \mp 100$ m, respectively (implying the back-scattering receiver is coincident with the source). Hence, total travel path length of the plane wave through the conductive background medium is about 200 m, for both reflection and transmission responses. Electric field E_x (V/m) and magnetic field B_y (T) responses are recorded; only the first 4 s (or one period) is plotted. In order to facilitate comparison of the various responses, amplitude scales for all E_x and B_y panels are held fixed.

We first illustrate how scattered responses are constructed via differencing of the actual model and reference model responses. Figure 6.1 below displays electric vector component (E_x) responses generated by reflection from (top panel) and transmission through (bottom panel) a geologic layer possessing strong conductivity contrast relative to the homogeneous background medium. Bed conductivity is $\sigma_{bed} = 100\,\text{S/m}$, or 5000 times larger than the background medium conductivity $\sigma_{bak} = 0.02\,\text{S/m}$. Bed permeability $\mu_{bed} = \mu_0$ and permittivity $\varepsilon_{bed} = 10\varepsilon_0$ are identical to the background values. Bed thickness is fixed at h_{bed} = 10 m.

The **green** trace in each panel is the reference model response, consisting of a plane wave (referred to here as the "direct wave") advancing in the +z direction through the homogeneous attenuating background medium. In the context of a hydraulic fracturing experiment, this is the "pre-frak" measured response. Since the back-scattering receiver z_r is co-incident with the source at z_s = –100 m, the green trace is the upper panel is identical to the source square pulse waveform. The green trace in the lower panel, recorded at z_r = +100 m, exhibits the familiar dispersed and attenuated character (i.e., slightly rounded square pulse onsets) due to propagation/diffusion through 200 m of conductive background medium.

The **black** trace in each panel is the actual model response, generated after emplacing the 10 m thick geologic layer in the homogeneous background. These are equivalent to "post-frak" measured responses. In the upper panel, this consists of the summed direct and reflected responses, and is not easily interpretable. [The low-amplitude high-frequency oscillations on the black trace are THEMBED numerical artifacts of present unknown origin; ignore these.] In the lower panel, the actual response is identical to the transmitted response. This is readily interpreted to be a severely attenuated version of the direct (green) response.

Finally, the **red** trace in each panel is the scattered response, obtained by subtracting the green trace from the black trace. Interestingly, the for-scattered response appear identical to the back-scattered response. The reason for this is found by numerically evaluating the low-frequency thin bed criterion of equation (5.11d) with the particular parameters at hand. We have:

1) $\sigma_2/\sigma_{ref} = 100\,\text{S/m}/1\,\text{S/m} = 10^2$,
2) $\mu_2/\mu_0 = 1$,
3) $f/f_{ref} = 1/Pf_{ref} = 1/(4\,\text{s}\times 1\,\text{Hz}) = 2.5\times 10^{-1}$,
4) $h^2 = 10^2\ \text{m}^2$.

Then, thin bed condition (5.11d) evaluates to $7.896\times 10^{-2} << 1$, which is only mildly true. Note that we use the dominant frequency $f = 1/P$ = ¼ Hz of the periodic response signal in this calculation.

Since the thin bed criterion is satisfied, examine the approximate formulae for low-frequency scattering from Table 1. Dimensionless conductivity ratio $\hat{\sigma} = \sigma_2/\sigma_1 = 5000$ and dimensionless permeability ratio $\hat{\mu} = \mu_2/\mu_1 = 1$. Then, the low-frequency backward-scattering and forward-scattering filters in Table 1 evaluate to the *same* number, since $\hat{\sigma} - \hat{\mu} = 4999$ and $\hat{\sigma} + \hat{\mu} - 2 = 4999$. Moreover, since the bed midpoint coordinate z_{mid} = 0, the incident plane electric wave in each case is evaluated at the *same* location z_r = +100 m. We conclude that back-scattered and for-scattered E-field responses should be identical (in the thin bed approximation), as indeed appears to be the case in the top and bottom panels of Figure 6.1.

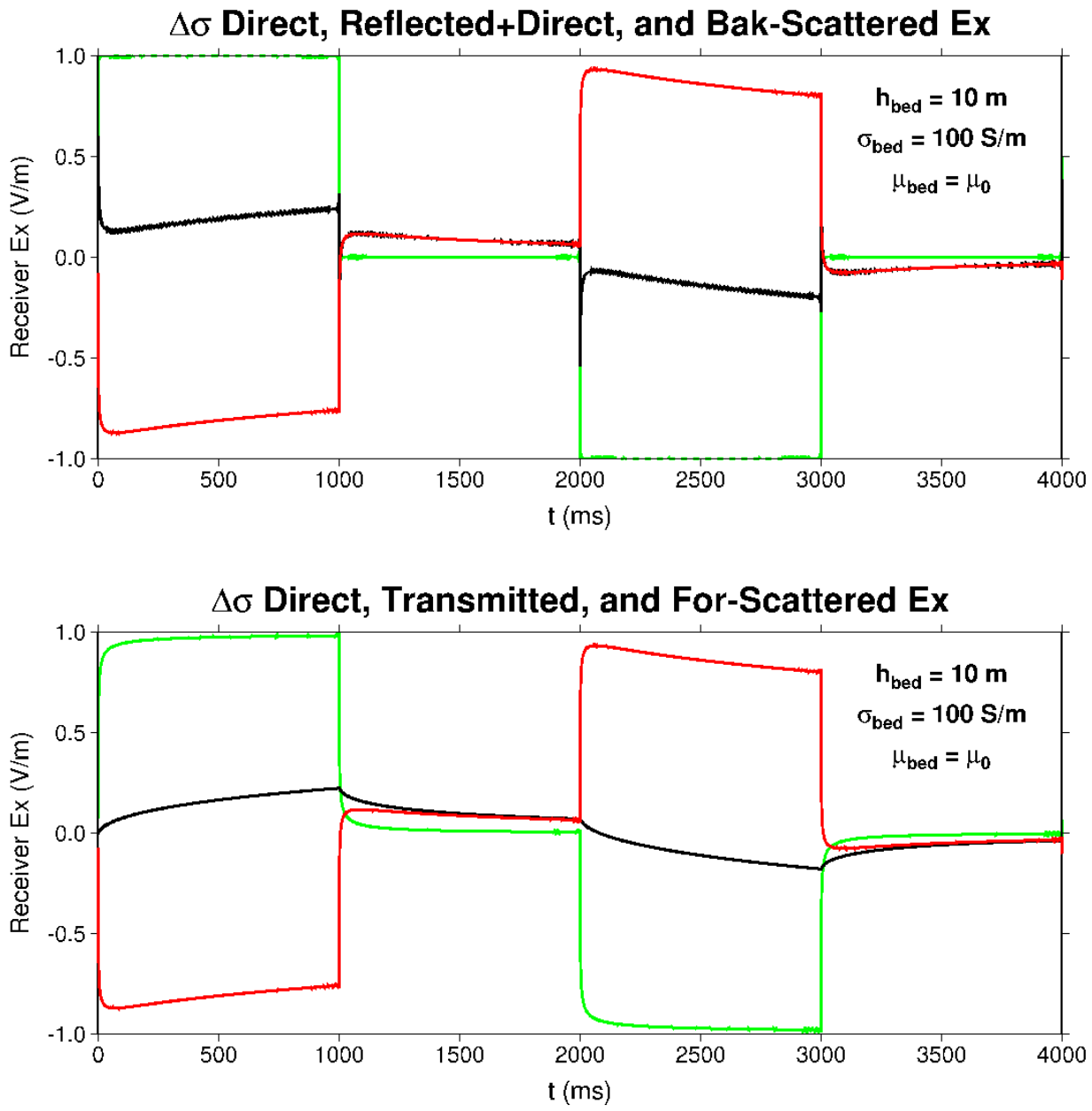

Figure 6.1. Electric vector component responses generated by a geologic bed with conductivity $\sigma_{bed} = 100\,\text{S/m}$ (5000 times larger than the background medium conductivity $\sigma_{bak} = 0.02\,\text{S/m}$). Top and bottom panels correspond to reflection and transmission measurement geometries, respectively. **Green** traces are homogeneous reference model responses and **black** traces are actual model (i.e., containing the geologic bed) responses. **Red** traces are scattered responses, equal to **black** *minus* **green** traces. Back-scattered and fore-scattered responses are nearly identical for this thin geologic bed.

The associated magnetic vector component (B_y) back- and for-scattered responses are illustrated in the top and bottom panels of Figure 6.2 below.

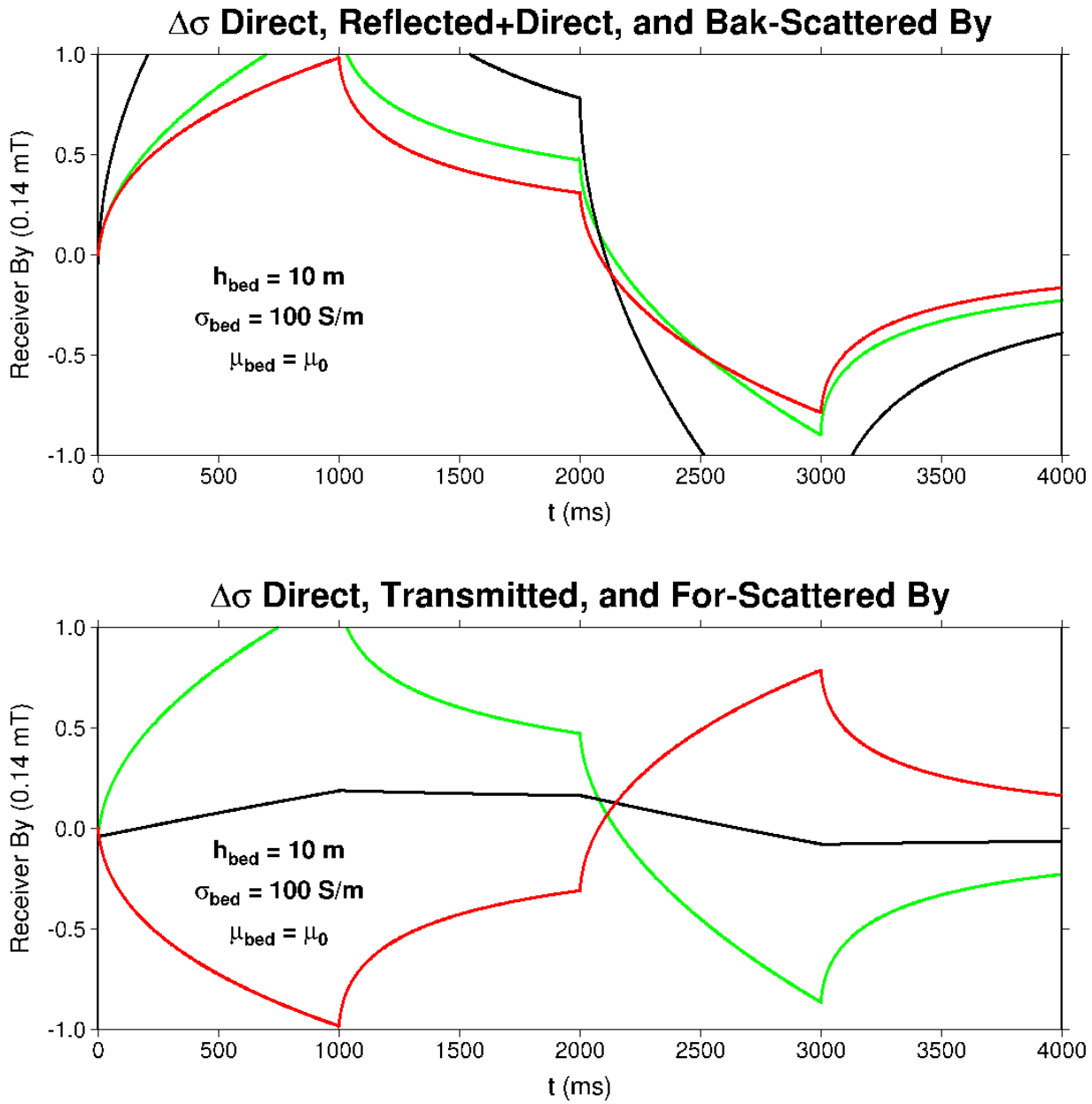

Figure 6.2. Magnetic vector component responses generated by the same geologic bed with medium parameters used for Figure 6.1. Top and bottom panels correspond to reflection and transmission measurement geometries, respectively. Except for a sign change, back-scattered and fore-scattered responses are nearly identical for this thin geologic bed.

Once again, scattered responses (**red** traces) are formed by subtracting the reference responses (**green** traces) from the actual (i.e., measured) responses (**black** traces). Except for a sign change, the scattered responses are nearly identical, consistent with equations (3.15b) and (4.6b).

Many of the numerical examples depicted below are taken from recent presentations delivered at the annual American Geophysical Union meeting (Aldridge, et al., 2014; Aldridge and Weiss, 2016). Backward and forward electric and magnetic scattering are illustrated.

6.1.1 Variable Bed Thickness

The first set of responses, illustrated in the following two figures, are back-scattered and for-scattered electric and magnetic vector components generated by geologic layers of varying thickness, and possessing a (fixed) strong conductivity contrast relative to the homogeneous background medium.

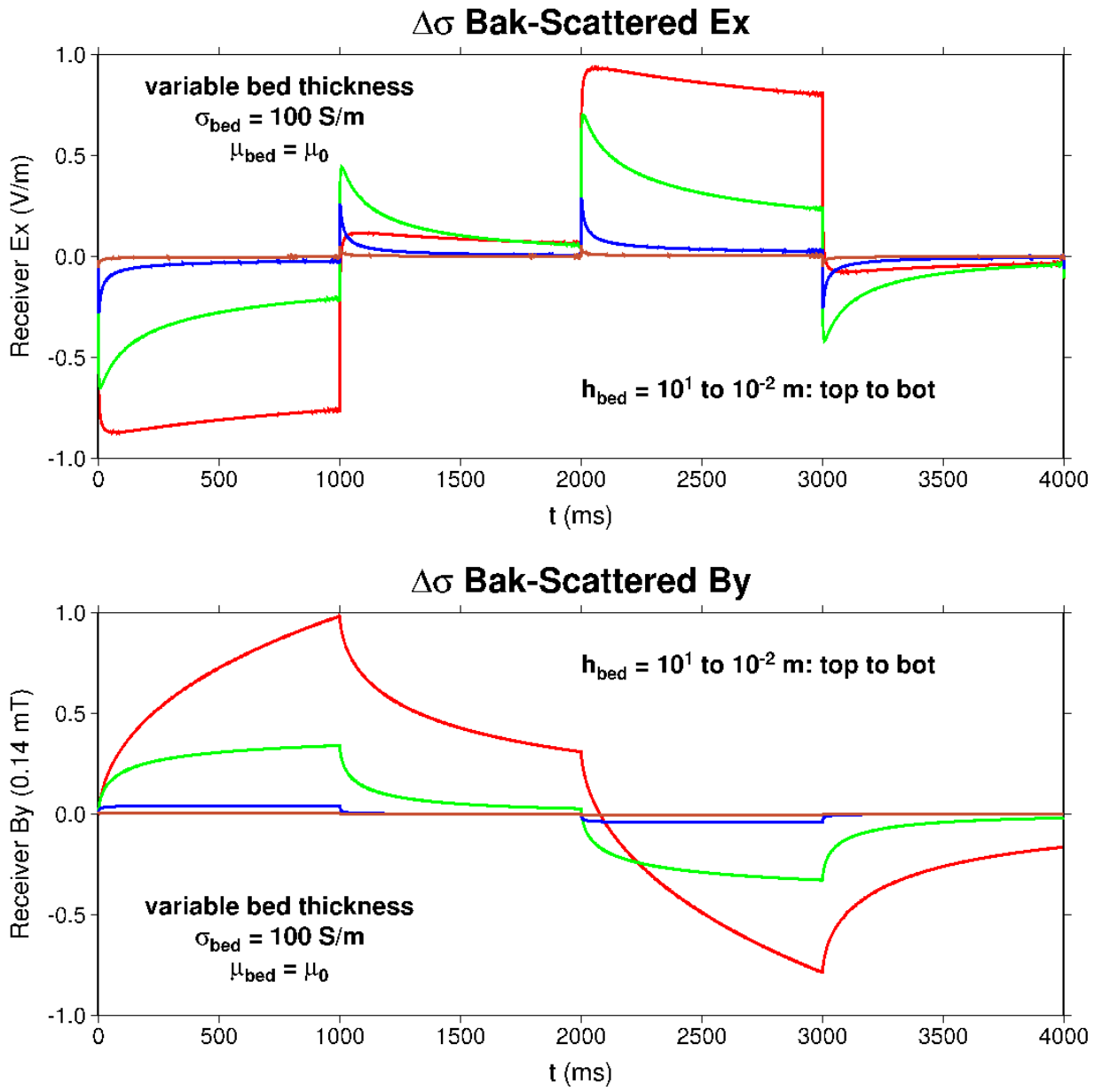

Figure 6.3. Back-scattered E_x electric vector components (top panel) and B_y magnetic vector components (bottom panel) generated by a geologic bed with conductivity $\sigma_{bed} = 100\,\text{S/m}$ (5000 times larger than the background medium conductivity $\sigma_{bak} = 0.02\,\text{S/m}$). Bed permeability $\mu_{bed} = \mu_0$ and permittivity $\varepsilon_{bed} = 10\varepsilon_0$ are identical to background values. Bed thickness varies from h = 10 m (red curves) to h = 1 cm (brown curves).

Clearly, a thicker bed gives rise to a larger amplitude response. Recall that the source electric field magnitude is 1 V/m (equal to full scale of the E_x panel); the vertical scale of the B_y panel is chosen so that the largest amplitude response plots at nearly full scale. The thinnest layer appears to give negligible E_x and B_y response at these receiver positions, 100 m from the bed mid-point.

Forward-scattered responses, for the same set of layer parameters, are given in the following Figure 6.4.

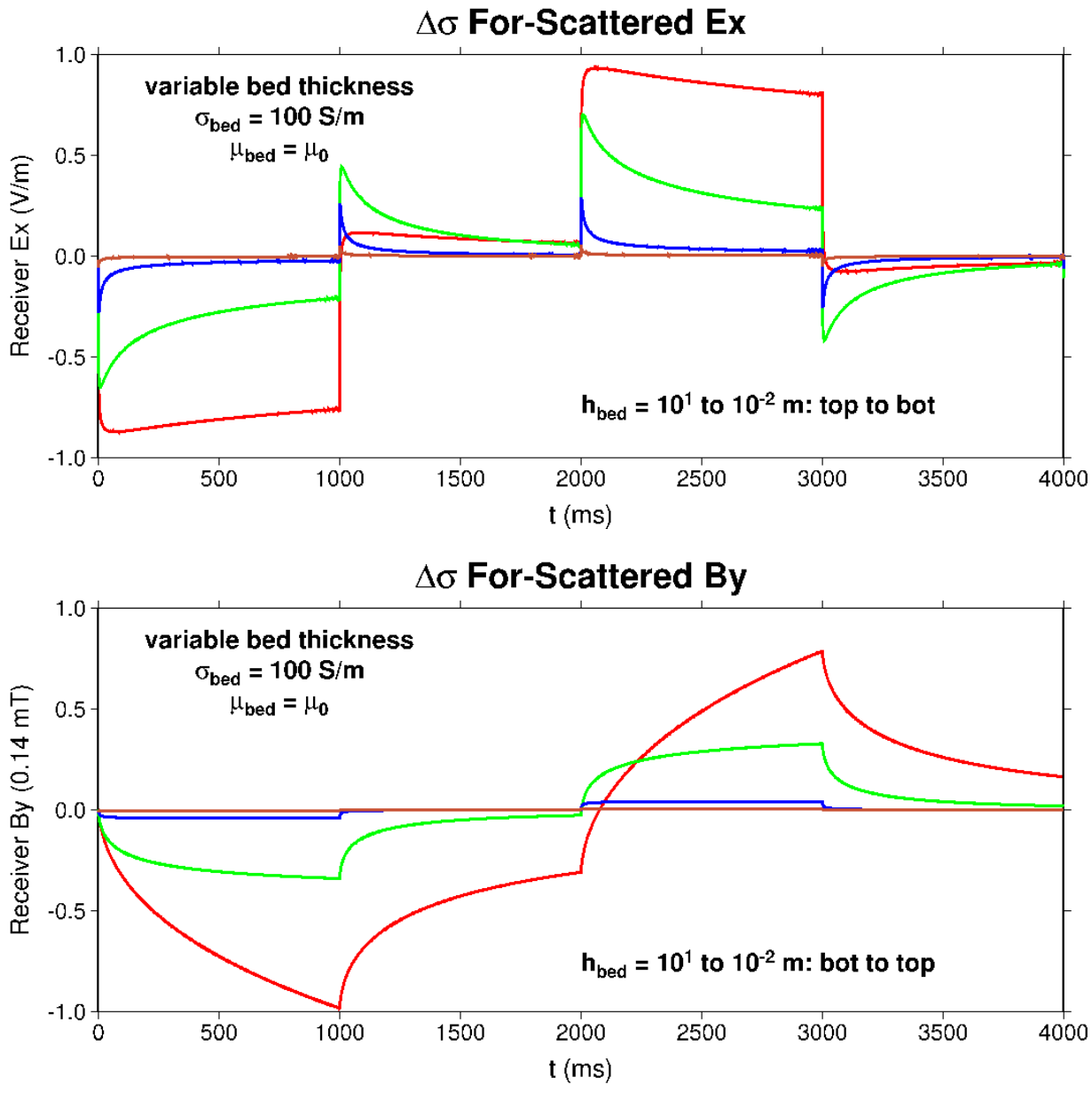

Figure 6.4. For-scattered E_x electric vector components (top panel) and B_y magnetic vector components (bottom panel) generated by the same conductivity contrast geologic bed as in Figure 6.3.

6.1.2 Variable Bed Conductivity

The next set of responses, illustrated in the following two figures, depict back-scattered and for-scattered EM fields generated by a relatively thin geologic bed of fixed thickness (1 cm), and current conductivity varying from 10^5 S/m to 10^2 S/m.

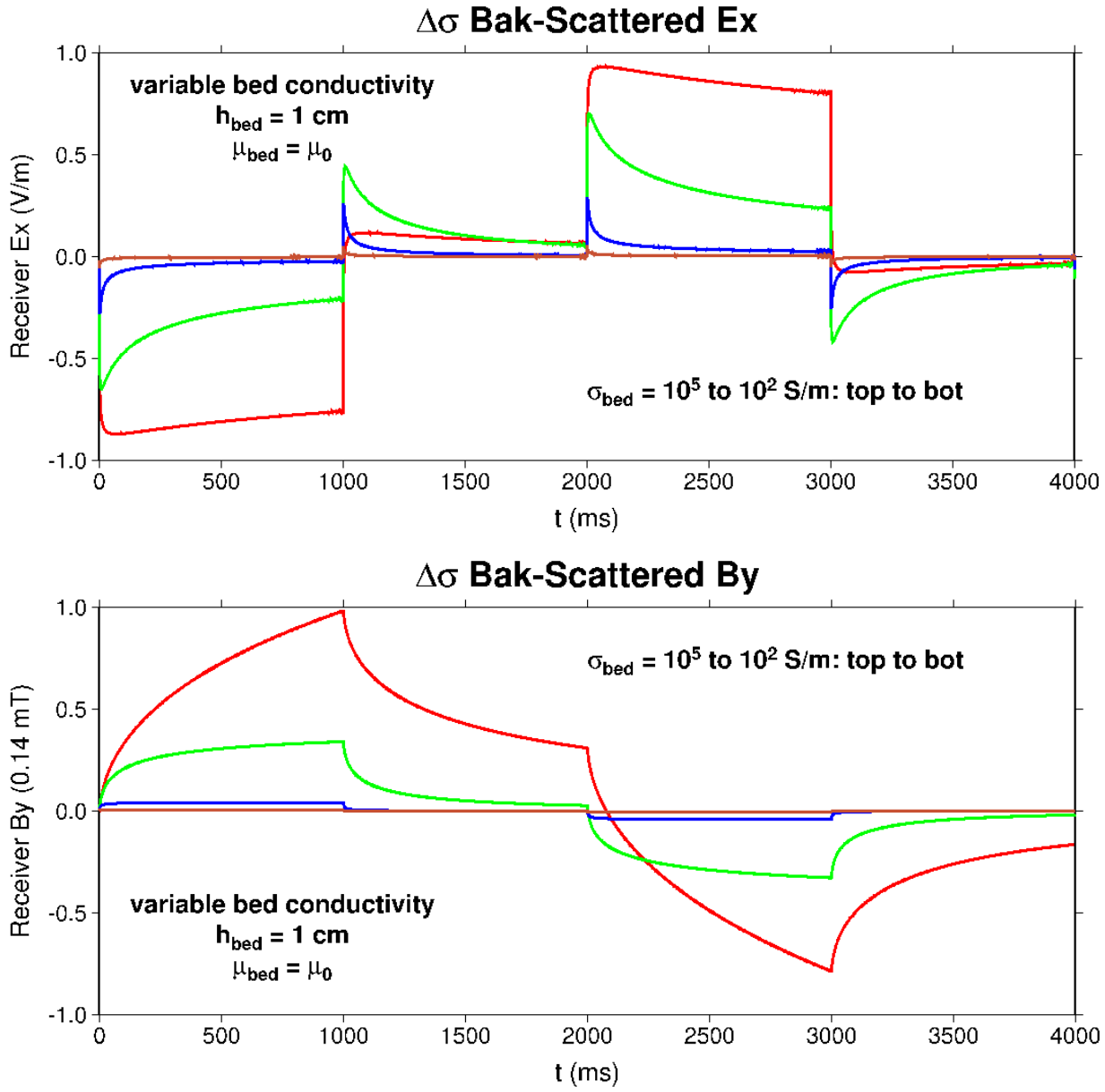

Figure 6.5. Back-scattered EM field components generated by a geologic bed with fixed thickness $h_{bed} = 1\,\text{cm}$, and current conductivity σ_{bed} varying between 10^5 S/m (red curves) and 10^2 S/m (brown curves). Bed permeability $\mu_{bed} = \mu_0$ and permittivity $\varepsilon_{bed} = 10\varepsilon_0$ are identical to background.

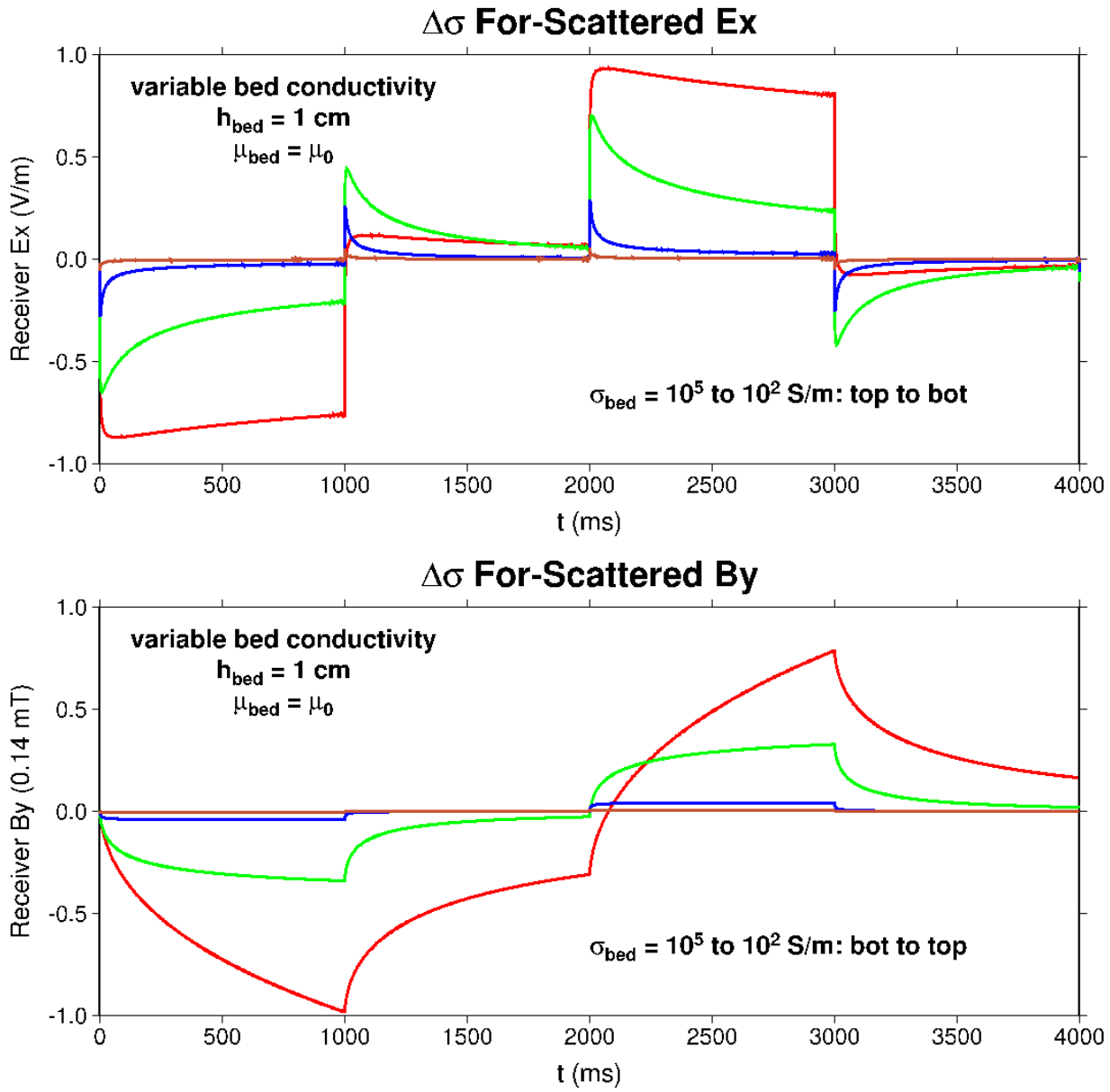

Figure 6.6. Fore-scattered EM field components generated by the same conductivity contrast geologic bed as in Figure 6.5.

Responses have the same general character as with variable bed thickness. In fact, the **red** traces, corresponding to $\sigma_{bed} = 10^5$ S/m are identical to the **red** traces in Figures 6.3 and 6.4. The reason for this will soon become apparent. This very thin bed ($h_{bed} = 1\,\text{cm}$) with large electrical conductivity ($\sigma_{bed} = 10^5$ S/m) might be an analogue of a hydraulic fracture injected with highly conducting proppant.

6.1.3 Variable Bed Permeability

The scattering effect of variable magnetic permeability, for fixed layer thickness $h_{bed} = 10\,\text{m}$ and conductivity $\sigma_{bed} = 0.02\,\text{S/m}$, is illustrated in the following two figures.

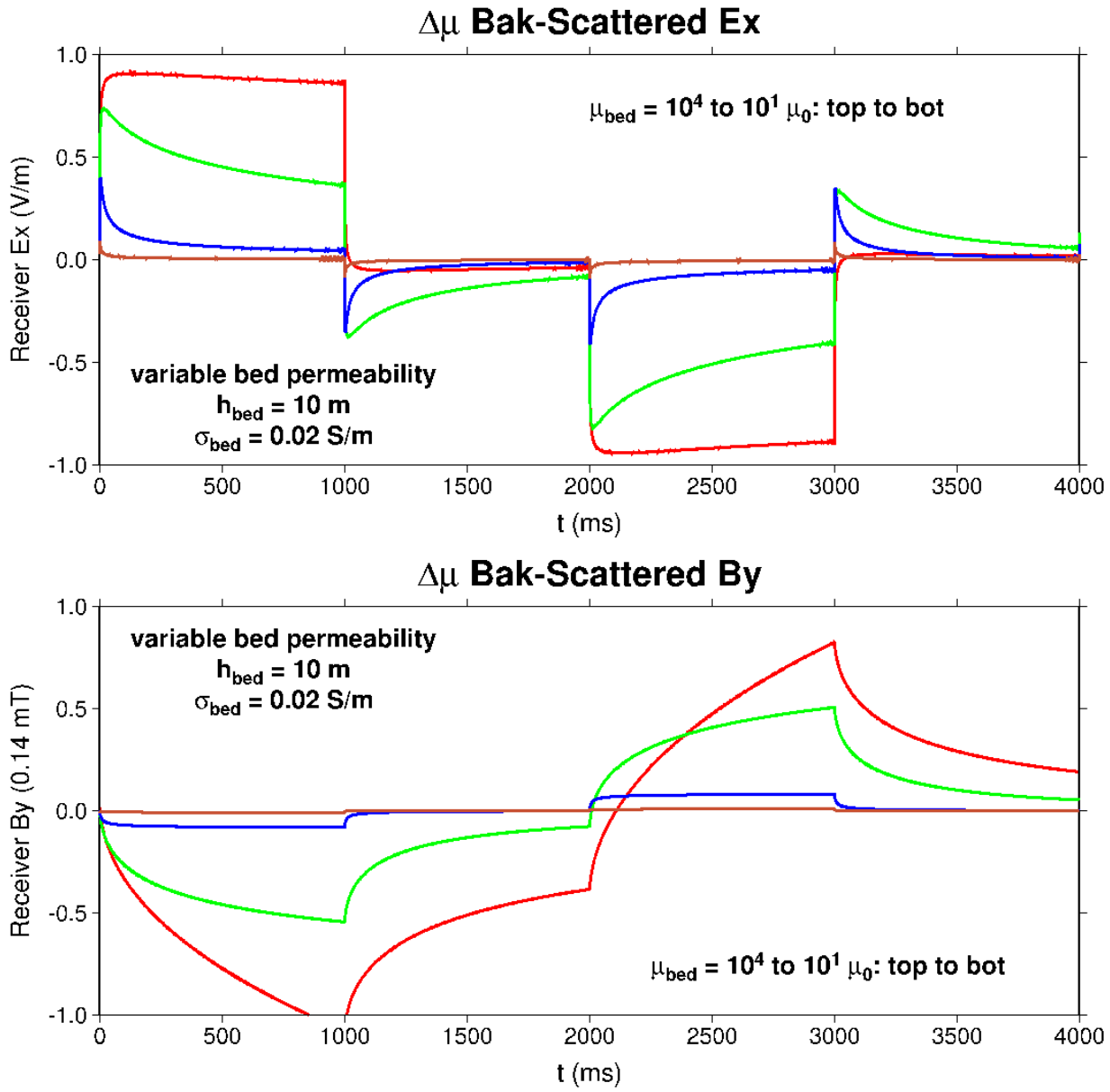

Figure 6.7. Back-scattered EM field components generated by a geologic bed with fixed thickness $h_{bed} = 10\,\text{m}$, and magnetic permeability μ_{bed} varying between $10^4\,\mu_0$ (red curves) and $10^1\,\mu_0$ (brown curves). Bed conductivity $\sigma_{bed} = 0.02\,\text{S/m}$ and permittivity $\varepsilon_{bed} = 10\varepsilon_0$ are identical to background.

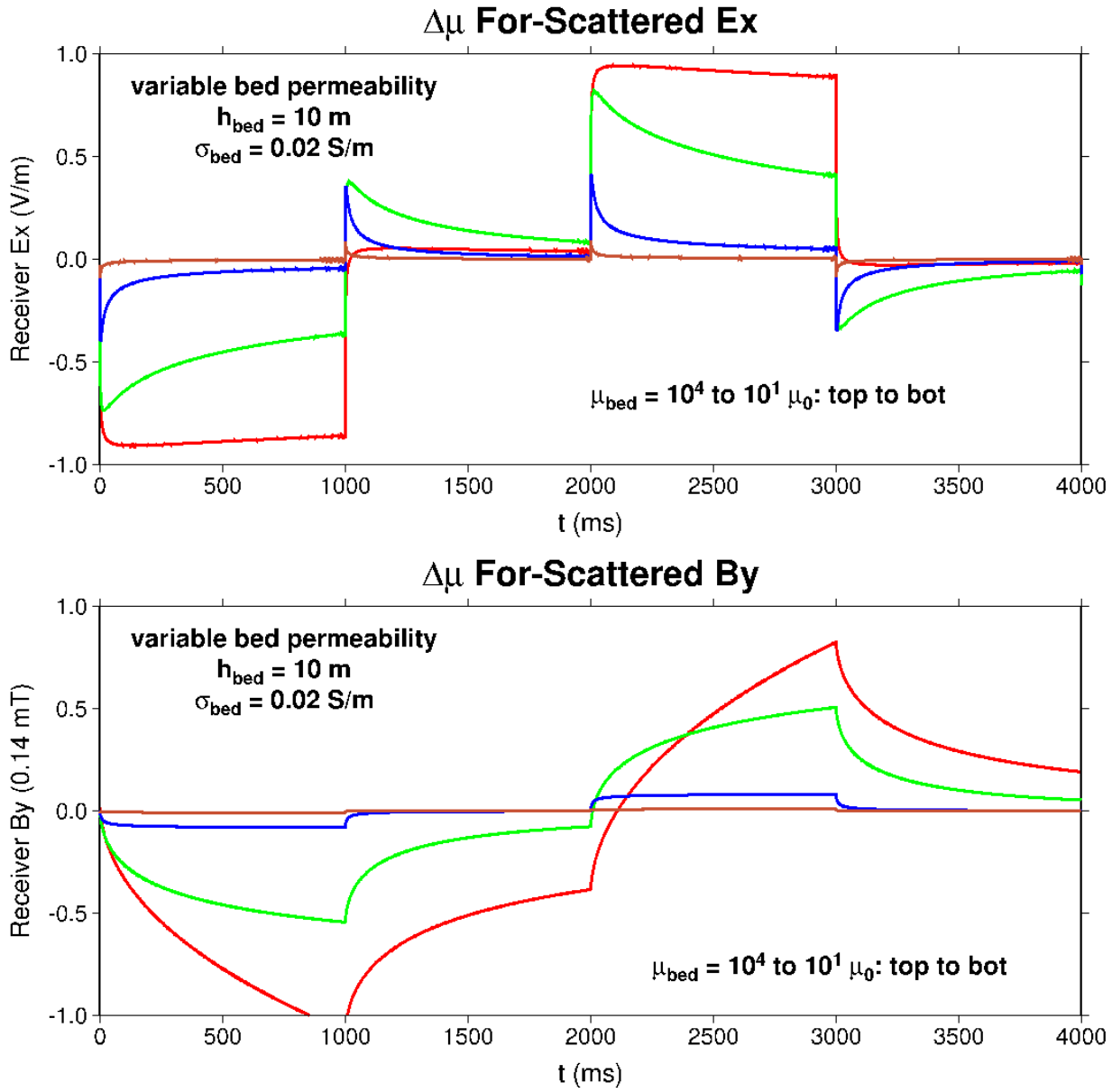

Figure 6.8. For-scattered EM field components generated by the same permeability contrast geologic bed as in Figure 6.7.

Back-scattered responses generated by a permeability contrast have opposite polarity (i.e., sign) compared to the analogous responses generated by a conductivity contrast (compare Figure 6.7 with Figure 6.5). However, for-scattered responses have the same sign (compare Figure 6.8 with Figure 6.6). Bed thickness and permeability are intentionally chosen to be rather large in order to generate an equivalent response magnitude as in the previous examples. [Note that plot scales are identical.] However, a relative magnetic permeability of 10^4 to 10^3 is probably unrealistic. Carbon steel has a relative permeability of $\sim 10^2$.

6.1.4 Joint Conductivity and Permeability Contrast; Variable Bed Thickness

The effect of joint current conductivity and magnetic permeability contrast, for variable bed thickness, is illustrated in the following two figures.

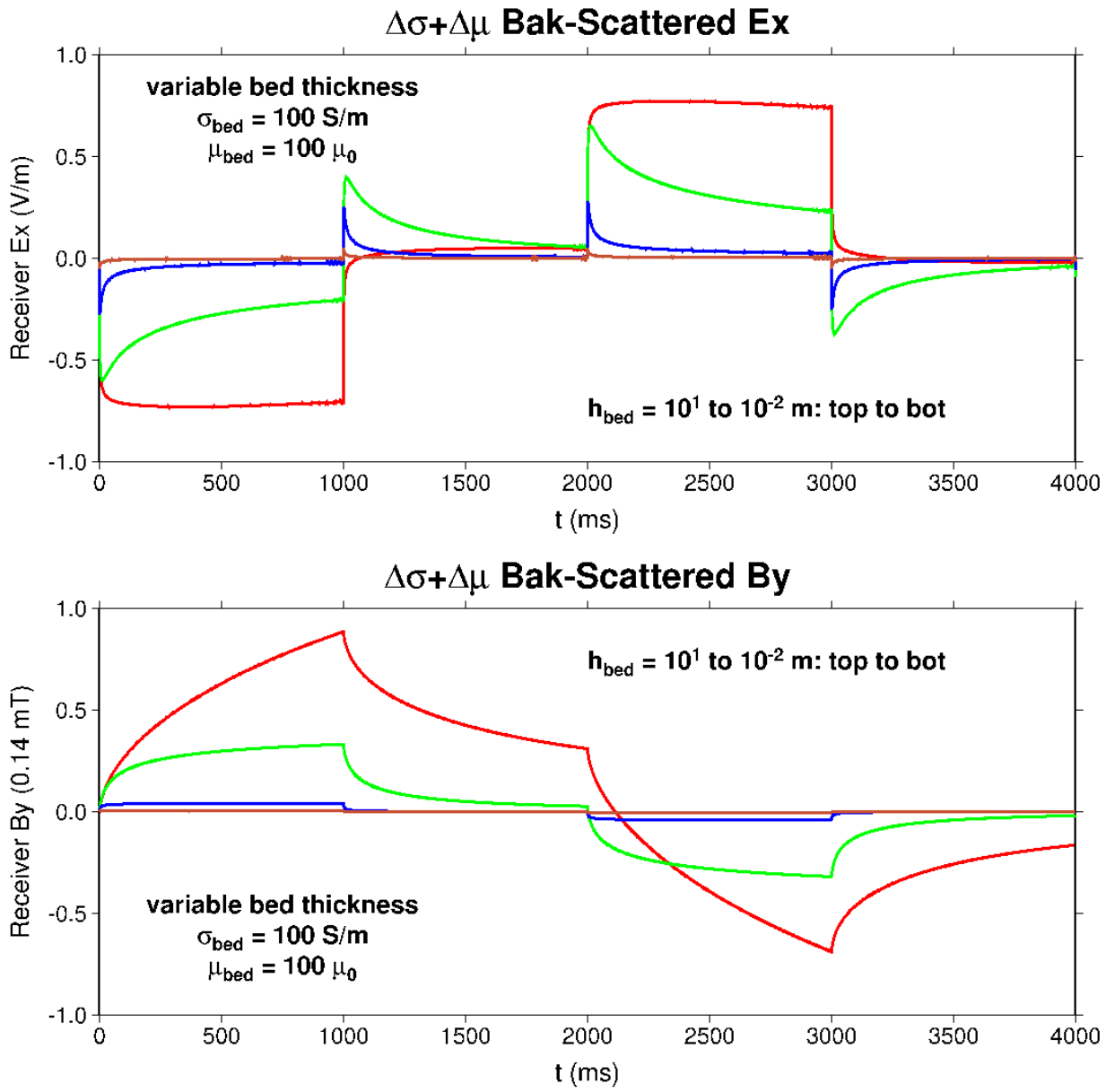

Figure 6.9. Back-scattered EM field components generated by a geologic bed with fixed current conductivity $\sigma_{bed} = 100\,\mathrm{S/m}$ and magnetic permeability $\mu_{bed} = 100\mu_0$, and with thickness varying between $h_{bed} = 10\,\mathrm{m}$ (red curves) to $h_{bed} = 1\,\mathrm{cm}$ (brown curves). Bed permittivity $\varepsilon_{bed} = 10\varepsilon_0$ is identical to background. These layers have strong conductivity contrast (×5000) and permeability contrast (×100) with the background medium.

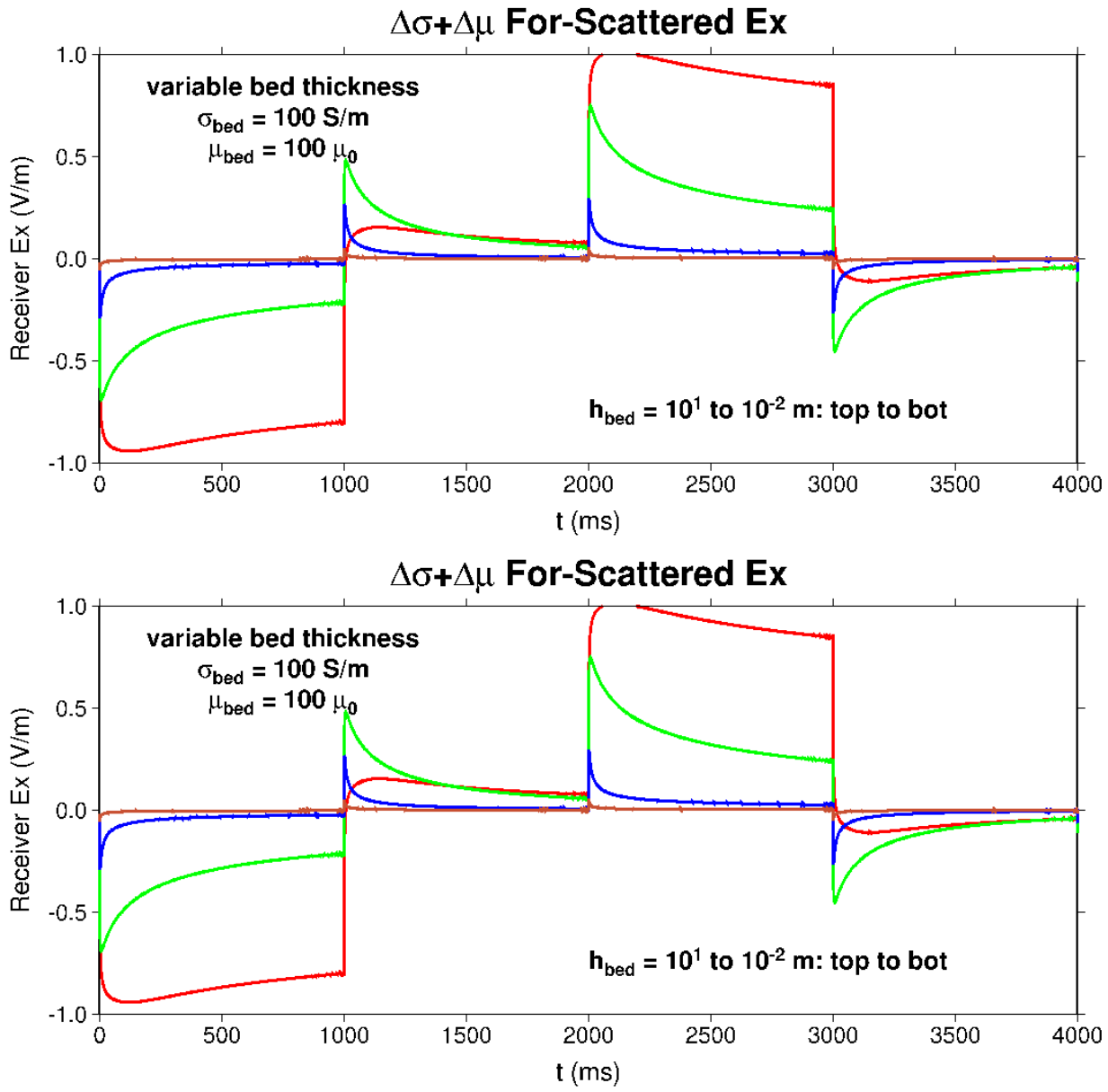

Figure 6.10. For-scattered EM field components generated by the same joint conductivity/permeability contrast geologic bed as in Figure 6.9.

Current conductivity assigned to these beds ($\sigma_{bed} = 100\,\text{S/m}$) is the same as in the variable bed thickness study of Figures 6.3 and 6.4. A careful comparison of these response amplitudes with those depicted in the previous figures indicates that joint permeability and conductivity contrast *diminishes* back-scattering and *enhances* fore-scattering. However, the effect does not appear to be particular large.

6.1.5 Fixed Bed Conductance; Backward-Scattering

Figure 6.11 below depicts back-scattered electric and magnetic responses generated by a suite of geologic layers with fixed conductivity × thickness product, or fixed *conductance* $(\sigma h)_{bed} = 100\,\mathrm{S}$.

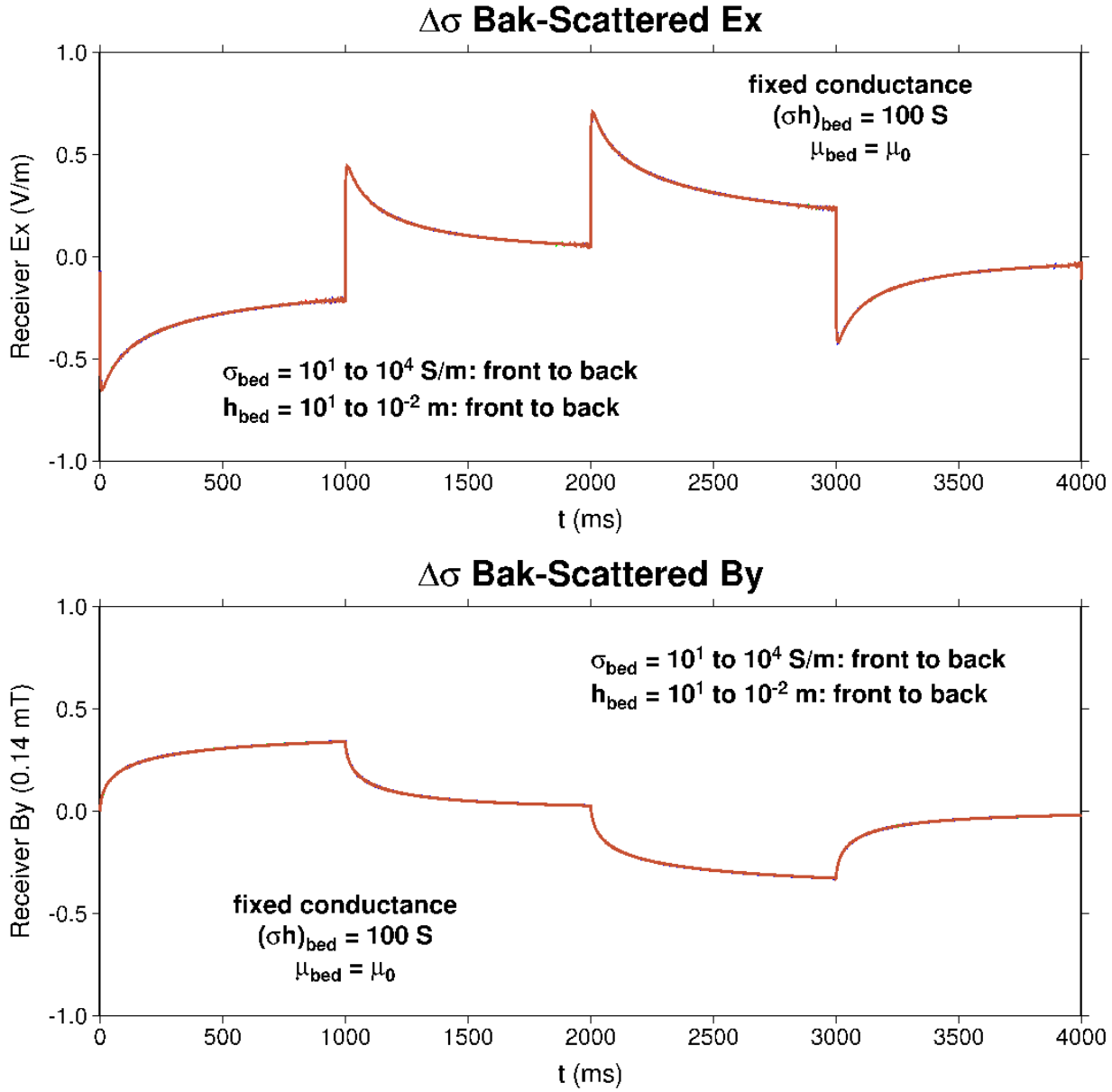

Figure 6.11. Back-scattered EM field components generated by a geologic bed with fixed conductance (i.e., conductivity × thickness product) equal to 100 S. Bed magnetic permeability $\mu_{bed} = \mu_0$ and electric permittivity $\varepsilon_{bed} = 10\varepsilon_0$ are identical to background values. All curves overplot at this plot scale.

All traces overplot, indicating that back-scattered responses are insensitive to varying bed thickness and conductivity, as long as the product conductance remains fixed. For-scattered responses (not plotted here) exhibit the same effect. This is consistent with First Born Approximation scattering, developed in the subsequent Section 7.0.

6.1.6 Fixed Bed Inductance; Forward-Scattering

Forward-scattered electric and magnetic responses generated by a suite of geologic layers with fixed permeability × thickness product, or fixed *inductance* $(\mu h)_{bed} = 10^4$ H, are displayed below:

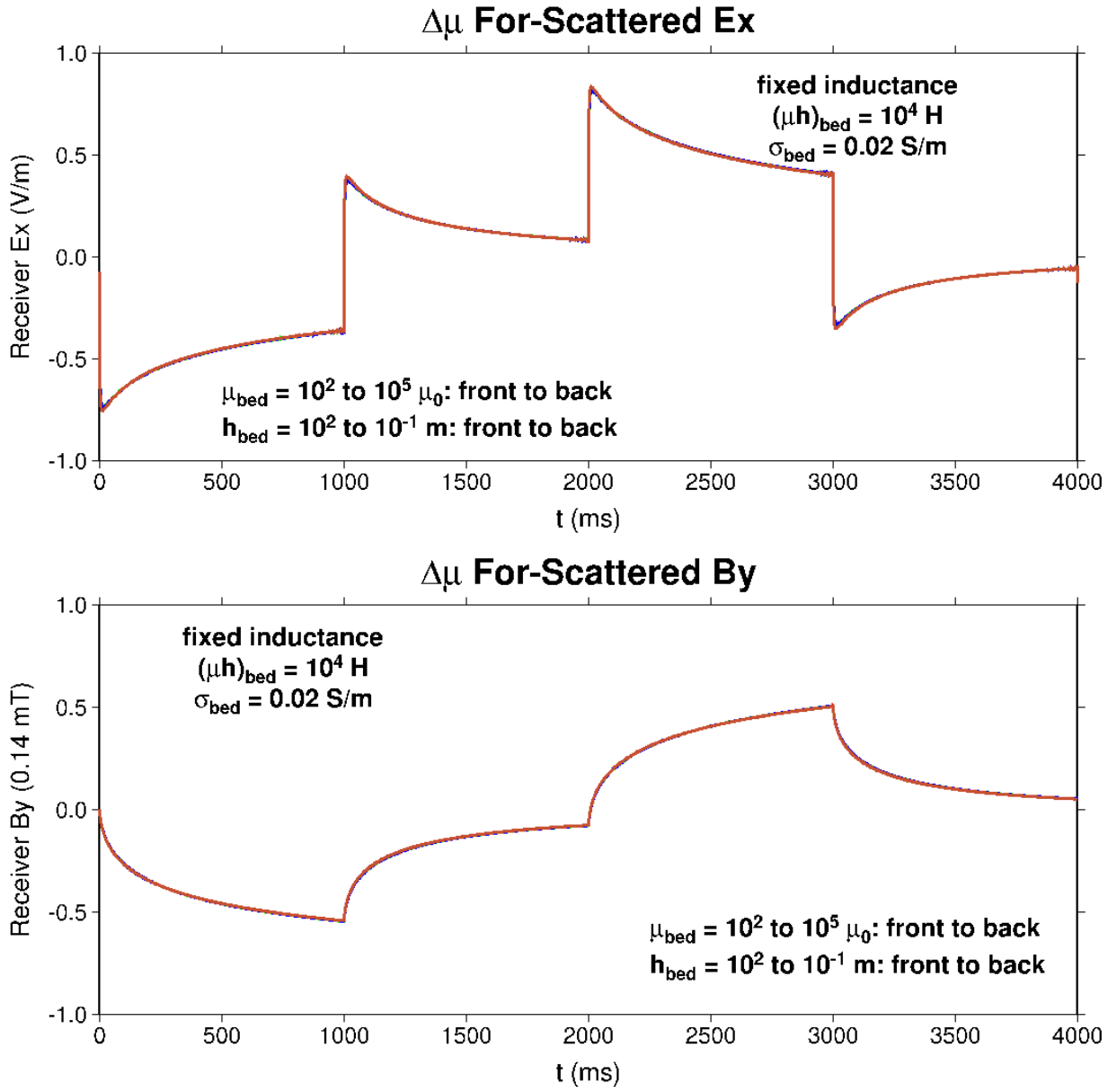

Figure 6.12. For-scattered EM field components generated by a geologic bed with fixed inductance (i.e., permeability × thickness product) equal to 10^4 H. Bed current conductivity $\sigma_{bed} = 0.02$ S/m and electric permittivity $\varepsilon_{bed} = 10\varepsilon_0$ are identical to background values. All curves overplot at this plot scale.

Similar to the fixed-conductance situation, all curves overplot. This is also consistent with First Born Approximation scattering theory.

6.1.7 Permittivity Contrast Scattering; Low-Frequency

The possibility of electromagnetic scattering induced solely via dielectric permittivity contrast has been raisaed by Aldridge and Bartel (2016) and LaBrecque et al. (2016). However, numerical simulations with program THEMBED indicate that the amplitude of the scattered electric field is negligible at the low-frequencies and dielectric permittivities typically encountered in EM exploration.

We use program THEMBED to replicate, as nearly as feasible, the forward-scattering numerical modeling results reported by LaBrecque *et al*. (2016) in their Figure 4(a). The homogeneous background medium is assigned EM parameters:

$$(\varepsilon_1, \mu_1, \sigma_1) = (\varepsilon_3, \mu_3, \sigma_3) = (18{,}411\varepsilon_0, \mu_0, 0.0039\ \text{S/m}).$$

Although the huge relative permittivity appears unrealistic, it is actually stated by LaBrecque *et al*. (2016) on their page 4. The thin bed has thickness $h_{bed} = 5\ \text{mm}$ and is given EM parameters:

$$(\varepsilon_2, \mu_2, \sigma_2) = (4\times10^6\varepsilon_0, \mu_0, 0.0039\ \text{S/m}).$$

Hence, this layer only possesses a contrast in permittivity. LaBreque *et al*. (2016) attribute the gargantuan relative permittivity $\varepsilon_2/\varepsilon_0$ to "the interaction of mobile ions in (an) electrolyte with the charged surface of the immersed contrast agent", and indicate that this is an experimentally *measured* value (appropriate for a 30% / 70% volume mixture of Lorenzo Coke Breeze / sand, wetted with 10 Ωm NaCl solution). LaBreque *et al*. (2016) cite Chew and Sen (1982) for theoretical justification of this very large relative permittivity.

For THEMBED modeling, we use a 100 Hz sinusoidal source waveform (period P = 10 ms) run for 0.5 seconds (or 50 full periods). This source frequency is chosen to agree with the LaBrecque *et al*. (2016) numerical modeling conducted "at a frequency of 100 Hz". Our source electric field amplitude is 1 V/m. Plane wave source and receiver are located at z_s = –2 m and z_r = +2 m, which are estimated from the poorly labeled Figure 1 in LaBrecque *et al*. (2016). We plot 10 periods of forward-scattered E_x response, ranging from 100 ms to 200 ms to avoid any starting transients near t = 0 ms.

As the following Figure 6.13 (top panel) indicates, the forward-scattered response is vanishingly small at this plot scale! This result is in marked contrast to the ~1.25% (max) scattered E_x field amplitude depicted in the analogous Figure 4(a) of LaBrecque *et al*. (2016). If the thin bed relative permittivity is increased about four orders of magnitude to 10^{10}, then a ~6.5% scattered response is observed (bottom panel).

At present, we do not have an explanation for the differing results of THEMBED modeling compared to those reported in LaBrecque *et al*. (2016). Perhaps the different geometric configuration (their proppant-filled thin layer is actually a finite-radius disk with a hole in the middle – like a washer – with outer/inner diameters 5.83 m/0.16 m) plays a significant role in enhancing the LaBrecque *et al*. forward-scattered amplitudes. Also, their EM source is rather localized as a "vertical electric line source of 0.375 m" co-axial with the fracture disk, and is not an extensive plane as with THEMBED modeling. This difference may play a role as well.

Finally, we anticipate that permittivity contrast scattering will be non-negligible at higher frequencies, as suggested by the formulae in Tables 1 and 2.

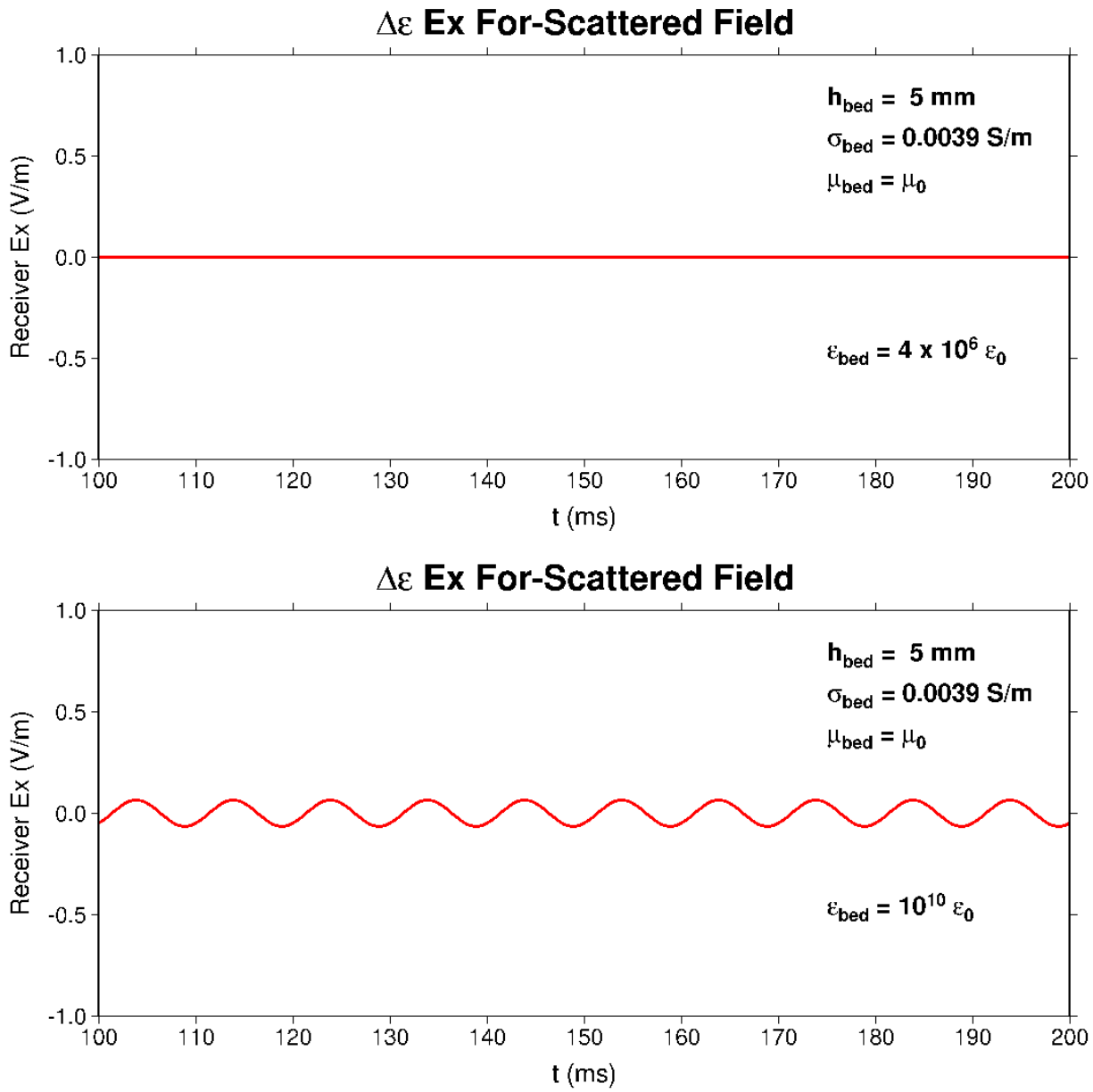

Figure 6.13. For-scattered E_x field components generated by a thin geologic bed (h_{bed} = 5 mm) with strong permittivity contrasts with the background medium. Top / bottom panels correspond to layer relative permittivities of 4×10^6 and 10^{10}, respectively. Bed conductivity and permeability are the same as the homogenous background medium.

6.2 Scattered Signal Amplitude Analysis

In this section, algorithm THEMBED is used to investigate range-dependent amplitudes of back-scattered and forward-scattered plane wave electric and magnetic fields. The study was presented at a recent American Geophysical Union meeting (Aldridge and Weiss, 2016). Figure 6.14 immediately below illustrates the modeling geometry.

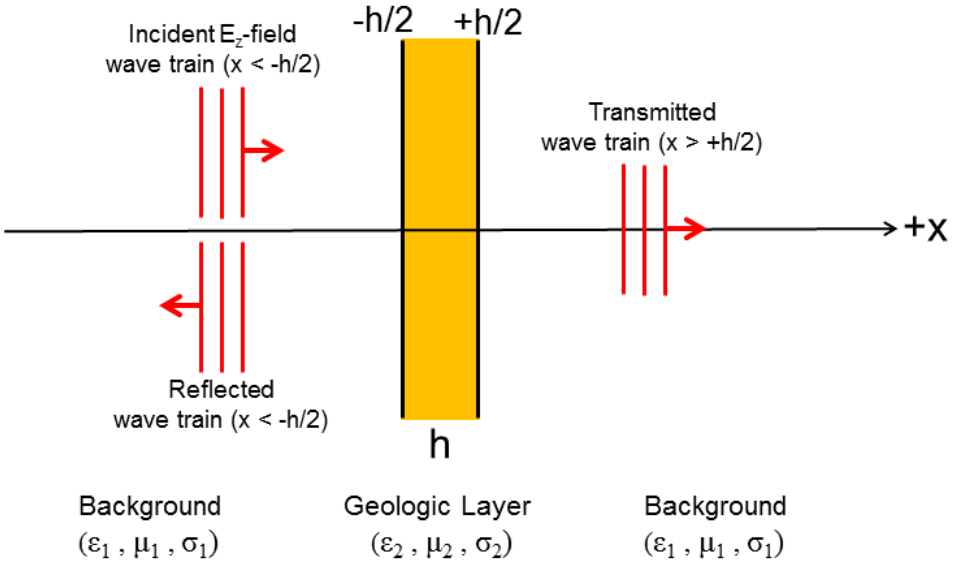

Figure 6.14. Reflection/Transmission modeling geometry. E_z-component electric field plane wave is incident from the left ($x < -h/2$) on a geologic layer of thickness h = 10 m. Both reflected ($x < -h/2$) and transmitted ($x > +h/2$) electromagnetic plane waves are generated.

The layer is h = 10 m thick, and is assigned EM parameters $(\varepsilon_2, \mu_2, \sigma_2) = (10\varepsilon_0, \mu_0 \text{ and } 10\mu_0, 10 \text{ S/m})$. Note that two different magnetic permeabilities are used. In this geometric configuration, the layer might represent a vertically-oriented hydraulic fracture stage (i.e., multiple individual fractures) infused with enhanced conductivity proppant. The x-axis is interpreted as aligned with the horizontal well track.

As in the previous examples, the background medium is taken to be a non-magnetic homogeneous wholespace (implying medium #3 = medium #1) with permittivity $\varepsilon_1 = 10\varepsilon_0$ and permeability $\mu_1 = \mu_0$. Various conductivities $\sigma_1 = (0.001, 0.01, 0.1, 1.0)$ S/m , ranging over four decades, are assigned to the background medium. These values strongly influence the signal amplitude level *vs*. distance from the layer.

The electric field source waveform is an alternating polarity square pulse sequence with period P = 1 s and d = 50% duty cycle. A detailed analysis of the frequency spectrum of this type of signal is presented in Appendix E. Source amplitude is 1 V/m. Two source positions are considered: a *proximal* source, immediately adjacent to the fracture zone, is located at z_s = –5.1 m, whereas a *distal* source is placed at z_s = –2000 m.

Finally, although the above Figure 6.14 refers to reflected and transmitted wave trains, the subsequent trace plots and amplitude curves pertain to the associated backward-scattered and forward-scattered signals. These are the signals directly attributed to the presence of the geologic layer.

Figure 6.15 below illustrates example scattered electric field responses generated by the near and far plane wave sources. Two seconds (equal to two full periods) of data are plotted at 40 receiver stations ranging ± 2 km from the center of the fracture zone; receiver interval is 100 m. The scattering layer has both a conductivity contrast $\sigma_2 = 10\,\text{S/m}$ and a permeability contrast $\mu_2 = 10\mu_0$ with respect to the background medium $(\sigma_1 = 0.1\,\text{S/m},\ \mu_1 = \mu_0)$.

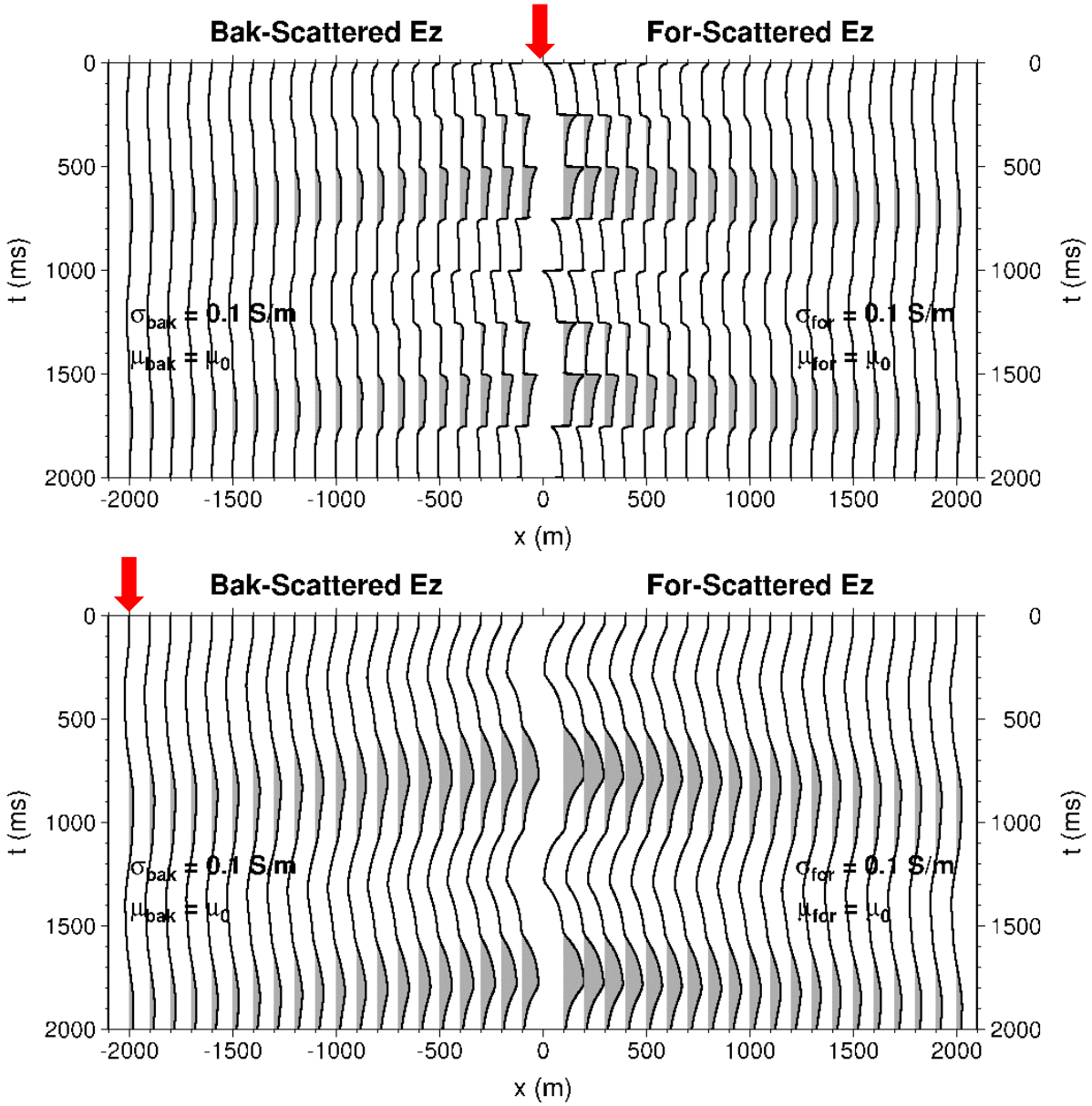

Figure 6.15. Back-scattered and for-scattered E_z-component traces generated by proximal (top panel) and distal (bottom panel) plane wave sources positioned at the vertical **red** arrows. Maximum absolute amplitude within each panel is plotted at one trace spacing; positive lobes of the traces are shaded grey.

Near-source and far-source traces clearly have different shapes, induced by different propagation path lengths through the conductive background medium. Far-source pulses have longer duration rise- and decay-times. In this case of joint conductivity and permeability contrast of the layer, the forward-

scattered traces have larger amplitudes than the backward-scattered traces. This is consistent with the previous Figure 6.9.

Relative amplitude *vs*. distance curves extracted from the calculated E_z-traces are illustrated in Figure 6.16. The maximum absolute value of a trace, divided by the maximum absolute value of the source signal (= 1 V/m), is plotted on a logarithmic scale. The four values of background medium conductivity are indicated via color-coding; the dashed **green** amplitude profiles are obtained from the example traces plotted in the previous Figure 6.15.

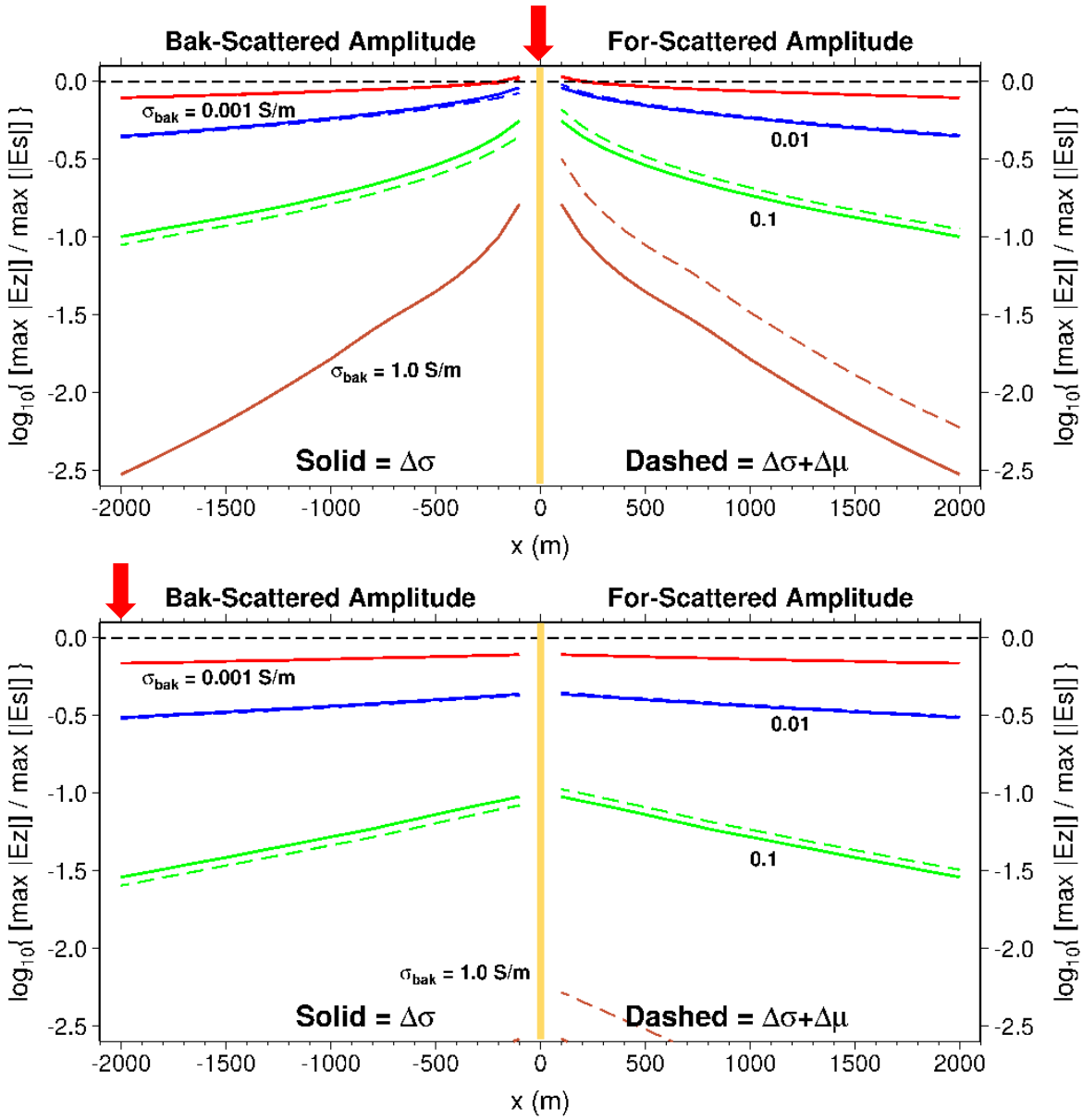

Figure 6.16. Logarithmic maximum relative E_z amplitude *vs*. receiver location for proximal (top) and distal (bottom) plane wave sources. Source amplitude level is indicated by the horizontal black dashed line at 0.0. Background medium conductivities are σ_2 = 0.001 S/m (**red** curves), 0.01 S/m (**blue** curves), 0.1 S/m (**green** curves), and 1.0 S/m (**brown** curves). Solid and dashed amplitude profiles correspond to conductivity-only scattering, and joint conductivity and permeability scattering, respectively. The scattering zone is represented by the thin vertical brown strip.

As expected, all amplitude profiles decay with increasing distance from the scattering layer. Additionally, an individual amplitude profile for the near-source (top panel) is larger than the corresponding profile for the far-source (bottom panel). Increasing the background conductivity reduces the scattered amplitude at any fixed receiver location, as the progression from **red** to **blue** to **green** to **brown** curves illustrates. Indeed, for large background conductivity $\sigma_1 = 1.0\,\text{S/m}$ (~water), the far-source amplitude plots off-scale (brown **curves** in bottom panel). Interestingly, the scattering amplitude observed at the nearest receiver locations $z_r = \pm 100\,\text{m}$ to the thin bed *exceeds* the source level when background conductivity is very low (**red** curves in top panel). The reason for this is unclear, although it may be a constructive interference phenomenon where intrabed multiple reflections reinforce. For a thin bed possessing only conductivity contrast, the backward- and forward-scattered amplitude profiles appear symmetric (at least at this plot scale). However, joint conductivity and permeability contrast enhances for-scattering and suppresses back-scattering (compare the dashed and solid amplitude profiles, of all colors). The amount of forward-scattering boost depends on the background conductivity, with low conductivity yielding the most (compare **brown** dashed and solid curves).

Finally, note the slight flexure in the amplitude decay profiles for the large conductivity background medium with the near-source (**brown** curves in top panel). The reason for this is that the time at which maximum amplitude is achieved on a calculated E_z-trace changes with receiver distance from the scattering layer. The effect is most pronounced for large conductivity media.

An initial conclusion from this signal amplitude study is that observable backward- and forward-scattered electric field amplitudes are predicted, out to 2 km from the scattering layer, provided the background conductivity is not too large. Note that the smallest logarithmic plot amplitude of –2.5 corresponds to a decay of ~316 relative to the source level. A proximal source is clearly superior to a distal source.

The final two figures display the same scattering amplitude information, but pertaining to the associated magnetic field component B_y observed at the receiver locations. Note that the magnetic field traces in Figure 6.17 appear (nearly) anti-symmetric about the thin bed position: forward-scattered traces are reversed in polarity compared to the backward-scattered traces. This is the same scattering layer as with the prior Figure 6.15, with both a conductivity contrast $\sigma_2 = 10\,\text{S/m}$ and a permeability contrast $\mu_2 = 10\mu_0$ with respect to the background medium $(\sigma_1 = 0.1\,\text{S/m},\ \mu_1 = \mu_0)$.

Relative amplitude profiles obtained from the calculated B_y traces are illustrated in Figure 6.18. The reference level is arbitrarily taken to be B_{ref} = 1 T, because these are *magnetic* field responses sourced by an incident *electric* field (different SI units!). Amplitudes observed at the far offset locations of ±2 km range down to $10^{-5.5}\,\text{T} \approx 3.2\,\mu\text{T}$. Although some features of these magnetic field amplitude profiles are similar to the analogous electric profiles (like decay with offset distance), there is at least one notable difference: increasing the background conductivity does not necessarily reduce amplitude at a fixed receiver location. This is most evident in the progression from **red** to **blue** curves; amplitude *increases* in this situation. Then, progressing from **blue** to **green** curves yields a mixed situation for the near source (top panel) and a uniform reduction in amplitude for the far source (bottom panel).

Finally, similar to the electric field situation, joint conductivity plus permeability contrasts enhances forward-scattering and diminishes backward-scattering. Somewhat different from the **E**-field responses, the **B**-field responses may be observable in a field experiment context, particularly with a near-source and with a near-offset receiver.

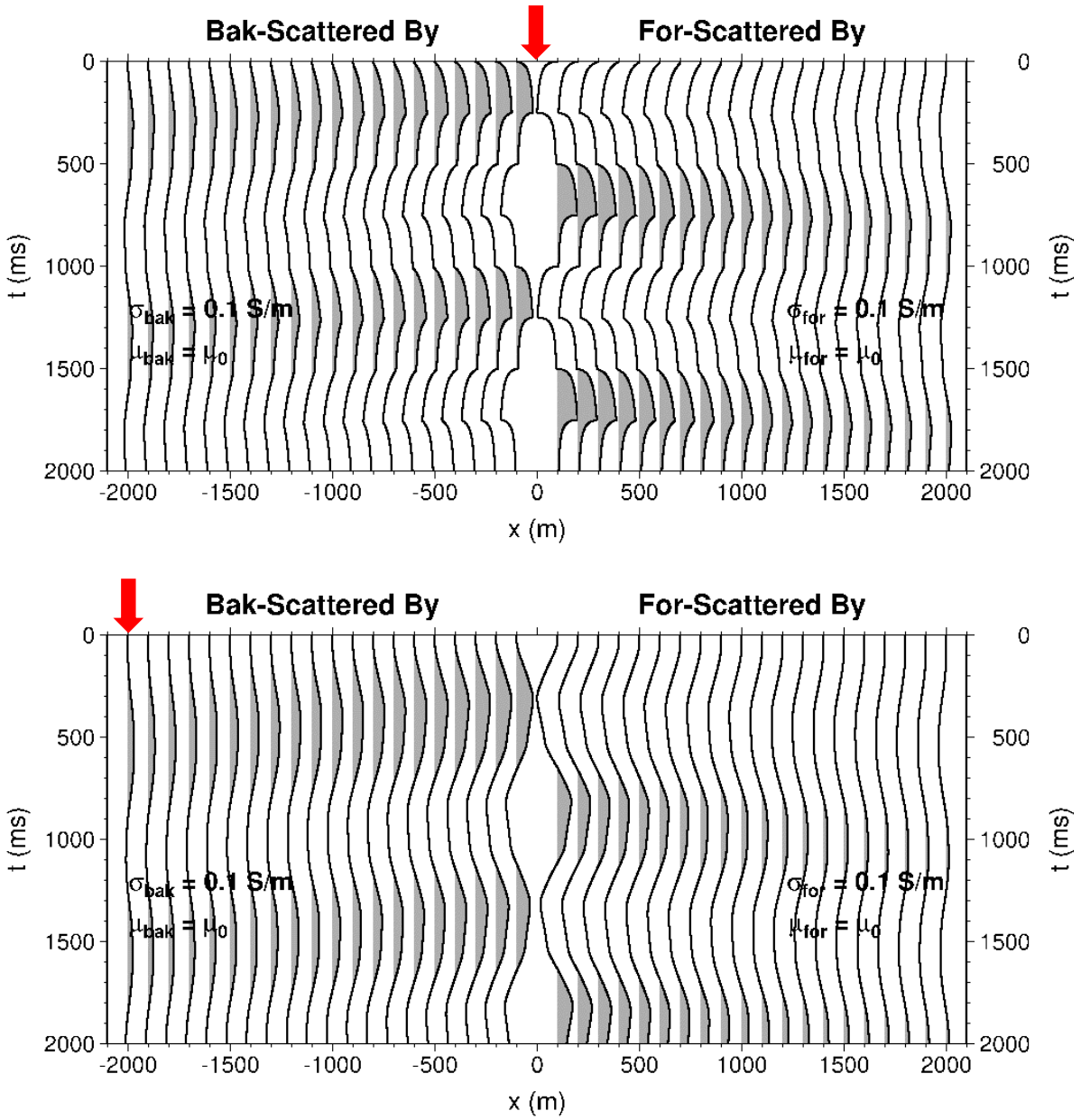

Figure 6.17. Back-scattered and for-scattered B_y-component traces generated by proximal (top panel) and distal (bottom panel) plane wave electric field sources positioned at the vertical **red** arrows. Maximum absolute amplitude within each panel is plotted at one trace spacing; positive lobes of the traces are shaded grey.

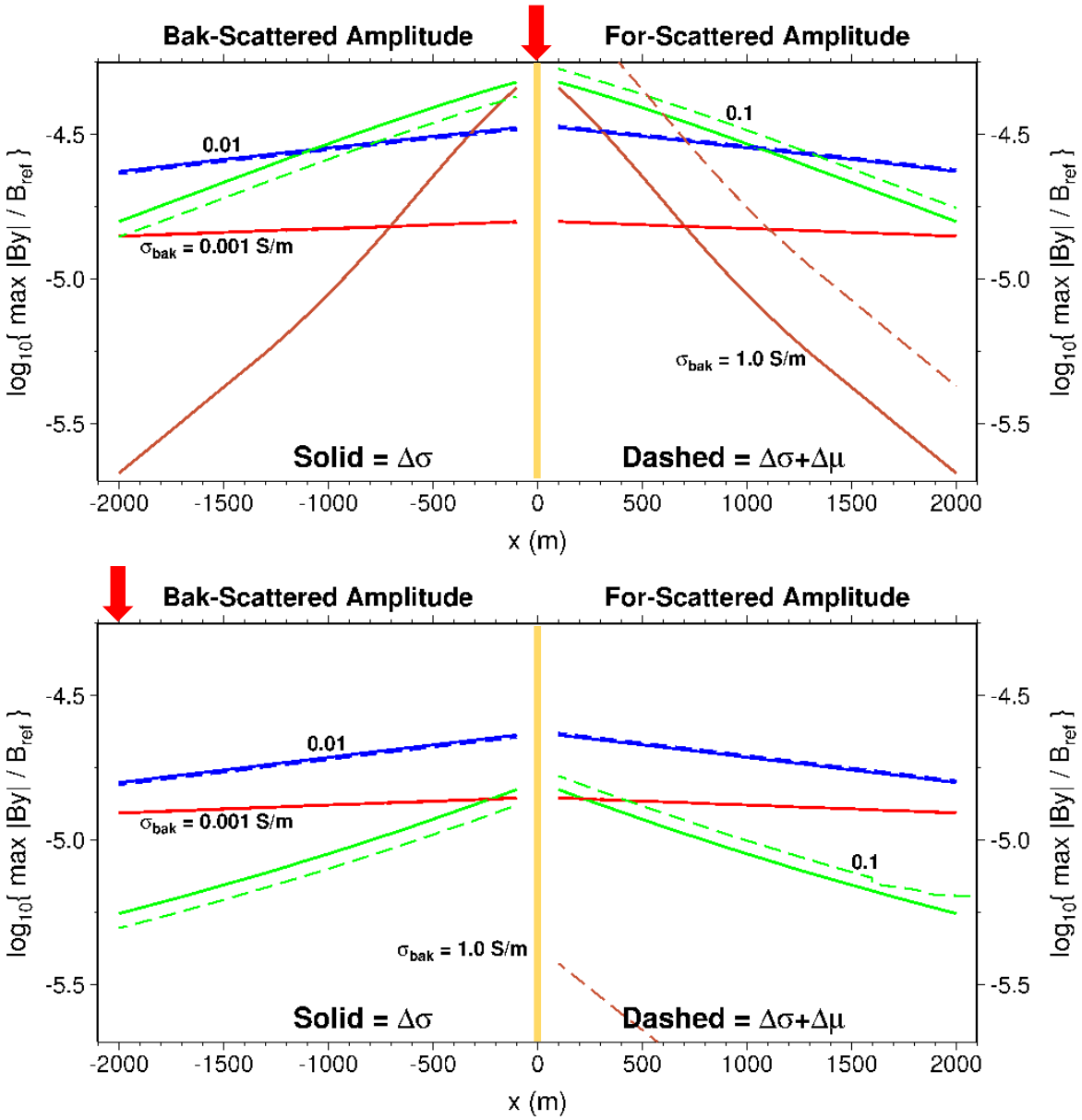

Figure 6.18. Logarithmic maximum relative B_y amplitude *vs*. receiver location for proximal (top) and distal (bottom) plane wave sources. Reference amplitude level is B_{ref} = 1 T. Background medium conductivities are $\sigma_2 = 0.001\,\mathrm{S/m}$ (**red** curves), 0.01 S/m (**blue** curves), 0.1 S/m (**green** curves), and 1.0 S/m (**brown** curves). Solid and dashed amplitude profiles correspond to conductivity-only scattering, and joint conductivity and permeability scattering, respectively. The scattering zone is represented by the thin vertical brown strip.

7.0 FIRST BORN APPROXIMATION SCATTERING

The physical essence of the *First Born Approximation* is a replacement of a material property perturbation with an equivalent (or "effective") body source of wavefields, at the same location(s) in space. The perturbation (in the EM context, in current conductivity σ, magnetic permeability μ, or electric permittivity ε) is considered small in magnitude, although it may be spatially extensive. Replacement of a material parameter perturbation by an effective body source offers an advantage for numerical modeling algorithms where gridding or meshing of a small scale perturbation is difficult to achieve.

The mathematical basis of the First Born Approximation (FBA) is developed in general three-dimensional (3D) form in Appendix D. In this section, we apply FBA theory to the 1D plane interface layer geometry. A geologic layer with enhanced electrical conductivity is replaced by a finite thickness "slab" of electric current; the magnitude of the current depends on the incident plane wave electric field. In turn, the EM fields generated by this current slab may be calculated in closed form. The 1D EM field solution methodology is outlined first, followed by the two illustrative examples of a thin "sheet" and thick "slab" of horizontal body source current flow. For the FBA scattered field calculations, we again adopt the simplifying assumption that medium #3 (the substratum) is identical to medium #1 (the overburden, from which the incident plane wave arrives): $(\varepsilon_3, \mu_3, \sigma_3) = (\varepsilon_1, \mu_1, \sigma_1)$. This enables a direct comparison with the exact scattered field responses of the previous Section 5.0.

7.1 Solution Methodology

Consider a homogeneous and isotropic wholespace characterized by electric permittivity ε, magnetic permeability μ, and current conductivity σ. In one space dimension, the two coupled first-order partial differential equations (PDEs) governing the components of the electric vector $e_x(z,t)$ and magnetic vector $h_y(z,t)$ are

$$\varepsilon \frac{\partial e_x(z,t)}{\partial t} + \sigma e_x(z,t) + \frac{\partial h_y(z,t)}{\partial z} = -j_{sx}(z,t) - \frac{\partial d_{sx}(z,t)}{\partial t}, \tag{7.1a}$$

and

$$\mu \frac{\partial h_y(z,t)}{\partial t} + \frac{\partial e_x(z,t)}{\partial z} = -\frac{\partial b_{sy}(z,t)}{\partial t}. \tag{7.1b}$$

Inhomogeneous (i.e., right-hand-side) terms represent three body sources of electromagnetic waves. These are:

Conduction current density: $j_{sx}(z,t)$ (SI unit: A/m^2),

Displacement current density: $k_{sx}(z,t) = \partial d_{sx}(z,t)/\partial t$ (A/m^2),

Magnetic current density: $l_{sy}(z,t) = \partial b_{sy}(z,t)/\partial t$ (V/m^2).

Note that the source magnetic current flows in the *y*-direction. Eliminating the magnetic vector component yields a single second-order inhomogeneous PDE for the electric vector component:

$$\frac{\partial^2 e_x(z,t)}{\partial z^2} - \varepsilon\mu \frac{\partial^2 e_x(z,t)}{\partial t^2} - \sigma\mu \frac{\partial e_x(z,t)}{\partial t} = \mu\left[\frac{\partial j_{sx}(z,t)}{\partial t} + \frac{\partial k_{sx}(z,t)}{\partial t}\right] - \frac{\partial l_{sy}(z,t)}{\partial z}. \tag{7.2}$$

Mathematically, source conduction current and displacement current appear indistinguishable in both equations (7.1a) and (7.2). Fourier transforming from time t to angular frequency ω yields the inhomogeneous Helmholtz equation (an ordinary differential equation):

$$\frac{d^2E_x(z,\omega)}{dz^2} + K(\omega)^2 E_x(z,\omega) = \mu(-i\omega)\left[J_{sx}(z,\omega) + K_{sx}(z,\omega)\right] - \frac{dL_{sy}(z,\omega)}{dz}, \tag{7.3}$$

where the squared complex wavenumber is $K(\omega)^2 = \varepsilon\mu\omega^2 + i\sigma\mu\omega$. Next, Fourier transforming from space coordinate z to angular wavenumber k yields

$$\left(K(\omega)^2 - k^2\right)\hat{E}_x(k,\omega) = \mu(-i\omega)\left[\hat{J}_{sx}(k,\omega) + \hat{K}_{sx}(k,\omega)\right] - ik\hat{L}_{sy}(k,\omega),$$

where the superposed "hat" symbol denotes a doubly-transformed quantity. The solution for the electric vector component is obviously

$$\hat{E}_x(k,\omega) = \frac{\mu(-i\omega)\left[\hat{J}_{sx}(k,\omega) + \hat{K}_{sx}(k,\omega)\right] - ik\hat{L}_{sy}(k,\omega)}{K(\omega)^2 - k^2}. \tag{7.4}$$

The inverse Fourier transform, from wavenumber k back to coordinate z, is defined by the integral

$$E(z,\omega) = \frac{1}{2\pi}\int_{-\infty}^{+\infty} \hat{E}(k,\omega)\, e^{+ikz}\, dk, \tag{7.5}$$

where, for notational simplicity, we omit subscript "x" indicating x-component. Finally, substituting for the doubly-transformed electric vector gives

$$E(z,\omega) = \frac{1}{2\pi}\int_{-\infty}^{+\infty} \frac{\mu(-i\omega)\left[\hat{J}_{sx}(k,\omega) + \hat{K}_{sx}(k,\omega)\right] - ik\hat{L}_{sy}(k,\omega)}{K(\omega)^2 - k^2}\; e^{+ikz}\, dk. \tag{7.6}$$

With known body sources, the above inverse Fourier transform may be performed with the aid of the definite integral

$$I(z,\omega) \equiv \frac{1}{2\pi}\int_{-\infty}^{+\infty} \frac{e^{+ikz}\,dk}{K(\omega)^2 - k^2} = \frac{1}{2\pi}\int_{-\infty}^{+\infty} \frac{(\cos kz + i\sin kz)\,dk}{K(\omega)^2 - k^2} = \frac{1}{\pi}\int_{0}^{+\infty} \frac{\cos kz\, dk}{K(\omega)^2 - k^2}$$

$$= \frac{-1}{\pi}\int_{0}^{+\infty} \frac{\cos kz\, dk}{\left(-iK(\omega)\right)^2 + k^2} = \frac{e^{+iK(\omega)|z|}}{2iK(\omega)}. \tag{7.7a}$$

The last step is via item 3.723(2) on page 445 in Gradshteyn and Ryzhik (1994). [The choice for complex parameter $\beta \equiv -iK(\omega) = -i\left[(\omega/c(\omega)) + i\alpha(\omega)\right] = \alpha(\omega) - i(\omega/c(\omega))$ has the required *positive* real part, whereas the alternative $\beta = +iK(\omega)$ does not.] With magnetic current sourcing, we require the space derivative

$$\frac{dI(z,\omega)}{dz} = \frac{\mathrm{sgn}(z)}{2} e^{+iK(\omega)|z|} = iK(\omega)\,\mathrm{sgn}(z) I(z,\omega), \tag{7.7b}$$

where sgn(*z*) is the signum (or sign) function. Then, the frequency-domain electric vector $E(z,\omega)$ may be formally written as spatial convolution over coordinate *z*:

$$E(z,\omega) = \left\{ \mu(-i\omega)\left[J_{sx}(z,\omega) + K_{sx}(z,\omega)\right] - \frac{\partial L_{sy}(z,\omega)}{\partial z} \right\} * I(z,\omega). \tag{7.8}$$

However, depending on the particular mathematical form of the body source terms, it may actually be easier to evaluate the Fourier transform integral (7.6) to obtain the frequency-domain field $E(z,\omega)$.

7.2 Two Simple Sourcing Scenarios

The 1D solution methodology outlined above is illustrated with two simple body source distributions: an infinitely thin "sheet" and a finite-thickness "slab" of conduction current.

7.2.1 Current Sheet

A particularly simple 1D body source consists of an infinitely-extended sheet of (lateral) current flow, localized at the coordinate $z = z_{mid}$. Hence, assume a source conduction current density $j_{sx}(z,t) = Jw(t)\delta(z - z_{mid})$, where magnitude scalar *J* has the SI unit A/m and *w*(*t*) is a dimensionless waveform (often normalized to unit maximum absolute amplitude). The doubly-transformed source current density is $\hat{J}_{sx}(k,\omega) = JW(\omega)e^{-ikz_{mid}}$. Then, from equation (6.6), the *x*-component electric vector is obtained as

$$E(z,\omega)\big|_{\text{sheet}} = J\mu(-i\omega)W(\omega)\frac{1}{2\pi}\int_{-\infty}^{+\infty}\frac{e^{+ik(z-z_{mid})}}{K(\omega)^2 - k^2}\,dk = J\mu(-i\omega)W(\omega)I(z - z_{mid},\omega)$$

$$= J\mu(-i\omega)W(\omega)\left[\frac{e^{+iK(\omega)|z-z_{mid}|}}{2iK(\omega)}\right] = \frac{J\mu}{2}\left[\frac{-i\omega}{iK(\omega)}\right]W(\omega)e^{+iK(\omega)|z-z_{mid}|}. \tag{7.9}$$

As expected, the electric field generated by a current sheet is symmetric about coordinate z_{mid}. Moreover, equation (7.9) satisfies the plane wave propagation relation

$$E(z_2,\omega)\big|_{\text{sheet}} = E(z_1,\omega)\big|_{\text{sheet}} e^{\pm iK(\omega)(z_2 - z_1)}, \tag{7.10}$$

where the + sign is used if $z_1, z_2 > z_{mid}$ and the – sign is used if $z_1, z_2 < z_{mid}$.

The space-frequency expression (7.9) suggests the equivalent space-time expression

$$e(z,t)\big|_{\text{sheet}} = \frac{J\mu}{2} w'(t) * \mathrm{F}^{-1}\left\{\frac{e^{+iK(\omega)|z-z_{mid}|}}{iK(\omega)}\right\}, \tag{7.11}$$

where $F^{-1}\{\ \}$ is the inverse Fourier transform of { }, an asterisk denotes convolution with respect to time *t*, and a prime denotes differentiation with respect to the argument of a function. In general, this inverse Fourier transform is difficult (perhaps impossible?) to perform. Hence, adopt a high-frequency approximation for the complex wavenumber as

$$K(\omega) \approx \frac{\omega}{c_\infty} + i\alpha_\infty ,$$

with infinite-frequency phase speed $c_\infty = 1/\sqrt{\varepsilon\mu}$ and infinite-frequency attenuation factor $\alpha_\infty = (\sigma/2)\sqrt{\mu/\varepsilon}$. Then, with the aid of items 3.722(2 and 4) on page 448 of Gradshteyn and Ryzhik (1994), it can be shown that

$$\mathrm{F}^{-1}\left\{ \frac{e^{+iK(\omega)|z-z_{mid}|}}{iK(\omega)} \right\} = -c_\infty e^{-\alpha_\infty |z-z_{mid}|} \left[e^{-\alpha_\infty c_\infty \left(t - \frac{|z-z_{mid}|}{c_\infty} \right)} H\left(t - \frac{|z-z_{mid}|}{c_\infty} \right) \right], \tag{7.12}$$

where $H(t)$ is the Heaviside unit step function. The inverse Fourier transform is a one-sided decaying exponential with onset time $|z-z_{mid}|/c_\infty$; the amplitude is also exponentially attenuated with distance $|z-z_{mid}|$ from the current sheet. The time-domain electric field (7.11) becomes

$$e(z,t)\big|_{\text{sheet}} \approx -\frac{J}{2}\sqrt{\frac{\mu}{\varepsilon}} e^{-\alpha_\infty |z-z_{mid}|}\ w'(t) * \left[e^{-\alpha_\infty c_\infty \left(t - \frac{|z-z_{mid}|}{c_\infty} \right)} H\left(t - \frac{|z-z_{mid}|}{c_\infty} \right) \right], \tag{7.13a}$$

where the approximate equality indicates this is a high-frequency expression. For vanishing conductivity $\sigma \to 0$ (corresponding to vacuum), then $\alpha_\infty = 0$ and the above reduces to

$$e(z,t)\big|_{\text{sheet}} = -\frac{J}{2}\sqrt{\frac{\mu}{\varepsilon}}\ w'(t) * H\left(t - \frac{|z-z_{mid}|}{c_\infty} \right) = -\frac{J}{2}\sqrt{\frac{\mu}{\varepsilon}}\ w\left(t - \frac{|z-z_{mid}|}{c_\infty} \right). \tag{7.13b}$$

The source waveform $w(t)$ propagates vertically away (i.e., up and down) from the current sheet at $z = z_{mid}$ with speed c_∞, without amplitude diminution or shape distortion. Note the negative sign out front! If waveform $w(t)$ is positive, then the electric vector *x*-component $e(z,t)$ is negative. This is a manifestation of *Lenz's Law* of electromagnetism: an induced electric current acts in a manner that opposes the action that generates it. Thus, a *positive* source current flow at $z = z_{mid}$ induces a *negative* conduction current flow for $z \neq z_{mid}$ (and vice versa) in order to satisfy conservation of electric charge.

7.2.2 Current Slab

Next, suppose the body source of current is confined to a slab of finite thickness *h*, centered at coordinate z_{mid}. The conduction current density vector is

$$j_{sx}(z,t) = Mw(t)\Pi\left(\frac{z - z_{mid}}{h}\right), \tag{7.14}$$

where amplitude scalar *M* has SI unit A/m^2 and $\Pi(x)$ is the rectangle function of unit height and area. The doubly-transformed source current is

$$\hat{J}_{sx}(k,\omega) = MhW(\omega)e^{-ikz_{mid}}\ \mathrm{sinc}\left(\frac{kh}{2\pi}\right), \tag{7.15}$$

where the well-known "sinc function" is defined as $\mathrm{sinc}(x) = \sin(\pi x)/\pi x$. Persisting through some algebra, the inverse transform to the space-frequency domain for the electric vector *x*-component can be put into the form:

$$E(z,\omega)\big|_{\mathrm{slab}} = \frac{M\mu(-i\omega)W(\omega)}{\pi}\left\{\int_0^\infty \frac{\sin\left[k(z - z_{bot})\right]}{k\left[\left(-iK(\omega)\right)^2 + k^2\right]}dk - \int_0^\infty \frac{\sin\left[k(z - z_{top})\right]}{k\left[\left(-iK(\omega)\right)^2 + k^2\right]}dk\right\}, \tag{7.16}$$

where $z_{top} = z_{mid} - h/2$ and $z_{bot} = z_{mid} + h/2$ are the "top" and "bottom" *z*-coordinates of the source current slab. Next, utilize item 3.725(1) on page 446 in Gradshteyn and Ryzhik (1994):

$$\int_0^{+\infty} \frac{\sin ax\,dx}{x\left(\beta^2 + x^2\right)} = \frac{\pi}{2\beta^2}\left[1 - e^{-a\beta}\right] \qquad \text{for} \quad \mathrm{Re}\{\beta\} > 0 \quad \text{and} \quad a > 0.$$

Then, for $z < z_{top}$:

$$E(z,\omega)\big|_{\mathrm{slab}} = \frac{M}{2}\frac{\mu(-i\omega)W(\omega)}{K(\omega)^2}\left[e^{+iK(\omega)(z_{top} - z)} - e^{+iK(\omega)(z_{bot} - z)}\right], \tag{7.17a}$$

and for $z > z_{bot}$:

$$E(z,\omega)\big|_{\mathrm{slab}} = \frac{M}{2}\frac{\mu(-i\omega)W(\omega)}{K(\omega)^2}\left[e^{+iK(\omega)(z - z_{bot})} - e^{+iK(\omega)(z - z_{top})}\right]. \tag{7.17b}$$

Alternately, the field external to the source current slab for $|z - z_{mid}| > h/2$ may be expressed in a single formula as

$$E(z,\omega)\big|_{\mathrm{slab}} = \frac{\mu Mh}{2}\left[\frac{\sinh\left[iK(\omega)h/2\right]}{iK(\omega)h/2}\right]\left[\frac{-i\omega}{iK(\omega)}\right]W(\omega)e^{+iK(\omega)|z - z_{mid}|}, \tag{7.18}$$

which exhibits the same dependence on coordinate *z* as the sheet source electric field of the previous equation (7.9).

Internal to the current slab, for $z_{top} < z < z_{bot}$, the electric vector component is

$$E(z,\omega)\big|_{\text{slab}} = M\,\frac{\mu(-i\omega)W(\omega)}{K(\omega)^2}\left\{1 - e^{+iK(\omega)(h/2)}\cosh\left[iK(\omega)(z-z_{mid})\right]\right\}. \tag{7.19}$$

Expressions (7.18 and 7.19) are clearly symmetric about the slab midpoint z_{mid}. Moreover, the formulae agree on $E(z_{mid} \pm h/2)$ at the slab boundaries. Finally, in the limit as the slab thickness h vanishes and the source current magnitude M simultaneously grows without bound, such that the product $Mh = J$ remains fixed, the *slab* external electric field (7.18) approaches the form (7.9) appropriate for *sheet* source current flow.

7.3 Conductivity Contrast

The FBA scattering situation for a contrast in electric current conductivity is pursued first, as it forms a template for the slightly more complicated cases of dielectric permittivity and magnetic permeability contrasts. In the First Born Approximation, an "effective body source" of conduction current, defined within the depth interval of the geologic layer $z_{top} < z < z_{bot}$, is given by the product of the conductivity difference and the incident electric field:

$$j_{sx}^{B}(z,t) = (\sigma_2 - \sigma_1)\,e_{inc}(z,t)\,\Pi\left(\frac{z - z_{mid}}{h}\right), \tag{7.20}$$

where $\Pi(x)$ is the rectangle function of unit height and area. See equation (D1.4a) of Appendix D. Superscript "*B*" indicates a First Born Approximation effective source. This form differs from the slab current body source (7.14) in that the incident electric field varies with coordinate z across the layer. Fourier transforming to the frequency-domain gives

$$J_{sx}^{B}(z,\omega) = (\sigma_2 - \sigma_1)\,E_{inc}(z,\omega)\,\Pi\left(\frac{z - z_{mid}}{h}\right). \tag{7.21a}$$

A trivial re-write is

$$J_{sx}^{B}(z,\omega) = \left[(\sigma_2 - \sigma_1)h\right]E_{inc}(z,\omega)\,\frac{1}{h}\,\Pi\left(\frac{z - z_{mid}}{h}\right). \tag{7.21b}$$

This form indicates that, in the limits of vanishing thickness $h \to 0$ and infinite conductivity contrast $\Delta\sigma = \sigma_2 - \sigma_1 \to \infty$, such that the product $\Delta\sigma\, h \equiv S$ remains fixed, then the Born source current reduces to the sheet source current form $SE_{inc}(z_{mid},\omega)\delta(z - z_{mid})$.

The incident electric field (x-component) is a plane wave propagating in the $+z$ direction. In the frequency-domain, we have

$$E_{inc}(z,\omega) = E_{inc}(z_s,\omega)e^{+iK_1(\omega)(z - z_s)}. \tag{7.22}$$

Substitute this into equation (7.21a) and Fourier transform to the wavenumber domain to obtain the doubly-transformed Born current source as (next page):

$$\hat{J}_{sx}^{B}(k,\omega) = (\sigma_2 - \sigma_1) E_{inc}(z_s,\omega) e^{-iK_1(\omega)z_s} \int_{z_{mid}-h/2}^{z_{mid}+h/2} e^{+i[K_1(\omega)-k]z} dz$$

$$= (\sigma_2 - \sigma_1) E_{inc}(z_s,\omega) e^{-iK_1(\omega)z_s} \frac{e^{+i[K_1(\omega)-k]z_{mid}}}{i[K_1(\omega)-k]} \left[e^{+i[K_1(\omega)-k](h/2)} - e^{-i[K_1(\omega)-k](h/2)} \right]$$

$$= (\sigma_2 - \sigma_1) E_{inc}(z_s,\omega) e^{+iK_1(\omega)(z_{mid}-z_s)} \left[\frac{e^{+iK_1(\omega)(h/2)} e^{-ik(z_{mid}+h/2)} - e^{-iK_1(\omega)(h/2)} e^{-ik(z_{mid}-h/2)}}{i[K_1(\omega)-k]} \right]$$

$$= (\sigma_2 - \sigma_1) E_{inc}(z_{mid},\omega) \left[\frac{e^{+iK_1(\omega)(h/2)} e^{-ik(z_{mid}+h/2)} - e^{-iK_1(\omega)(h/2)} e^{-ik(z_{mid}-h/2)}}{i[K_1(\omega)-k]} \right]$$

$$= [(\sigma_2 - \sigma_1)h] E_{inc}(z_{mid},\omega) \left[\frac{e^{+iK_1(\omega)(h/2)} e^{-ikz_{bot}} - e^{-iK_1(\omega)(h/2)} e^{-ikz_{top}}}{i[K_1(\omega)-k]h} \right]. \qquad (7.23)$$

In the last equality, the ratio in square brackets approaches the expected form $e^{-ikz_{mid}}$ as h approaches zero. Next, substitute this into equation (7.6) for the doubly-transformed electric field (assuming no displacement current and magnetic current sources) to obtain

$$\hat{E}_B(k,\omega) = (-i\omega)\mu_1 \frac{[(\sigma_2 - \sigma_1)h] E_{inc}(z_{mid},\omega)}{K_1(\omega)^2 - k^2} \left[\frac{e^{+iK_1(\omega)(h/2)} e^{-ikz_{bot}} - e^{-iK_1(\omega)(h/2)} e^{-ikz_{top}}}{i[K_1(\omega)-k]h} \right]. \qquad (7.24)$$

Subscript "*B*" on the left-hand-side indicates this is an *x*-component electric vector generated by a First Born Approximation effective current source.

We have not located a tabulated integral form for the inverse Fourier transform (from wavenumber *k* to coordinate *z*) of expression (7.24). Hence, we pursue an alternative solution strategy. By inspection, the inverse Fourier transform of (7.24) may be written as

$$E_B(z,\omega) = (-i\omega)\mu_1 [(\sigma_2 - \sigma_1)h] E_{inc}(z_{mid},\omega) \left[e^{+iK_1(\omega)(h/2)} \delta(z - z_{bot}) - e^{-iK_1(\omega)(h/2)} \delta(z - z_{top}) \right] *$$
$$\frac{1}{h} \mathrm{F}^{-1} \left\{ \frac{1}{K_1(\omega)^2 - k^2} \right\} * \frac{1}{i} \mathrm{F}^{-1} \left\{ \frac{1}{K_1(\omega) - k} \right\}, \qquad (7.25)$$

where the asterisks now denote convolution with respect to the spatial coordinate *z*. From equation (7.7a) above, we already have the result

$$\frac{1}{h} \mathrm{F}^{-1} \left\{ \frac{1}{K_1(\omega)^2 - k^2} \right\} = \frac{e^{+iK_1(\omega)|z|}}{2iK_1(\omega)h}.$$

Next, using the Residue Theorem, it is readily demonstrated that

$$\frac{1}{i}\mathrm{F}^{-1}\left\{\frac{1}{K_1(\omega)-k}\right\}=-e^{+iK_1(\omega)z}H(z),$$

where $H(z)$ is the Heaviside unit step function. The spatial convolution of these two factors is

$$\frac{1}{h}\mathrm{F}^{-1}\left\{\frac{1}{K_1(\omega)^2-k^2}\right\}*\frac{1}{i}\mathrm{F}^{-1}\left\{\frac{1}{K_1(\omega)-k}\right\}=\frac{1}{4hK_1(\omega)^2}\begin{cases}\left[2iK_1(\omega)z-1\right]e^{+iK_1(\omega)z}, & \text{for } z>0,\\ -e^{-iK_1(\omega)z}, & \text{for } z<0,\end{cases}$$

$$=\frac{1}{4hK_1(\omega)^2}\left[2iK_1(\omega)zH(z)-1\right]e^{+iK_1(\omega)|z|}.$$

Inserting this result into equation (7.25) and performing the final convolutions yields the frequency-domain Born scattered electric vector *x*-component as

$$E_B(z,\omega)=(-i\omega)\mu_1\left[(\sigma_2-\sigma_1)h\right]E_{inc}(z_{mid},\omega)\frac{1}{4hK_1(\omega)^2}\times$$

$$\left\{\left[2iK_1(\omega)(z-z_{bot})H(z-z_{bot})-1\right]e^{+iK_1(\omega)|z-z_{bot}|}\,e^{+iK_1(\omega)(h/2)}\right.$$

$$\left.-\left[2iK_1(\omega)(z-z_{top})H(z-z_{top})-1\right]e^{+iK_1(\omega)|z-z_{top}|}\,e^{-iK_1(\omega)(h/2)}\right\}. \qquad (7.26)$$

As with the slab current source electric field (7.17a and b), the top and bottom boundaries of the geologic layer play an important role. For $z < z_{top}$, the above expression simplifies to

$$E_B(z,\omega)\big|_{\Delta\sigma}=\frac{\mu_1\left[(\sigma_2-\sigma_1)h\right]}{2}\left[\frac{\sinh\left[iK_1(\omega)h\right]}{iK_1(\omega)h}\right]\left[\frac{-i\omega}{iK_1(\omega)}\right]E_{inc}(z_{mid},\omega)e^{+iK_1(\omega)(z_{mid}-z)}, \qquad (7.27a)$$

whereas for $z > z_{bot}$ we have

$$E_B(z,\omega)\big|_{\Delta\sigma}=\frac{\mu_1\left[(\sigma_2-\sigma_1)h\right]}{2}\left[\frac{-i\omega}{iK_1(\omega)}\right]E_{inc}(z_{mid},\omega)e^{+iK_1(\omega)(z-z_{mid})}. \qquad (7.27b)$$

The left-hand-side notation indicates that these are Born scattered fields generated by a conductivity contrast $\Delta\sigma\equiv\sigma_2-\sigma_1$. Unlike the electric field generated by a finite-thickness slab of source current, the Born scattered electric field is *not* symmetric about the midpoint z_{mid}; the reflected response (7.27a) contains a "modulating factor" in the bed thickness h. This asymmetry is expected, because the illuminating electromagnetic field $E_{inc}(z,\omega)$ is incident onto the geologic bed from above (i.e., from smaller z-coordinate). In fact, the Born reflected response is quite similar to the (total) slab response:

$$E(z,\omega)\big|_{\text{slab}}=\frac{\mu Mh}{2}\left[\frac{\sinh\left[iK(\omega)h/2\right]}{iK(\omega)h/2}\right]\left[\frac{-i\omega}{iK(\omega)}\right]W(\omega)e^{+iK(\omega)|z-z_{mid}|}, \qquad (7.18 \text{ again})$$

but note the interesting slight difference in the bed thickness modulating factors.

Expressions (7.27a and b) for the Born back-scattered and fore-scattered wavefields can be simplified further, by recognizing the incident EM wavefield at level z is $E_{inc}(z,\omega) = E_{inc}(z_s,\omega)e^{+iK_1(\omega)(z-z_s)}$. Then, for $z < z_{top}$, we have

$$E_B(z,\omega)\big|_{\Delta\sigma} = \frac{\mu_1[(\sigma_2-\sigma_1)h]}{2}\left[\frac{\sinh[iK_1(\omega)h]}{iK_1(\omega)h}\right]\left[\frac{-i\omega}{iK_1(\omega)}\right]e^{+iK_1(\omega)2(z_{mid}-z)}E_{inc}(z,\omega)\,, \tag{7.27c}$$

whereas for $z > z_{bot}$ we have

$$E_B(z,\omega)\big|_{\Delta\sigma} = \frac{\mu_1[(\sigma_2-\sigma_1)h]}{2}\left[\frac{-i\omega}{iK_1(\omega)}\right]E_{inc}(z,\omega)\,. \tag{7.27d}$$

Note the asymmetry. The back-scattered response contains a "layer thickness modulation factor" involving the hyperbolic sine function. Additionally, it contains a complex-exponential that accounts for extra dispersion/attenuation as the incident EM wave propagates from the source level z_s down to the layer midpoint z_{mid}, and then back to a receiver at level $z < z_{top}$.

In the limit of small layer thickness h, the responses reduce to the common form

$$E_B(z,\omega)\big|_{\Delta\sigma} \approx \frac{\mu_1[(\sigma_2-\sigma_1)h]}{2}\left[\frac{-i\omega}{iK_1(\omega)}\right]E_{inc}(z_{mid},\omega)e^{+iK_1(\omega)|z-z_{mid}|}\,. \tag{7.28}$$

In the limits of vanishing bed thickness $h \to 0$ and infinite conductivity contrast $\sigma_2 - \sigma_1 \to +\infty$, such that the product $(\sigma_2 - \sigma_1)h \equiv S$ remains fixed, the Born scattered response reduces to

$$\lim_{\substack{h\to 0\\ \sigma_2\to\infty}} E_B(z,\omega)\big|_{\Delta\sigma} = \frac{\mu_1 S}{2}\left[\frac{-i\omega}{iK_1(\omega)}\right]E_{inc}(z_{mid},\omega)e^{+iK_1(\omega)|z-z_{mid}|},$$

which is identical in form to the body source current sheet electric field of equation (7.9), as expected.

Internal to the geologic bed, for $z_{top} < z < z_{bot}$, the Born scattered electric vector component is

$$E_B(z,\omega)\big|_{\Delta\sigma} = \frac{(\sigma_2-\sigma_1)}{2}\frac{\mu_1(-i\omega)E_{inc}(z,\omega)}{K_1(\omega)^2}\times \frac{1}{2}\left\{\left[1-2iK_1(\omega)\left(z-z_{mid}+\frac{h}{2}\right)\right]e^{+iK_1(\omega)(h/2)}-1\right\}. \tag{7.29}$$

We intentionally write the electric field in this manner in order to compare with the analogous field inside the finite-thickness source current slab:

$$E(z,\omega)\big|_{\text{slab}} = M\,\frac{\mu(-i\omega)W(\omega)}{K(\omega)^2}\left\{1-e^{+iK(\omega)(h/2)}\cosh[iK(\omega)(z-z_{mid})]\right\}. \tag{7.19 again}$$

Clearly, there are similarities and differences. Both vanish as bed thickness $h \to 0$.

7.4 Permittivity Contrast

First Born Approximation scattered wavefields generated by an electric permittivity contrast $\Delta\varepsilon = \varepsilon_2 - \varepsilon_1$ assigned to the geologic layer are easily obtained from the previously-derived equations for a current conductivity contrast $\Delta\sigma$. As per equation (D1.4b) in Appendix D, an "effective electric displacement vector body source", defined within the depth interval of the layer $z_{top} < z < z_{bot}$, is given by the product of the permittivity difference and the incident electric field:

$$d_{sx}^{B}(z,t) = (\varepsilon_2 - \varepsilon_1)\, e_{inc}(z,t)\, \Pi\left(\frac{z - z_{mid}}{h}\right). \tag{7.30}$$

Once again, $\Pi(z)$ is the rectangle function of unit height and area. Comparing this with equation (7.20) for an "effective current density vector body source" indicates

$$d_{sx}^{B}(z,t) = \frac{\varepsilon_2 - \varepsilon_1}{\sigma_2 - \sigma_1}\, j_{sx}^{B}(z,t)\,. \tag{7.31}$$

The "effective electric displacement current" is the time-derivative

$$k_{sx}^{B}(z,t) \equiv \frac{\partial d_{sx}^{B}(z,t)}{\partial t} = \frac{\varepsilon_2 - \varepsilon_1}{\sigma_2 - \sigma_1}\frac{\partial j_{sx}^{B}(z,t)}{\partial t}, \tag{7.32a}$$

or, in the doubly-Fourier transformed domain

$$\hat{K}_{sx}^{B}(k,\omega) = \frac{\varepsilon_2 - \varepsilon_1}{\sigma_2 - \sigma_1}(-i\omega)\, \hat{J}_{sx}^{B}(k,\omega)\,. \tag{7.32b}$$

In general, the frequency-domain electric vector generated by the three different body source types is given by inverse Fourier transform equation (7.6) above as

$$E(z,\omega) = \frac{1}{2\pi}\int_{-\infty}^{+\infty} \frac{\mu(-i\omega)\left[\hat{J}_{sx}(k,\omega) + \hat{K}_{sx}(k,\omega)\right] - ik\hat{L}_{sy}(k,\omega)}{K(\omega)^2 - k^2}\; e^{+ikz}\, dk\,. \tag{7.6 again}$$

In the present situation, the only active body source is the effective displacement current. Hence

$$E_B(z,\omega)\big|_{\Delta\varepsilon} = \frac{\mu_1(-i\omega)}{2\pi}\int_{-\infty}^{+\infty}\frac{\hat{K}_{sx}^{B}(k,\omega)}{K(\omega)^2 - k^2}\; e^{+ikz}\, dk = \frac{\varepsilon_2 - \varepsilon_1}{\sigma_2 - \sigma_1}\;\frac{(-i\omega)}{2\pi}\int_{-\infty}^{+\infty}\frac{\mu_1(-i\omega)\hat{J}_{sx}^{B}(k,\omega)}{K(\omega)^2 - k^2}\; e^{+ikz}\, dk\,.$$

By equation (7.6), this is clearly

$$E_B(z,\omega)\big|_{\Delta\varepsilon} = \frac{\varepsilon_2 - \varepsilon_1}{\sigma_2 - \sigma_1}(-i\omega)E_B(z,\omega)\big|_{\Delta\sigma}\,. \tag{7.33}$$

The Born scattered EM wavefield generated by a permittivity contrast $\Delta\varepsilon$ is proportional to the analogous wavefield generated by a conductivity contrast $\Delta\sigma$. However, the proportionality coefficient is frequency-dependent. In the time-domain, this becomes

$$e_B(z,t)\big|_{\Delta\varepsilon} = \frac{\varepsilon_2 - \varepsilon_1}{\sigma_2 - \sigma_1}\frac{\partial}{\partial t} e_B(z,t)\big|_{\Delta\sigma}. \tag{7.34}$$

Now, for $z < z_{top}$, we have the conductivity contrast Born scattered field

$$E_B(z,\omega)\big|_{\Delta\sigma} = \frac{\mu_1\left[(\sigma_2 - \sigma_1)h\right]}{2}\left[\frac{\sinh\left[iK_1(\omega)h\right]}{iK_1(\omega)h}\right]\left[\frac{-i\omega}{iK_1(\omega)}\right]E_{inc}(z_{mid},\omega)e^{+iK_1(\omega)(z_{mid}-z)}, \tag{7.27a again}$$

whereas for $z > z_{bot}$ we have

$$E_B(z,\omega)\big|_{\Delta\sigma} = \frac{\mu_1\left[(\sigma_2 - \sigma_1)h\right]}{2}\left[\frac{-i\omega}{iK_1(\omega)}\right]E_{inc}(z_{mid},\omega)e^{+iK_1(\omega)(z-z_{mid})}. \tag{7.27b again}$$

Hence, from equation (6733), the permittivity contrast First Born Approximation scattered fields become: For $z < z_{top}$:

$$E_B(z,\omega)\big|_{\Delta\varepsilon} = \frac{\mu_1\left[(\varepsilon_2 - \varepsilon_1)h\right]}{2}\left[\frac{\sinh\left[iK_1(\omega)h\right]}{iK_1(\omega)h}\right]\left[\frac{(-i\omega)^2}{iK_1(\omega)}\right]E_{inc}(z_{mid},\omega)e^{+iK_1(\omega)(z_{mid}-z)}, \tag{7.35a}$$

whereas for $z > z_{bot}$ we have

$$E_B(z,\omega)\big|_{\Delta\varepsilon} = \frac{\mu_1\left[(\varepsilon_2 - \varepsilon_1)h\right]}{2}\left[\frac{(-i\omega)^2}{iK_1(\omega)}\right]E_{inc}(z_{mid},\omega)e^{+iK_1(\omega)(z-z_{mid})}. \tag{7.35b}$$

Once again, there is a slight asymmetry in the back-scattered and fore-scattered responses. In the limit of small layer thickness *h*, the responses reduce to the common form

$$E_B(z,\omega)\big|_{\Delta\varepsilon} \approx \frac{\mu_1\left[(\varepsilon_2 - \varepsilon_1)h\right]}{2}\left[\frac{(-i\omega)^2}{iK_1(\omega)}\right]E_{inc}(z_{mid},\omega)e^{+iK_1(\omega)|z-z_{mid}|}. \tag{7.36}$$

Internal to the geologic bed, for $z_{top} < z < z_{bot}$, the Born scattered electric vector component is

$$E_B(z,\omega)\big|_{\Delta\varepsilon} = \frac{(\varepsilon_2 - \varepsilon_1)}{2}\frac{\mu_1(-i\omega)^2 E_{inc}(z_{mid},\omega)}{K_1(\omega)^2} \times$$

$$\frac{1}{2}\left\{\left[1 - 2iK_1(\omega)(z - z_{top})\right]e^{+iK_1(\omega)(z-z_{mid})} - e^{+iK_1(\omega)(h/2)}e^{-iK_1(\omega)(z-z_{bot})}\right\}. \tag{7.37}$$

7.5 Permeability Contrast

The final First Born Approximation scattering situation to consider is a contrast in magnetic permeability $\Delta\mu = \mu_2 - \mu_1$. From equation (D1.4c) of Appendix D, the effective magnetic induction body source is given by

$$b_{sy}^{B}(z,t) = (\mu_2 - \mu_1)\, h_{inc}(z,t)\, \Pi\left(\frac{z - z_{mid}}{h}\right) = \frac{\mu_2 - \mu_1}{\mu_1}\, b_{inc}(z,t)\, \Pi\left(\frac{z - z_{mid}}{h}\right), \tag{7.38}$$

where again the rectangle function $\Pi(x)$ localizes the body source to the depth interval $z_{top} < z < z_{bot}$. The y-component of the incident magnetic induction (or magnetic flux) vector is $b_{inc}(z,t)$. Fourier transforming to the frequency-domain gives

$$B_{sy}^{B}(z,\omega) = \frac{\mu_2 - \mu_1}{\mu_1}\, B_{inc}(z,\omega)\, \Pi\left(\frac{z - z_{mid}}{h}\right). \tag{7.39}$$

Now, from Faraday's Law:

$$B_{inc}(z,\omega) = \frac{K_1(\omega)}{\omega} E_{inc}(z,\omega) = \frac{K_1(\omega)}{\omega} E_{inc}(z_s,\omega) e^{+iK_1(\omega)(z - z_s)}. \qquad \text{(from B3a)}$$

Then, we have

$$B_{sy}^{B}(z,\omega) = \frac{\mu_2 - \mu_1}{\mu_1} \frac{K_1(\omega)}{\omega} E_{inc}(z,\omega)\, \Pi\left(\frac{z - z_{mid}}{h}\right), \tag{7.40}$$

where the obvious $E_{inc}(z_s,\omega) e^{+iK_1(\omega)(z - z_s)} = E_{inc}(z,\omega)$ is used. But we already have the effective FBA current density body source

$$J_{sx}^{B}(z,\omega) = (\sigma_2 - \sigma_1)\, E_{inc}(z,\omega)\, \Pi\left(\frac{z - z_{mid}}{h}\right). \qquad \text{(7.21a again)}$$

So this implies

$$B_{sy}^{B}(z,\omega) = \frac{\mu_2 - \mu_1}{\sigma_2 - \sigma_1} \frac{K_1(\omega)}{\omega\mu_1} J_{sx}^{B}(z,\omega), \tag{7.41a}$$

and after Fourier transforming to the wavenumber domain

$$\hat{B}_{sy}^{B}(k,\omega) = \frac{\mu_2 - \mu_1}{\sigma_2 - \sigma_1} \frac{K_1(\omega)}{\omega\mu_1} \hat{J}_{sx}^{B}(k,\omega). \tag{7.41b}$$

Next, recall the general solution for the x-component electric field due to the three body source types as

$$E(z,\omega) = \frac{1}{2\pi}\int_{-\infty}^{+\infty} \frac{\mu(-i\omega)\left[\hat{J}_{sx}(k,\omega) + \hat{K}_{sx}(k,\omega)\right] - ik\hat{L}_{sy}(k,\omega)}{K(\omega)^2 - k^2}\; e^{+ikz}\, dk\,. \qquad \text{(7.6 again)}$$

Retaining only the magnetic current density source $\hat{L}_{sy}(k,\omega) = (-i\omega)\hat{B}_{sy}(k,\omega)$ gives the Born scattered electric field as

$$\begin{aligned} E_B(z,\omega)\big|_{\Delta\mu} &= -\frac{1}{2\pi}\int_{-\infty}^{+\infty} \frac{(ik)\hat{L}^B_{sy}(k,\omega)}{K(\omega)^2 - k^2}\; e^{+ikz}\, dk \\ &= -\frac{1}{2\pi}\int_{-\infty}^{+\infty} \frac{(ik)(-i\omega)\hat{B}^B_{sy}(k,\omega)}{K(\omega)^2 - k^2}\; e^{+ikz}\, dk \\ &= -\frac{\mu_2 - \mu_1}{\sigma_2 - \sigma_1}\frac{K_1(\omega)}{\omega\mu_1}\frac{1}{2\pi}\int_{-\infty}^{+\infty} \frac{(ik)(-i\omega)\hat{J}^B_{sx}(k,\omega)}{K(\omega)^2 - k^2}\; e^{+ikz}\, dk \\ &= -\frac{\mu_2 - \mu_1}{\sigma_2 - \sigma_1}\frac{K_1(\omega)}{\omega\mu_1^2}\frac{1}{2\pi}\int_{-\infty}^{+\infty} \frac{(ik)\mu_1(-i\omega)\hat{J}^B_{sx}(k,\omega)}{K(\omega)^2 - k^2}\; e^{+ikz}\, dk\,. \end{aligned}$$

But by the general solution expression (7.6) again, this reduces to the space derivative

$$\begin{aligned} E_B(z,\omega)\big|_{\Delta\mu} &= -\frac{\mu_2 - \mu_1}{\sigma_2 - \sigma_1}\frac{K_1(\omega)}{\omega\mu_1^2}\frac{\partial}{\partial z}E_B(z,\omega)\big|_{\Delta\sigma} \\ &= -\left[\frac{\mu_2}{\mu_1} - 1\right]\left[\frac{K_1(\omega)}{(\sigma_2 - \sigma_1)\omega\mu_1}\right]\frac{\partial}{\partial z}E_B(z,\omega)\big|_{\Delta\sigma}\,. \end{aligned} \qquad \text{(7.42)}$$

The FBA scattered field generated by a permeability contrast is proportional to the derivative (with respect to depth coordinate z) of the field generated by a conductivity contrast. Now, for $z < z_{top}$, we have the previous expression for a conductivity contrast field as

$$E_B(z,\omega)\big|_{\Delta\sigma} = \frac{\mu_1\left[(\sigma_2 - \sigma_1)h\right]}{2}\left[\frac{\sinh\left[iK_1(\omega)h\right]}{iK_1(\omega)h}\right]\left[\frac{-i\omega}{iK_1(\omega)}\right]E_{inc}(z_{mid},\omega)e^{+iK_1(\omega)(z_{mid}-z)}\,, \quad \text{(7.27a again)}$$

whereas for $z > z_{bot}$ we have

$$E_B(z,\omega)\big|_{\Delta\sigma} = \frac{\mu_1\left[(\sigma_2 - \sigma_1)h\right]}{2}\left[\frac{-i\omega}{iK_1(\omega)}\right]E_{inc}(z_{mid},\omega)e^{+iK_1(\omega)(z-z_{mid})}\,. \qquad \text{(7.27b again)}$$

Hence, it is easy to show

$$\frac{\partial}{\partial z}E_B(z,\omega)\big|_{\Delta\sigma} = \pm iK_1(\omega)\,E_B(z,\omega)\big|_{\Delta\sigma}\,, \qquad (7.43)$$

where the + sign is used for $z > z_{bot}$ and the – sign is used for $z < z_{top}$. Thus, putting it all together yields the First Born Approximation scattered fields generated by a magnetic permeability contrast as:

For $z < z_{top}$:

$$E_B(z,\omega)\big|_{\Delta\mu} = \frac{1}{2}\left(1-\frac{\mu_2}{\mu_1}\right)\sinh\left[iK_1(\omega)h\right]E_{inc}(z_{mid},\omega)e^{+iK_1(\omega)(z_{mid}-z)}, \tag{7.44a}$$

whereas for $z > z_{bot}$

$$E_B(z,\omega)\big|_{\Delta\mu} = \frac{1}{2}\left(\frac{\mu_2}{\mu_1}-1\right)\left[iK_1(\omega)h\right]E_{inc}(z_{mid},\omega)e^{+iK_1(\omega)(z-z_{mid})}. \tag{7.44b}$$

Again note the interesting asymmetry between these two expressions. First-order expansions in layer thickness *h* are obviously:

For $z < z_{top}$:

$$E_B(z,\omega)\big|_{\Delta\mu} \approx \left(1-\frac{\mu_2}{\mu_1}\right)\frac{h}{2}\left[iK_1(\omega)\right]E_{inc}(z_{mid},\omega)e^{+iK_1(\omega)(z_{mid}-z)}, \tag{7.45a}$$

and for $z > z_{bot}$:

$$E_B(z,\omega)\big|_{\Delta\mu} \approx \left(\frac{\mu_2}{\mu_1}-1\right)\frac{h}{2}\left[iK_1(\omega)\right]E_{inc}(z_{mid},\omega)e^{+iK_1(\omega)(z-z_{mid})}, \tag{7.45b}$$

which exhibit a remarkable similarity, although the back-scattered field (7.45a) has the opposite sign as the fore-scattered field (7.45b).

Finally, internal to the geologic layer, the Born scattered electric vector component is for $z_{top} < z < z_{bot}$:

$$E_B(z,\omega)\big|_{\Delta\mu} = \left(\frac{\mu_2}{\mu_1}-1\right)\frac{E_{inc}(z_{mid},\omega)}{2} \times$$

$$\frac{1}{2}\left\{\left[1+2iK_1(\omega)(z-z_{top})\right]e^{+iK_1(\omega)(z-z_{mid})} - e^{+iK_1(\omega)(h/2)}e^{-iK_1(\omega)(z-z_{bot})}\right\}. \tag{7.46}$$

7.6 FBA Scattering Response Summary

The various frequency-domain expressions for FBA scattered responses, in both the backward ($z < z_{top}$) and forward ($z > z_{bot}$) scattering zones, are summarized in this section. Responses recorded within the geologic layer ($z_{top} < z < z_{bot}$) are also given, although these may be of lesser practical interest. General (i.e., exact) expressions for these responses are then specialized to the low-frequency electromagnetic induction regime and a thin geologic layer.

7.6.1 Exact Born Approximations

Admittedly, the phraseology "exact…approximation" sounds somewhat odd. The intent is to re-state the FBA-derived scattering responses prior to adopting an additional thin bed and/or low-frequency approximation.

1) *Current conductivity contrast*: $\Delta\sigma = \sigma_2 - \sigma_1$.

For $z < z_{top}$:

$$E_B(z,\omega)\big|_{\Delta\sigma} = \frac{\mu_1\left[(\sigma_2-\sigma_1)h\right]}{2}\left[\frac{\sinh\left[iK_1(\omega)h\right]}{iK_1(\omega)h}\right]\left[\frac{-i\omega}{iK_1(\omega)}\right]E_{inc}(z_{mid},\omega)\,e^{+iK_1(\omega)(z_{mid}-z)}, \tag{7.47a}$$

and for $z > z_{bot}$ we have

$$E_B(z,\omega)\big|_{\Delta\sigma} = \frac{\mu_1\left[(\sigma_2-\sigma_1)h\right]}{2}\left[\frac{-i\omega}{iK_1(\omega)}\right]E_{inc}(z_{mid},\omega)\,e^{+iK_1(\omega)(z-z_{mid})}. \tag{7.47b}$$

Responses are proportional to the conductivity contrast $\Delta\sigma$, and the incident plane wave electric field at the layer midpoint $E_{inc}(z_{mid},\omega)$. Note again the asymmetry between the back-scattered and fore-scattered formulae. Although the fore-scattered response (7.47b) is directly proportional to the layer half-thickness $h/2$, the back-scattered response (7.47a) is not.

Internal to the geologic bed, for $z_{top} < z < z_{bot}$, the Born scattered electric vector component is

$$E_B(z,\omega)\big|_{\Delta\sigma} = \frac{\mu_1(\sigma_2-\sigma_1)}{2}\left[\frac{(-i\omega)}{K_1(\omega)^2}\right]E_{inc}(z_{mid},\omega)\ \times$$
$$\frac{1}{2}\left\{\left[1-2iK_1(\omega)(z-z_{top})\right]e^{+iK_1(\omega)(z-z_{mid})} - e^{+iK_1(\omega)h}e^{-iK_1(\omega)(z-z_{mid})}\right\}. \tag{7.47c}$$

2) *Dielectric permittivity contrast*: $\Delta\varepsilon = \varepsilon_2 - \varepsilon_1$.

For $z < z_{top}$:

$$E_B(z,\omega)\big|_{\Delta\varepsilon} = \frac{\mu_1\left[(\varepsilon_2-\varepsilon_1)h\right]}{2}\left[\frac{\sinh\left[iK_1(\omega)h\right]}{iK_1(\omega)h}\right]\left[\frac{(-i\omega)^2}{iK_1(\omega)}\right]E_{inc}(z_{mid},\omega)e^{+iK_1(\omega)(z_{mid}-z)}, \tag{7.48a}$$

and for $z > z_{bot}$ we have

$$E_B(z,\omega)\big|_{\Delta\varepsilon} = \frac{\mu_1\left[(\varepsilon_2-\varepsilon_1)h\right]}{2}\left[\frac{(-i\omega)^2}{iK_1(\omega)}\right]E_{inc}(z_{mid},\omega)e^{+iK_1(\omega)(z-z_{mid})}. \tag{7.48b}$$

Interestingly (and perhaps obviously), these $\Delta\varepsilon$ responses may be obtained from the corresponding $\Delta\sigma$ responses by multiplying by $(-i\omega)$ and making the replacement $\Delta\sigma \rightarrow \Delta\varepsilon$. Thus, permittivity contrast scattering has higher frequency content compared to conductivity contrast scattering.

Internal to the geologic bed, for $z_{top} < z < z_{bot}$, the Born scattered electric vector component is

$$E_B(z,\omega)\big|_{\Delta\varepsilon} = \frac{\mu_1(\varepsilon_2-\varepsilon_1)}{2}\left[\frac{(-i\omega)^2}{K_1(\omega)^2}\right]E_{inc}(z_{mid},\omega)\ \times$$
$$\frac{1}{2}\left\{\left[1-2iK_1(\omega)(z-z_{top})\right]e^{+iK_1(\omega)(z-z_{mid})} - e^{+iK_1(\omega)h}e^{-iK_1(\omega)(z-z_{mid})}\right\}. \tag{7.48c}$$

3) *Magnetic permeability contrast*: $\Delta\mu = \mu_2 - \mu_1$.

For $z < z_{top}$:

$$E_B(z,\omega)\big|_{\Delta\mu} = \frac{1}{2}\left(1-\frac{\mu_2}{\mu_1}\right)\sinh\left[iK_1(\omega)h\right]E_{inc}(z_{mid},\omega)e^{+iK_1(\omega)(z_{mid}-z)}, \tag{7.49a}$$

and for $z > z_{bot}$:

$$E_B(z,\omega)\big|_{\Delta\mu} = \frac{1}{2}\left(\frac{\mu_2}{\mu_1}-1\right)\left[iK_1(\omega)h\right]E_{inc}(z_{mid},\omega)e^{+iK_1(\omega)(z-z_{mid})}. \tag{7.49b}$$

In all cases, the forward-scattered responses are directly proportional to the layer half thickness $h/2$, whereas the backward-scattered responses are not. Moreover, back-scattered and fore-scattered $\Delta\mu$ responses have opposite sign.

Internal to the geologic layer, the Born scattered electric vector component is for $z_{top} < z < z_{bot}$:

$$E_B(z,\omega)\big|_{\Delta\mu} = \frac{1}{2}\left(\frac{\mu_2}{\mu_1} - 1\right) E_{inc}(z_{mid},\omega) \times$$

$$\frac{1}{2}\left\{\left[1 + 2iK_1(\omega)(z - z_{top})\right] e^{+iK_1(\omega)(z - z_{mid})} - e^{+iK_1(\omega)h} e^{-iK_1(\omega)(z - z_{mid})}\right\}. \quad (7.49c)$$

Note a sign difference compared to equations (7.47c) and (7.48c)!

All of the above FBA scattered responses are considered "exact" in the sense that the full-frequency complex wavenumber $K_1(\omega)$ (constructed with medium #1 parameters) is used in the expressions:

$$K_1(\omega) = \frac{1}{c_{1\infty}}\left[\frac{\omega}{s(\omega/\omega_1)} + i\frac{\omega_1 s(\omega/\omega_1)}{2}\right], \quad (2.2 \text{ again})$$

where the dimensionless function $s(x)$ is defined as

$$s(x) \equiv \sqrt{2|x|}\left[\sqrt{1 + x^2} - |x|\right]^{+1/2}. \quad (2.3 \text{ again})$$

The infinite-frequency phase speed $c_{1\infty}$ for medium #1 is defined as $c_{1\infty} = 1/\sqrt{\varepsilon_1\mu_1}$. (2.4a again)

7.6.2 Multi-Parameter Scattering

It should be obvious from the previous derivations that FBA scattered electric fields generated by contrasts in multiple layer parameters are given by the sum of formulae appropriate for single parameter scattering. Thus, combining the FBA back-scattering formulae (7.47a), (7.48a), and (7.49a) yields:

For $z < z_{top}$:

$$E_B(z,\omega)\big|_{\Delta\sigma+\Delta\varepsilon+\Delta\mu} = E_B(z,\omega)\big|_{\Delta\sigma} + E_B(z,\omega)\big|_{\Delta\varepsilon} + E_B(z,\omega)\big|_{\Delta\mu}$$

$$= \frac{h}{2}\left[\frac{\sinh[iK_1(\omega)h]}{[iK_1(\omega)h]}\right]\left\{\frac{\mu_1(-i\omega)}{iK_1(\omega)}\left[(\sigma_2 - \sigma_1) + (-i\omega)\varepsilon_1\left(\frac{\varepsilon_2}{\varepsilon_1} - 1\right)\right] - iK_1(\omega)\left(\frac{\mu_2}{\mu_1} - 1\right)\right\} \times$$

$$E_{inc}(z_{mid},\omega) e^{+iK_1(\omega)(z_{mid} - z)}, \quad (7.50a)$$

whereas the FBA fore-scattering formulae (7.47b), (7.48b), and (7.49b) give

For $z > z_{bot}$:

$$E_B(z,\omega)\big|_{\Delta\sigma+\Delta\varepsilon+\Delta\mu} = \frac{h}{2}\left\{\frac{\mu_1(-i\omega)}{iK_1(\omega)}\left[(\sigma_2 - \sigma_1) + (-i\omega)\varepsilon_1\left(\frac{\varepsilon_2}{\varepsilon_1} - 1\right)\right] + iK_1(\omega)\left(\frac{\mu_2}{\mu_1} - 1\right)\right\} \times$$

$$E_{inc}(z_{mid},\omega) e^{+iK_1(\omega)(z - z_{mid})}. \quad (7.50b)$$

The forward-scattering expression lacks the bed thickness modulation factor involving the hyperbolic sine function (and has opposite algebraic sign in the permeability scattering term).

For $z_{top} < z < z_{bot}$, the three intrabed FBA scattering formulae (7.47c), (7.48c), and (7.49c) are combined and re-written in a different form as

$$E_B(z,\omega)\big|_{\Delta\sigma+\Delta\varepsilon+\Delta\mu} = E_{inc}(z_{mid},\omega)e^{+iK_1(\omega)(z-z_{mid})}\frac{1}{4}\times$$
$$\left\{\frac{\mu_1(-i\omega)}{K_1(\omega)^2}\left[(\sigma_2-\sigma_1)+(-i\omega)\varepsilon_1\left(\frac{\varepsilon_2}{\varepsilon_1}-1\right)\right]\left[1-2iK_1(\omega)(z-z_{top})-e^{-2iK_1(\omega)(z-z_{bot})}\right]\right.$$
$$\left.+\left(\frac{\mu_2}{\mu_1}-1\right)\left[1+2iK_1(\omega)(z-z_{top})-e^{-2iK_1(\omega)(z-z_{bot})}\right]\right\}. \qquad (7.50c)$$

The above forms, utilizing the dimensionless parameter ratios $\varepsilon_2/\varepsilon_1$ and μ_2/μ_1,are preferred for numerical calculation purposes. However, recalling the notation $\hat{\varepsilon}=\varepsilon_2/\varepsilon_1$, $\hat{\mu}=\mu_2/\mu_1$, and $\hat{\sigma}=\sigma_2/\sigma_1$ yields the alternative forms:

For $z < z_{top}$:

$$E_B(z,\omega)\big|_{\Delta\sigma+\Delta\varepsilon+\Delta\mu} = E_{inc}(z_{mid},\omega)e^{+iK_1(\omega)(z_{mid}-z)}\times$$
$$\frac{h}{2}\left[\frac{\sinh[iK_1(\omega)h]}{[iK_1(\omega)h]}\right]\left\{\frac{\sigma_1\mu_1(-i\omega)}{iK_1(\omega)}\left[(\hat{\sigma}-1)-i(\hat{\varepsilon}-1)\frac{\omega}{\omega_1}\right]-iK_1(\omega)(\hat{\mu}-1)\right\}, \qquad (7.51a)$$

and for $z > z_{bot}$:

$$E_B(z,\omega)\big|_{\Delta\sigma+\Delta\varepsilon+\Delta\mu} = E_{inc}(z_{mid},\omega)e^{+iK_1(\omega)(z-z_{mid})}\times$$
$$\frac{h}{2}\left\{\frac{\sigma_1\mu_1(-i\omega)}{iK_1(\omega)}\left[(\hat{\sigma}-1)-i(\hat{\varepsilon}-1)\frac{\omega}{\omega_1}\right]+iK_1(\omega)(\hat{\mu}-1)\right\}. \qquad (7.51b)$$

Note the sign difference (i.e., within the braces { }). For $z_{top} < z < z_{bot}$ the exact FBA intrabed scattering response becomes

$$E_B(z,\omega)\big|_{\Delta\sigma+\Delta\varepsilon+\Delta\mu} = E_{inc}(z_{mid},\omega)e^{+iK_1(\omega)(z-z_{mid})}\frac{1}{4}\times$$
$$\left\{\frac{\sigma_1\mu_1(-i\omega)}{K_1(\omega)^2}\left[(\hat{\sigma}-1)-i(\hat{\varepsilon}-1)\frac{\omega}{\omega_1}\right]\left[1-2iK_1(\omega)(z-z_{top})-e^{-2iK_1(\omega)(z-z_{bot})}\right]\right.$$
$$\left.+(\hat{\mu}-1)\left[1+2iK_1(\omega)(z-z_{top})-e^{-2iK_1(\omega)(z-z_{bot})}\right]\right\}. \qquad (7.51c)$$

An important observation is that the FBA scattering formulae (7.51a,b,c) are linear in the three dimensionless parameter contrast quantifiers $\hat{\sigma}-1$, $\hat{\varepsilon}-1$, and $\hat{\mu}-1$. In other words, if any two of them are zero, then the FBA scattered response scales directly with the third. An obvious implication is that ever increasing parameter contrast leads to ever increasing scattered wavefield magnitudes. The limits of this approximation are examined in a subsequent section.

7.6.3 Low-Frequency Approximations

Next, we impose a low-frequency approximation on the above-derived First Born Approximations. From equation (A4.15) of Appendix A, the complex wavenumber (evaluated with the reference model parameters) at low frequency is given by

$$K_1(\omega) \approx \sqrt{\sigma_1 \mu_1 |\omega|}\, \mathrm{sgn}(\omega) e^{+i\frac{\pi}{4}\mathrm{sgn}(\omega)}, \qquad \text{(A4.15 again)}$$

where sgn(x) is the sign function. This approximation is appropriate for $\omega << \omega_1 = \sigma_1/\varepsilon_1$, where ω_1 is the transition frequency for medium #1. So, in the low-frequency (or electromagnetic induction) regime, the phase speed and attenuation factor are both proportional to the square root of frequency, and dielectric permittivity ε does not play a role. As per the development in section 5.5 (entitled Scattering Ratio), we have the low-frequency form

$$iK_1(\omega) = \sqrt{-i\omega\sigma_1\mu_1}\,.$$

Substituting this into the above expressions (7.51a,b,c) for the FBA scattered responses gives:

For $z < z_{top}$:

$$E_B(z,\omega)\big|_{\Delta\sigma+\Delta\mu} = \frac{\hat{\sigma}-\hat{\mu}}{2}\sinh\left[\sqrt{\sigma_1\mu_1(-i\omega)}\; h\right] E_{inc}(z_{mid},\omega) e^{+\sqrt{\sigma_1\mu_1(-i\omega)}(z_{mid}-z)}. \qquad (7.52a)$$

For $z > z_{bot}$:

$$E_B(z,\omega)\big|_{\Delta\sigma+\Delta\mu} = \frac{\hat{\sigma}+\hat{\mu}-2}{2}\left[\sqrt{\sigma_1\mu_1(-i\omega)}\; h\right] E_{inc}(z_{mid},\omega) e^{+\sqrt{\sigma_1\mu_1(-i\omega)}(z-z_{mid})}. \qquad (7.52b)$$

For $z_{top} < z < z_{bot}$:

$$E_B(z,\omega)\big|_{\Delta\sigma+\Delta\mu} = \left\{ \frac{\hat{\sigma}-\hat{\mu}}{2}\sinh\left[\sqrt{\sigma_1\mu_1(-i\omega)}\,(z_{bot}-z)\right] e^{+\sqrt{\sigma_1\mu_1(-i\omega)}(z_{bot}-z)} \right.$$

$$\left. + \frac{\hat{\sigma}+\hat{\mu}-2}{2}\left[\sqrt{\sigma_1\mu_1(-i\omega)}(z-z_{top})\right] \right\} E_{inc}(z_{mid},\omega) e^{+\sqrt{\sigma_1\mu_1(-i\omega)}(z-z_{mid})}. \qquad (7.52c)$$

In this low-frequency approximation, where $\omega << \omega_1$, scattering by dielectric permittivity contrast $\Delta\varepsilon = \varepsilon_2 - \varepsilon_1$ is considered negligible (at least for "normal" values of relative permittivity), and hence is omitted from both sides of the above expressions. Only conductivity and permeability contrasts are relevant. Clearly, if $\hat{\sigma} = \hat{\mu} = 1$ (implying no parameter contrast), then all three scattered responses

vanish, as expected. The forward-scattered response is directly proportional to the bed thickness *h*, whereas the back-scattered response is not. Moreover, responses are continuous at top and bottom bed boundaries (i.e., as $z \rightarrow z_{top}$ and $z \rightarrow z_{bot}$).

7.6.4 Low-Frequency *and* Thin-Bed Approximations

Finally, we impose an additional thin-bed approximation on the above low-frequency response equations. Expanding the above expressions to third-order in the small quantity

$$iK_1(\omega)h = \sqrt{\sigma_1\mu_1(-i\omega)}\, h\,,$$

yields the back-scattered FBA response

For $z < z_{top}$:

$$E_B(z,\omega)\big|_{\Delta\sigma+\Delta\mu} \approx (\hat{\sigma}-\hat{\mu})\frac{h}{2}\sqrt{\sigma_1\mu_1(-i\omega)}\left[1+\frac{\sigma_1\mu_1(-i\omega)h^2}{6}\right]E_{inc}(z_{mid},\omega)e^{+\sqrt{\sigma_1\mu_1(-i\omega)}(z_{mid}-z)}. \qquad (7.53a)$$

[Recall that $\sinh(z) \approx z + z^3/6$.] The fore-scattered response (7.52b) is already (and truncates) at first-order in *h*, and is repeated as

For $z > z_{bot}$:

$$E_B(z,\omega)\big|_{\Delta\sigma+\Delta\mu} = (\hat{\sigma}+\hat{\mu}-2)\frac{h}{2}\sqrt{\sigma_1\mu_1(-i\omega)}\; E_{inc}(z_{mid},\omega)e^{+\sqrt{\sigma_1\mu_1(-i\omega)}(z-z_{mid})}. \qquad (7.53b)$$

Hence, to first-order in *h*, the back- and fore-scattered low-frequency FBA responses are proportional to i) the half-bed thickness h/2, ii) complex wavenumber $\sqrt{\sigma_1\mu_1(-i\omega)}$ with SI unit 1/m, and iii) the incident electric field at the bed mid-point $E_{inc}(z_{mid},\omega)$. The thin intrabed response is

For $z_{top} < z < z_{bot}$:

$$E_B(z,\omega)\big|_{\Delta\sigma+\Delta\mu} = \left\{ (\hat{\sigma}-\hat{\mu})\frac{(z_{bot}-z)}{2}\sqrt{\sigma_1\mu_1(-i\omega)}\left[1+\frac{\sigma_1\mu_1(-i\omega)(z_{bot}-z)^2}{6}\right]e^{+\sqrt{\sigma_1\mu_1(-i\omega)}(h/2)} \right.$$
$$\left. + (\hat{\sigma}+\hat{\mu}-2)\frac{(z-z_{top})}{2}\sqrt{\sigma_1\mu_1(-i\omega)}\; e^{+\sqrt{\sigma_1\mu_1(-i\omega)}(z-z_{mid})} \right\} E_{inc}(z_{mid},\omega)\,, \qquad (7.53c)$$

which is also proportional to the mid-bed electric field value.

How do these thin-bed, low-frequency FBA scattering formulae compare to the *exact* scattering expressions of Section 5.0? Equation (5.19) gives the exact back-scattered response, expanded to first-order in bed thickness *h*, as

$$E_{bak}(z_s,z_r,\omega)\big|_{lo} \approx \frac{h}{2}(\hat{\sigma}-\hat{\mu})\sqrt{\sigma_1\mu_1}\;\left[E_{inc}(2z_{mid}-z_r,\omega)\sqrt{|\omega|}e^{+i\,\mathrm{sgn}(\omega)(3\pi/4)}\right]. \qquad (5.19\text{ again})$$

But we know $\sqrt{|\omega|}e^{+i\,\mathrm{sgn}(\omega)(3\pi/4)} = (-i\omega)^{1/2}$ and $E_{inc}(2z_{mid} - z_r, \omega) = E_{inc}(z_{mid}, \omega)e^{+iK_1(\omega)(z_{mid} - z_r)}$ and $iK_1(\omega) \approx \sqrt{\sigma_1\mu_1(-i\omega)}$. Substituting in gives

$$E_{bak}(z_s, z_r, \omega)\big|_{lo} \approx \frac{h}{2}(\hat{\sigma} - \hat{\mu})\sqrt{\sigma_1\mu_1(-i\omega)}\ E_{inc}(z_{mid}, \omega)e^{+\sqrt{\sigma_1\mu_1(-i\omega)}\,(z_{mid} - z_r)}. \tag{7.54a}$$

This is identical to the first-order term in the FBA back-scattered response (7.53a)! Similarly, the exact fore-scattered response, expanded to first-order in bed thickness *h* is

$$E_{for}(z_r, z_s, \omega)\big|_{lo} \approx \frac{h}{2}(\hat{\sigma} + \hat{\mu} - 2)\sqrt{\sigma_1\mu_1}\left[E_{inc}(z_r, \omega)\sqrt{|\omega|}e^{+i\,\mathrm{sgn}(\omega)(3\pi/4)}\right], \tag{5.27 again}$$

or alternately

$$E_{for}(z_r, z_s, \omega)\big|_{lo} \approx \frac{h}{2}(\hat{\sigma} + \hat{\mu} - 2)\sqrt{\sigma_1\mu_1(-i\omega)}\ E_{inc}(z_r, \omega). \tag{7.54b}$$

This is identical to the first-order (in *h*) FBA fore-scattered response (7.53b), when the substitution $E_{inc}(z, \omega) = E_{inc}(z_{mid}, \omega)e^{+\sqrt{\sigma_1\mu_1(-i\omega)}(z - z_{mid})}$ is made! These deductions lead to an important theoretical statement linking exact and FBA scattering expressions as:

The exact formulae for the electric field scattered by a geologic layer, when expanded in both the low-frequency and thin-bed approximations, are identical to the First Born Approximation scattering expressions in these same limits.

7.6.5 Primaries Only Comparison

The mathematical development of the First Born Approximation in Appendix D indicates that the scattered (or perturbed) wavefield propagates within the original (or reference, or background, or incident medium) earth model. This has led to numerous statements in the geophysical literature to the effect that the FBA is a "single scattering" theory that does not accommodate "multiple scattering" between physically separated scattering loci. We concur with this understanding. In the FBA approach, a distinct scatterer (i.e., a perturbation in material properties) is removed from the earth model, and is subsequently replaced with a body source distribution within the background medium.

The single scattering aspect of FBA theory motivates an examination of the "primaries only" reflection and transmission responses of a geologic layer, wherein all intrabed multiples are neglected. Admittedly, ignoring the intrabed multiples is nonphysical (and this will be elaborated upon later). However, the resulting scattering responses are useful for comparison with the analogous FBA responses, and also enable as assessment of the importance of the multiples. Interestingly, the original treatment of the thin bed reflection response issue in seismic reflection exploration (Widess, 1957-58 and 1973) considered *only* top-bed and bottom-bed primary reflections, and ignored all the intrabed multiples.

Following the summation approach of section 3, the *primaries only reflection response*, consisting of just the top-bed and bottom-bed reflections recorded at a receiver $z_r < z_{top}$, is given by (next page):

$$\Re(z_s, z_r, \omega)\big|_{\text{primaries}} = E_{inc}(2z_{mid} - z_r, \omega) e^{-iK_1(\omega)h} R_{top}(\omega) \left\{1 - T_{12}(\omega) T_{21}(\omega) e^{+iK_2(\omega)2h}\right\}, \qquad (7.55a)$$

where $R_{top}(\omega)$ is the normal-incidence reflection coefficient at the upper bounding interface, and $T_{12}(\omega)$ and $T_{21}(\omega)$ are the downward and upward transmission coefficients through this interface. We have $T_{12}(\omega)T_{21}(\omega) = \big(1 + R_{top}(\omega)\big)\big(1 + R_{bot}(\omega)\big) = 1 - R_{top}(\omega)^2$ because the usual assumption that medium #1 = medium #3 is adopted. The primaries only reflection response becomes

$$\Re(z_s, z_r, \omega)\big|_{\text{primaries}} = E_{inc}(2z_{mid} - z_r, \omega) e^{-iK_1(\omega)h} R_{top}(\omega) \left\{1 - \left[1 - R_{top}(\omega)^2\right] e^{+iK_2(\omega)2h}\right\}$$

$$= E_{inc}(2z_{mid} - z_r, \omega) R_{top}(\omega) \left\{R_{top}(\omega)^2 e^{+iK_2(\omega)h} - 2\sinh\left[iK_2(\omega)h\right]\right\} e^{+i[K_2(\omega) - K_1(\omega)]h}.$$

Next, the top-bed reflection coefficient is

$$R_{top}(\omega) = \frac{1 - \left(\hat{K}(\omega)/\hat{\mu}\right)}{1 + \left(\hat{K}(\omega)/\hat{\mu}\right)}, \qquad \text{(5.16 again)}$$

where two dimensionless ratios are $\hat{K}(\omega) = K_2(\omega)/K_1(\omega)$ and $\hat{\mu}(\omega) = \mu_2/\mu_1$. In the low-frequency approximation, $iK(\omega)h = \sqrt{-i\omega\sigma\mu}\, h$. Hence $\hat{K}(\omega) = \sqrt{\hat{\sigma}\hat{\mu}}$ where $\hat{\sigma}(\omega) = \sigma_2/\sigma_1$ is a third dimensionless parameter ratio. Moreover, in the low-frequency approximation

$$iK_1(\omega)h = \sqrt{-i\omega\sigma_1\mu_1}\, h = 2\pi(1-i)\frac{h}{\lambda_1(\omega)} \equiv \beta_1(\omega),$$

where the low-frequency wavelength in the incident medium is given by $\lambda_1(\omega) = 2\pi\sqrt{\dfrac{2}{\sigma_1\mu_1\omega}}$, and we recall from section 5.5 the definition of dimensionless parameter $\beta_1(\omega)$. Substituting these forms yields the primaries only reflection response as

$$\Re(z_s, z_r, \omega)\big|_{\text{primaries}} = E_{inc}(2z_{mid} - z_r, \omega)\left[\frac{\sqrt{\hat{\sigma}} - \sqrt{\hat{\mu}}}{\sqrt{\hat{\sigma}} + \sqrt{\hat{\mu}}}\right] e^{+\left[\sqrt{\hat{\sigma}\hat{\mu}} - 1\right]\beta_1(\omega)} \times$$

$$\left\{2\sinh\left[\sqrt{\hat{\sigma}\hat{\mu}}\,\beta_1(\omega)\right] - \left[\frac{\sqrt{\hat{\sigma}} - \sqrt{\hat{\mu}}}{\sqrt{\hat{\sigma}} + \sqrt{\hat{\mu}}}\right]^2 e^{+\sqrt{\hat{\sigma}\hat{\mu}}\beta_1(\omega)}\right\} = E_{bak}(z, \omega)\big|_{\text{primaries}}. \qquad (7.55b)$$

Recognize that, in this case where medium #1 = medium #3, the reflection response is identical to the back-scattered response. As a simple check, note that $\hat{\sigma} = \hat{\mu} = 1$ (i.e., no material parameter contrast) implies that the reflection response vanishes, as expected. In fact, $\hat{\sigma} = \hat{\mu} = r \neq 1$ yields the same result.

A similar development yields the *primaries only transmission response*, for a receiver at $z_r > z_{bot}$ as

$$\mathfrak{I}(z_s, z_r, \omega)\big|_{\text{primaries}} = E_{inc}(z_r, \omega) T_{12}(\omega) T_{21}(\omega) e^{+i[K_2(\omega) - K_1(\omega)]h}$$

$$= E_{inc}(z_r, \omega)\left[1 - R_{top}(\omega)^2\right] e^{+i[K_2(\omega) - K_1(\omega)]h}, \tag{7.56a}$$

or, at low frequencies:

$$\mathfrak{I}(z_s, z_r, \omega)\big|_{\text{primaries}} = E_{inc}(z_r, \omega)\left[\frac{4\sqrt{\hat{\sigma}\hat{\mu}}}{\left(\sqrt{\hat{\sigma}} + \sqrt{\hat{\mu}}\right)^2}\right] e^{+\left[\sqrt{\hat{\sigma}\hat{\mu}} - 1\right]\beta_1(\omega)}. \tag{7.56b}$$

Subtracting off the direct arrival gives the forward-scattered primaries only response as

$$E_{for}(z_r, \omega)\big|_{\text{primaries}} = E_{inc}(z_r, \omega)\left\{\left[\frac{4\sqrt{\hat{\sigma}\hat{\mu}}}{\left(\sqrt{\hat{\sigma}} + \sqrt{\hat{\mu}}\right)^2}\right] e^{+\left[\sqrt{\hat{\sigma}\hat{\mu}} - 1\right]\beta_1(\omega)} - 1\right\}. \tag{7.56c}$$

In the no-contrast situation $\hat{\sigma} = \hat{\mu} = 1$, the transmitted response is just the incident field, and the for-scattered response vanishes. However, $\hat{\sigma} = \hat{\mu} = r > 1$ leads to enhanced forward scattering.

The product $T_{12}(\omega) T_{21}(\omega) = 1 - R_{top}(\omega)^2$ used in the development of both the back- and for-scattered responses accounts for plane wave transmission through the top and bottom interfaces of the geologic layer. For small parameter contrast, the top bed reflection coefficient $\left\|R_{top}(\omega)\right\| << 1$, and the transmission coefficient product is well-approximated as unity. This leads to the two additional scattering approximations, without transmission loss, as

$$E_{bak}(z, \omega)\big|_{\text{primaries-notrans}} = E_{inc}(2z_{mid} - z_r, \omega)\left[\frac{\sqrt{\hat{\sigma}} - \sqrt{\hat{\mu}}}{\sqrt{\hat{\sigma}} + \sqrt{\hat{\mu}}}\right] 2\sinh\left[\sqrt{\hat{\sigma}\hat{\mu}}\beta_1(\omega)\right] e^{+\left[\sqrt{\hat{\sigma}\hat{\mu}} - 1\right]\beta_1(\omega)}, \tag{7.57a}$$

$$E_{for}(z_r, \omega)\big|_{\text{primaries-notrans}} = E_{inc}(z_r, \omega)\left[e^{+\left[\sqrt{\hat{\sigma}\hat{\mu}} - 1\right]\beta_1(\omega)} - 1\right]. \tag{7.57b}$$

The following table summarizes four back-scattering responses in the common parameterization $\left(\hat{\sigma}, \hat{\mu}, \beta_1(\omega)\right)$. [The exact back-scattering expression (top line of table) is obtained in this form in a subsequent section.] All four expressions indicate that the back-scattered field is proportional to the incident electric field at position $2z_{mid} - z_r$. However, the four formulae possess a rather different mathematical "look"; dependence on the two dimensionless parameter ratios $\hat{\sigma}$ and $\hat{\mu}$ clearly differs. Moreover, dependence on layer thickness *h* (via the argument $\beta_1(\omega) = 2\pi(1-i)h/\lambda_1(\omega)$) varies. Despite the apparent "multiple free" assumption embedded in the FBA response (bottom line of table), it does not compare well with the two "primaries only" responses (second and third lines). Finally, let the bed thickness *h* vanish, holding the other two parameters fixed. Surprisingly, the primaries-only back-scattered response (second line) does *not* vanish, but approaches a nonzero value! This feature arises because two-way transmission through the top interface is included in the derivation. Ignoring two-way transmission (by setting the transmission coefficient product to unity) leads to the correct result.

Backward Scattering Formulae ($z_r < z_{top}$)

Exact Back-Scattering (including all intrabed multiples):

$$E_{bak}(z_r,\omega) = E_{inc}(2z_{mid} - z_r,\omega)\left\{\frac{\frac{1}{2}\left(\sqrt{\frac{\hat{\sigma}}{\hat{\mu}}} - \sqrt{\frac{\hat{\mu}}{\hat{\sigma}}}\right)\sinh\left[\sqrt{\hat{\sigma}\hat{\mu}}\,\beta_1(\omega)\right]}{\cosh\left[\sqrt{\hat{\sigma}\hat{\mu}}\beta_1(\omega)\right] - \frac{1}{2}\left(\sqrt{\frac{\hat{\sigma}}{\hat{\mu}}} + \sqrt{\frac{\hat{\mu}}{\hat{\sigma}}}\right)\sinh\left[\sqrt{\hat{\sigma}\hat{\mu}}\beta_1(\omega)\right]}\right\} e^{-\beta_1(\omega)}.$$

Primaries-Only Back-Scattering:

$$E_{bak}(z_r,\omega)\big|_{\text{primaries}} = E_{inc}(2z_{mid} - z_r,\omega)\left[\frac{\sqrt{\hat{\sigma}} - \sqrt{\hat{\mu}}}{\sqrt{\hat{\sigma}} + \sqrt{\hat{\mu}}}\right] e^{+\left[\sqrt{\hat{\sigma}\hat{\mu}}-1\right]\beta_1(\omega)} \times$$
$$\left\{2\sinh\left[\sqrt{\hat{\sigma}\hat{\mu}}\beta_1(\omega)\right] - \left[\frac{\sqrt{\hat{\sigma}} - \sqrt{\hat{\mu}}}{\sqrt{\hat{\sigma}} + \sqrt{\hat{\mu}}}\right]^2 e^{+\sqrt{\hat{\sigma}\hat{\mu}}\beta_1(\omega)}\right\}.$$

Primaries-Only and No-Transmission Loss Back-Scattering:

$$E_{bak}(z_r,\omega)\big|_{\text{primaries-notrans}} = E_{inc}(2z_{mid} - z_r,\omega)\left[\frac{\sqrt{\hat{\sigma}} - \sqrt{\hat{\mu}}}{\sqrt{\hat{\sigma}} + \sqrt{\hat{\mu}}}\right] 2\sinh\left[\sqrt{\hat{\sigma}\hat{\mu}}\beta_1(\omega)\right] e^{+\left[\sqrt{\hat{\sigma}\hat{\mu}}-1\right]\beta_1(\omega)}.$$

First Born Approximation Back-Scattering:

$$E_B(z_r,\omega)\big|_{\Delta\sigma+\Delta\mu} = E_{inc}(2z_{mid} - z_r,\omega)\left(\frac{\hat{\sigma} - \hat{\mu}}{2}\right)\sinh\left[\beta_1(\omega)\right].$$

Table 7.1. Backward scattering formulae ($z_r < z_{top}$).

The analogous forward-scattering expressions are summarized in the following table. All responses are proportional to the incident electric field at position z_r. Once again, there is no obvious similarity between the FBA response and the two "primaries only" responses. All four responses vanish for $\hat{\sigma} = \hat{\mu} = 1$ (i.e., no parameter contrast), but the "primaries-only" formula (second line of table) predicts a nonzero forward-scattered field in the limit of vanishing bed thickness. This is clearly non-physical.

Forward Scattering Formulae ($z_r > z_{bot}$)

Exact For-Scattering (including all intrabed multiples):

$$E_{for}(z_r,\omega) = E_{inc}(z_r,\omega)\left\{\frac{e^{-\beta_1(\omega)} - \left[\cosh\left[\sqrt{\hat{\sigma}\hat{\mu}}\beta_1(\omega)\right] - \frac{1}{2}\left(\sqrt{\frac{\hat{\sigma}}{\hat{\mu}}} + \sqrt{\frac{\hat{\mu}}{\hat{\sigma}}}\right)\sinh\left[\sqrt{\hat{\sigma}\hat{\mu}}\beta_1(\omega)\right]\right]}{\cosh\left[\sqrt{\hat{\sigma}\hat{\mu}}\beta_1(\omega)\right] - \frac{1}{2}\left(\sqrt{\frac{\hat{\sigma}}{\hat{\mu}}} + \sqrt{\frac{\hat{\mu}}{\hat{\sigma}}}\right)\sinh\left[\sqrt{\hat{\sigma}\hat{\mu}}\beta_1(\omega)\right]}\right\}.$$

Primaries-Only For-Scattering:

$$E_{for}(z_r,\omega)\Big|_{\text{primaries}} = E_{inc}(z_r,\omega)\left\{\left[\frac{4\sqrt{\hat{\sigma}\hat{\mu}}}{\left(\sqrt{\hat{\sigma}} + \sqrt{\hat{\mu}}\right)^2}\right]e^{+\left[\sqrt{\hat{\sigma}\hat{\mu}}-1\right]\beta_1(\omega)} - 1\right\}.$$

Primaries-Only and No-Transmission Loss For-Scattering:

$$E_{for}(z_r,\omega)\Big|_{\text{primaries-notrans}} = E_{inc}(z_r,\omega)\left[e^{+\left[\sqrt{\hat{\sigma}\hat{\mu}}-1\right]\beta_1(\omega)} - 1\right].$$

First Born Approximation For-Scattering:

$$E_B(z_r,\omega)\Big|_{\Delta\sigma+\Delta\mu} = E_{inc}(z_r,\omega)\left(\frac{\hat{\sigma}+\hat{\mu}}{2} - 1\right)\beta_1(\omega).$$

Table 7.2. Forward-scattering formulae ($z_r > z_{bot}$).

7.7 Born Scattering Examples

As indicated previously, the physical essence of the First Born Approximation is a *replacement* of a material parameter perturbation by an effective (i.e., roughly equivalent in effects) body source of electromagnetic waves. This body source distribution coincides with the material perturbation in 3D space. The mathematical development in Appendix D indicates that perturbations in current conductivity $\sigma(\mathbf{x})$, electric permittivity $\varepsilon(\mathbf{x})$, and magnetic permeability $\mu(\mathbf{x})$ generate effective conduction current, displacement current, and magnetic current body sources, respectively:

$$\mathbf{j}_{eff}(\mathbf{x},t) \equiv \delta\sigma(\mathbf{x})\mathbf{e}_{inc}(\mathbf{x},t), \qquad \text{(D1.4a again)}$$

$$\mathbf{k}_{eff}(\mathbf{x},t) \equiv \delta\varepsilon(\mathbf{x})\frac{\partial \mathbf{e}_{inc}(\mathbf{x},t)}{\partial t}, \qquad \text{(modification of D1.4b)}$$

$$\mathbf{l}_{eff}(\mathbf{x},t) \equiv \delta\mu(\mathbf{x})\frac{\partial \mathbf{h}_{inc}(\mathbf{x},t)}{\partial t}. \qquad \text{(modification of D1.4c)}$$

[The "δ" pre-symbol denotes a perturbation in a material parameter.] Conduction and displacement current body sources have SI unit A/m^2 (areal current density), whereas the magnetic current body source has SI unit V/m^2 (areal potential density). Sources are also proportional to the primary (or "incident" or "reference") electromagnetic field vectors $\mathbf{e}_{inc}(\mathbf{x},t)$ and $\mathbf{h}_{inc}(\mathbf{x},t)$.

Figure 7.1 below illustrates a First Born Approximation (FBA) scattering situation for the case of a thin geologic layer possessing a conductivity contrast with a surrounding homogeneous wholepace (i.e., medium #1 = medium #3 in prior notation). The contrasting geologic layer (depicted as light **brown** color in the earlier Figure 2.1) is now replaced by body source distribution of electric current, intentionally shown by a different **green** color. The original top and bottom bed-bounding interfaces are now drawn as dashed, indicating that the layer as a physical medium parameter contrast no longer exists; rather, it has EM parameters $(\varepsilon_1, \mu_1, \sigma_1)$ identical to the overburden and substratum. The effective current density body source is illustrated by the set of horizontally-directed green arrows. These decrease in magnitude from top to bottom because the incident electric field (downward-propagating **red** plane wavefronts in upper left) decays as it traverses the *original* layer with contrasting conductivity $\sigma_2 \neq \sigma_1$. The current density body source gives rise to back-scattered (upward-propagating) and for-scattered (downward-propagating) plane electric field wavefronts, also illustrated in **red**.

Our first examples of FBA scattered responses are displayed in the following Figure 7.2. Back-scattered (i.e., $z_r < z_{top}$) E_x-component signals generated by four thin beds (h_{bed} = 1 cm) having strong conductivity contrasts with the background are plotted. The source waveform consists of 100 periods of a 1 Hz sinusoid, with unit amplitude 1 V/m; source is coincident with the back-scattering receiver at $z_s = z_r = -100$ m. Four full periods of the recorded scattered signals are plotted (from 4 s to 8 s in order to avoid turn-on effects at t=0 s). The background medium is characterized by $(\varepsilon_1, \mu_1, \sigma_1) = (10\varepsilon_0, \mu_0, 0.02\ \text{S/m})$.

Top and bottom panels of Figure 7.2 compare *exact* and *First Born Approximation* back-scattered responses, respectively, as the conductivity assigned to the thin layer ranges from $\sigma_{bed} = \sigma_2 = 10^3$ S/m (**red** curves), to 10^4 S/m (**green** curves), to 10^5 S/m (**blue** curves), to 10^6 S/m (**brown** curves). Hence, the dimensionless conductivity contrast ratio $\hat{\sigma} = \sigma_2/\sigma_1$ ranges from 10^5 to 10^8, implying that these are *very* strong conductivity contrast beds.

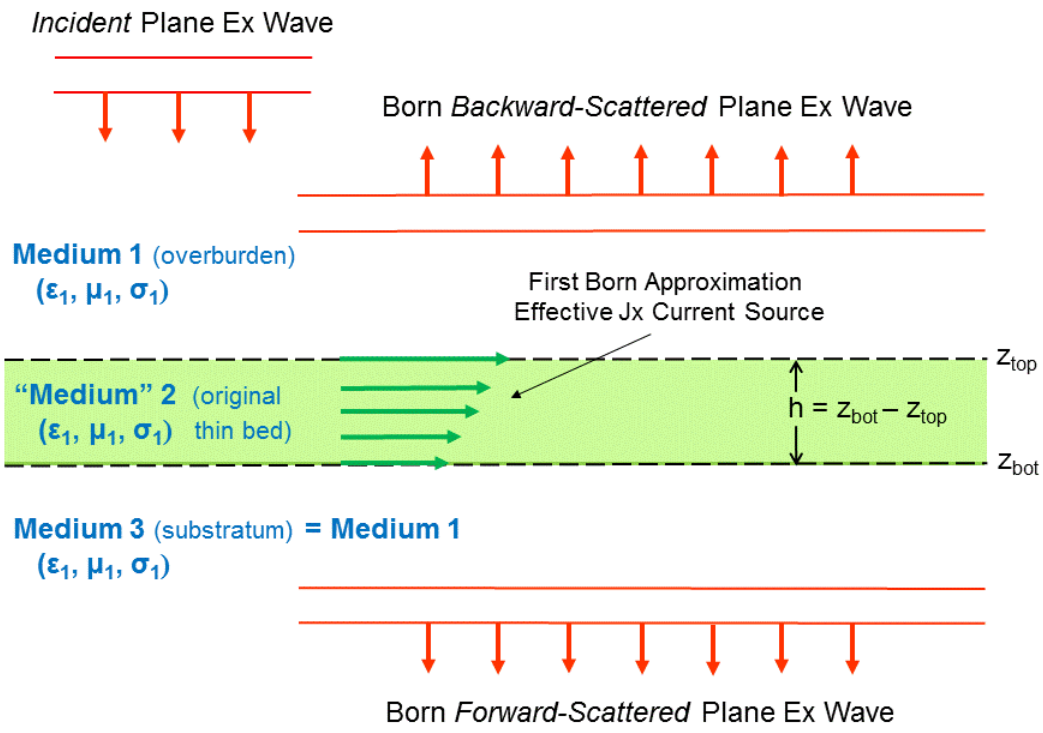

Figure 7.1. Schematic depiction of First Born Approximation scattered wavefields (upward and downward propagating **red** plane wavefronts) for the case of a thin geologic layer possessing a contrast in current conductivity with respect to a homogeneous background. The material parameter contrast of the layer is replaced by a horizontally-directed electric current body source (**green** arrows) with the same vertical extent.

Exact and FBA back-scattered responses are calculated via formulae (5.30a) and (7.51a) respectively, specialized to this case of no permeability and no permittivity contrast (i.e., $\hat{\mu} = \hat{\varepsilon} = 1$):

$$E_{bak}(z_r,\omega) = E_{inc}(2z_{mid} - z_r,\omega)\left\{\frac{\frac{1}{2}\left[\frac{\hat{K}(\omega)}{1} - \frac{1}{\hat{K}(\omega)}\right]\tanh\left[\hat{K}(\omega)iK_1(\omega)h\right]}{1 - \frac{1}{2}\left[\frac{\hat{K}(\omega)}{1} + \frac{1}{\hat{K}(\omega)}\right]\tanh\left[\hat{K}(\omega)iK_1(\omega)h\right]}\right\} e^{-iK_1(\omega)h}, \qquad (7.58a)$$

and

$$E_B(z_r,\omega)\big|_{\Delta\sigma} = E_{inc}(2z_{mid} - z_r,\omega)\left\{\frac{(\hat{\sigma}-1)h}{2}\left[\frac{\sinh\left[iK_1(\omega)h\right]}{\left[iK_1(\omega)h\right]}\right]\left[\frac{\sigma_1\mu_1(-i\omega)}{iK_1(\omega)}\right]\right\}. \qquad (7.58b)$$

The low-frequency complex-wavenumber ratio, highly accurate for the source frequency of 1 Hz, is given by $\hat{K}(\omega) \equiv K_2(\omega)/K_1(\omega) = \sqrt{\hat{\sigma}}$. However, algorithm THEMBED utilizes the exact (i.e., full spectral band) expression for the complex wavenumber ratio for its internal calculations.

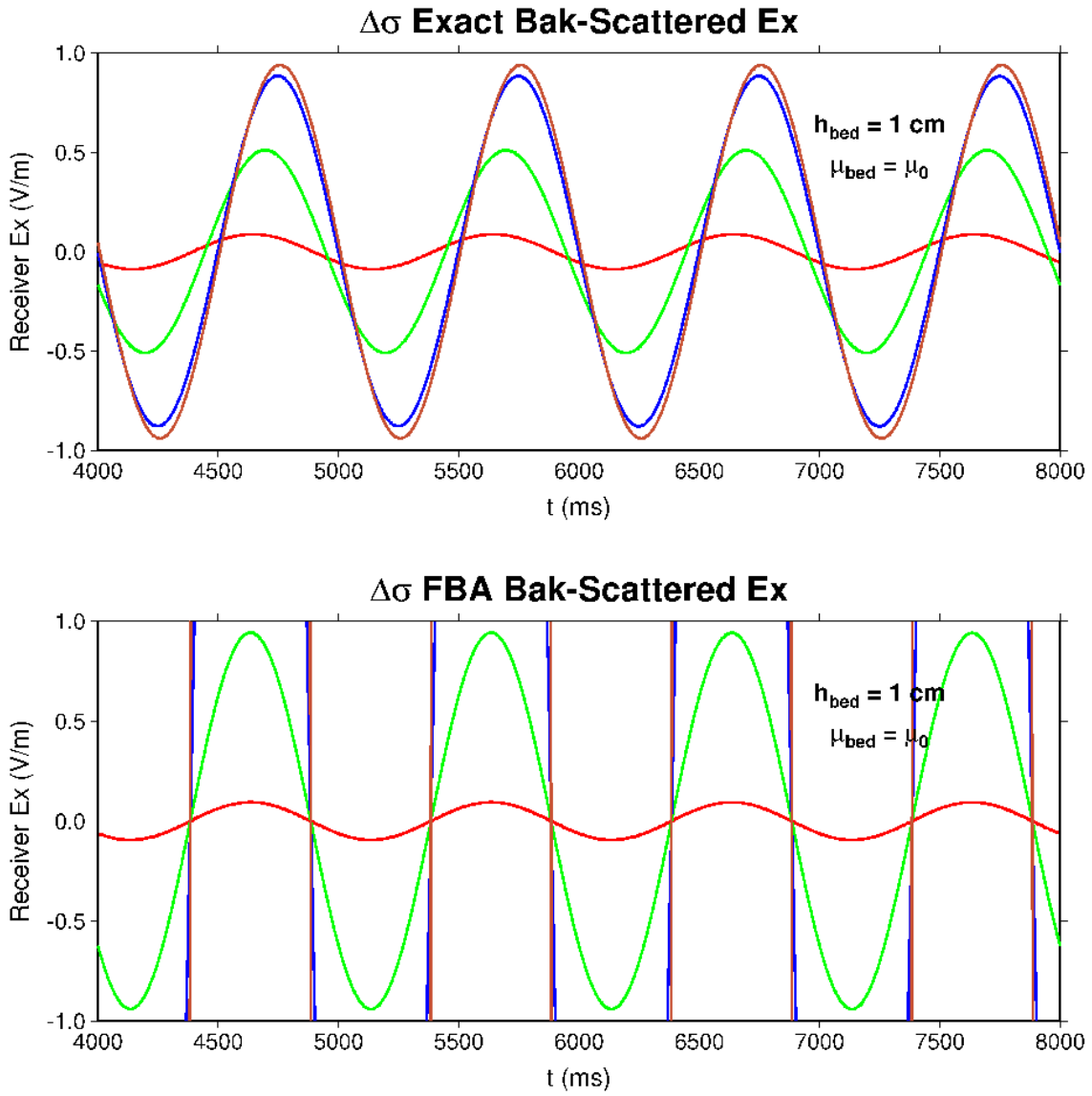

Figure 7.2. Exact (upper panel) and First Born Approximation (lower panel) back-scattered responses induced by a strong current conductivity contrast in a thin geologic layer with thickness h_{bed} = 1 cm. **Red**, **green**, **blue**, and **brown** curves correspond to $\sigma_{bed} = 10^3$, 10^4, 10^5, and 10^6 S/m, respectively. Blue and brown sinusoidal curves plot well off scale in bottom panel.

Exact back-scattered wavefields plotted in the top panel of Figure 7.2 approach a limiting value (equal to the source level 1 V/m) as conductivity contrast $\hat{\sigma}$ increases. This is consistent with equation (7.58a) above (which approaches –1 as $\hat{\sigma} \to +\infty$). Note the interesting phase lag of the sinusoidal signals. However, the FBA back-scattered wavefields in the bottom panel grow without bound as $\hat{\sigma}$ increases, consistent with equation (7.58b). There does not appear to be a progressive phase lag with increasing bed conductivity.

The two **red** curves in Figure 7.2, appropriate for the smaller bed conductivity $\sigma_{bed} = 10^3$ S/m, are nearly identical. The next Figure 7.3 plots both exact (solid curves) and FBA (dashed curves) back-scattered responses on the same set of axes, for more moderate contrasts in bed conductivity. The red curves are the same as in Figure 7.2, but note the expanded (×10) vertical plot scale.

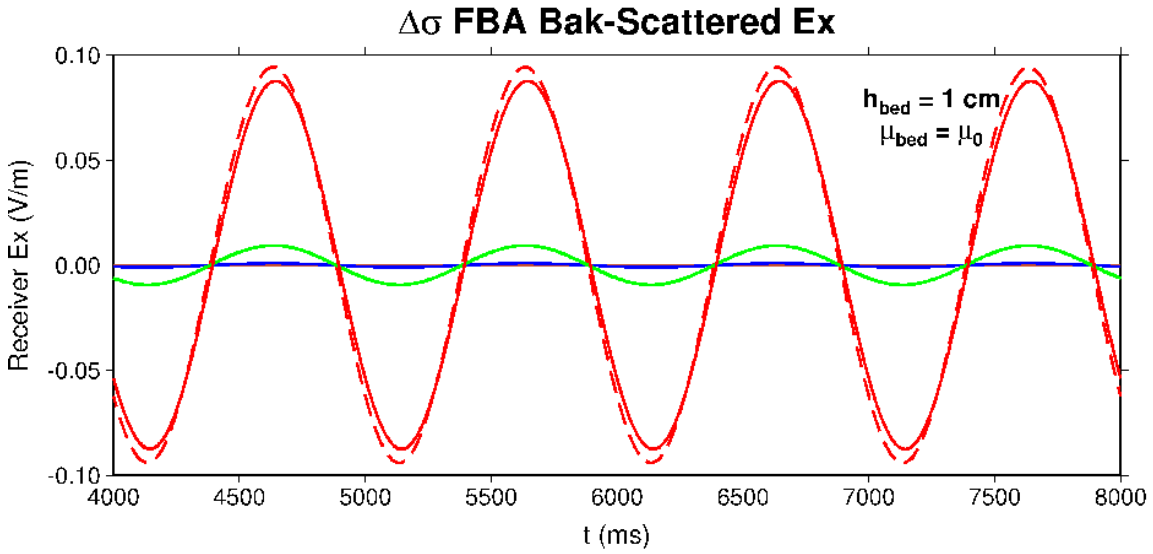

Figure 7.3. Exact (solid curves) and First Born Approximation (dashed curves) back-scattered responses induced by moderate current conductivity contrast in a thin geologic layer with thickness h_{bed} = 1 cm. **Brown**, **blue**, **green**, and **red** curves correspond to $\sigma_{bed} = 10^0$, 10^1, 10^2, and 10^3 S/m, respectively. Solid red curve is identical to previous Figure 7.2. Note expanded vertical scale of 10× compared with prior figures.

For low values of bed conductivity contrast, dashed and solid curves overplot in Figure 7.3, indicating that the FBA is a reasonable approximation in this regime. However, $\sigma_{bed} = 10^3$ S/m (corresponding to $\hat{\sigma} = 10^5$) leads to a discernable amplitude difference between exact and FBA back-scattered response at this plot scale. The obvious conclusion is that the FBA becomes progressively more inaccurate (in the sense of over-estimating the scattered field magnitude) as bed conductivity contrast increases. Interestingly, Figure 7.3 appears to indicate that the FBA response *lags* the exact response in time.

7.8 Born Scattering Accuracy

The numerical examples displayed in the previous section motivate an examination of the accuracy of the First Born Approximation for scattered EM wavefields. We seek to determine the ranges of the controlling parameters (i.e., bed thickness *h*, conductivity contrast ratio $\hat{\sigma}$, and permeability contrast ratio $\hat{\mu}$) where the FBA constitutes a reasonably accurate estimate of the exact scattered wavefields. The philosophy is identical to that in Hudson and Heritage (1981), although their work is in the context of elastic scattering by a small spherical inclusion. By slightly modifying the previous equations (5.32a and b), we obtain the following expressions for the exact back-scattered and for-scattered electric fields as

$$E_{bak}(z_r,\omega) = E_{inc}(2z_{mid} - z_r,\omega)\left\{\frac{\frac{1}{2}\left(\sqrt{\frac{\hat{\sigma}}{\hat{\mu}}} - \sqrt{\frac{\hat{\mu}}{\hat{\sigma}}}\right)\sinh\left[\sqrt{\hat{\sigma}\hat{\mu}}\,\beta_1(\omega)\right]}{\cosh\left[\sqrt{\hat{\sigma}\hat{\mu}}\beta_1(\omega)\right] - \frac{1}{2}\left(\sqrt{\frac{\hat{\sigma}}{\hat{\mu}}} + \sqrt{\frac{\hat{\mu}}{\hat{\sigma}}}\right)\sinh\left[\sqrt{\hat{\sigma}\hat{\mu}}\beta_1(\omega)\right]}\right\} e^{-\beta_1(\omega)}, \tag{7.59a}$$

and

$$E_{for}(z_r,\omega) = E_{inc}(z_r,\omega)\left\{ \frac{e^{-\beta_1(\omega)} - \left[\cosh\left[\sqrt{\hat{\sigma}\hat{\mu}}\beta_1(\omega)\right] - \frac{1}{2}\left(\sqrt{\frac{\hat{\sigma}}{\hat{\mu}}} + \sqrt{\frac{\hat{\mu}}{\hat{\sigma}}}\right)\sinh\left[\sqrt{\hat{\sigma}\hat{\mu}}\beta_1(\omega)\right]\right]}{\cosh\left[\sqrt{\hat{\sigma}\hat{\mu}}\beta_1(\omega)\right] - \frac{1}{2}\left(\sqrt{\frac{\hat{\sigma}}{\hat{\mu}}} + \sqrt{\frac{\hat{\mu}}{\hat{\sigma}}}\right)\sinh\left[\sqrt{\hat{\sigma}\hat{\mu}}\beta_1(\omega)\right]} \right\}, \tag{7.59b}$$

respectively. Recall that the dimensionless frequency-dependent parameter $\beta_1(\omega)$ is given by

$$\beta_1(\omega) \equiv 2\pi(1-i)\left(h/\lambda_1(\omega)\right) = \sqrt{-i\omega\sigma_1\mu_1}\; h = iK_1(\omega)h\,,$$

where we adopt the usual low-frequency approximation for the complex-wavenumber. In this frequency range $\omega << \omega_1 = \sigma_1/\varepsilon_1$, the wavelength of the EM wave is given by $\lambda_1(\omega) = 2\pi\sqrt{2/\sigma_1\mu_1\omega}$.

Expanding the above formulae to first-order in the assumed small parameter $\sqrt{\hat{\sigma}\hat{\mu}}\beta_1(\omega)$ gives the interesting approximations

$$E_{bak}(z_r,\omega) \approx E_{inc}(2z_{mid} - z_r,\omega)\left(\frac{\hat{\sigma}-\hat{\mu}}{2}\right)\beta_1(\omega)\;, \tag{7.60a}$$

and

$$E_{for}(z_r,\omega) \approx E_{inc}(z_r,\omega)\left(\frac{\hat{\sigma}+\hat{\mu}}{2} - 1\right)\beta_1(\omega)\;. \tag{7.60b}$$

In each expression we also take $e^{-\beta_1(\omega)} \approx 1$. The layer midpoint position z_{mid} is held fixed. Each expression is directly proportional to $\beta_1(\omega)$. A small magnitude for both $\sqrt{\hat{\sigma}\hat{\mu}}\beta_1(\omega)$ and $\beta_1(\omega)$ is readily achieved by taking the thickness-to-wavelength ratio $h/\lambda_1(\omega) << 1$, independent of the two parameter contrast ratios $\hat{\sigma}$ and $\hat{\mu}$. [However, it is clear that if $\sqrt{\hat{\sigma}\hat{\mu}}$ is a large number, then $\beta_1(\omega) \sim h/\lambda_1(\omega)$ must be made *very* small in order for (7.60a and b) to hold.]

Expressions (7.60a and b) also provide a (partial) mathematical explanation for the numerical results illustrated in subsection 6.1.5 (Fixed Bed Conductance; Backward-Scattering) and 6.1.6 (Fixed Bed Inductance; Forward-Scattering). The product of $\hat{\sigma}$ and $\beta_1(\omega)$ is directly proportional to the bed conductance $S_2 \equiv \sigma_2 h$ (SI unit: S); similarly, the product of $\hat{\mu}$ and $\beta_1(\omega)$ is proportional to the bed inductance $L_2 \equiv \mu_2 h$ (SI unit: H). Working with equation (7.60a) as an example, the thin-bed back-scattered response re-written as

$$E_{bak}(z_r,\omega) \approx E_{inc}(2z_{mid} - z_r,\omega)\,\frac{\pi(1-i)}{\lambda_1(\omega)}\left[\frac{S_2}{\sigma_1} - \frac{L_2}{\mu_1}\right].$$

Next, suppose the background medium parameters σ_1, μ_1 (and hence $\lambda_1(\omega)$) are held fixed, and the bed parameters σ_2 and h are varied such that the conductance S_2 remains invariant. Then, the above expression indicates that the back-scattered field E_{bak} is also (nearly) invariant, *provided* that the term $L_2/\lambda_1(\omega)\mu_1 = \mu_2 h/\mu_1\lambda_1(\omega)$ is small. This is indeed the case for Figure 6.11. A similar argument applies to the fixed-inductance forward-scattered responses of Figure 6.12, for which expression (7.60b) is recast as

$$E_{for}(z_r,\omega) \approx E_{inc}(z_r,\omega)\,\frac{\pi(1-i)}{2\lambda_1(\omega)}\left[\frac{S_2}{\sigma_1}+\frac{L_2}{\mu_1}-2\right].$$

Fixed inductance L_2 leads to a fixed for-scattered field E_{for}, *provided* the term involving conductance S_2 remains small. An important proviso is that the bed is considered thin with respect to the incident medium wavelength, so that any term with $h/\lambda_1(\omega) << 1$ can be neglected. The *exact* scattering formulae (7.59a and b), appropriate for arbitrary bed thickness, do not exhibit this invariance.

Next, working with the previous equations (7.52a and b) for the FBA back-scattering and for-scattering formulae yield the variants:

For $z_r < z_{top}$:

$$E_B(z_r,\omega)\big|_{\Delta\sigma+\Delta\mu} = E_{inc}(2z_{mid}-z_r,\omega)\left(\frac{\hat{\sigma}-\hat{\mu}}{2}\right)\sinh[\beta_1(\omega)]. \qquad (7.61a)$$

For $z_r > z_{bot}$:

$$E_B(z_r,\omega)\big|_{\Delta\sigma+\Delta\mu} = E_{inc}(z_r,\omega)\left(\frac{\hat{\sigma}+\hat{\mu}}{2}-1\right)\beta_1(\omega). \qquad (7.61b)$$

The second expression (7.61b) is identical to the thin-bed for-scattering expression (7.60b). Moreover, for $\|\beta_1(\omega) << 1\|$ we have $\sinh[\beta_1(\omega)] \approx \beta_1(\omega)$, and the first expression (7.61a) reduces to the thin-bed back-scattering expression (7.60a). So, the important conclusion is that a thin bed, defined by the condition $h/\lambda_1(\omega) << 1$, has an FBA scattering response the same as the exact scattering response. This is consistent with the deduction of the previous sub-section 7.6.4, although via a slightly different route.

In order to quantify the accuracy of FBA scattering, consider two complex-valued ratios formed from the FBA and exact scattered EM fields as

$$BE(\omega)\big|_{bak} \equiv \frac{E_B(z_r,\omega)\big|_{bak}}{E_{bak}(z_r,\omega)}, \qquad BE(\omega)\big|_{for} \equiv \frac{E_B(z_r,\omega)\big|_{for}}{E_{for}(z_r,\omega)}. \qquad (7.62a,b)$$

Substituting in the above expressions and simplifying yields (next page):

$$BE(\omega)\big|_{bak} = \sqrt{\hat{\sigma}\hat{\mu}}\left\{\frac{\cosh\left[\sqrt{\hat{\sigma}\hat{\mu}}\beta_1(\omega)\right]-\hat{g}\sinh\left[\sqrt{\hat{\sigma}\hat{\mu}}\beta_1(\omega)\right]}{\sinh\left[\sqrt{\hat{\sigma}\hat{\mu}}\beta_1(\omega)\right]}\right\}\sinh\left[\beta_1(\omega)\right]e^{+\beta_1(\omega)}, \tag{7.63a}$$

and

$$BE(\omega)\big|_{for} = \left(\frac{\hat{\sigma}+\hat{\mu}-2}{2}\right)\left\{\frac{\cosh\left[\sqrt{\hat{\sigma}\hat{\mu}}\beta_1(\omega)\right]-\hat{g}\sinh\left[\sqrt{\hat{\sigma}\hat{\mu}}\beta_1(\omega)\right]}{e^{-\beta_1(\omega)}-\left[\cosh\left[\sqrt{\hat{\sigma}\hat{\mu}}\beta_1(\omega)\right]-\hat{g}\sinh\left[\sqrt{\hat{\sigma}\hat{\mu}}\beta_1(\omega)\right]\right]}\right\}\beta_1(\omega), \tag{7.63b}$$

where $\hat{g} \equiv \dfrac{\hat{\sigma}+\hat{\mu}}{2\sqrt{\hat{\sigma}\hat{\mu}}}$ is a real-valued parameter formed from the parameter contrast ratios. [Interestingly, parameter $\hat{g}$ is the ratio of the arithmetic mean to the geometric mean of $\hat{\sigma}$ and $\hat{\mu}$. Does this mean anything profound? Probably not.] As a check, we immediately find that as $h/\lambda_1(\omega) \to 0$, then

$$BE(\omega)\big|_{bak} \to 1, \qquad\qquad BE(\omega)\big|_{for} \to 1,$$

which is consistent with the above analysis. In the thin bed limit, the FBA and exact scattered responses become identical. Additionally, consider a layer where the conductivity and permeability contrast ratios have the same value: $\hat{\sigma} = \hat{\mu} = r$, implying $\hat{g} = 1$. Then we have

$$BE(\omega)\big|_{bak} = r\left\{\frac{\cosh\left[r\beta_1(\omega)\right]-\sinh\left[r\beta_1(\omega)\right]}{\sinh\left[r\beta_1(\omega)\right]}\right\}\sinh\left[\beta_1(\omega)\right]e^{+\beta_1(\omega)} = r\left(\frac{e^{+2\beta_1}-1}{e^{+2r\beta_1}-1}\right),$$

and

$$BE(\omega)\big|_{for} = \left(\frac{2r-2}{2}\right)\left\{\frac{\cosh\left[r\beta_1(\omega)\right]-\sinh\left[r\beta_1(\omega)\right]}{e^{-\beta_1(\omega)}-\left[\cosh\left[r\beta_1(\omega)\right]-\sinh\left[r\beta_1(\omega)\right]\right]}\right\}\beta_1(\omega) = \frac{(r-1)\beta_1}{e^{(r-1)\beta_1}-1}.$$

Hence, as $r \to 1$ (implying *no* material property contrast for the layer), the Born-to-Exact scattering ratios again approach

$$BE(\omega)\big|_{bak} \to 1, \qquad\qquad BE(\omega)\big|_{for} \to 1.$$

The latter limiting case is easily obtained via L'Hopital's Rule. Both the FBA and the exact scattered fields vanish (obviously) for this "no contrast layer" case. However, their *ratios* approaches unity.

The Born-to-Exact scattering response ratios (7.63a and b) (as well as the underlying exact responses (7.56a and b) and FBA responses (7.59a and b)) are exceedingly important, in that they clearly exhibit dependency on only *three* dimensionless parameters $\hat{\sigma} = \sigma_2/\sigma_1$, $\hat{\mu} = \mu_2/\mu_1$, and $\hat{h}(\omega) \equiv h/\lambda_1(\omega)$ [Since we have already specialized to low-frequency, or the geophysical induction regime, the remaining dimensionless parameter ratio $\hat{\varepsilon} = \varepsilon_2/\varepsilon_1$ does not enter the formulae.] The following figures illustrate ratios (7.63a and b), plotted as a logarithmic amplitude ratio above the 2D plane of $\log_{10}\hat{\sigma}$ and $\log_{10}\hat{\mu}$.

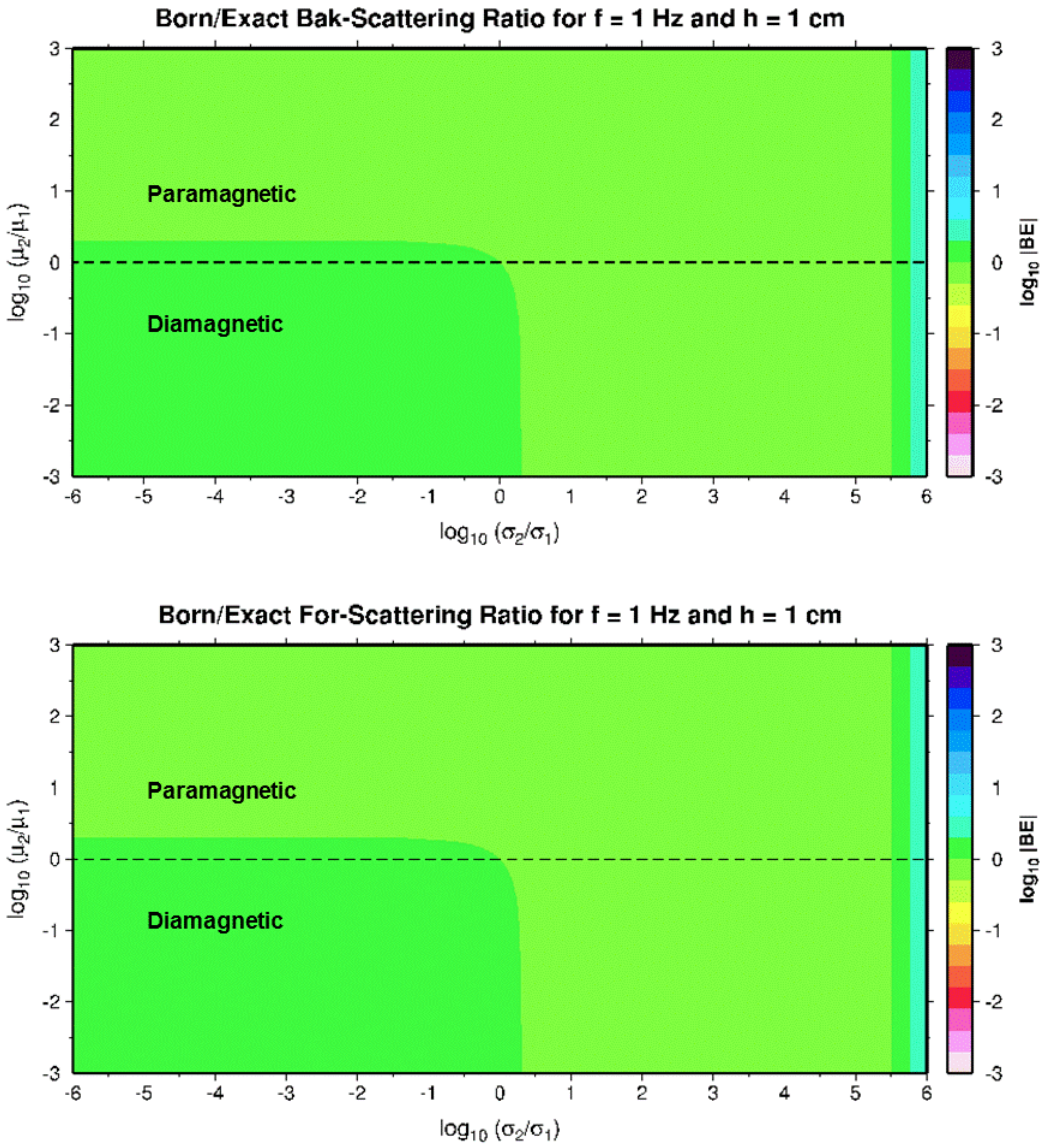

Figure 7.4. Backward-scattering (top panel) and forward-scattering (bottom panel) logarithmic amplitude ratios of FBA to Exact scattered responses, calculated for a thin layer (h = 1 cm) and an incident EM sinusoidal signal with frequency f = 1 Hz. Background conductivity σ_1 = 0.1 S/m and permeability $\mu_1 = \mu_0$, implying thickness-to-wavelength ratio is $h/\lambda_1 = 10^{-6}$. Paramagnetic/diamagnetic regions reside above/below the horizontal dashed lines.

Figure 7.4 above depicts the Born-to-Exact amplitude ratios, for both backward- and forward scattering. The choice of incident medium #1 parameters implies $h/\lambda_1 = 10^{-2}\,\mathrm{m}/10^{+4}\,\mathrm{m} = 10^{-6}$, so that the calculation is well within the thin bed regime. Consistent with the above analysis, the FBA and exact responses are nearly the same, and hence their ratio is unity; both plots are nearly completely green (logarithm 0). Only at very large conductivity contrast $\hat{\sigma} \sim 10^6$ does the FBA amplitude exceed the exact amplitude. The horizontal dashed lines at $\log_{10} \hat{\mu} = 0$ separate zones of paramagnetic ($\mu_2 > \mu_0$) and

diamagnetic ($\mu_2 < \mu_0$) material for the layer. If diamagnetism in geologic materials is considered rare or impossible, then the zone below the dashed lines should be ignored. However, some common materials possess relative magnetic permeabilities slightly less than unity (i.e., copper: 0.999994, water: 0.999992, bismuth: 0.999834; see https:/en.wikipedia.org/wiki/Permeability_(electromagnetism)).

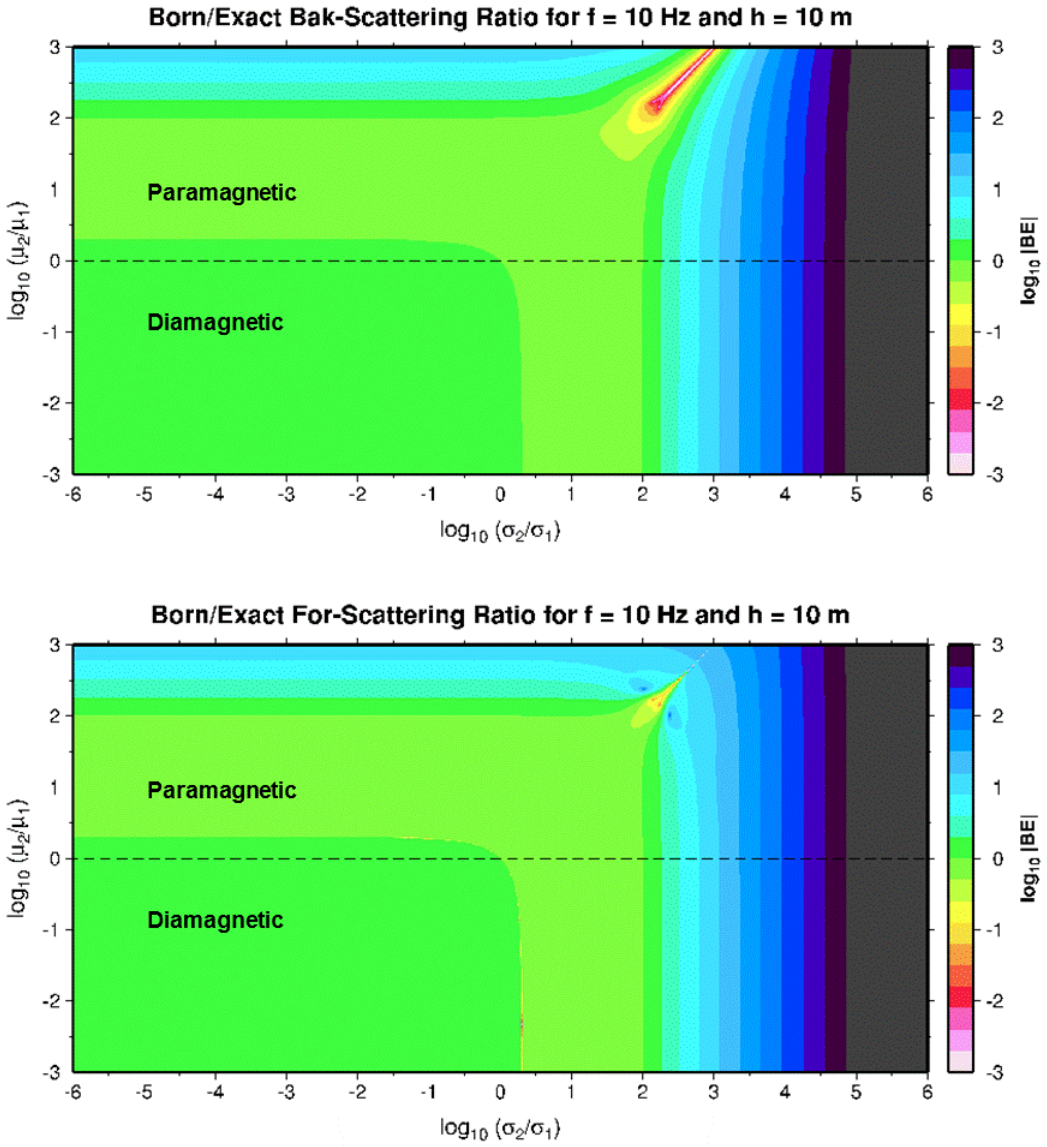

Figure 7.5. Same as Figure 7.4, except for a thicker layer (h = 10 m) and a higher frequency incident signal (f = 10 Hz).

FBA-to-Exact logarithmic amplitude ratios for a thicker layer (h = 10 m) and a higher frequency (f = 10 Hz) are illustrated in Figure 7.5. The thickness-to-wavelength ratio is $h/\lambda_1 \approx 3.162\times10^{-3}$, which is still small. However, FBA scattering response amplitudes are now significantly greater than exact amplitudes for large conductivity contrasts. Moreover, back- and for-scattered ratios have different appearances, particularly near the line defined by $\hat{\sigma} = \hat{\mu}$, where a "valley" develops in the backward response.

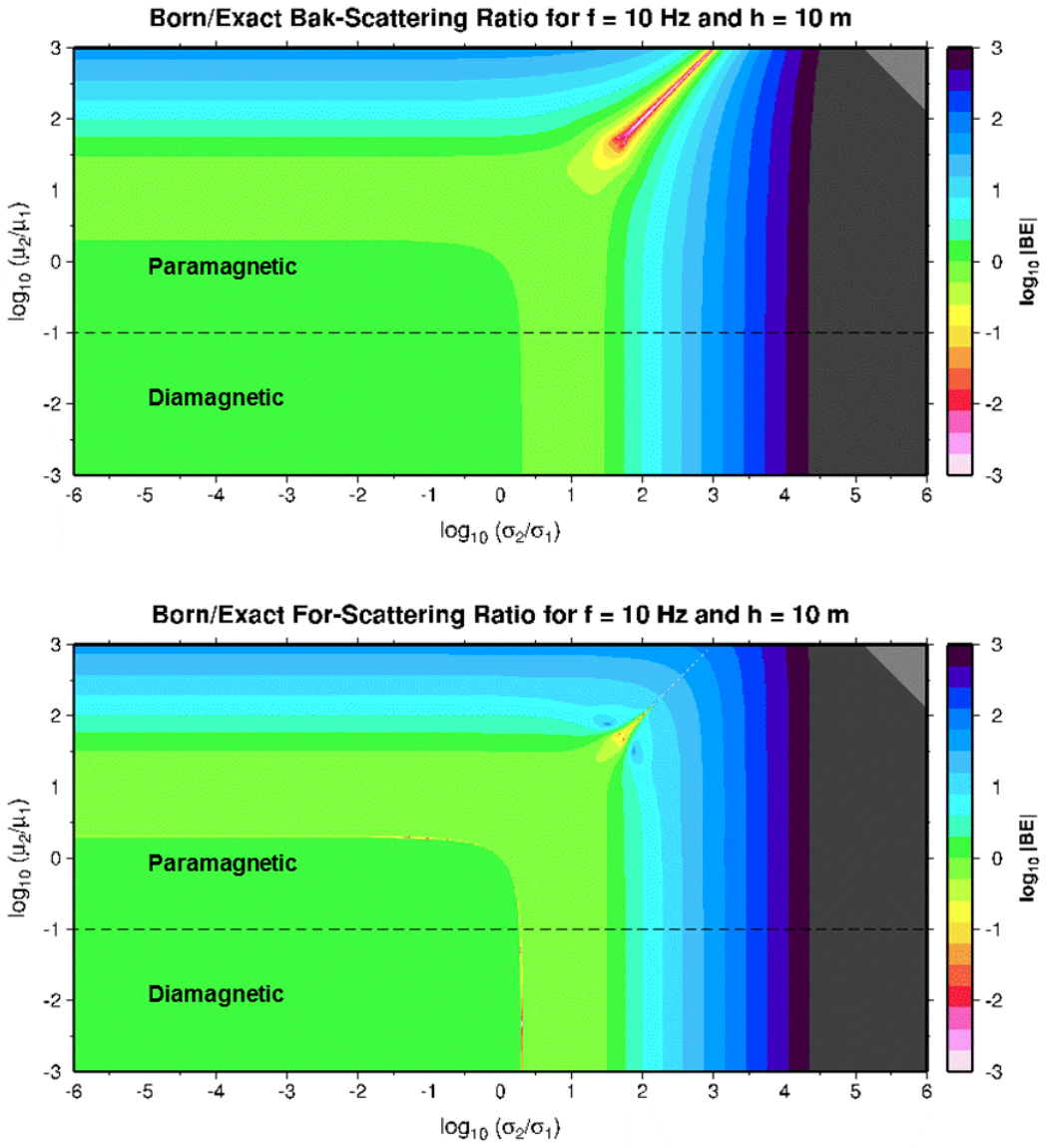

Figure 7.6. Same as Figure 7.5, except a larger magnetic permeability $\mu_1 = 10\mu_0$ is assigned to the background medium.

Finally, Figure 7.6 depicts the two logarithmic amplitude ratios (again for h = 10 m and f = 10 Hz) where the background medium magnetic permeability is increased to $\mu_1 = 10\mu_0$. The dividing line between zones of paramagnetism and diamagnetism is depressed to $\log_{10}\hat{\mu} = -1$. Layer thickness-to-incident wavelength ratio is now $h/\lambda_1 \approx 10^{-2}$. FBA response significantly exceeds the exact response over a broader range of conductivity contrast, and the valley of dimished FBA responses pulls in closer to the origin. In the upper right corner, a zone of NANs (grey color) develops, suggesting that the numerical evaluation is not well-posed in this area.

A conclusion evident in all three figures is that the FBA scattered response amplitude exceeds the exact scattered response if the layer possesses strong conductivity contrast with the surrounding medium. Moreover, this effect is enhanced by thicker layers and higher frequencies, as this increases ratio h/λ_1.

8.0 SUMMARY AND CONCLUSIONS

Plane wave reflection and transmission responses, for the electric **E** and magnetic **B** wavefields, have been developed for a simple geologic model consisting of a homogeneous and isotropic layer situated between two (potentially dissimilar) halfspaces. A plane electric wave is normally incident upon the top interface of the layer. The *reflected* response includes the two primary reflections from top and bottom interfaces, as well as all intrabed multiples. The *transmitted* response is formed from the direct (i.e., propagating straight through) wave, together with all trailing intrabed multiples. Each multiple is delayed by the two-way traveltime within the layer, and is also attenuated by the electrically conductive material. In general, layer thickness *h* need not be small compared to an incident wavelength. A novel aspect of the present development is inclusion of *intrabed* **E** and **B** responses, which might be observed via borehole emplacement of a receiver within the layer.

Scattered wavefields (in the backward and forward directions) are obtained by subtracting a suitable reference (or background) medium response. Hence, a scattered response may be thought of as directly attributable to perturbations in medium properties induced by the presence of the layer. A common reference medium is a homogeneous and isotropic wholespace, for which the reference response is a plane progressing EM wave. Then, the *back-scattered* response is the same as the reflected response, and the *for-scattered* response equals the transmitted response *minus* the direct wave. This situation applies to a hydraulic fracture created entirely within a spatially-extensive homogeneous geologic formation. However, a fracture might follow a pre-existing path of weakness, like an interface between two different rock formations. Our mathematical formalism applies to either case, although our numerical simulations, performed with algorithm THEMBED, apply to the simpler situation of a fracture emplaced within a homogeneous wholespace.

Extensive numerical simulations with algorithm THEMBED reveal the basic characteristics of reflected and transmitted responses, as well as back- and for-scattered responses, as layer characteristics (i.e., bed thickness, bed conductivity, permeability, and permittivity) are varied. In the low frequency regime commonly used in EM exploration geophysics, permittivity contrast appears to have negligible influence.

The First Born Approximation (FBA) scattering response is, as the name obviously implies, an *approximation* to the actual scattered response of a geologic layer, and is developed by replacing the layer with an "equivalent" or "effective" body source distribution of EM waves. Perturbations in conductivity/permeability/permittivity imply body sources of conduction/magnetic/displacement current, respectively. In the limit of a thin layer (with respect to a wavelength of the incident wave within the background medium) and mild medium parameter contrasts, the FBA scattering response agrees with the actual scattering response, both mathematically and numerically. However, as parameter contrast increases, the FBA scattering response grows without bound, whereas the actual scattering response asymptotes to a fixed value. This interesting effect has been recently observed in DC potential field calculations by Weiss et al. (2015). Clearly, FBA scattering over-estimates the amplitudes of actual scattering as medium parameter contrasts increase. FBA theory also indicates invariant back- and for-scattering responses, for layers with fixed conductance (thickness × conductivity), inductance (thickness × permeability), and capacitance (thickness × permittivity) product. This invariance is not predicted by the actual, or exact, scattering formulae. Thus, the ability to resolve layer thickness and a corresponding layer parameter in an EM scattering experiment is probably severely limited.

The importance of the First Born Approximation formalism resides in its simple description of wavefield scattering phenomena, as well as its practical utility in numerical representation of small-spatial-scale perturbations on a 3D grid via an equivalent body source. However, it should always be remembered that the FBA is an *approximation* to reality.

Finally, we remind the reader that an obvious extension of the present analysis involves a non-normal incident plane EM wave onto the geologic layer. Figure 8.1 below depicts raypaths of reflected and

transmitted responses. Unlike the previous Figure 2.1, these are *actual* raypaths, inclined from the vertical.

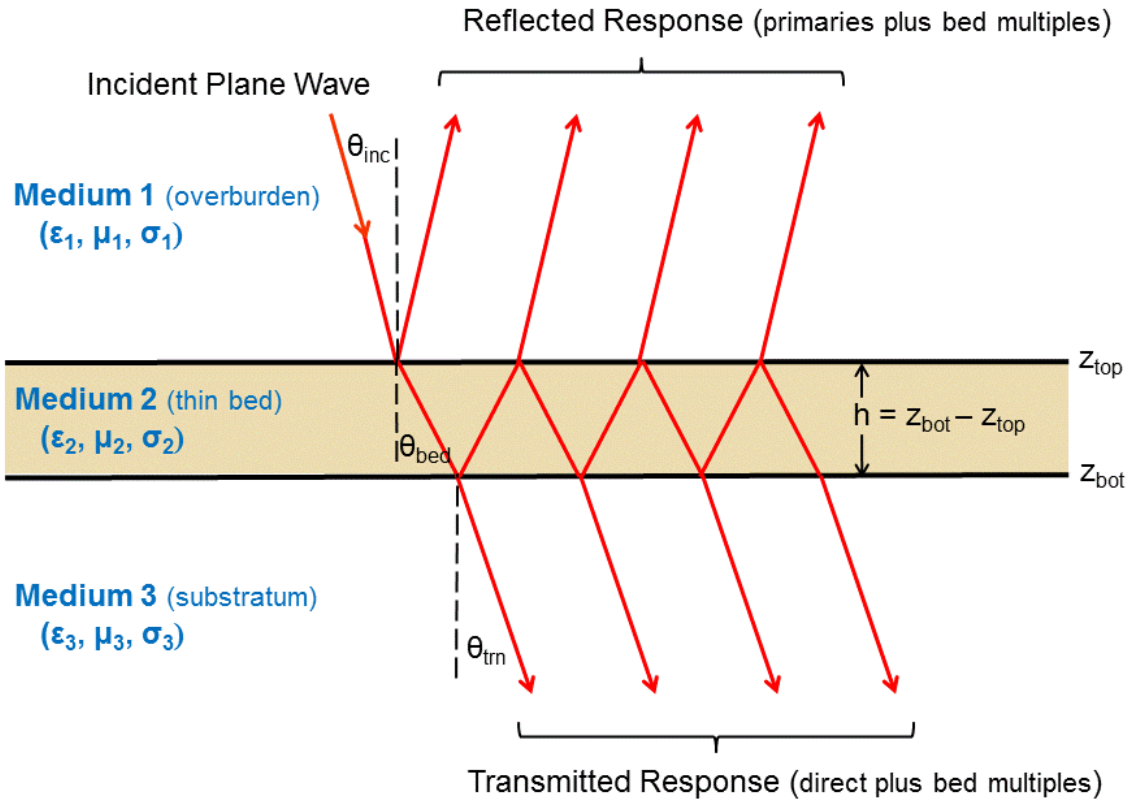

Figure 8.1. Non-normal incidence plane wave reflected and transmitted responses of a geologic layer.

Note that in general, the raypaths, and hence the wavefronts, have *different* (non-vertical and non-horizontal) angular orientations in the overburden and substratum. Angles within the layer and substratum are governed by Snells' Law of Refraction: $\sin\theta_{bed} = \left(c_2(f)/c_1(f)\right)\sin\theta_{inc}$ and $\sin\theta_{trn} = \left(c_3(f)/c_2(f)\right)\sin\theta_{bed}$. In the simpler (and perhaps more realistic) case where medium #3 = medium #1, then $\theta_{trn} = \theta_{inc}$ and raypaths/wavefronts are oriented similarly in both media. In the low-frequency range commonly employed in geophysical electromagnetics, the phase speed ratios in Snells' Law are independent of frequency: $c_2(f)/c_1(f) = \sqrt{(\sigma_1/\sigma_2)(\mu_1/\mu_2)} = 1/\sqrt{\hat{\sigma}\hat{\mu}}$. Careful analysis of this situation awaits a future generation of geophysicists!

9.0 REFERENCES

Aldridge, D.F., 2013, Electromagnetic radiation from point sources in a homogeneous wholespace: Technical report SAND2013-4857, Sandia National Laboratories.

Aldridge, D.F., 2014, A data volume estimation formula for use in geophysical electromagnetic recording: Unpublished technical notes, Sandia National Laboratories.

Aldridge, D.F., Bartel, L.C., Knox, H.A., Schramm, K.A., and Weiss, C.J., 2014, Numerical studies of electromagnetic resolution: American Geophysical Union Annual Fall Meeting, 15-19 December 2014, San Francisco, CA, USA.

Aldridge, D.F., Weiss, C.J., Knox, H.A., Schramm, K.A., and Bartel, L.C., 2015, Is a steel-cased borehole an electrical transmission line?, Expanded Abstract and Oral Presentation, Society of Exploration Geophysicists Annual International Meeting, 18-23 October 2015, New Orleans, LA.

Aldridge, D.F., and Bartel, L.C., 2016, Systems and methods for locating and imaging proppant in an induced fracture: US patent #9,250,351 B2, issued 2 February 2016, assigned to Carbo Ceramics Inc., Houston, TX.

Aldridge, D.F., and Weiss, C.J., 2016, Plane wave electromagnetic reflection and transmission from a thin geologic layer: American Geophysical Union Annual Fall Meeting, 12-16 December 2016, San Francisco, CA, USA.

Aki, K., and Richards, P.G., 1980, Quantitative seismology, theory and methods, volume 1: W.H. Freeman and Company.

Bracewell, R., 1965, The Fourier transform and its applications: McGraw-Hill Book Company.

Chew, W.C., and Sen, P.N., 1982, Dielectric enhancement due to electrochemical double layer: Thin double layer approximation: Journal of Chemical Physics, volume 77, number 9, pages 4683-4693.

Gradshteyn, I.S., and Ryzhik, I.M., 1994, Table of integrals, series, and products, fifth edition: Academic Press.

de Hoop, A.T., 1992, Reciprocity, causality, and Huygens' principle in electromagnetic wave theory, pages 171-192 *in* Huygens' Principle 1690-1990: Theory and Applications, *edited by* H. Blok, H.A. Ferwerda, and H.K. Kuiken: Elsevier Science Publishers.

Hudson, J.A., and Heritage, J.R., 1981, The use of the Born approximation in seismic scattering problems: Geophysical Journal of the Royal Astronomical Society, volume 66, pages 221-240.

LeBrecque, D., Brigham, R., Denison, J., Murdoch, L., Slack, W., Liu, Q.H., Fang, Y., Dai, J., Hu, Y., Yu, Z., Kleinhammes, A., Doyle, P., Wu, Y., and Ahmadian, M., 2016, Remote imaging of proppants in hydraulic fracture networks using electromagnetic methods: results of small-scale field experiments: paper SPE-179170-MS, Society of Petroleum Engineers Hydraulic Fracturing Technology Conference, 9-11 February 2016, The Woodlands, Texas, USA.

Levin, F.K., 1986, When reflection coefficients are zero: Geophysics, volume 5, pages 736-741.

Løseth, L.O., Pedersen, H.M., Ursin, B., Amundsen, L., and Ellingsrud, S., 2006, Low-frequency electromagnetic fields in applied geophysics: Waves or diffusion?: Geophysics, volume 71, pages w29-w40.

Marsala, A.F., Hibbs, A.D., Petrov, T.R., and Pendelton, J.M., 2013, Six-component tensor of the surface electromagnetic field produced by a borehole source recorded by innovative capacitive sensors: Expanded Abstract, Society of Exploration Geophysicists Annual International Meeting, doi:10.1190/segam/2013-0946.1.

O'Connell, R.J., and Budiansky, B., 1978, Measures of dissipation in viscoelastic media: Geophysical Research Letters, volume 5, pages 5-8.

Palisch, T., Al-Tailji, W., Bartel, L., Cannan, C., Czapski, M., and Lynch, K., 2016, Recent advancements in far-field proppant detection: Paper number SPE-179161-MS, Society of Petroleum Engineers Hydraulic Fracturing Technology Conference, 9-11 February 2016, The Woodlands, TX.

Palisch, T., Al-Tailji, W., Bartel, L., Cannan, C., Zhang, J., Czapski, M., and Lynch, K., 2017, Far-field proppant detection using electromagnetic methods – latest field results: Paper number SPE-184880-MS, Society of Petroleum Engineers Hydraulic Fracturing Technology Conference and Exhibition, 24-26 January 2017, The Woodlands, TX.

Reitz, J.R., and Milford, F.J., 1967, Foundations of electromagnetic theory: Addison-Wesley Publishing Company.

Snieder, R., and Aldridge, D.F., 1995, Perturbation theory for travel times: Journal of the Acoustical Society of America, volume 98, pages 1565-1569.

Ward, S.H., and Hohmann, G.W., 1987, Electromagnetic theory for geophysical applications, pages 131-311 *in* Electromagnetic methods in applied geophysics, *edited by* M.N. Nabighian: Society of Exploration Geophysicists.

Weiss, C.J., Aldridge, D.F., Knox, H.A., Schramm, K.A., and Bartel, L.C., 2016, The direct-current response of electrically conducting fractures excited by a grounded current source: Geophysics, volume 81, pages E201-E210.

Widess, M.B., 1957-58, How thin is a thin bed?: Proceedings of the Geophysical Society of Tulsa.

Widess, M.B., 1973, How thin is a thin bed?: Geophysics, volume 38, 1176-1180; *reprinted from* the Proceedings of the Geophysical Society of Tulsa, 1957-1958.

10.0 APPENDIX A: PLANE ELECTROMAGNETIC WAVES

In this Appendix, we develop the mathematics of plane electromagnetic wave propagation within a homogeneous and isotropic medium from fundamental principles of electromagnetism.

A1.0 EH Partial Differential System

We start with two of the fundamental Maxwell equations that govern electromagnetic phenomena:

$$\frac{\partial \mathbf{b}(\mathbf{x},t)}{\partial t} + \mathbf{curl}\ \mathbf{e}(\mathbf{x},t) = \mathbf{0}\,, \qquad \text{(Faraday law)} \qquad \text{(A1.1a)}$$

$$\frac{\partial \mathbf{d}(\mathbf{x},t)}{\partial t} - \mathbf{curl}\ \mathbf{h}(\mathbf{x},t) + \mathbf{j}(\mathbf{x},t) = \mathbf{0}\,, \qquad \text{(Ampere – Maxwell law)} \qquad \text{(A1.1b)}$$

where the four dependent variables are

$\mathbf{b}(\mathbf{x},t)$**:** magnetic induction vector, SI unit: $\mathrm{T} = \dfrac{\mathrm{V-s}}{\mathrm{m}^2}$,

$\mathbf{d}(\mathbf{x},t)$**:** electric displacement vector, SI unit: $\dfrac{\mathrm{C}}{\mathrm{m}^2} = \dfrac{\mathrm{A-s}}{\mathrm{m}^2}$,

$\mathbf{e}(\mathbf{x},t)$**:** electric field vector, SI unit: $\dfrac{\mathrm{N}}{\mathrm{C}} = \dfrac{\mathrm{V}}{\mathrm{m}}$,

$\mathbf{h}(\mathbf{x},t)$**:** magnetic intensity vector, SI unit: $\dfrac{\mathrm{A}}{\mathrm{m}}$.

The particular variable names used here are taken from Reitz and Milford (1967). Within the geophysical discipline, **e**(**x**,*t*) and **h**(**x**,*t*) are commonly referred to as the "electric" and "magnetic" field vectors, respectively. Ward and Hohmann (1987, p. 132) refer to **d**(**x**,*t*) as the "dielectric displacement" vector and **e**(**x**,*t*) as the "electric field intensity" vector. Alternately, **e**(**x**,*t*) and **h**(**x**,*t*) are called the electric and magnetic "field strength" vectors, and **d**(**x**,*t*) and **b**(**x**,*t*) are the associated electric and magnetic "flux density" vectors, respectively (de Hoop, 1992).

Next, introduce three electromagnetic constitutive relations appropriate for linear, time-independent, and isotropic media as:

$$\mathbf{b}(\mathbf{x},t) = \mu(\mathbf{x})\,\mathbf{h}(\mathbf{x},t) + \mathbf{b}_s(\mathbf{x},t)\,, \qquad \text{(A1.2a)}$$

$$\mathbf{d}(\mathbf{x},t) = \varepsilon(\mathbf{x})\,\mathbf{e}(\mathbf{x},t) + \mathbf{d}_s(\mathbf{x},t)\,, \qquad \text{(A1.2b)}$$

$$\mathbf{j}(\mathbf{x},t) = \sigma(\mathbf{x})\,\mathbf{e}(\mathbf{x},t) + \mathbf{j}_s(\mathbf{x},t)\,. \qquad \text{(A1.2c)}$$

The medium is characterized by the three scalar parameters

$\mu(\mathbf{x})$: magnetic permeability, SI unit: $\dfrac{\text{V/m}}{\text{A/s}} = \dfrac{\text{H}}{\text{m}}$,

$\varepsilon(\mathbf{x})$: electric permittivity, SI unit: $\dfrac{\text{A/m}}{\text{V/s}} = \dfrac{\text{F}}{\text{m}}$,

$\sigma(\mathbf{x})$: current conductivity, SI unit: $\dfrac{\text{A/V}}{\text{m}} = \dfrac{1}{\Omega - \text{m}} = \dfrac{\text{S}}{\text{m}}$.

We take the magnetic permeability and electric permittivity to be intrinsically positive (and bounded from below by the corresponding free space values ε_0 and μ_0). However, the current conductivity may equal zero, as in an absolute vacuum containing no electric charges.

Symbols with subscript "s" on the right hand sides in the above constitutive relations represent body sources (i.e., impressed or imposed or artificially generated values) of the various quantities. An electric current source, represented by the current density vector $\mathbf{j}_s(\mathbf{x},t)$, is probably the commonly-used type of source in electromagnetic geophysics. However, the magnetic induction source $\mathbf{b}_s(\mathbf{x},t)$ is not unusual, although it often shows up in the time-differentiated form $\mathbf{k}_s(\mathbf{x},t) \equiv \partial \mathbf{b}_s(\mathbf{x},t)/\partial t$ and is referred to as a *magnetic current* body source. The *displacement current* body source $\mathbf{l}_s(\mathbf{x},t) \equiv \partial \mathbf{d}_s(\mathbf{x},t)/\partial t$ appears to be novel, and is included here mainly for completeness and consistency. However, it will be demonstrated in Appendix D that all three body source types are required for a proper description of EM scattering in the First Born Approximation.

Substituting the three constitutive equations into the two Maxwell equations yields the coupled first-order system of inhomogeneous partial differential equations:

$$\varepsilon(\mathbf{x})\frac{\partial \mathbf{e}(\mathbf{x},t)}{\partial t} + \sigma(\mathbf{x})\mathbf{e}(\mathbf{x},t) - \mathbf{curl}\,\mathbf{h}(\mathbf{x},t) = -\mathbf{j}_s(\mathbf{x},t) - \frac{\partial \mathbf{d}_s(\mathbf{x},t)}{\partial t}, \tag{A1.3a}$$

$$\mu(\mathbf{x})\frac{\partial \mathbf{h}(\mathbf{x},t)}{\partial t} + \mathbf{curl}\,\mathbf{e}(\mathbf{x},t) = -\frac{\partial \mathbf{b}_s(\mathbf{x},t)}{\partial t}. \tag{A1.3b}$$

These are six coupled PDEs governing six dependent variables (three components of $\mathbf{e}(\mathbf{x},t)$ and three components of $\mathbf{h}(\mathbf{x},t)$). There are three medium parameters and three distinct body source types. We refer to the PDE system (A1.3a and b) as the "EH equations" or the "EH system", after the two dependent variables contained therein. Interestingly, the derivation of the EH PDE system does not explicitly utilize the two Gauss laws of Maxwell's equations. Rather, only the Faraday law and the Ampere-Maxwell law are used.

A2.0 Separated Partial Differential Equations

Next, specialize to a homogeneous body where the medium parameters do not depend on position $\mathbf{x}$: $\varepsilon(\mathbf{x}) = \varepsilon$, $\mu(\mathbf{x}) = \mu$, and $\sigma(\mathbf{x}) = \sigma$. Then the two first-order PDEs of the EH system may be combined to yield two separated second-order PDEs governing the electric vector and the magnetic vector. These are (next page):

$$\nabla^2 \mathbf{e}(\mathbf{x},t) - \mathbf{grad}\ \mathrm{div}\ \mathbf{e}(\mathbf{x},t) - \sigma\mu \frac{\partial \mathbf{e}(\mathbf{x},t)}{\partial t} - \varepsilon\mu \frac{\partial^2 \mathbf{e}(\mathbf{x},t)}{\partial t^2}$$
$$= \mu \frac{\partial \mathbf{j}_s(\mathbf{x},t)}{\partial t} + \frac{\partial\, \mathbf{curl}\, \mathbf{b}_s(\mathbf{x},t)}{\partial t} + \mu \frac{\partial^2 \mathbf{d}_s(\mathbf{x},t)}{\partial t^2}, \qquad \text{(A2.1a)}$$

$$\nabla^2 \mathbf{h}(\mathbf{x},t) - \mathbf{grad}\ \mathrm{div}\ \mathbf{h}(\mathbf{x},t) - \sigma\mu \frac{\partial \mathbf{h}(\mathbf{x},t)}{\partial t} - \varepsilon\mu \frac{\partial^2 \mathbf{h}(\mathbf{x},t)}{\partial t^2}$$
$$= -\mathbf{curl}\ \mathbf{j}_s(\mathbf{x},t) + \sigma \frac{\partial \mathbf{b}_s(\mathbf{x},t)}{\partial t} + \varepsilon \frac{\partial^2 \mathbf{b}_s(\mathbf{x},t)}{\partial t^2} - \frac{\partial\, \mathbf{curl}\, \mathbf{d}_s(\mathbf{x},t)}{\partial t}, \qquad \text{(A2.1b)}$$

where the vector differential operator identity $\mathbf{curl}\ \mathbf{curl} = \mathbf{grad}\ \mathrm{div} - \nabla^2$ is used. Interestingly, the left-hand-sides of both expressions possess the same mathematical form. However, the second-order spatial derivative terms **grad** div **e**(**x**,*t*) and **grad** div **h**(**x**,*t*) may be simplified by exploiting the two Gauss laws of Maxwell's equations and the charge continuity equation. The Gauss laws are

$$\mathrm{div}\ \mathbf{b}(\mathbf{x},t) = 0, \qquad \text{(magnetic Gauss law)} \qquad \text{(A2.2a)}$$

$$\mathrm{div}\ \mathbf{d}(\mathbf{x},t) - \theta(\mathbf{x},t) = 0, \qquad \text{(electric Gauss law)} \qquad \text{(A2.2b)}$$

where $\theta(\mathbf{x},t)$ is an additional (scalar-valued) dependent variable called the free charge density or the mobile charge density (SI unit: C/m^3). The charge continuity equation is

$$\frac{\partial \theta(\mathbf{x},t)}{\partial t} + \mathrm{div}\ \mathbf{j}(\mathbf{x},t) = 0, \qquad \text{(charge continuity equation)} \qquad \text{(A2.2c)}$$

which links the charge density to the current density vector **j**(**x**,*t*).

Combining the magnetic Gauss law div **b**(**x**,*t*) = 0 with the constitutive relation (A1.2a) gives (for homogeneous media) div **h**(**x**,*t*) = (–1/μ) div **b**$_s$(**x**,*t*). Thus

$$\mathbf{grad}\ \mathrm{div}\ \mathbf{h}(\mathbf{x},t) = -\frac{1}{\mu}\mathbf{grad}\ \mathrm{div}\ \mathbf{b}_s(\mathbf{x},t). \qquad \text{(A2.3a)}$$

This expression will be used to eliminate the **grad** div **h**(**x**,*t*) term in (A2.1b). The analogous situation for the **grad** div **e**(**x**,*t*) term in (A2.1a) is more complicated. Combining the electric Gauss law div **d**(**x**,*t*) = θ(**x**,*t*) with the constitutive relation (A1.2b) gives (again for homogeneous media)

$$\mathrm{div}\ \mathbf{e}(\mathbf{x},t) = \frac{1}{\varepsilon}\theta(\mathbf{x},t) - \frac{1}{\varepsilon}\mathrm{div}\ \mathbf{d}_s(\mathbf{x},t).$$

Now, differentiate with respect to time, and substitute from the charge continuity equation (A2.2c) to obtain

$$\frac{\partial}{\partial t}\mathrm{div}\ \mathbf{e}(\mathbf{x},t) = -\frac{1}{\varepsilon}\mathrm{div}\ \mathbf{j}(\mathbf{x},t) - \frac{1}{\varepsilon}\frac{\partial}{\partial t}\mathrm{div}\ \mathbf{d}_s(\mathbf{x},t).$$

Next, substitute from the constitutive relation (A1.2c) for the current density vector **j** to obtain

$$\frac{\partial}{\partial t}\operatorname{div}\mathbf{e}(\mathbf{x},t)+\frac{\sigma}{\varepsilon}\operatorname{div}\mathbf{e}(\mathbf{x},t)=-\frac{1}{\varepsilon}\operatorname{div}\mathbf{j}_s(\mathbf{x},t)-\frac{1}{\varepsilon}\frac{\partial}{\partial t}\operatorname{div}\mathbf{d}_s(\mathbf{x},t)\,.$$

This is a first-order, inhomogeneous *ordinary* differential equation for the divergence of the electric field vector div **e**(**x**,*t*). The solution is

$$\operatorname{div}\mathbf{e}(\mathbf{x},t)=-\frac{1}{\varepsilon}H(t)\exp\left(-\frac{\sigma}{\varepsilon}t\right)*\left\{\operatorname{div}\mathbf{j}_s(\mathbf{x},t)+\frac{\partial}{\partial t}\operatorname{div}\mathbf{d}_s(\mathbf{x},t)\right\},$$

where $H(t)$ is the Heaviside unit step function, and the asterisk denotes convolution with respect to the independent variable t. Taking the gradient gives the required expression

$$\mathbf{grad}\operatorname{div}\mathbf{e}(\mathbf{x},t)=-\frac{1}{\varepsilon}H(t)\exp\left(-\frac{\sigma}{\varepsilon}t\right)*\left\{\mathbf{grad}\operatorname{div}\mathbf{j}_s(\mathbf{x},t)+\frac{\partial}{\partial t}\mathbf{grad}\operatorname{div}\mathbf{d}_s(\mathbf{x},t)\right\},\qquad\text{(A2.3b)}$$

since the gradient operation distributes over temporal convolution and differentiation.

Expressions (A2.3a and b) indicate that the **grad** div terms on the left sides of equations (A2.1a and b) may be exchanged for body source terms, yielding

$$\begin{aligned}\nabla^2\mathbf{e}(\mathbf{x},t)-\sigma\mu\frac{\partial\mathbf{e}(\mathbf{x},t)}{\partial t}-\varepsilon\mu\frac{\partial^2\mathbf{e}(\mathbf{x},t)}{\partial t^2}&\\ =\mu\frac{\partial\mathbf{j}_s(\mathbf{x},t)}{\partial t}+\frac{\partial\,\mathbf{curl}\,\mathbf{b}_s(\mathbf{x},t)}{\partial t}+\mu\frac{\partial^2\mathbf{d}_s(\mathbf{x},t)}{\partial t^2}&\\ -\frac{1}{\varepsilon}H(t)\exp\left(-\frac{\sigma}{\varepsilon}t\right)*\left\{\mathbf{grad}\operatorname{div}\mathbf{j}_s(\mathbf{x},t)+\frac{\partial}{\partial t}\mathbf{grad}\operatorname{div}\mathbf{d}_s(\mathbf{x},t)\right\},&\qquad\text{(A2.4a)}\end{aligned}$$

and

$$\begin{aligned}\nabla^2\mathbf{h}(\mathbf{x},t)-\sigma\mu\frac{\partial\mathbf{h}(\mathbf{x},t)}{\partial t}-\varepsilon\mu\frac{\partial^2\mathbf{h}(\mathbf{x},t)}{\partial t^2}&\\ =-\mathbf{curl}\,\mathbf{j}_s(\mathbf{x},t)+\sigma\frac{\partial\mathbf{b}_s(\mathbf{x},t)}{\partial t}+\varepsilon\frac{\partial^2\mathbf{b}_s(\mathbf{x},t)}{\partial t^2}-\frac{1}{\mu}\mathbf{grad}\operatorname{div}\mathbf{b}_s(\mathbf{x},t)-\frac{\partial\,\mathbf{curl}\,\mathbf{d}_s(\mathbf{x},t)}{\partial t}\,.&\qquad\text{(A2.4b)}\end{aligned}$$

These are uncoupled three-dimensional (3D) inhomogeneous partial differential equations for the electric and magnetic field vectors. Ward and Hohmann (1987, page 136) give homogeneous (i.e., vanishing right side) versions of these expressions.

Compared to the first-order EH system (A1.3a and b), the second-order PDEs (A2.4a and b) exhibit greater complexity in the inhomogeneous terms representing body sources of EM waves. In particular, all three medium parameters appear, and various terms contain higher-order space and time (and even mixed) partial derivatives. There is also a temporal convolution.

The PDEs may be re-written in terms of a wavespeed c_∞ and a "transition" angular frequency ω_t defined as

$$c_\infty \equiv 1/\sqrt{\varepsilon\mu}\,, \qquad \omega_t \equiv \sigma/\varepsilon\,, \tag{A2.5a,b}$$

respectively. Thus

$$\begin{aligned}\nabla^2\mathbf{e}(\mathbf{x},t) - \frac{\omega_t}{c_\infty^2}\frac{\partial\,\mathbf{e}(\mathbf{x},t)}{\partial t} - \frac{1}{c_\infty^2}\frac{\partial^2\mathbf{e}(\mathbf{x},t)}{\partial t^2} \\ = \mu\frac{\partial\,\mathbf{j}_s(\mathbf{x},t)}{\partial t} + \frac{\partial\,\mathbf{curl}\,\mathbf{b}_s(\mathbf{x},t)}{\partial t} + \mu\frac{\partial^2\mathbf{d}_s(\mathbf{x},t)}{\partial t^2} \\ - \mu c_\infty^2 H(t)\exp(-\omega_t t) * \left\{\mathbf{grad}\ \mathrm{div}\ \mathbf{j}_s(\mathbf{x},t) + \frac{\partial}{\partial t}\mathbf{grad}\ \mathrm{div}\ \mathbf{d}_s(\mathbf{x},t)\right\},\end{aligned} \tag{A2.6a}$$

and

$$\begin{aligned}\nabla^2\mathbf{h}(\mathbf{x},t) - \frac{\omega_t}{c_\infty^2}\frac{\partial\,\mathbf{h}(\mathbf{x},t)}{\partial t} - \frac{1}{c_\infty^2}\frac{\partial^2\mathbf{h}(\mathbf{x},t)}{\partial t^2} \\ = -\mathbf{curl}\,\mathbf{j}_s(\mathbf{x},t) - \frac{1}{\mu}\left[\mathbf{grad}\ \mathrm{div}\,\mathbf{b}_s(\mathbf{x},t) - \frac{\omega_t}{c_\infty^2}\frac{\partial\,\mathbf{b}_s(\mathbf{x},t)}{\partial t} - \frac{1}{c_\infty^2}\frac{\partial^2\mathbf{b}_s(\mathbf{x},t)}{\partial t^2}\right] - \frac{\partial\,\mathbf{curl}\,\mathbf{d}_s(\mathbf{x},t)}{\partial t}\,.\end{aligned} \tag{A2.6b}$$

It will become apparent that c_∞ is the phase speed of the infinite frequency plane wave Fourier component. Moreover, ω_t is an angular frequency that (roughly) corresponds to the transition from EM diffusion (for $\omega < \omega_t$) to EM wave propagation (for $\omega > \omega_t$). The remaining parameter in (A2.6a,b) is the magnetic permeability μ, which occurs only in conjunction with body source terms.

A3.0 One-Dimensional Plane Waves

Assume that all medium parameters, body sources, and wavefield variables depend only on the single space coordinate z. Partial derivatives with respect to x and y vanish. Then, in Cartesian coordinates, the six PDEs of the first-order EH system (A1.3a and b) are written as

$$\varepsilon(z)\frac{\partial\,e_x(z,t)}{\partial t} + \sigma(z)e_x(z,t) + \frac{\partial h_y(z,t)}{\partial z} = -j_{sx}(z,t) - \frac{\partial d_{sx}(z,t)}{\partial t}\,, \tag{A3.1a}$$

$$\mu(z)\frac{\partial\,h_y(z,t)}{\partial t} + \frac{\partial e_x(z,t)}{\partial z} = -\frac{\partial b_{sy}(z,t)}{\partial t}\,, \tag{A3.1b}$$

and

$$\varepsilon(z)\frac{\partial\,e_y(z,t)}{\partial t} + \sigma(z)e_y(z,t) - \frac{\partial h_x(z,t)}{\partial z} = -j_{sy}(z,t) - \frac{\partial d_{sy}(z,t)}{\partial t}\,, \tag{A3.2a}$$

$$\mu(z)\frac{\partial\,h_x(z,t)}{\partial t} - \frac{\partial e_y(z,t)}{\partial z} = -\frac{\partial b_{sx}(z,t)}{\partial t}\,, \tag{A3.2b}$$

and

$$\varepsilon(z)\frac{\partial\,e_z(z,t)}{\partial t} + \sigma(z)e_z(z,t) = -j_{sz}(z,t) - \frac{\partial d_{sz}(z,t)}{\partial t}\,, \tag{A3.3a}$$

$$\mu(z)\frac{\partial h_z(z,t)}{\partial t} = -\frac{\partial b_{sz}(z,t)}{\partial t}. \tag{A3.3b}$$

The particular grouping of the equations facilitates subsequent analysis. The mathematical structure of system (A3.1) (containing e_x and h_y) and is identical to that of system (A3.2) containing (e_y and h_x). Hence, in the present study, we choose to work with the first system (A3.1). The third system (A3.3) indicates that the e_z and h_z components of the field vectors are activated independently in this one-dimensional (1D) situation. It is straightforward to demonstrate that the solutions are

$$e_z(z,t) = -\frac{1}{\varepsilon(z)}\exp\left(-\omega_t(z)t\right)H(t) * \left[j_{sz}(z,t) + \frac{\partial d_{sz}(z,t)}{\partial t} \right],$$

and

$$h_z(z,t) = -\frac{1}{\mu(z)} b_{sz}(z,t),$$

respectively. The asterisk denotes temporal convolution and $H(t)$ is the Heaviside unit step function. $\omega_t(z) = \sigma(z)/\varepsilon(z)$ is the depth-dependent transition angular frequency. Thus, the e_z and h_z components are coincident in depth z with the 1D body source terms. For vanishing z-component body sources, which we assume in this study, both components must also vanish. Hence, we are left with the first-order system (A3.1a and b).

Next, assume a homogeneous electromagnetic medium with $\varepsilon(z) = \varepsilon$, $\mu(z) = \mu$, and $\sigma(z) = \sigma$. Then, equations (A3.1a and b) may be combined to yield the two separated second-order PDEs

$$\frac{\partial^2 e_x(z,t)}{\partial z^2} - \sigma\mu\frac{\partial e_x(z,t)}{\partial t} - \varepsilon\mu\frac{\partial^2 e_x(z,t)}{\partial t^2} = \mu\frac{\partial j_{sx}(z,t)}{\partial t} + \mu\frac{\partial^2 d_{sx}(z,t)}{\partial t^2} - \frac{\partial^2 b_{sy}(z,t)}{\partial z \partial t}, \tag{A3.4a}$$

and

$$\frac{\partial^2 h_y(z,t)}{\partial z^2} - \sigma\mu\frac{\partial h_y(z,t)}{\partial t} - \varepsilon\mu\frac{\partial^2 h_y(z,t)}{\partial t^2} = -\frac{\partial j_{sx}(z,t)}{\partial z} - \frac{\partial^2 d_{sx}(z,t)}{\partial z \partial t} + \varepsilon\frac{\partial^2 b_{sy}(z,t)}{\partial t^2} + \sigma\frac{\partial b_{sy}(z,t)}{\partial t}, \tag{A3.4b}$$

governing the x-component of the electric vector and the y-component of the magnetic vector, respectively. The left hand sides are identical, whereas body source terms on the right hand sides differ. As expected, the exact same equations are obtained by specializing the second-order PDEs (A2.4a and b) to the one spatial dimension z. Although each equation may be solved independently, it is often simpler to solve (A3.4a) for the electric vector component, and then use the 1D form of Faraday's law (A3.1b) to obtain the derivative $\partial h_y / \partial t$.

In terms of the transition frequency ω_t and infinite frequency phase speed c_∞, PDEs (A3.4a and b) become

$$\frac{\partial^2 e_x(z,t)}{\partial z^2} - \frac{\omega_t}{c_\infty^2}\frac{\partial e_x(z,t)}{\partial t} - \frac{1}{c_\infty^2}\frac{\partial^2 e_x(z,t)}{\partial t^2} = \mu\frac{\partial j_{sx}(z,t)}{\partial t} + \mu\frac{\partial^2 d_{sx}(z,t)}{\partial t^2} - \frac{\partial^2 b_{sy}(z,t)}{\partial z \partial t}, \tag{A3.5a}$$

and

$$\frac{\partial^2 h_y(z,t)}{\partial z^2} - \frac{\omega_t}{c_\infty^2}\frac{\partial h_y(z,t)}{\partial t} - \frac{1}{c_\infty^2}\frac{\partial^2 h_y(z,t)}{\partial t^2} = -\frac{\partial j_{sx}(z,t)}{\partial z} - \frac{\partial^2 d_{sx}(z,t)}{\partial z \partial t} + \varepsilon\frac{\partial^2 b_{sy}(z,t)}{\partial t^2} + \sigma\frac{\partial b_{sy}(z,t)}{\partial t}. \quad \text{(A3.5b)}$$

Perhaps a wave propagation geophysicist would be more inclined to write the two PDEs in this particular form. For $\omega_t = 0$ (corresponding to vanishing conductivity $\sigma = 0$), the expressions reduce to (inhomogeneous) scalar wave equations. Expression (A3.4) or (A3.5) correspond to plane electromagnetic wave propagation in the $\pm z$-directions.

A4.0 Frequency-Domain Equations

Mathematical theory in electromagnetism is often facilitated by transforming to the frequency-domain. The definition of the forward Fourier transform, from time t to angular frequency ω, used in this study is

$$E_x(z,\omega) = \int_{-\infty}^{+\infty} e_x(z,t)\, e^{+i\omega t} dt. \quad \text{(A4.1)}$$

An upper case letter denotes the Fourier transform of the lower case counterpart. Definition (A4.1) implies the differentiation theorem

$$\frac{\partial e_x(z,t)}{\partial t} \leftrightarrow (-i\omega) E_x(z,\omega),$$

where the double-headed arrow signifies Fourier transform pairing.

A4.1 Helmholtz Equation

Fourier transforming PDE (A3.5a) yields the inhomogeneous Helmholtz equation (an *ordinary* differential equation or ODE):

$$\frac{d^2 E_x(z,\omega)}{dz^2} + K(\omega)^2 E_x(z,\omega) = \mu(-i\omega) J_{sx}(z,\omega) + \mu(-i\omega)^2 D_{sx}(z,\omega) - (-i\omega)\frac{dB_{sy}(z,\omega)}{dz}, \quad \text{(A4.2)}$$

where the squared *complex wavenumber* is given by

$$K(\omega)^2 = \frac{\omega^2 + i\omega_t\omega}{c_\infty^2} = \varepsilon\mu\omega^2 + i\sigma\mu\omega. \quad \text{(A4.3)}$$

Recall that the infinite-frequency phase speed c_∞ and transition frequency ω_t are defined by

$$c_\infty = \frac{1}{\sqrt{\varepsilon\mu}}, \qquad \omega_t = \frac{\sigma}{\varepsilon}, \quad \text{(A2.5a,b again)}$$

respectively. The transition frequency separates (roughly) the frequency ranges for electromagnetic wave diffusion ($|\omega| << \omega_t$) and electromagnetic wave propagation ($|\omega| >> \omega_t$). Equation (A4.3) is often referred to as the *dispersion relation* for EM wave propagation.

The general solution of Helmholtz equation (A4.2) consists of i) the general solution of the homogeneous version (i.e., with vanishing right-hand-side), plus ii) any particular solution of the inhomogeneous version. The homogeneous Helmholtz equation is

$$\frac{d^2 E_x(z,\omega)}{dz^2} + K(\omega)^2 E_x(z,\omega) = 0, \tag{A4.4}$$

with general solution on a finite interval $z_1 \le z \le z_2$ given by

$$E_x(z,\omega) = A(\omega)e^{+iK(\omega)z} + B(\omega)e^{-iK(\omega)z}. \tag{A4.5}$$

$A(\omega)$ and $B(\omega)$ are complex-valued constants (depending only on frequency ω) that are determined by prescribing boundary conditions on the electric vector.

Suppose values of the electric vector at the two endpoints are prescribed. Then

$$A(\omega) = \frac{E_x(z_2,\omega)e^{-iK(\omega)z_1} - E_x(z_1,\omega)e^{-iK(\omega)z_2}}{2\sinh\left[iK(\omega)(z_2 - z_1)\right]}, \qquad B(\omega) = \frac{E_x(z_1,\omega)e^{+iK(\omega)z_2} - E_x(z_2,\omega)e^{+iK(\omega)z_1}}{2\sinh\left[iK(\omega)(z_2 - z_1)\right]},$$

Where the hyperbolic sine of a complex number $Z = X+iY$ is $\sinh(Z) = \left(e^{+Z} - e^{-Z}\right)/2$. The general solution becomes

$$E_x(z,\omega) = E_x(z_1,\omega)\left[\frac{e^{-iK(\omega)(z_2 - z)} - e^{+iK(\omega)(z_2 - z)}}{e^{-iK(\omega)(z_2 - z_1)} - e^{+iK(\omega)(z_2 - z_1)}}\right] + E_x(z_2,\omega)\left[\frac{e^{-iK(\omega)(z - z_1)} - e^{+iK(\omega)(z - z_1)}}{e^{-iK(\omega)(z_2 - z_1)} - e^{+iK(\omega)(z_2 - z_1)}}\right]. \tag{A4.6a}$$

We re-write this in the seemingly more complicated form

$$E_x(z,\omega) = E_x(z_1,\omega)e^{+iK(\omega)(z - z_1)}\left[\frac{1 - e^{+iK(\omega)2(z_2 - z)}}{1 - e^{+iK(\omega)2(z_2 - z_1)}}\right] + E_x(z_2,\omega)e^{+iK(\omega)(z_2 - z)}\left[\frac{1 - e^{+iK(\omega)2(z - z_1)}}{1 - e^{+iK(\omega)2(z_2 - z_1)}}\right]. \tag{A4.6b}$$

The value of this re-formulation will become evident by considering the following two cases:

Case 1: $z_2 \to +\infty$. Then, since the complex wavenumber $K(\omega)$ has a positive imaginary part, $e^{+iK(\omega)z_2} \to 0$ (this will be demonstrated in the next sub-section). We have

$$E_x(z,\omega) = E_x(z_1,\omega)e^{+iK(\omega)(z - z_1)}. \tag{A4.7a}$$

This corresponds to plane wave propagation in the +z direction. The boundary condition prescribed at endpoint z_2 is "infinitely far away" and has no influence on the solution.

Case 2: $z_1 \to -\infty$. Then $e^{-iK(\omega)z_1} \to 0$ and we have

$$E_x(z,\omega) = E_x(z_2,\omega)e^{+iK(\omega)(z_2-z)}. \tag{A4.7b}$$

This corresponds to plane wave propagation in the −*z* direction. The boundary condition prescribed at endpoint z_1 is also "infinitely far away" and has no influence on the solution.

The mathematical "tag" identifying plane wave propagation in the + or – *z*-directions is the sign of coordinate *z* in the exponents of equations (A4.7a and b). A physical requirement of plane electromagnetic wave propagation is that attenuation (associated with the imaginary part of the complex wavenumber $K(\omega)$) must always "accumulate" (implying amplitude diminishes) for *either* propagation direction. This is achieved by *z increasing* in (A4.6a) (implying $(z-z_1)$ gets larger) and *z decreasing* in (A4.6b) (implying (z_2-z) gets larger). We repeatedly use this rule in the main text in developing the reflection and transmission responses of a geologic layer, even when plane wave propagation intervals are not semi-infinite.

A4.2 Phase Speed and Attenuation Factor

Following Aki and Richards (1980, equation (5.71) on page 172), the *phase speed* $c(\omega)$ and *attenuation factor* $\alpha(\omega)$ are defined in terms of the real and imaginary parts of the complex wavenumber as

$$K(\omega) = \frac{\omega}{c(\omega)} + i\alpha(\omega). \tag{A4.8}$$

The complex wavenumber must be anti-Hermitian (i.e., $K(-\omega) = -K(\omega)^*$) in order that the Fourier-transformed electric vector component $E_x(z,\omega) = E_x(0,\omega)\exp\left[\pm iK(\omega)z\right]$ is Hermitian. (i.e., $E_x(z,-\omega) = E_x(z,\omega)^*$). This is a requirement for the time-domain electric vector $e_x(z,t)$ to be real-valued (see Bracewell, 1965, page 178). Hence, the phase speed and attenuation factors are even functions of angular frequency. The frequency-domain solution form can be written as

$$E_x(z,\omega) = E_x(0,\omega)\exp\left[\pm i\omega\frac{z}{c(\omega)}\right]\exp\left[\mp\alpha(\omega)z\right]. \tag{A4.9}$$

The plane wave electric field vector advances with speed $c(\omega)$ in the ±*z*-directions, and its amplitude diminishes exponentially with distance according to the factor $\alpha(\omega)$. Upper and lower signs are used for +*z*-direction propagation (where coordinate *z* increases) and –*z*-direction propagation (where *z* decreases), respectively. The phase speed and attenuation factor are positive (or non-negative at non-zero frequency) and even functions of angular frequency. Clearly, the amplitude of the Fourier component will decay by the amount $1/e \approx 0.37$ in a distance $\delta(\omega) = 1/\alpha(\omega)$. Distance $\delta(\omega)$ is referred to as the *skin depth*.

Explicit expressions for the phase speed and attenuation factor in terms of angular frequency are readily derived. Squaring expression (A4.8) for the complex wavenumber gives

$$K(\omega^2) = \left[\frac{\omega^2}{c(\omega)^2} - \alpha(\omega)^2\right] + i\left[\frac{2\omega\alpha(\omega)}{c(\omega)}\right],$$

and this must equal (from the dispersion relation (A4.3))

$$K(\omega)^2 = \frac{\omega^2}{c_\infty^2} + i\frac{\omega_t \omega}{c_\infty^2}.$$

Equating real and imaginary parts gives a pair of nonlinear algebraic equations for $c(\omega)$ and $\alpha(\omega)$:

$$\frac{\omega^2}{c(\omega)^2} - \alpha(\omega)^2 = \frac{\omega^2}{c_\infty^2}, \qquad \frac{2\omega\alpha(\omega)}{c(\omega)} = \frac{\omega_t \omega}{c_\infty^2}.$$

Interestingly, the second expression implies that the attenuation factor is directly proportional to the phase speed: $\alpha(\omega) = \left(\omega_t / 2c_\infty^2\right) c(\omega)$. Solving for each yields

$$\frac{c(\omega)}{c_\infty} = \sqrt{\frac{2|\omega|}{\omega_t}} \left[\sqrt{1 + \left(\frac{\omega}{\omega_t}\right)^2} - \frac{|\omega|}{\omega_t} \right]^{1/2}, \qquad \text{(A4.10a)}$$

and

$$\frac{\alpha(\omega)}{\alpha_\infty} = \sqrt{\frac{2|\omega|}{\omega_t}} \left[\sqrt{1 + \left(\frac{\omega}{\omega_t}\right)^2} - \frac{|\omega|}{\omega_t} \right]^{1/2}, \qquad \text{(A4.10b)}$$

where $\alpha_\infty \equiv \omega_t / 2c_\infty$. These expressions are appropriate for non-zero conductivity σ (implying non-zero transition frequency ω_t). If conductivity vanishes, then we have $c(\omega) = c_\infty$ and $\alpha(\omega) = 0$. The common right-hand-side of (4.10a and b) is consistent with the functional form given in Løseth et al. (2006)).

Limiting values of the phase speed are

$$c(0) = 0, \qquad c(+\infty) = c_\infty = \frac{1}{\sqrt{\varepsilon\mu}}.$$

This justifies using the symbol c_∞ for $1/\sqrt{\varepsilon\mu}$. The analogous limiting values of the attenuation factor are

$$\alpha(0) = 0, \qquad \alpha(+\infty) = \alpha_\infty = \frac{\omega_t}{2c_\infty} = \frac{\sigma}{2}\sqrt{\frac{\mu}{\varepsilon}}.$$

α_∞ is referred to as the *infinite-frequency attenuation factor*. At the transition frequency $\omega = \omega_t$, we have

$$\frac{c(\omega_t)}{c_\infty} = \frac{a(\omega_t)}{a_\infty} = \sqrt{2\left(\sqrt{2} - 1\right)} \approx 0.910.$$

Thus, the phase speed and attenuation factor achieve about 91% of their infinite-frequency values at the transition frequency. For small values of dimensionless angular frequency $|\omega|/\omega_t << 1$, the above expression (A4.10a or b) for phase speed/attenuation factor is expanded to first order, yielding

$$\frac{c(\omega)}{c_\infty} = \frac{\alpha(\omega)}{\alpha_\infty} \approx \sqrt{\frac{2|\omega|}{\omega_t}}\,. \tag{A4.11}$$

This square root dependence on frequency is appropriate for a diffusion process. Substituting the expressions for c_∞, α_∞, and ω_t gives the equivalent forms

$$c(\omega) \approx \sqrt{\frac{2|\omega|}{\sigma\mu}}\,, \qquad \alpha(\omega) \approx \sqrt{\frac{\sigma\mu|\omega|}{2}}\,. \tag{A4.12a,b}$$

For low frequencies, phase speed and attenuation factor are independent of the electric permittivity ε of the medium.

For large values $|\omega|/\omega_t >> 1$, the expansion is

$$\frac{c(\omega)}{c_\infty} = \frac{\alpha(\omega)}{\alpha_\infty} \approx 1 - \frac{1}{8}\left(\frac{\omega_t}{\omega}\right)^2, \tag{A4.13}$$

which clearly indicates the two limiting values $c(+\infty) = c_\infty$ and $\alpha(+\infty) = \alpha_\infty$.

The explicit functional forms of equations (A4.10a and b) are useful for determining limiting values and understanding dependencies on parameters, etc. However, for numerical evaluation purposes, phase speed and attenuation factor are conveniently obtained from the real and imaginary parts of the complex wavevector $K(\omega)$ of equation (A4.8) as:

$$c(\omega) = \frac{\omega}{\mathrm{Re}\{K(\omega)\}}, \qquad \alpha(\omega) = \mathrm{Im}\{K(\omega)\}. \tag{A4.14a,b}$$

A low-frequency approximation to the complex wavenumber is readily assembled from the phase speed and attenuation factor approximations as

$$K(\omega) \approx \frac{\omega_t}{c_\infty}\sqrt{\frac{|\omega|}{\omega_t}}\left[\frac{\mathrm{sgn}(\omega) + i\left(1-\delta_0(\omega)\right)}{\sqrt{2}}\right] = \sqrt{\sigma\mu|\omega|}\left[\frac{\mathrm{sgn}(\omega) + i\left(1-\delta_0(\omega)\right)}{\sqrt{2}}\right]$$
$$= \sqrt{\sigma\mu|\omega|}\,\mathrm{sgn}(\omega)e^{+i\frac{\pi}{4}\mathrm{sgn}(\omega)}, \tag{A4.15}$$

where $\mathrm{sgn}(\omega)$ is the sign function (= $\omega/|\omega|$ for $\omega \neq 0$, zero otherwise) and $\delta_0(\omega)$ is the null function (= 0 for $\omega \neq 0$, one otherwise) (Bracewell, 1965). Note that this approximation is Hermitian anti-symmetric (i.e., real part odd and imaginary part even) as required. The low-frequency approximation is independent of the electric permittivity ε.

Finally, a high-frequency approximation to the complex wavenumber is

$$K(\omega) \approx \frac{\omega}{c_\infty} + i\alpha_\infty = \sqrt{\varepsilon\mu}\left(\omega + i\frac{\sigma}{2\varepsilon}\right). \tag{A4.16}$$

Retaining a non-zero imaginary part in the approximation enables attenuation of a propagating high-frequency EM wave. Otherwise, vanishing conductivity $\sigma = 0$ implies the complex wavenumber is $K(\omega) = \omega/c_\infty$ (i.e., pure real) appropriate for wave propagation without attenuation and dispersion.

A4.3 Group Speed

Group speed $g(\omega)$ is obtained from the phase speed $c(\omega)$ via the formula

$$g(\omega) = \frac{c(\omega)}{1 - \dfrac{\omega}{c(\omega)}\dfrac{\partial c(\omega)}{\partial \omega}}. \tag{A4.17}$$

Then, from the above phase speed expression, we have

$$\frac{1}{1 - \dfrac{\omega}{c(\omega)}\dfrac{\partial c(\omega)}{\partial \omega}} = 2\sqrt{1+\left(\frac{\omega}{\omega_t}\right)^2}\left[\sqrt{1+\left(\frac{\omega}{\omega_t}\right)^2} - \frac{|\omega|}{\omega_t}\right].$$

Hence, the explicit expression for group speed is

$$\frac{g(\omega)}{c_\infty} = 2\sqrt{\frac{2|\omega|}{\omega_t}}\sqrt{1+\left(\frac{\omega}{\omega_t}\right)^2}\left[\sqrt{1+\left(\frac{\omega}{\omega_t}\right)^2} - \frac{|\omega|}{\omega_t}\right]^{3/2}, \tag{A4.18}$$

with specific values

$$g(0) = 0, \qquad g(\omega_t) = 4\left(\sqrt{2}-1\right)^{3/2} c_\infty \approx 1.066 c_\infty, \qquad g(\infty) = c_\infty.$$

Low-frequency and high-frequency expansions are

$$\frac{g(\omega)}{c_\infty} \approx 2\sqrt{\frac{2|\omega|}{\omega_t}}, \qquad \frac{g(\omega)}{c_\infty} \approx 1 + \frac{1}{2}\left(\frac{\omega_t}{\omega}\right)^2, \tag{A4.19a,b}$$

respectively. At low frequencies, group speed is exactly *twice* the phase speed (see equation (A4.11) above). Interestingly, the high frequency approximation indicates that group speed $g(\omega)$ *exceeds* the infinite frequency phase speed c_∞ (in contrast with the analogous situation for phase speed $c(\omega)$).

For numerical calculations, group speed may be obtained from the derivative of the complex wavenumber via

$$g(\omega) = \frac{1}{\mathrm{Re}\{dK(\omega)/d\omega\}}, \tag{A4.20}$$

as in Aldridge (2013) for seismic wave propagation.

A4.4 Quality Factor

The *quality factor* function $Q(\omega)$ is another diagnostic frequency function for wave propagation problems (although it is much more common in seismics than in electromagnetics). Quality factor may be written as a combination of phase speed and attenuation factor as

$$Q(\omega) = \frac{1}{2}\left[\frac{\omega}{c(\omega)\alpha(\omega)} - \frac{c(\omega)\alpha(\omega)}{\omega} \right], \tag{A4.21}$$

(O'Connell and Budiansky, 1978). Since phase speed and attenuation factor are *even* functions of frequency, the quality factor is an *odd* function of frequency. Substituting expressions (A4.10a and b) for $c(\omega)$ and $\alpha(\omega)$ and engaging in some algebraic manipulation yields the remarkably simple result

$$Q(\omega) = \frac{\omega}{\omega_t}. \tag{A4.22}$$

The quality factor for electromagnetic wave propagation is a linear function of frequency which vanishes at DC. At the transition frequency $\omega_t = \sigma/\varepsilon$, quality factor equals unity.

In the special case of a vacuum where the medium conductivity σ vanishes, then the transition angular frequency $\omega_t = 0$. The phase and group speeds are independent of frequency and equal c_∞. The attenuation factor vanishes and the quality factor is infinite. Substitution of the low-frequency approximations (A4.12a and b) for the phase speed and attenuation factor into the quality factor definition yields $Q(f) \approx 0$, which is characteristic of a diffusion process (e.g., Aldridge, 2013).

Figure A1 displays curves of phase speed, attenuation factor, group speed and quality factor as functions of dimensionless frequency f / f_t, for an electromagnetic medium defined by the parameter values:

relative electric permittivity $\varepsilon/\varepsilon_0 = 10.0$,

relative magnetic permeability $\mu/\mu_0 = 1.0$,

current conductivity $\sigma = 0.01$ (A/V)/m = S/m .

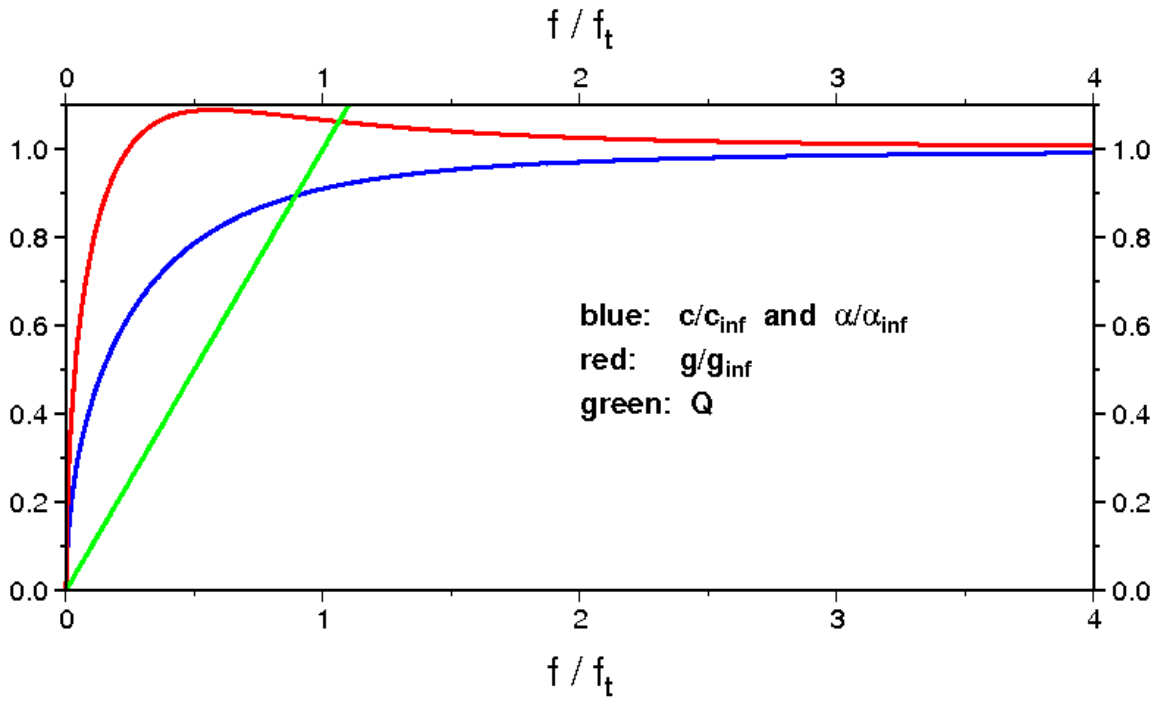

Figure A1. Diagnostic frequency functions for electromagnetic wave propagation, plotted with respect to dimensionless frequency f / f_t. **Blue** curve is phase speed $c(f)$ and attenuation factor $\alpha(f)$, normalized by the respective infinite frequency values. **Red** curve is group speed $g(f)$, also normalized by the infinite frequency value. **Green** curve (linear with frequency) is quality factor $Q(f) = f / f_t$.

Phase speed, attenuation factor, and group speed are normalized by their respective infinite frequency values. With this normalization, phase speed and attenuation factor curves are identical, and thus are plotted as the single **blue** curve. For large values of frequency, the dimensionless phase and group speed curves approach unity (from below and above) implying that the physical phase and group speeds approach $c_\infty = 1/\sqrt{\varepsilon\mu} = 9.480 \times 10^7$ m/s . This is about 31.6% of the speed of electromagnetic waves in a vacuum ($c_{vac} = 1/\sqrt{\varepsilon_0 \mu_0} = 2.998 \times 10^8$ m/s). Group speed exceeds the asymptotic limit by about 8.9% at $0.58 f_t$. The transition frequency is f_t = 1.798 × 10^7 Hz (or about 18 MHz). Quality factor equals unity at this frequency, and phase speed, group speed, and attenuation factor are (roughly) constant above f_t , corresponding to wavelike propagation. The infinite frequency attenuation factor is α_∞ = 0.596 m^{-1}.

The electromagnetic spectral range used in geophysical exploration is typically much lower than the transition frequency f_t . Hence, Figure A2 depicts normalized phase speed, attenuation factor, and group speed *vs*. frequency from DC up to 10 kilohertz. These curves, calculated via the exact formulae, are indistinguishable from the approximations (A4.12a and b) over this low frequency range. Quality factor is nearly zero, indicating that EM propagation is almost perfectly diffusive.

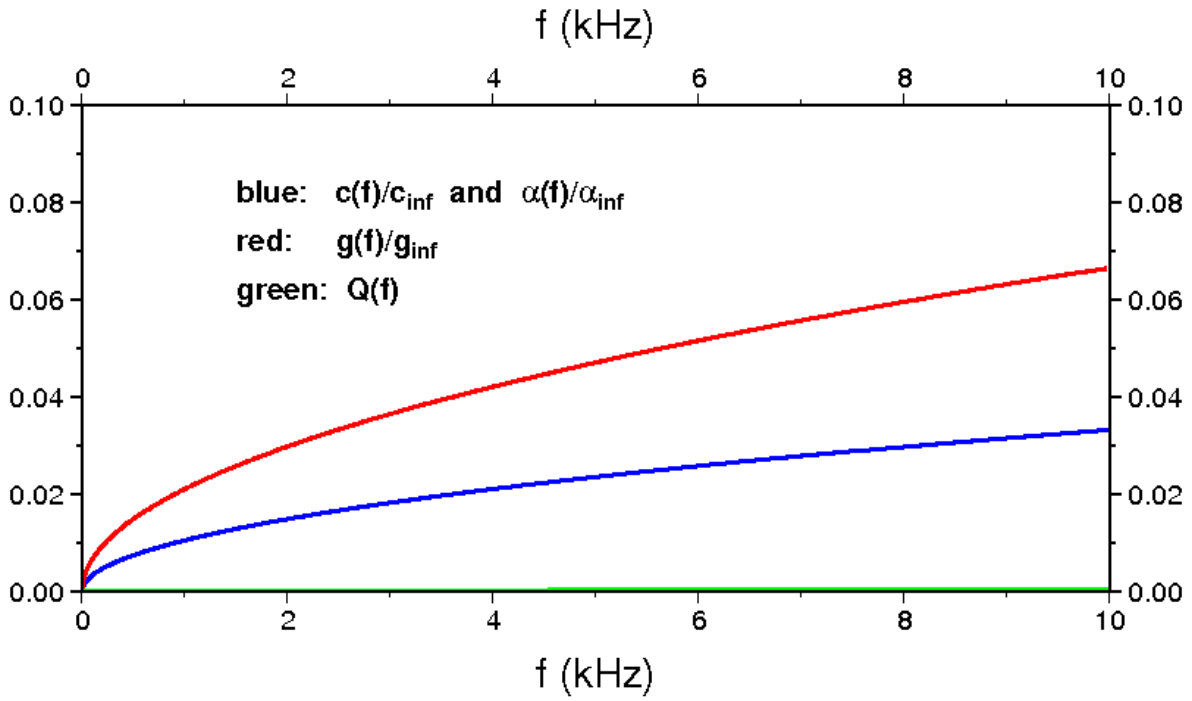

Figure A2. Diagnostic frequency functions for electromagnetic wave propagation, plotted with respect to physical frequency *f* in kilohertz. **Blue** curve is phase speed $c(f)$ and attenuation factor $\alpha(f)$, normalized by the respective infinite frequency values. **Red** curve is group speed $g(f)$, also normalized by the infinite frequency value. **Green** curve (linear with frequency) is quality factor $Q(f)$.

11.0 APPENDIX B: REFLECTION AND TRANSMISSION COEFFICIENTS

B1.0 Derivation

Figure B1 below depicts the geometric framework used for deriving expressions for normal incidence plane wave reflection and transmission coefficients. Medium #1 (characterized by homogeneous and isotropic EM parameters ε_1, μ_1, σ_1) is separated from medium #2 (ε_2, μ_2, σ_2) by a plane horizontal interface located at level $z = z_{int}$. A plane EM wave is incident onto the interface from medium #1; this gives rise to reflected (in medium #1) and transmitted (in medium #2) plane waves.

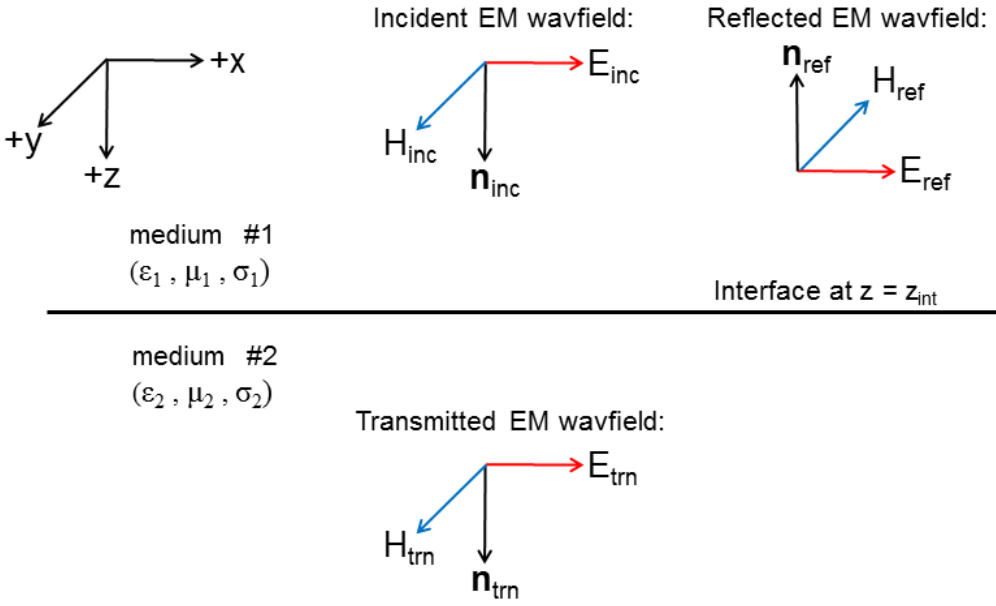

Figure B1. Geometric setup of the normal incidence plane wave reflection / transmission problem. Unit propagation direction vectors of the plane wavefronts are $\mathbf{n}_{inc} = \mathbf{n}_{trn} = +\mathbf{e}_z$ and $\mathbf{n}_{ref} = -\mathbf{e}_z$.

Incident, reflected, and transmitted electric fields are given by

$$\mathbf{E}_{inc}(z,\omega) = \mathbf{e}_x E_{inc}(z_s,\omega) e^{+iK_1(\omega)(z-z_s)}, \tag{B1a}$$

$$\mathbf{E}_{ref}(z,\omega) = \mathbf{e}_x E_{ref}(z_{\text{int}},\omega) e^{+iK_1(\omega)(z_{\text{int}}-z)}, \tag{B1b}$$

$$\mathbf{E}_{trn}(z,\omega) = \mathbf{e}_x E_{trn}(z_{\text{int}},\omega) e^{+iK_2(\omega)(z-z_{\text{int}})}. \tag{B1c}$$

Note that the reflected plane electric wave propagates in the –z direction. The associated incident, reflected, and transmitted magnetic fields are calculated from the Faraday law via

$$\mathbf{H}(z,\omega) = \frac{1}{i\omega\mu}\mathbf{curl}\,\mathbf{E}(z,\omega) = \mathbf{e}_y \frac{1}{i\omega\mu}\frac{\partial E_x(z,\omega)}{\partial z}. \tag{B2}$$

Hence, we obtain

$$\mathbf{H}_{inc}(z,\omega) = \mathbf{e}_y \frac{K_1(\omega)}{\mu_1 \omega} E_{inc}(z_s,\omega) e^{+iK_1(\omega)(z-z_s)}, \tag{B3a}$$

$$\mathbf{H}_{ref}(z,\omega) = -\mathbf{e}_y \frac{K_1(\omega)}{\mu_1 \omega} E_{ref}(z_{\text{int}},\omega) e^{+iK_1(\omega)(z_{\text{int}}-z)}, \tag{B3b}$$

$$\mathbf{H}_{trn}(z,\omega) = \mathbf{e}_y \frac{K_2(\omega)}{\mu_2 \omega} E_{trn}(z_{\text{int}},\omega) e^{+iK_2(\omega)(z-z_{\text{int}})}. \tag{B3c}$$

Note that the polarity of the reflected magnetic vector component is reversed with respect to the incident magnetic vector component (and this is depicted in Figure B1).

At the interface, the tangential components of both the electric and magnetic vectors must be continuous:

$$E_x(z_{\text{int}},\omega)\big|_{\text{medium1}} = E_x(z_{\text{int}},\omega)\big|_{\text{medium2}} \qquad \text{and} \qquad H_y(z_{\text{int}},\omega)\big|_{\text{medium1}} = H_y(z_{\text{int}},\omega)\big|_{\text{medium2}}.$$

Then, substituting from the above expressions yields

$$E_{inc}(z_{\text{int}},\omega) + E_{ref}(z_{\text{int}},\omega) = E_{trn}(z_{\text{int}},\omega), \tag{B4a}$$

$$\frac{K_1(\omega)}{\mu_1 \omega} E_{inc}(z_{\text{int}},\omega) - \frac{K_1(\omega)}{\mu_1 \omega} E_{ref}(z_{\text{int}},\omega) = \frac{K_2(\omega)}{\mu_2 \omega} E_{trn}(z_{\text{int}},\omega), \tag{B4b}$$

where the incident *x*-component of the electric vector at the horizontal interface $z = z_{\text{int}}$ is defined as

$$E_{inc}(z_{\text{int}},\omega) = E_{inc}(z_s,\omega) e^{+iK_1(\omega)(z_{\text{int}}-z_s)}. \tag{B5}$$

These two wavefield continuity conditions are re-written in matrix/vector form as

$$\begin{bmatrix} +1 & -1 \\ K_1(\omega)/\mu_1 & K_2(\omega)/\mu_2 \end{bmatrix} \begin{bmatrix} E_{ref}(z_{\text{int}},\omega) \\ E_{trn}(z_{\text{int}},\omega) \end{bmatrix} = \begin{bmatrix} -E_{inc}(z_{\text{int}},\omega) \\ \left(K_1(\omega)/\mu_1\right) E_{inc}(z_{\text{int}},\omega) \end{bmatrix}, \tag{B6}$$

where a common divisor by angular frequency ω has been canceled from the second equation. Next, we define the *reflection coefficient* $R(\omega)$ and *transmission coefficient* $T(\omega)$ as

$$R(\omega) \equiv E_{ref}(z_{\text{int}},\omega)/E_{inc}(z_{\text{int}},\omega) \qquad \text{and} \qquad T(\omega) \equiv E_{trn}(z_{\text{int}},\omega)/E_{inc}(z_{\text{int}},\omega). \tag{B7a,b}$$

Then, the above matrix/vector equation is put into the form

$$\begin{bmatrix} +1 & -1 \\ +1 & \dfrac{\mu_1 K_2(\omega)}{\mu_2 K_1(\omega)} \end{bmatrix} \begin{bmatrix} R(\omega) \\ T(\omega) \end{bmatrix} = \begin{bmatrix} -1 \\ +1 \end{bmatrix}. \tag{B8}$$

The determinant of the 2 × 2 coefficient matrix is $\Delta(\omega) = 1 + \mu_1 K_2(\omega)/\mu_2 K_1(\omega)$, which is non-zero. Hence, the reflection and transmission coefficient solutions are

$$R(\omega) = \frac{1 - \dfrac{\mu_1 K_2(\omega)}{\mu_2 K_1(\omega)}}{1 + \dfrac{\mu_1 K_2(\omega)}{\mu_2 K_1(\omega)}} = \frac{K_1(\omega)/\mu_1 - K_2(\omega)/\mu_2}{K_1(\omega)/\mu_1 + K_2(\omega)/\mu_2}, \tag{B9a}$$

and

$$T(\omega) = \frac{2}{1 + \dfrac{\mu_1 K_2(\omega)}{\mu_2 K_1(\omega)}} = \frac{2K_1(\omega)/\mu_1}{K_1(\omega)/\mu_1 + K_2(\omega)/\mu_2} = 1 + R(\omega). \tag{B9b}$$

These expressions are consistent with equations (3.50) and (3.51) on page 188 in Ward and Hohmann (1987).

The reflection and transmission coefficients are complex-valued and frequency-dependent. The complex wavenumbers are Hermitian skew-symmetric (i.e., $K(-\omega) = -K(\omega)^*$ where the asterisk denotes complex-conjugation). Hence, it is straightforward to demonstrate that the reflection and transmission coefficients are Hermitian symmetric (which is equivalent to real part even in ω and imaginary part odd in ω):

$$R(-\omega) = R(\omega)^*, \qquad T(-\omega) = T(\omega)^*. \tag{B10a,b}$$

In turn, Hermitian symmetry implies that the time-domain reflected and transmitted electric vectors are real-valued, as is required.

Low- and high-frequency approximations to the reflection/transmission coefficients may be obtained. At low frequencies, the complex wavenumber is approximated by

$$K(\omega) \approx \sqrt{\frac{\sigma\mu|\omega|}{2}}\,\left[\mathrm{sgn}(\omega) + i\left(1 - \delta_0(\omega)\right)\right], \tag{B11}$$

where $\mathrm{sgn}(\omega)$ is the sign function and $\delta_0(\omega)$ is the null function. The second factor in expression (B11) is necessary to obtain Hermitian skew-symmetry, but is often omitted. The low-frequency reflection and transmission coefficients become

$$R \approx \frac{\sqrt{\sigma_1/\mu_1} - \sqrt{\sigma_2/\mu_2}}{\sqrt{\sigma_1/\mu_1} + \sqrt{\sigma_2/\mu_2}}, \qquad T \approx \frac{2\sqrt{\sigma_1/\mu_1}}{\sqrt{\sigma_1/\mu_1} + \sqrt{\sigma_2/\mu_2}}. \tag{B12a,b}$$

The low-frequency approximations are real-valued and independent of frequency (and independent of electric permittivity ε). Note that $T = 1+R$ still holds. In the limit as one or the other conductivity approaches infinity (corresponding to say, pure metal) we have

$$\sigma_1 \to \infty \Rightarrow R = +1 \text{ and } T = 2, \qquad \text{and} \qquad \sigma_2 \to \infty \Rightarrow R = -1 \text{ and } T = 0.$$

[In fact, these two results hold for the exact reflection/transmission coefficient formulae (B9a and b), without low-frequency approximation.] So, an electromagnetic wave incident onto pure metal (i.e., from medium #1 with σ_1 finite to medium #2 with $\sigma_2 = \infty$) is totally reflected, with no transmission into the metal. Although it is tempting to consider the other limiting situation where one or the other halfspace is

vacuum, corresponding to zero-valued conductivity σ, that would violate the low-frequency assumption inherent in (B11).

The high-frequency approximation to the complex wavenumber is

$$K(\omega) \approx \sqrt{\varepsilon\mu}\left(\omega + i\frac{\sigma}{2\varepsilon}\right). \tag{B13}$$

Dependence on current conductivity σ is retained in the imaginary part. The reflection and transmission coefficients become

$$R(\omega) \approx \frac{\omega\left(\sqrt{\frac{\varepsilon_1}{\mu_1}} - \sqrt{\frac{\varepsilon_2}{\mu_2}}\right) + \frac{i}{2}\left(\frac{\sigma_1}{\sqrt{\varepsilon_1\mu_1}} - \frac{\sigma_2}{\sqrt{\varepsilon_2\mu_2}}\right)}{\omega\left(\sqrt{\frac{\varepsilon_1}{\mu_1}} + \sqrt{\frac{\varepsilon_2}{\mu_2}}\right) + \frac{i}{2}\left(\frac{\sigma_1}{\sqrt{\varepsilon_1\mu_1}} + \frac{\sigma_2}{\sqrt{\varepsilon_2\mu_2}}\right)}, \tag{B14a}$$

$$T(\omega) \approx \frac{2\omega\sqrt{\frac{\varepsilon_1}{\mu_1}} + i\frac{\sigma_1}{\sqrt{\varepsilon_1\mu_1}}}{\omega\left(\sqrt{\frac{\varepsilon_1}{\mu_1}} + \sqrt{\frac{\varepsilon_2}{\mu_2}}\right) + \frac{i}{2}\left(\frac{\sigma_1}{\sqrt{\varepsilon_1\mu_1}} + \frac{\sigma_2}{\sqrt{\varepsilon_2\mu_2}}\right)}, \tag{B14b}$$

with $T(\omega) = 1 + R(\omega)$. Reflection and transmission coefficients are complex-valued and frequency-dependent. However, in the *infinite* frequency limit, we obtain the real-valued and frequency-independent forms

$$R = \frac{\sqrt{\varepsilon_1/\mu_1} - \sqrt{\varepsilon_2/\mu_2}}{\sqrt{\varepsilon_1/\mu_1} + \sqrt{\varepsilon_2/\mu_2}}, \qquad T = \frac{2\sqrt{\varepsilon_1/\mu_1}}{\sqrt{\varepsilon_1/\mu_1} + \sqrt{\varepsilon_2/\mu_2}}, \tag{B15a,b}$$

where the expressions are written as equalities. Note the interestingly mathematical similarity to the low-frequency analogues (B12a,b). If both conductivities vanish in (B14a,b) (implying both media are vacuum with $\varepsilon_1 = \varepsilon_2 = \varepsilon_0$ and $\mu_1 = \mu_2 = \mu_0$) then $R = 0$ and $T = 1$. [This result also holds for the exact reflection/transmission coefficient formulae (B9a and b).] Moreover, as conductivity approaches infinity (implying media are pure metal) then the previous results remain valid:

$$\sigma_1 \to \infty \Rightarrow R = +1 \text{ and } T = 2, \qquad \text{and} \qquad \sigma_2 \to \infty \Rightarrow R = -1 \text{ and } T = 0.$$

B2.0 Reflection Coefficient Magnitude

The series summation approach pursued in the main text for deriving the total reflection response of a thin geologic bed requires the inequality $\left\|R_{top}(\omega)R_{bot}(\omega)\right\| < 1$, where $R_{top}(\omega)$ and $R_{bot}(\omega)$ are the normal incidence reflection coefficients associated with the top and bottom bed-bounding interfaces. This condition enables the summation to pass from a finite number N to an infinite number $N \to \infty$ of terms.

We now establish the inequality. Since $\left\| R_{top}(\omega) R_{bot}(\omega) \right\| = \left\| R_{top}(\omega) \right\| \left\| R_{bot}(\omega) \right\|$, it is sufficient to show that the modulus of a single reflection coefficient is less than unity.

From equation (B9a) above, write the normal incidence reflection coefficient as

$$R(\omega) = \frac{1 - Z(\omega)}{1 + Z(\omega)}, \tag{B16a}$$

where the dimensionless complex number $Z(\omega) = X(\omega) + i\, Y(\omega)$ is defined as

$$Z(\omega) \equiv \frac{\mu_1 K_2(\omega)}{\mu_2 K_1(\omega)}. \tag{B16b}$$

Substituting in the complex wavenumber $K(\omega) = \omega / c(\omega) + i\alpha(\omega)$ in terms of phase speed $c(\omega)$ and attenuation factor $\alpha(\omega)$ gives the real and imaginary parts of $Z(\omega)$ as

$$X(\omega) = \left[\frac{\mu_1 / \mu_2}{\dfrac{\omega^2}{c_1(\omega)^2} + \alpha_1(\omega)^2} \right] \left[\frac{\omega^2}{c_1(\omega) c_2(\omega)} + \alpha_1(\omega)\alpha_2(\omega) \right], \tag{B17a}$$

and

$$Y(\omega) = \left[\frac{\mu_1 / \mu_2}{\dfrac{\omega^2}{c_1(\omega)^2} + \alpha_1(\omega)^2} \right] \omega \left[\frac{\alpha_2(\omega)}{c_1(\omega)} - \frac{\alpha_1(\omega)}{c_2(\omega)} \right]. \tag{B17b}$$

Recall that the phase speed and attenuation factor are even and positive functions of angular frequency ω (although they both vanish at $\omega = 0$). Hence, real and imaginary parts are even and odd in angular frequency, respectively. Moreover, the real part $X(\omega)$ is strictly positive, whereas the imaginary part $Y(\omega)$ may be positive, zero, or negative. Clearly, if the two media are identical, then $X(\omega) = 1$ and $Y(\omega) = 0$, and the reflection coefficient $R(\omega)$ vanishes. At DC frequency $X(0) = \sqrt{\mu_1 \sigma_2 / \mu_2 \sigma_1}$ and $Y(0) = 0$, and the real-valued R/T coefficients of (B12a and b) are obtained. As frequency approaches infinity $X(\infty) = \sqrt{\mu_1 \varepsilon_2 / \mu_2 \varepsilon_1}$ and $Y(\infty) = 0$, and the real-valued R/T coefficients of (B15a and b) are obtained.

We work with the squared modulus of the reflection coefficient. It is straightforward to show that

$$\left\| R(\omega) \right\|^2 = \left\| \frac{1 - Z(\omega)}{1 + Z(\omega)} \right\|^2 = \frac{\left\| 1 - Z(\omega) \right\|^2}{\left\| 1 + Z(\omega) \right\|^2} = \frac{\left(1 - X(\omega)\right)^2 + Y(\omega)^2}{\left(1 + X(\omega)\right)^2 + Y(\omega)^2} = \frac{\left(1 + X(\omega)^2 + Y(\omega)^2\right) - 2X(\omega)}{\left(1 + X(\omega)^2 + Y(\omega)^2\right) + 2X(\omega)}. \tag{B18}$$

Hence, the squared modulus is the ratio of the *difference* of two positive numbers to the *sum* of the same two positive numbers. [As the third term on the RHS above indicates, the difference in the numerator is always positive.] This implies that the squared modulus is less than unity, which is sufficient proof that the modulus of the reflection coefficient is also less than unity. If follows that the modulus of the reflection coefficient product $\left\| R_{top}(\omega) R_{bot}(\omega) \right\| < 1$. QED.

The maximum modulus of the normal incidence reflection coefficient is unity. What about the minimum modulus? The foregoing analysis prompts an interesting question: can the normal incidence electromagnetic reflection coefficient vanish, for a model other than the trivial situation where medium #1 is identical to medium #2? Equation (B16a) above indicates that the reflection coefficient $R(\omega)$ equals zero when the complex number $Z(\omega)$ equals unity. Proceed by squaring the definition (B16b) for $Z(\omega)$, and then substituting in the squared complex wavenumber

$$K(\omega)^2 = i\omega\sigma\mu\left[1 - i(\omega/\omega_t)\right],$$

where $\omega_t = \sigma/\varepsilon$ is the transition (angular) frequency. The result is

$$Z(\omega)^2 = \frac{(\sigma_2/\sigma_1)}{(\mu_2/\mu_1)}\left[\frac{1 - i(\omega/\omega_2)}{1 - i(\omega/\omega_1)}\right], \qquad \text{(B19)}$$

where ω_1 and ω_2 are transition frequencies for media #1 and #2, respectively. Next, define three dimensionless ratios of medium properties as

$$r_\sigma = \sigma_2/\sigma_1, \qquad r_\mu = \mu_2/\mu_1, \qquad r_\varepsilon = \varepsilon_2/\varepsilon_1, \qquad \text{(B20a,b,c)}$$

and recognize that $\omega_2/\omega_1 = r_\sigma/r_\varepsilon$. Then quantity $Z(\omega)^2$ can be recast as

$$Z(\omega)^2 = \frac{r_\sigma}{r_\mu}\left[\frac{1 - i(r_\varepsilon/r_\sigma)(\omega/\omega_1)}{1 - i(\omega/\omega_1)}\right]. \qquad \text{(B21)}$$

Interestingly, this relation indicates that the normal incidence plane wave reflection coefficient between two homogeneous and isotropic media (which includes *six* independently-specifiable EM parameters) can be expressed in terms of *four* parameters (three dimensionless ratios and a single transition frequency).

We now ask an equivalent question: can $Z(\omega)^2 = +1$? Inspection reveals two obvious cases where the answer is clearly "yes":

Case 1: DC frequency $\omega = 0$. Then choose $r_\sigma = r_\mu = r$, where r is any positive real number. Then $Z(0)^2 = +1$, implying $Z(0) = \pm 1$, implying $R(0) = 0$ or $R(0) = \infty$. [The latter is an extraneous root introduced into the solution.] Even though the electric permittivities ε_1 and ε_2 of the two media may differ, the DC reflection coefficient vanishes.

Case 2: Choose $r_\sigma = r_\mu = r_\varepsilon = r$. Then $Z(\omega)^2 = +1$, implying $Z(\omega) = \pm 1$, implying $R(\omega) = 0$ or $R(\omega) = \infty$. The reflection coefficient vanishes for *all* frequencies. This is the interesting case where medium #2 is a scaled version of medium #1: $(\sigma_2, \mu_2, \varepsilon_2) = r(\sigma_1, \mu_1, \varepsilon_1)$. In effect, medium #2 is

completely transparent to an incident EM wave; the transmission coefficient is $T(\omega) = 1 + R(\omega) = 1$. This constitutes a generalization of the previously-noted trivial case where $r = 1$.

Moreover, these appear to be the *only* two cases with vanishing normal-incidence reflection coefficient. Solving expression (B21) with $Z(\omega)^2 = +1$ for the dimensionless frequency ω/ω_1 gives

$$\frac{\omega}{\omega_1} = -i\left[\frac{1-(r_\sigma/r_\mu)}{1-(r_\varepsilon/r_\mu)}\right].$$

Hence for general $r_\sigma, r_\mu, \text{and } r_\varepsilon$, there is no real-valued frequency that satisfies this relation. For $r_\sigma/r_\mu = 1$ (Case 1), real-valued $\omega = 0$ satisfies; if in addition $r_\varepsilon/r_\mu = 1$ (Case 2), then the frequency for vanishing $R(\omega)$ is indeterminate.

Upon further reflection (ha ha!), equation (B19) above suggests that only *three* parameters determine a normal incidence reflection coefficient:

$$\omega_1 \equiv \frac{\sigma_1}{\varepsilon_1}, \qquad p \equiv \frac{r_\sigma}{r_\mu} = \frac{\sigma_2\mu_1}{\sigma_1\mu_2}, \qquad q \equiv \frac{r_\varepsilon}{r_\sigma} = \frac{\varepsilon_2\sigma_1}{\varepsilon_1\sigma_2}. \qquad \text{(B22a,b,c)}$$

Note that parameters p and q are dimensionless. Quantity $Z(\omega)$ is re-written in terms of the parameters as

$$Z(\omega) = p^{1/2}\left[1 - iq(\omega/\omega_1)\right]^{1/2}\left[1 - i(\omega/\omega_1)\right]^{-1/2}.$$

Expanding to first-order in dimensionless frequency ω/ω_1 yields

$$Z(\omega) \approx p^{1/2}\left[1 + \left(\frac{1-q}{2}\right)i(\omega/\omega_1)\right].$$

Finally, substituting this into equation (B16a) for the normal incidence reflection coefficient gives the first-order expansion

$$R(\omega) \approx R(0) + \left[\frac{p^{1/2}(1-q)}{(1+p^{1/2})^2}\right]\left(\frac{-i\omega}{\omega_1}\right), \qquad \text{(B23a)}$$

where the DC reflection coefficient is

$$R(0) \equiv \frac{1-p^{1/2}}{1+p^{1/2}} = \frac{1-\sqrt{\dfrac{r_\sigma}{r_\mu}}}{1+\sqrt{\dfrac{r_\sigma}{r_\mu}}} = \frac{1-\sqrt{\dfrac{\sigma_2\mu_1}{\sigma_1\mu_2}}}{1+\sqrt{\dfrac{\sigma_2\mu_1}{\sigma_1\mu_2}}}. \qquad \text{(B23b)}$$

The dependence on only three parameters is obvious in approximation (B23a); note that the first-order term vanishes for $q = 1$. Re-writing the reflection coefficient in terms of the material parameter ratios (B20a,b,c) yields the form

$$R(\omega) \approx \frac{1-\sqrt{r_\sigma / r_\mu}}{1+\sqrt{r_\sigma / r_\mu}} - \left[\frac{\sqrt{r_\sigma / r_\mu}\left[1-\left(r_\varepsilon / r_\sigma\right)\right]}{\left(1+\sqrt{r_\sigma / r_\mu}\right)^2} \right] \left(\frac{i\omega}{\omega_1} \right). \tag{B24}$$

So, the zeroth-order term DC reflection coefficient $R(0)$ vanishes for $r_\sigma = r_\mu = r$ (as per Case 1 above) yielding the first-order approximation

$$R(\omega)\big|_{r_\sigma = r_\mu = r} \approx -\left[\frac{1-\left(r_\varepsilon / r\right)}{4} \right] \left(\frac{i\omega}{\omega_1} \right). \tag{B25a}$$

If in addition $r_\varepsilon = r$ (as per Case 2 above), then the first-order term also vanishes. The analysis for Case 2 clearly indicates that *all* higher-order terms in a frequency series expansion must vanish.

Figure B2 illustrates the phenomenon of zero-valued EM reflection coefficients. A three layer earth model is considered, with relative (i.e., dimensionless) permittivity $\hat{\varepsilon} = \varepsilon / \varepsilon_0$, permeability $\hat{\mu} = \mu / \mu_0$, and conductivity $\hat{\sigma} = \sigma / \sigma_{ref}$ (with $\sigma_{ref} = 1\,\mathrm{S/m}$) for the three media given by:

Medium #1: $\left(\hat{\varepsilon}_1, \hat{\mu}_1, \hat{\sigma}_1\right) = (1,1,1)$,
Medium #2: $\left(\hat{\varepsilon}_2, \hat{\mu}_2, \hat{\sigma}_2\right) = (10,10,10)$,
Medium #3: $\left(\hat{\varepsilon}_3, \hat{\mu}_3, \hat{\sigma}_3\right) = (1,1,1)$.

Hence, layer parameters are 10 times larger than those of the overlying and underlying halfspaces. Both the top-bed and bottom-bed reflection coefficients vanish. The total reflection response of the bed, as indicated in the top panel of Figure B2, equals zero. In effect, the embedded layer (h = 10 m thick) is transparent to EM plane waves normally incident from the overlying medium #1. When the conductivity of the layer is changed to $\hat{\sigma}_2 = 15\,\mathrm{S/m}$ (and all other medium parameters remain the same), the results depicted in Figure B3 are obtained. A weak inverted-polarity reflection appears, although the transmitted response appears virtually identical to that in Figure B2.

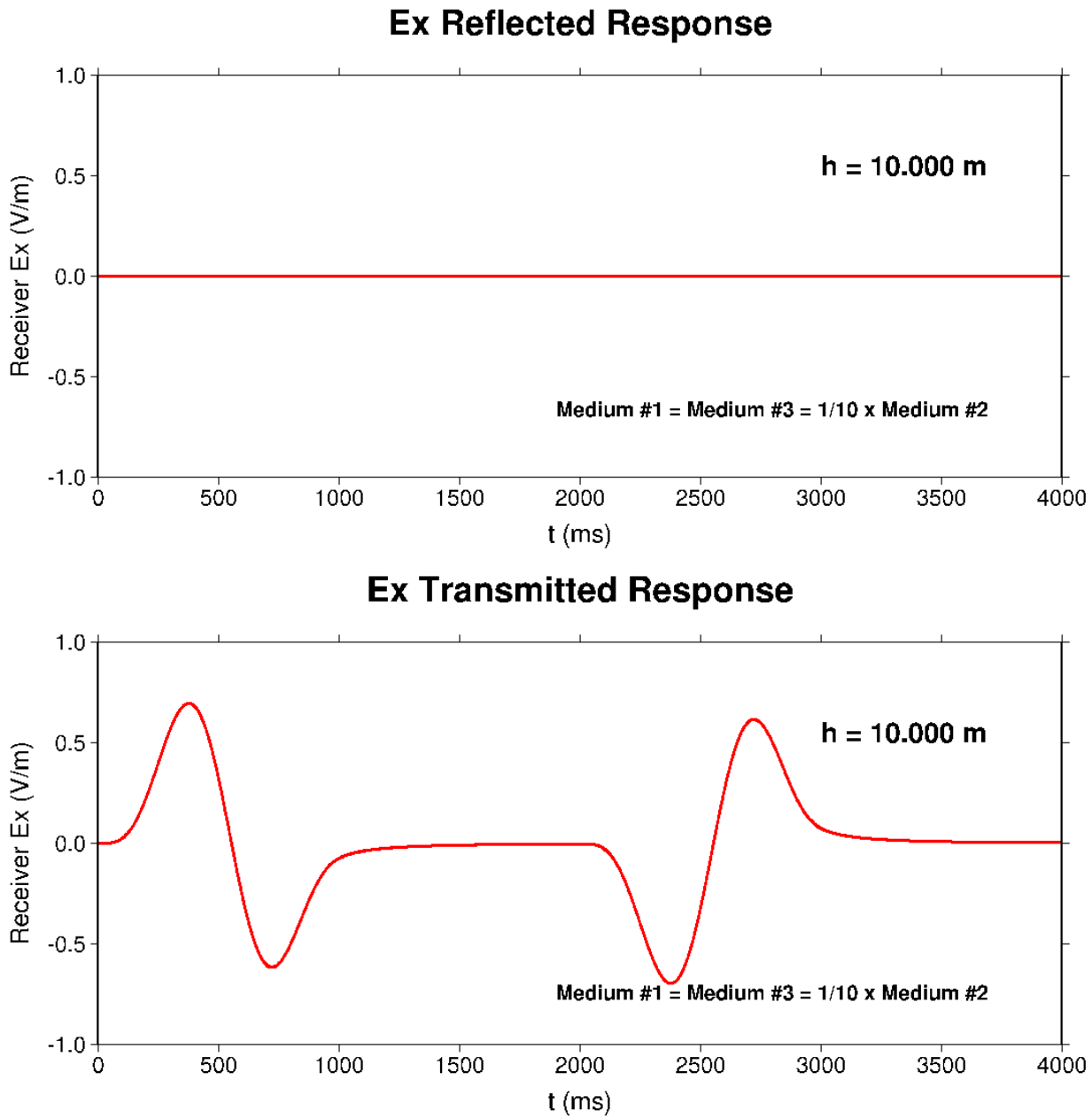

Figure B2. Reflected (top panel) and transmitted (bottom panel) electric vector *x*-components from an "invisible" or "transparent" geologic layer with thickness h = 10 m. Relative (i.e., dimensionless) permittivity $\hat{\varepsilon} = \varepsilon/\varepsilon_0$, permeability $\hat{\mu} = \mu/\mu_0$, and conductivity $\hat{\sigma} = \sigma/\sigma_{ref}$ (with $\sigma_{ref} = 1\,\text{S/m}$) for the three media are: $(\hat{\varepsilon}_1, \hat{\mu}_1, \hat{\sigma}_1) = (1,1,1)$, $(\hat{\varepsilon}_2, \hat{\mu}_2, \hat{\sigma}_2) = (10,10,10)$, $(\hat{\varepsilon}_3, \hat{\mu}_3, \hat{\sigma}_3) = (1,1,1)$. The reflected response vanishes because both the top-bed and bottom-bed reflection coefficients numerically equal 0.0.

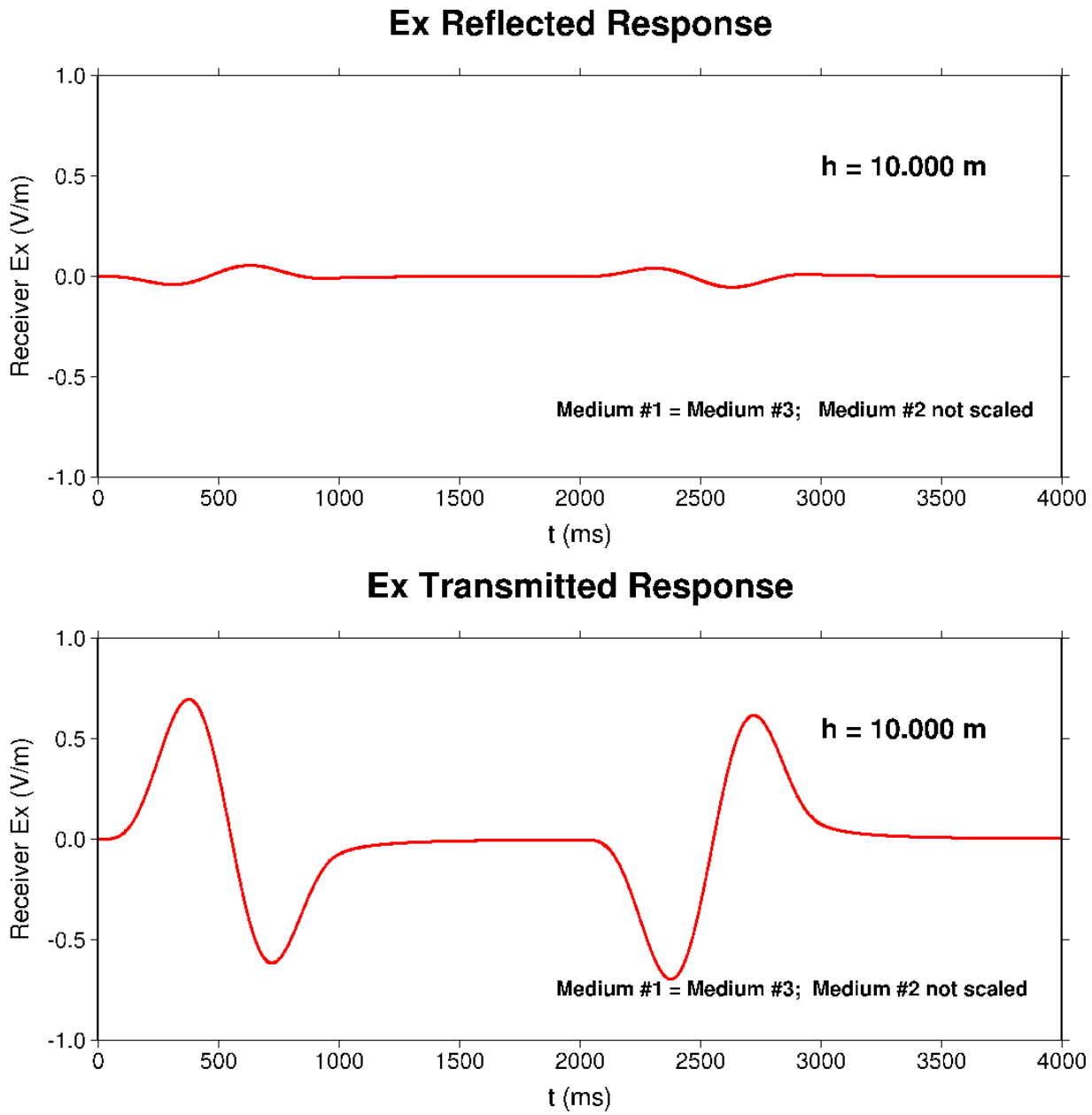

Figure B3. Reflected (top panel) and transmitted (bottom panel) electric vector *x*-components from a geologic layer with thickness h = 10 m. All medium parameters are the same as in Figure B2, except the relative (i.e., dimensionless) conductivity $\hat{\sigma}$ assigned to the layer (medium #2) is $\hat{\sigma}_3 = 15\,\text{S/m}$. A weak reflected response is generated, and the transmitted response appears to be nearly unchanged (compare with Figure B2).

We have obtained a similar "reflectionless" response using an embedded layer with parameters equal to 1/10 of the enclosing two halfspaces, although these are not displayed here. Modeling results in Figures B2 and B3 are obtained with an EK source wavelet (see Aldridge, 2013, page 36) with duration T = 1 second and unit amplitude. A 50% duty cycle alternating-polarity sequence of wavelets is used; the first two pulses are visible in the bottom panels. Receivers sensing reflected and transmitted EM responses are located 50 m from the center of the embedded geologic layer.

The existence of a zero-valued normal incidence reflection coefficient does not appear to be well-known in electromagnetic geophysics. Perhaps it is difficult to engineer a material where all three EM medium parameters scale identically. Some discussion of the analogous phenomenon in seismic geophysics is given by Levin (1986), who considers a non-normal incident compressional elastic wave. The normal incidence elastic (P-wave or S-wave) reflection coefficient is commonly given by

$$R = \frac{\rho_2 v_2 - \rho_1 v_1}{\rho_2 v_2 + \rho_1 v_1} = \frac{Z-1}{Z+1},$$

where ρ is mass density and v is wavespeed (either P or S). Quantity Z is defined as $Z = \dfrac{\rho_2 v_2}{\rho_1 v_1} = r_\rho r_v$, or the *product* of the two dimensionless parameter ratios $r_\rho = \rho_2/\rho_1$ and $r_v = v_2/v_1$. Clearly $r_\rho = r_v = 1$ implies $R = 0$. However, if density and velocity of medium #2 are scaled by the same factor r, a vanishing reflection coefficient is *not* obtained. Consider re-parameterizing the reflection coefficient in terms of mass buoyancy $b \equiv 1/\rho$ or slowness $s \equiv 1/v$. The reflection coefficient becomes

$$R == \frac{Z-1}{Z+1} \quad \text{with } Z = \frac{r_v}{r_b} = \frac{r_\rho}{r_s} \quad \text{with } r_b = b_2/b_1 \text{ and } r_s = s_2/s_1 .$$

Quantity Z is now re-cast as a *quotient* of two dimensionless parameter ratios. If both ratios scale by the same factor, then $Z = 1$ and the reflection coefficient vanishes. So, the key to obtaining a zero-valued reflection coefficient is to find a suitable parameterization that makes quantity Z contain only quotients of dimensionless parameter ratios, as equation (B21) above is.

B3.0 Electromagnetic Fields

Finally, we give the reflected and transmitted electric and magnetic vector components. From equations (B1b and c) above, the Fourier transformed *electric* vectors are

$$\mathbf{E}_{ref}(z,\omega) = \mathbf{e}_x R(\omega) E_{inc}(z_{\text{int}},\omega) e^{+iK_1(\omega)(z_{\text{int}}-z)}$$

$$= \mathbf{e}_x R(\omega) E_{inc}(z_s,\omega) e^{+iK_1(\omega)(2z_{\text{int}}-z_s-z)}, \qquad \text{for } z < z_{\text{int}}. \tag{B26a}$$

$$\mathbf{E}_{trn}(z,\omega) = \mathbf{e}_x T(\omega) E_{inc}(z_{\text{int}},\omega) e^{+iK_2(\omega)(z-z_{\text{int}})}$$

$$= \mathbf{e}_x T(\omega) E_{inc}(z_s,\omega) e^{+iK_1(\omega)(z_{\text{int}}-z_s)+iK_2(\omega)(z-z_{\text{int}})}, \qquad \text{for } z > z_{\text{int}}. \tag{B26b}$$

Reflected and transmitted Fourier transformed *magnetic* fields, from equations (B3b and c), are

$$\mathbf{H}_{ref}(z,\omega) = -\mathbf{e}_y \frac{K_1(\omega)}{\mu_1 \omega} R(\omega) E_{inc}(z_{\text{int}},\omega) e^{+iK_1(\omega)(z_{\text{int}}-z)}$$

$$= -\mathbf{e}_y \frac{K_1(\omega)}{\mu_1 \omega} R(\omega) E_{inc}(z_s,\omega) e^{+iK_1(\omega)(2z_{\text{int}}-z_s-z)}, \qquad \text{for } z < z_{\text{int}}. \tag{B27a}$$

$$\mathbf{H}_{trn}(z,\omega) = \mathbf{e}_y \frac{K_2(\omega)}{\mu_2 \omega} T(\omega) E_{inc}(z_{\text{int}},\omega) e^{+iK_2(\omega)(z-z_{\text{int}})}$$

$$= \mathbf{e}_y \frac{K_2(\omega)}{\mu_2 \omega} T(\omega) E_{inc}(z_s,\omega) e^{+iK_1(\omega)(z_{\text{int}}-z_s)+iK_2(\omega)(z-z_{\text{int}})}, \quad \text{for } z > z_{\text{int}}. \tag{B27b}$$

At low frequencies, the multiplicative factor $K(\omega)/\omega$ is given by

$$\frac{K(\omega)}{\omega} \approx \sqrt{\frac{\sigma\mu}{2|\omega|}} \left[1 + i\,\text{sgn}(\omega)\right],$$

which presents a problem for numerical evaluation at DC frequency.

12.0 APPENDIX C: ALTERNATIVE DERIVATIONAL APPROACH

The derivational approach pursued in the main text involves summing terms in an infinite series. Each term represents a particular reflected or transmitted phase. Remarkably, the series may be evaluated in closed form via the famous geometric progression formula. In this Appendix, we pursue an alternative derivational approach that yields (as fully expected!) identical results for the reflected and transmitted responses. In the limit as the number of terms in the series becomes infinite (and provided a mathematical condition on the reflection coefficients is satisfied; see Appendix B) the two approaches are demonstrated to be equivalent.

Within a homogeneous and isotropic medium, plane wave solutions of the frequency-domain Maxwell equations are proportional to the complex exponentials $\exp\left[\pm iK(\omega)z\right]$, where $K(\omega)$ is the complex wavenumber. Hence, within media #1, #2, and #3, the *x*-components of the electric vector may be written in the general forms

$$E_x(z,\omega)\big|_{\text{medium1}} = E_{inc}(z_s,\omega)e^{+iK_1(\omega)(z-z_s)} + A(\omega)e^{-iK_1(\omega)z}, \tag{C1a}$$

$$E_x(z,\omega)\big|_{\text{medium2}} = B(\omega)e^{+iK_2(\omega)z} + C(\omega)e^{-iK_2(\omega)z}, \tag{C1b}$$

$$E_x(z,\omega)\big|_{\text{medium3}} = D(\omega)e^{+iK_3(\omega)z}. \tag{C1c}$$

Terms proportional to $\exp\left[+iK(\omega)z\right]$ represent downward propagating (+*z* direction) energy, whereas those proportional to $\exp\left[-iK(\omega)z\right]$ represent upward propagating (–*z* direction) energy. The four frequency-dependent coefficients $A(\omega)$, $B(\omega)$, $C(\omega)$, and $D(\omega)$ are determined by imposing boundary conditions at the two horizontal interfaces. Note that, as per expression (C1b), there are both upward and downward propagating waves within the thin bed.

Magnetic vector *y*-components are obtained from the Fourier-transformed Faraday law via

$$\mathbf{H}(z,\omega) = \frac{1}{i\omega\mu}\mathbf{curl}\,\mathbf{E}(z,\omega) = \mathbf{e}_y\frac{1}{i\omega\mu}\frac{\partial E_x(z,\omega)}{\partial z}. \tag{C2}$$

Hence, the *y*-components of the magnetic vector are given by

$$H_y(z,\omega)\big|_{\text{medium1}} = \frac{K_1(\omega)}{\omega\mu_1}\left[E_{inc}(z_s,\omega)e^{+iK_1(\omega)(z-z_s)} - A(\omega)e^{-iK_1(\omega)z}\right], \tag{C3a}$$

$$H_y(z,\omega)\big|_{\text{medium2}} = \frac{K_2(\omega)}{\omega\mu_2}\left[B(\omega)e^{+iK_2(\omega)z} - C(\omega)e^{-iK_2(\omega)z}\right], \tag{C3b}$$

$$H_y(z,\omega)\big|_{\text{medium3}} = \frac{K_3(\omega)}{\omega\mu_3}D(\omega)e^{+iK_3(\omega)z}. \tag{C3c}$$

At the two interfaces $z = z_{top}$ and $z = z_{bot}$, the electric and magnetic vector components are continuous. Application of these boundary conditions yields the four expressions

$$E_{inc}(z_s,\omega)e^{+iK_1(\omega)(z_{top}-z_s)} + A(\omega)e^{-iK_1(\omega)z_{top}} = B(\omega)e^{+iK_2(\omega)z_{top}} + C(\omega)e^{-iK_2(\omega)z_{top}}, \tag{C4a}$$

$$\frac{K_1(\omega)}{\mu_1}\left[E_{inc}(z_s,\omega)e^{+iK_1(\omega)(z_{top}-z_s)}\exp - A(\omega)e^{-iK_1(\omega)z_{top}}\right]$$

$$= \frac{K_2(\omega)}{\mu_2}\left[B(\omega)e^{+iK_2(\omega)z_{top}} - C(\omega)e^{-iK_2(\omega)z_{top}}\right], \tag{C4b}$$

$$B(\omega)e^{+iK_2(\omega)z_{bot}} + C(\omega)e^{-iK_2(\omega)z_{bot}} = D(\omega)e^{+iK_3(\omega)z_{bot}}, \tag{C4c}$$

$$\frac{K_2(\omega)}{\mu_2}\left[B(\omega)e^{+iK_2(\omega)z_{bot}} - C(\omega)e^{-iK_2(\omega)z_{bot}}\right] = \frac{K_3(\omega)}{\mu_3}D(\omega)e^{+iK_3(\omega)z_{bot}}. \tag{C4d}$$

Or, organized as a 4 × 4 system of linear algebraic equations:

$$\begin{bmatrix} e^{-iK_1(\omega)z_{top}} & -e^{+iK_2(\omega)z_{top}} & -e^{-iK_2(\omega)z_{top}} & 0 \\ e^{-iK_1(\omega)z_{top}} & \frac{\mu_1 K_2(\omega)}{\mu_2 K_1(\omega)}e^{+iK_2(\omega)z_{top}} & -\frac{\mu_1 K_2(\omega)}{\mu_2 K_1(\omega)}e^{-iK_2(\omega)z_{top}} & 0 \\ 0 & -e^{+iK_2(\omega)z_{bot}} & -e^{-iK_2(\omega)z_{bot}} & e^{+iK_3(\omega)z_{bot}} \\ 0 & -\frac{\mu_3 K_2(\omega)}{\mu_2 K_3(\omega)}e^{+iK_2(\omega)z_{bot}} & \frac{\mu_3 K_2(\omega)}{\mu_2 K_3(\omega)}e^{-iK_2(\omega)z_{bot}} & e^{+iK_3(\omega)z_{bot}} \end{bmatrix} \begin{bmatrix} A(\omega) \\ B(\omega) \\ C(\omega) \\ D(\omega) \end{bmatrix}$$

$$= \begin{bmatrix} -E_{inc}(z_s,\omega)e^{+iK_1(\omega)(z_{top}-z_s)} \\ E_{inc}(z_s,\omega)e^{+iK_1(\omega)(z_{top}-z_s)} \\ 0 \\ 0 \end{bmatrix}. \tag{C5}$$

Rather than solve this 4 × 4 system directly, we reduce it to a simpler 2 × 2 system. The first and last equations of (C5) are written as

$$A(\omega)e^{-iK_1(\omega)z_{top}} = B(\omega)e^{+iK_2(\omega)z_{top}} + C(\omega)e^{-iK_2(\omega)z_{top}} - E_{inc}(z_s,\omega)e^{+iK_1(\omega)z_{top}-z_s)}, \tag{C6a}$$

$$D(\omega)e^{+iK_3(\omega)z_{bot}} = B(\omega)\frac{\mu_3 K_2(\omega)}{\mu_2 K_3(\omega)}e^{+iK_2(\omega)z_{bot}} - C(\omega)\frac{\mu_3 K_2(\omega)}{\mu_2 K_3(\omega)}e^{-iK_2(\omega)z_{bot}}, \tag{C6b}$$

respectively. Then, eliminating coefficients $A(\omega)$ and $D(\omega)$ from system (C5) yields

$$B(\omega)e^{+iK_2(\omega)z_{top}}\left[1+\frac{\mu_1 K_2(\omega)}{\mu_2 K_1(\omega)}\right] + C(\omega)e^{-iK_2(\omega)z_{top}}\left[1-\frac{\mu_1 K_2(\omega)}{\mu_2 K_1(\omega)}\right] = 2E_{inc}(z_s,\omega)e^{+iK_1(\omega)(z_{top}-z_s)}, \tag{C7a}$$

$$B(\omega)e^{+iK_2(\omega)z_{bot}}\left[1-\frac{\mu_3 K_2(\omega)}{\mu_2 K_3(\omega)}\right] + C(\omega)e^{-iK_2(\omega)z_{bot}}\left[1+\frac{\mu_3 K_2(\omega)}{\mu_2 K_3(\omega)}\right] = 0. \tag{C7b}$$

The determinant of this 2 × 2 system is

$$\Delta = (1+p)(1+q)e^{-iK_2(\omega)(z_{bot}-z_{top})} - (1-p)(1-q)e^{+iK_2(\omega)(z_{bot}-z_{top})},$$

with p and q defined by $p \equiv \dfrac{\mu_1 K_2(\omega)}{\mu_2 K_1(\omega)}$ and $q \equiv \dfrac{\mu_3 K_2(\omega)}{\mu_2 K_3(\omega)}$. From Appendix B, normal incidence reflection coefficients at the top and bottom interfaces are given in terms of p and q by

$$R_{top} = \frac{1-p}{1+p}, \qquad \text{and} \qquad R_{bot} = \frac{q-1}{q+1}.$$

This implies $p = \dfrac{1-R_{top}}{1+R_{top}}$ and $q = \dfrac{1+R_{bot}}{1-R_{bot}}$. Hence, we have

$$1+p = \frac{2}{1+R_{top}}, \qquad 1-p = \frac{2R_{top}}{1+R_{top}}, \qquad 1+q = \frac{2}{1-R_{bot}}, \qquad 1-q = \frac{-2R_{bot}}{1-R_{bot}}.$$

Then, the determinant of 2 × 2 system (C7a,b) is re-expressed as

$$\Delta = \frac{4e^{-iK_2(\omega)h}}{(1+R_{top})(1-R_{bot})}\left(1+R_{top}R_{bot}e^{+iK_2(\omega)2h}\right),$$

where bed thickness is $h = z_{bot} - z_{top}$. Interestingly (and not surprisingly), the determinant contains the factor obtained from summing the infinite series (3.4b). Solution of 2 × 2 system (C7) for coefficients $B(\omega)$ and $C(\omega)$ yields

$$B(\omega) = \frac{E_{inc}(z_s,\omega)(1+R_{top})e^{+iK_1(\omega)(z_{top}-z_s)}e^{+iK_2(\omega)h}e^{-iK_2(\omega)z_{bot}}}{1+R_{top}R_{bot}e^{+iK_2(\omega)2h}}, \tag{C8a}$$

$$C(\omega) = \frac{E_{inc}(z_s,\omega)(1+R_{top})R_{bot}e^{+iK_1(\omega)(z_{top}-z_s)}e^{+iK_2(\omega)h}e^{+iK_2(\omega)z_{bot}}}{1+R_{top}R_{bot}e^{+iK_2(\omega)2h}}. \tag{C8b}$$

Substituting into equations (C6a and b) gives solutions for the remaining coefficients $A(\omega)$ and $D(\omega)$ as

$$A(\omega) = \frac{E_{inc}(z_s,\omega)e^{+iK_1(\omega)(2z_{top}-z_s)}\left(R_{top}+R_{bot}e^{+iK_2(\omega)2h}\right)}{1+R_{top}R_{bot}e^{+iK_2(\omega)2h}}, \tag{C8c}$$

$$D(\omega) = \frac{E_{inc}(z_s,\omega)(1+R_{top})(1+R_{bot})e^{+iK_1(\omega)(z_{top}-z_s)}e^{+iK_2(\omega)h}e^{-iK_3(\omega)z_{bot}}}{1+R_{top}R_{bot}e^{+iK_2(\omega)2h}}. \tag{C8d}$$

Finally, introducing the coefficients into equations (C1a,b,c) gives the electric vector x-components in the three media as (next page):

$$E_x(z_r,\omega)\big|_{\text{medium1}} = E_{inc}(z_s,\omega)e^{+iK_1(\omega)(z_r-z_s)} + E_{inc}(z_s,\omega)e^{+iK_1(\omega)(2z_{top}-z_r-z_s)}\left[\frac{R_{top}(\omega)+R_{bot}(\omega)e^{+iK_2(\omega)2h}}{1+R_{top}(\omega)R_{bot}(\omega)e^{+iK_2(\omega)2h}}\right], \quad \text{(C9a)}$$

$$E_x(z_r,\omega)\big|_{\text{medium2}} = E_{inc}(z_s,\omega)e^{+iK_1(\omega)(z_{top}-z_s)}e^{+iK_2(\omega)(z_r-z_{top})} \times\left[\frac{\left(1+R_{top}(\omega)\right)\left(1+R_{bot}(\omega)e^{+iK_2(\omega)2(z_{bot}-z_r)}\right)}{1+R_{top}(\omega)R_{bot}(\omega)e^{+iK_2(\omega)2h}}\right], \quad \text{(C9b)}$$

$$E_x(z_r,\omega)\big|_{\text{medium3}} = E_{inc}(z_s,\omega)e^{+iK_1(\omega)(z_{top}-z_s)}e^{+iK_2(\omega)h}e^{+iK_3(\omega)(z_r-z_{bot})} \times\left[\frac{\left(1+R_{top}(\omega)\right)\left(1+R_{bot}(\omega)\right)}{1+R_{top}(\omega)R_{bot}(\omega)e^{+iK_2(\omega)2h}}\right], \quad \text{(C9c)}$$

where we have explicitly re-introduced the frequency-dependence of the two reflection coefficients. Equation (C9a) contains the thin bed reflection response (in addition to the incident wave), and equation (C9c) is the thin-bed transmission response. These are identical to equations (3.13) and (4.3b) of the main text. Expression (C9b) is new; it yields the response *within* the thin bed (i.e, for $z_{top} < z < z_{bot}$), and is comprised of both upward and downward propagating waves.

Equations (C3a,b,c) above give the magnetic vector *y*-components within the three media. Thus, magnetic induction vector components (= μH_y) are

$$B_y(z_r,\omega)\big|_{\text{medium1}} = \mu_1 H_y(z,\omega)\big|_{\text{medium1}} = \left(\frac{K_1(\omega)}{\omega}\right)E_{inc}(z_s,\omega)e^{+iK_1(\omega)(z_r-z_s)} - \left(\frac{K_1(\omega)}{\omega}\right)E_{inc}(z_s,\omega)e^{+iK_1(\omega)(2z_{top}-z_r-z_s)}\left[\frac{R_{top}(\omega)+R_{bot}(\omega)e^{+iK_2(\omega)2h}}{1+R_{top}(\omega)R_{bot}(\omega)e^{+iK_2(\omega)2h}}\right], \quad \text{(C10a)}$$

$$B_y(z_r,\omega)\big|_{\text{medium2}} = \mu_2 H_y(z_r,\omega)\big|_{\text{medium2}} = \left(\frac{K_2(\omega)}{\omega}\right)E_{inc}(z_s,\omega)e^{+iK_1(\omega)(z_{top}-z_s)}e^{+iK_2(\omega)(z_r-z_{top})} \times\left[\frac{\left(1+R_{top}(\omega)\right)\left(1-R_{bot}(\omega)e^{+iK_2(\omega)2(z_{bot}-z_r)}\right)}{1+R_{top}(\omega)R_{bot}(\omega)e^{+iK_2(\omega)2h}}\right], \quad \text{(C10b)}$$

and

$$B_y(z_r,\omega)\Big|_{\text{medium3}} = \mu_3 H_y(z,\omega)\Big|_{\text{medium3}}$$

$$= \left(\frac{K_3(\omega)}{\omega}\right) E_{inc}(z_s,\omega) e^{+iK_1(\omega)(z_{top}-z_s)}\ e^{+iK_2(\omega)h}\ e^{+iK_3(\omega)(z_r-z_{bot})}$$

$$\times \left[\frac{\big(1+R_{top}(\omega)\big)\big(1+R_{bot}(\omega)\big)}{1+R_{top}(\omega)R_{bot}(\omega)e^{+iK_2(\omega)2h}}\right]. \qquad \text{(C10c)}$$

Expressions (C10a and c) are consistent with equations (3.15a) and (4.6a) of the main text. Note the sign changes in equations (C10a and b) compared with (C9a and b)!

An interesting observation from the analysis in this Appendix is that the inequality condition $\left\|R_{top}(\omega)R_{bot}(\omega)\right\| < 1$ is *not* required to establish the correct reflection, transmission, and intrabed EM responses. This contrasts with the series summation approach utilized in the main text, where this condition is explicitly required for the number of terms in the finite sum to become infinite. Hence, we conclude that the inequality condition is an "automatic" or "necessary" result arising from basic electromagnetic theory, not requiring an additional proof (as we give in Appendix A).

13.0 APPENDIX D: FIRST BORN APPROXIMATION

D1.0 Heterogeneous Medium

Consider a set of electromagnetic body sources (i.e., current density $\mathbf{j}_s(\mathbf{x},t)$, magnetic induction $\mathbf{b}_s(\mathbf{x},t)$, and electric displacement $\mathbf{d}_s(\mathbf{x},t)$) applied to an isotropic medium characterized by permittivity $\varepsilon(\mathbf{x})$, permeability $\mu(\mathbf{x})$, and conductivity $\sigma(\mathbf{x})$. Within the three-dimensional volume V occupied by the body, the electric field vector $\mathbf{e}(\mathbf{x},t)$ and magnetic field vector $\mathbf{h}(\mathbf{x},t)$ satisfy the coupled first-order partial differential system (i.e., the EH PDE system (A1.3a and b)):

$$\varepsilon(\mathbf{x})\frac{\partial\,\mathbf{e}(\mathbf{x},t)}{\partial t}+\sigma(\mathbf{x})\mathbf{e}(\mathbf{x},t)-\mathbf{curl}\,\mathbf{h}(\mathbf{x},t)=-\mathbf{j}_s(\mathbf{x},t)-\frac{\partial\mathbf{d}_s(\mathbf{x},t)}{\partial t}, \tag{D1.1a}$$

$$\mu(\mathbf{x})\frac{\partial\,\mathbf{h}(\mathbf{x},t)}{\partial t}+\mathbf{curl}\,\mathbf{e}(\mathbf{x},t)=-\frac{\partial\,\mathbf{b}_s(\mathbf{x},t)}{\partial t}. \tag{D1.1b}$$

Electric and magnetic boundary conditions are applied to the surface S bounding V (this surface may be infinitely far away). We adopt a general point of view that these boundary conditions are represented by linear differential operators acting on the electric and magnetic vectors:

$$\mathbf{G}_e\{\mathbf{e}(\mathbf{x},t)\}=\mathbf{v}(\mathbf{x},t)\quad\text{for}\quad\mathbf{x}\in S_v,\qquad\qquad \mathbf{G}_h\{\mathbf{h}(\mathbf{x},t)\}=\mathbf{w}(\mathbf{x},t)\quad\text{for}\quad\mathbf{x}\in S_w, \tag{D1.1c,d}$$

where $S_v\cup S_w=S$, and $\mathbf{v}(\mathbf{x},t)$ and $\mathbf{w}(\mathbf{x},t)$ are prescribed vector-valued functions. Operators $\mathbf{G}_e$ and $\mathbf{G}_h$ may involve space and time differentiations, but linearity in the sense of the additive superposition

$$\mathbf{G}\{c_1\mathbf{e}_1(\mathbf{x},t)+c_2\mathbf{e}_2(\mathbf{x},t)\}=c_1\mathbf{G}\{\mathbf{e}_1(\mathbf{x},t)\}+c_2\mathbf{G}\{\mathbf{e}_2(\mathbf{x},t)\},$$

must hold. Finally, at time t_0, the initial conditions

$$\mathbf{e}(\mathbf{x},t_0)=\mathbf{e}_0(\mathbf{x}),\qquad\qquad \mathbf{h}(\mathbf{x},t_0)=\mathbf{h}_0(\mathbf{x}), \tag{D1.1e,f}$$

hold throughout V and on S.

Now consider a medium occupying the same volume V, but characterized by the *slightly different* electromagnetic parameters

$$\varepsilon(\mathbf{x})+\delta\varepsilon(\mathbf{x}),\qquad\qquad \mu(\mathbf{x})+\delta\mu(\mathbf{x}),\qquad\qquad \sigma(\mathbf{x})+\delta\sigma(\mathbf{x}).$$

The two space-dependent perturbations $\delta\varepsilon(\mathbf{x})$ and $\delta\mu(\mathbf{x})$ are considered small compared to $\varepsilon(\mathbf{x})$ and $\mu(\mathbf{x})$, respectively. However, in the case where the conductivity $\sigma(\mathbf{x})$ vanishes (i.e., the medium at $\mathbf{x}$ is vacuum), then perturbation $\delta\sigma(\mathbf{x})$ is obviously not small compared to $\sigma(\mathbf{x})$. Moreover, a *slightly different* set of body sources, boundary conditions, and initial conditions are applied to this perturbed medium. These new sources of electromagnetic waves are given by

$$\mathbf{j}_s(\mathbf{x},t)+\boldsymbol{\delta}\mathbf{j}_s(\mathbf{x},t),\qquad \mathbf{b}_s(\mathbf{x},t)+\boldsymbol{\delta}\mathbf{b}_s(\mathbf{x},t),\qquad \mathbf{d}_s(\mathbf{x},t)+\boldsymbol{\delta}\mathbf{d}_s(\mathbf{x},t),$$

$$\mathbf{v}(\mathbf{x},t)+\boldsymbol{\delta}\mathbf{v}(\mathbf{x},t),\qquad \mathbf{w}(\mathbf{x},t)+\boldsymbol{\delta}\mathbf{w}(\mathbf{x},t),$$

$$\mathbf{e}_0(\mathbf{x}) + \boldsymbol{\delta}\mathbf{e}_0(\mathbf{x}), \qquad \mathbf{h}_0(\mathbf{x}) + \boldsymbol{\delta}\mathbf{h}_0(\mathbf{x}).$$

The above EM wavefield body sources, boundary conditions, and initial conditions generate perturbed electric and magnetic field vectors given by

$$\mathbf{e}(\mathbf{x},t) + \boldsymbol{\delta}\mathbf{e}(\mathbf{x},t), \qquad \mathbf{h}(\mathbf{x},t) + \boldsymbol{\delta}\mathbf{h}(\mathbf{x},t),$$

respectively, where $\boldsymbol{\delta}\mathbf{e}(\mathbf{x},t)$ and $\boldsymbol{\delta}\mathbf{h}(\mathbf{x},t)$ represent corresponding small variations. These new electric and magnetic fields satisfy the coupled EH PDE system

$$\left[\varepsilon(\mathbf{x}) + \delta\varepsilon(\mathbf{x})\right]\left[\frac{\partial\,\mathbf{e}(\mathbf{x},t)}{\partial t} + \frac{\partial\,\boldsymbol{\delta}\mathbf{e}(\mathbf{x},t)}{\partial t}\right] + \left[\sigma(\mathbf{x}) + \delta\sigma(\mathbf{x})\right]\left[\mathbf{e}(\mathbf{x},t) + \boldsymbol{\delta}\mathbf{e}(\mathbf{x},t)\right]$$

$$-\,\mathbf{curl}\,\mathbf{h}(\mathbf{x},t) - \mathbf{curl}\,\boldsymbol{\delta}\mathbf{h}(\mathbf{x},t) = -\mathbf{j}_s(\mathbf{x},t) - \boldsymbol{\delta}\mathbf{j}_s(\mathbf{x},t) - \frac{\partial\mathbf{d}_s(\mathbf{x},t)}{\partial t} - \frac{\partial\,\boldsymbol{\delta}\mathbf{d}_s(\mathbf{x},.t)}{\partial t}, \tag{D1.2a}$$

$$\left[\mu(\mathbf{x}) + \delta\mu(\mathbf{x})\right]\left[\frac{\partial\,\mathbf{h}(\mathbf{x},t)}{\partial t} + \frac{\partial\,\boldsymbol{\delta}\mathbf{h}(\mathbf{x},t)}{\partial t}\right] + \mathbf{curl}\,\mathbf{e}(\mathbf{x},t) + \mathbf{curl}\,\boldsymbol{\delta}\mathbf{e}(\mathbf{x},t) = -\frac{\partial\,\mathbf{b}_s(\mathbf{x},t)}{\partial t} - \frac{\partial\,\boldsymbol{\delta}\mathbf{b}_s(\mathbf{x},t)}{\partial t}, \tag{D1.2b}$$

for $\mathbf{x}$ within V. On the bounding surface S, the electric and magnetic conditions

$$\mathbf{G}_e\left\{\mathbf{e}(\mathbf{x},t) + \boldsymbol{\delta}\mathbf{e}(\mathbf{x},t)\right\} = \mathbf{v}(\mathbf{x},t) + \boldsymbol{\delta}\mathbf{v}(\mathbf{x},t) \;\text{ for }\; \mathbf{x} \in S_v, \tag{D1.2c}$$

$$\mathbf{G}_h\left\{\mathbf{h}(\mathbf{x},t) + \boldsymbol{\delta}\mathbf{h}(\mathbf{x},t)\right\} = \mathbf{w}(\mathbf{x},t) + \boldsymbol{\delta}\mathbf{w}(\mathbf{x},t) \;\text{ for }\; \mathbf{x} \in S_w, \tag{D1.2d}$$

hold. Finally, at time t_0, the total EM wavefield satisfies the initial conditions

$$\mathbf{e}(\mathbf{x},t_0) + \boldsymbol{\delta}\mathbf{e}(\mathbf{x},t_0) = \mathbf{e}_0(\mathbf{x}) + \boldsymbol{\delta}\mathbf{e}_0(\mathbf{x}), \tag{D1.2e}$$

$$\mathbf{h}(\mathbf{x},t_0) + \boldsymbol{\delta}\mathbf{h}(\mathbf{x},t_0) = \mathbf{h}_0(\mathbf{x}) + \boldsymbol{\delta}\mathbf{h}_0(\mathbf{x}), \tag{D1.2f}$$

throughout V and on S.

Subtracting equations (D1.1a,b) from (D1.2a,b) gives

$$\varepsilon(\mathbf{x})\frac{\partial\,\boldsymbol{\delta}\mathbf{e}(\mathbf{x},t)}{\partial t} + \sigma(\mathbf{x})\boldsymbol{\delta}\mathbf{e}(\mathbf{x},t) - \mathbf{curl}\,\boldsymbol{\delta}\mathbf{h}(\mathbf{x},t) + \left[\delta\varepsilon(\mathbf{x})\frac{\partial\,\boldsymbol{\delta}\mathbf{e}(\mathbf{x},t)}{\partial t} + \delta\sigma(\mathbf{x})\boldsymbol{\delta}\mathbf{e}(\mathbf{x},t)\right]$$

$$= -\boldsymbol{\delta}\mathbf{j}_s(\mathbf{x},t) - \frac{\partial\,\boldsymbol{\delta}\mathbf{d}_s(\mathbf{x},t)}{\partial t} - \delta\varepsilon(\mathbf{x})\frac{\partial\mathbf{e}(\mathbf{x},t)}{\partial t} - \delta\sigma(\mathbf{x})\,\mathbf{e}(\mathbf{x},t),$$

and

$$\mu(\mathbf{x})\frac{\partial\,\boldsymbol{\delta}\mathbf{h}(\mathbf{x},t)}{\partial t}+\mathbf{curl}\,\boldsymbol{\delta}\mathbf{e}(\mathbf{x},t)+\left[\delta\mu(\mathbf{x})\frac{\partial\,\boldsymbol{\delta}\mathbf{h}(\mathbf{x},t)}{\partial t}\right]=-\frac{\partial\,\boldsymbol{\delta}\mathbf{b}_s(\mathbf{x},t)}{\partial t}-\delta\mu(\mathbf{x})\frac{\partial\,\mathbf{h}(\mathbf{x},t)}{\partial t}.$$

This system is simplified by neglecting the terms (in square brackets) that are products in (presumed) small quantities. Thus, the PDEs governing the perturbation electromagnetic wavefield become

$$\varepsilon(\mathbf{x})\frac{\partial\,\boldsymbol{\delta}\mathbf{e}(\mathbf{x},t)}{\partial t}+\sigma(\mathbf{x})\boldsymbol{\delta}\mathbf{e}(\mathbf{x},t)-\mathbf{curl}\,\boldsymbol{\delta}\mathbf{h}(\mathbf{x},t)$$
$$\approx-\boldsymbol{\delta}\mathbf{j}_s(\mathbf{x},t)-\delta\sigma(\mathbf{x})\,\mathbf{e}(\mathbf{x},t)-\frac{\partial\,\boldsymbol{\delta}\mathbf{d}_s(\mathbf{x},t)}{\partial t}-\delta\varepsilon(\mathbf{x})\frac{\partial\mathbf{e}(\mathbf{x},t)}{\partial t},\qquad\text{(D1.3a)}$$

$$\mu(\mathbf{x})\frac{\partial\,\boldsymbol{\delta}\mathbf{h}(\mathbf{x},t)}{\partial t}+\mathbf{curl}\,\boldsymbol{\delta}\mathbf{e}(\mathbf{x},t)\approx-\frac{\partial\,\boldsymbol{\delta}\mathbf{b}_s(\mathbf{x},t)}{\partial t}-\delta\mu(\mathbf{x})\frac{\partial\,\mathbf{h}(\mathbf{x},t)}{\partial t},\qquad\text{(D1.3b)}$$

where approximate equality symbols indicate that the expressions are appropriate for small material parameter perturbations. Additionally, subtracting equations (D1.1c-f)) from (D1.2c-f)) implies that the perturbation wavefield satisfies (exactly!) the boundary and initial conditions

$$\mathbf{G}_e\left\{\boldsymbol{\delta}\mathbf{e}(\mathbf{x},t)\right\}=\boldsymbol{\delta}\mathbf{v}(\mathbf{x},t)\ \text{ for }\ \mathbf{x}\in S_v,\qquad \mathbf{G}_h\left\{\boldsymbol{\delta}\mathbf{h}(\mathbf{x},t)\right\}=\boldsymbol{\delta}\mathbf{w}(\mathbf{x},t)\ \text{ for }\ \mathbf{x}\in S_w,\qquad\text{(D1.3c,d)}$$

$$\boldsymbol{\delta}\mathbf{e}(\mathbf{x},t_0)=\boldsymbol{\delta}\mathbf{e}_0(\mathbf{x}),\qquad \boldsymbol{\delta}\mathbf{h}(\mathbf{x},t_0)=\boldsymbol{\delta}\mathbf{h}_0(\mathbf{x}).\qquad\text{(D1.3e,f)}$$

Note that we have appealed to the linearity property of differential operators $\mathbf{G}_e$ and $\mathbf{G}_h$ in obtaining equations (D1.3c and d).

The solution of equations (D1.3) constitutes the *First Born Approximation* for the perturbation wavefield. These expressions have a straightforward interpretation. The perturbation wavefield [$\boldsymbol{\delta}\mathbf{e}(\mathbf{x},t)$ and $\boldsymbol{\delta}\mathbf{h}(\mathbf{x},t)$] propagates within the original (i.e., unperturbed) medium characterized by parameters $\varepsilon(\mathbf{x})$, $\mu(\mathbf{x})$, and $\sigma(\mathbf{x})$. This wavefield is generated by a combination of time-varying body sources [$\boldsymbol{\delta}\mathbf{j}_s(\mathbf{x},t)$, $\boldsymbol{\delta}\mathbf{d}_s(\mathbf{x},t)$, and $\boldsymbol{\delta}\mathbf{b}_s(\mathbf{x},t)$], time-varying boundary conditions [$\boldsymbol{\delta}\mathbf{v}(\mathbf{x},t)$ and $\boldsymbol{\delta}\mathbf{w}(\mathbf{x},t)$], as well as time-invariant initial conditions [$\boldsymbol{\delta}\mathbf{e}_0(\mathbf{x})$ and $\boldsymbol{\delta}\mathbf{h}_0(\mathbf{x})$]. However, in a typical electromagnetic experiment, it is unlikely that all of these source types will be simultaneously active. Finally, the perturbation wavefield is also sourced by *effective body sources* that depend on the material parameter perturbations:

$$\boldsymbol{\delta}\mathbf{j}_{eff}(\mathbf{x},t)\equiv\delta\sigma(\mathbf{x})\mathbf{e}(\mathbf{x},t),\qquad\text{(D1.4a)}$$

$$\boldsymbol{\delta}\mathbf{d}_{eff}(\mathbf{x},t)\equiv\delta\varepsilon(\mathbf{x})\mathbf{e}(\mathbf{x},t),\qquad\text{(D1.4b)}$$

$$\boldsymbol{\delta}\mathbf{b}_{eff}(\mathbf{x},t)\equiv\delta\mu(\mathbf{x})\mathbf{h}(\mathbf{x},t).\qquad\text{(D1.4c)}$$

Clearly, these effective body sources vanish at positions $\mathbf{x}$ in V where the material property perturbations equal zero. The sources are also directly proportional to the primary (or "incident" or "reference") electromagnetic field vectors $\mathbf{e}(\mathbf{x},t)$ and $\mathbf{h}(\mathbf{x},t)$.

The first Born approximation may be advantageously utilized in electromagnetic modeling in the following manner: First, given a "background" model represented by the three EM parameters

$\sigma(\mathbf{x}), \varepsilon(\mathbf{x}),$ and $\mu(\mathbf{x})$, the EH partial differential system (D1.1a,b) is solved for the electric vector **e**(**x**,*t*) and magnetic vector **h**(**x**,*t*) [subject to the boundary conditions (D1.1c,d) and initial conditions (D1.1e,f)]. This electromagnetic field is referred to as the "primary" or "incident" EM wavefield. During this modeling run **e**(**x**,*t*) and **h**(**x**,*t*) are stored at all positions **x** in the model where perturbations to the three medium parameters $\delta\sigma(\mathbf{x}), \delta\varepsilon(\mathbf{x}),$ and $\delta\mu(\mathbf{x})$ are subsequently inserted into the background model. Next, partial differential system (D1.3a,b) is solved for perturbations **δe**(**x**,*t*) and **δh**(**x**,*t*) to the primary electric and magnetic vectors. PDE system (D1.3a,b) is mathematically identical to the original system (D1.1a,b); only the right-hand-side terms representing body sources of EM waves change. Hence, the *same* numerical algorithm may be used for solution. According to equations (D1.4a,b,c), the effective body sources (conduction current, electric displacement, magnetic induction) for this second modeling run are localized in the EM earth model at precisely those positions where corresponding perturbations to medium parameters $\delta\sigma(\mathbf{x}), \delta\varepsilon(\mathbf{x}),$ and $\delta\mu(\mathbf{x})$ are inserted. The sources are directly proportional to the strength of the perturbations, as well as the primary field vectors. The total electromagnetic response at any receiver position $\mathbf{x}_r$ is well-approximated by the sums **e**($\mathbf{x}_r$,*t*) + **δe**($\mathbf{x}_r$,*t*) and **h**($\mathbf{x}_r$,*t*) + **δh**($\mathbf{x}_r$,*t*).

An advantage of this First Born Approximation approach is that it provides a mechanism for modeling the electromagnetic response to variations (or perturbations) in medium parameters that are small with respect to the spatial discretization basis (i.e., grid interval) of a numerical algorithm. The obvious disadvantages are that 1) two modeling runs are necessary, and 2) the mathematical underpinning of the approach is approximate. In particular, the method does not account for any wave scattering between the perturbations and the background earth model. Nevertheless, if the magnitudes of the perturbations are small, the First Born Approximation is considered by geophysicists to be reasonably accurate.

D2.0 Homogeneous Medium

The first-order "**δe-δh** system" (D1.3a and b) above applies to heterogeneous media. For homogeneous media (i.e., $\varepsilon(\mathbf{x}) = \varepsilon$, $\mu(\mathbf{x}) = \mu$, $\sigma(\mathbf{x}) = \sigma$), the equations may be combined to yield separated second-order partial differential equations for **δe** and **δh:**

$$\varepsilon\mu\frac{\partial^2\,\boldsymbol{\delta}\mathbf{e}(\mathbf{x},t)}{\partial t^2}+\sigma\mu\frac{\partial\,\boldsymbol{\delta}\mathbf{e}(\mathbf{x},t)}{\partial t}+\mathbf{curl}\;\mathbf{curl}\;\boldsymbol{\delta}\mathbf{e}(\mathbf{x},t)$$
$$=-\mu\frac{\partial\,\boldsymbol{\delta}\mathbf{j}_s(\mathbf{x},t)}{\partial t}-\mu\frac{\partial^2\,\boldsymbol{\delta}\mathbf{d}_s(\mathbf{x},t)}{\partial t^2}-\frac{\partial\,\mathbf{curl}\;\boldsymbol{\delta}\mathbf{b}_s(\mathbf{x},t)}{\partial t}$$
$$-\mu\frac{\partial\,\boldsymbol{\delta}\mathbf{j}_{eff}(\mathbf{x},t)}{\partial t}-\mu\frac{\partial^2\,\boldsymbol{\delta}\mathbf{d}_{eff}(\mathbf{x},t)}{\partial t^2}-\frac{\partial\,\mathbf{curl}\;\boldsymbol{\delta}\mathbf{b}_{eff}(\mathbf{x},t)}{\partial t},$$

$$\varepsilon\mu\frac{\partial^2\,\boldsymbol{\delta}\mathbf{h}(\mathbf{x},t)}{\partial t^2}+\sigma\mu\frac{\partial\,\boldsymbol{\delta}\mathbf{h}(\mathbf{x},t)}{\partial t}+\mathbf{curl}\;\mathbf{curl}\;\boldsymbol{\delta}\mathbf{h}(\mathbf{x},t)$$
$$=\mathbf{curl}\;\boldsymbol{\delta}\mathbf{j}_s(\mathbf{x},t)+\frac{\partial\,\mathbf{curl}\;\boldsymbol{\delta}\mathbf{d}_s(\mathbf{x},t)}{\partial t}-\sigma\frac{\partial\,\boldsymbol{\delta}\mathbf{b}_s(\mathbf{x},t)}{\partial t}-\varepsilon\frac{\partial^2\,\boldsymbol{\delta}\mathbf{b}_s(\mathbf{x},t)}{\partial t^2}$$
$$+\mathbf{curl}\;\boldsymbol{\delta}\mathbf{j}_{eff}(\mathbf{x},t)+\frac{\partial\,\mathbf{curl}\;\boldsymbol{\delta}\mathbf{d}_{eff}(\mathbf{x},t)}{\partial t}-\sigma\frac{\partial\,\boldsymbol{\delta}\mathbf{b}_{eff}(\mathbf{x},t)}{\partial t}-\varepsilon\frac{\partial^2\,\boldsymbol{\delta}\mathbf{b}_{eff}(\mathbf{x},t)}{\partial t^2}.$$

Note that each physical EM wavefield source term is mimicked by an analogous effective source (e.g., $\boldsymbol{\delta}\mathbf{j}_s(\mathbf{x},t)$ and $\boldsymbol{\delta}\mathbf{j}_{\text{eff}}(\mathbf{x},t)$, etc.). Eliminating the double **curl** partial differential operations via $\mathbf{curl}\;\mathbf{curl}=\mathbf{grad}\;\text{div}-\nabla^2$ yields the variants (next page):

$$\nabla^2 \boldsymbol{\delta e}(\mathbf{x},t) - \mathbf{grad}\ \mathrm{div}\ \boldsymbol{\delta e}(\mathbf{x},t) - \sigma\mu \frac{\partial\, \boldsymbol{\delta e}(\mathbf{x},t)}{\partial t} - \varepsilon\mu \frac{\partial^2\, \boldsymbol{\delta e}(\mathbf{x},t)}{\partial t^2}$$
$$= \mu \frac{\partial\, \boldsymbol{\delta j}_s(\mathbf{x},t)}{\partial t} + \mu \frac{\partial^2\, \boldsymbol{\delta d}_s(\mathbf{x},t)}{\partial t^2} + \frac{\partial\, \mathbf{curl}\, \boldsymbol{\delta b}_s(\mathbf{x},t)}{\partial t}$$
$$+ \mu \frac{\partial\, \boldsymbol{\delta j}_{eff}(\mathbf{x},t)}{\partial t} + \mu \frac{\partial^2\, \boldsymbol{\delta d}_{eff}(\mathbf{x},t)}{\partial t^2} + \frac{\partial\, \mathbf{curl}\, \boldsymbol{\delta b}_{eff}(\mathbf{x},t)}{\partial t}, \qquad \text{(D2.1a)}$$

$$\nabla^2 \boldsymbol{\delta h}(\mathbf{x},t) - \mathbf{grad}\ \mathrm{div}\ \boldsymbol{\delta h}(\mathbf{x},t) - \sigma\mu \frac{\partial\, \boldsymbol{\delta h}(\mathbf{x},t)}{\partial t} - \varepsilon\mu \frac{\partial^2\, \boldsymbol{\delta h}(\mathbf{x},t)}{\partial t^2}$$
$$= -\mathbf{curl}\, \boldsymbol{\delta j}_s(\mathbf{x},t) - \frac{\partial\, \mathbf{curl}\, \boldsymbol{\delta d}_s(\mathbf{x},t)}{\partial t} + \sigma \frac{\partial\, \boldsymbol{\delta b}_s(\mathbf{x},t)}{\partial t} + \varepsilon \frac{\partial^2\, \boldsymbol{\delta b}_s(\mathbf{x},t)}{\partial t^2}$$
$$- \mathbf{curl}\, \boldsymbol{\delta j}_{eff}(\mathbf{x},t) - \frac{\partial\, \mathbf{curl}\, \boldsymbol{\delta d}_{eff}(\mathbf{x},t)}{\partial t} + \sigma \frac{\partial\, \boldsymbol{\delta b}_{eff}(\mathbf{x},t)}{\partial t} + \varepsilon \frac{\partial^2\, \boldsymbol{\delta b}_{eff}(\mathbf{x},t)}{\partial t^2}. \qquad \text{(D2.1b)}$$

The left-hand-sides of these two equations have the same mathematical form. We now investigate whether the two **grad** div terms can be eliminated in favor of electromagnetic body sources, as in Appendix A. Pursuing exactly the same analysis as there yields the two expressions

$$\mathbf{grad}\ \mathrm{div}\ \boldsymbol{\delta e}(\mathbf{x},t) = -\frac{1}{\varepsilon} H(t) \exp\left(-\frac{\sigma}{\varepsilon} t\right) * \left\{ \mathbf{grad}\ \mathrm{div}\left(\boldsymbol{\delta j}_s(\mathbf{x},t) + \boldsymbol{\delta j}_{eff}(\mathbf{x},t)\right) \right.$$
$$\left. \mathbf{grad}\ \mathrm{div}\left(\boldsymbol{\delta j}_s(\mathbf{x},t) + \boldsymbol{\delta j}_{eff}(\mathbf{x},t)\right) \right\},$$

and

$$\mathbf{grad}\ \mathrm{div}\ \boldsymbol{\delta h}(\mathbf{x},t) = -\frac{1}{\mu} \mathbf{grad}\ \mathrm{div}\left(\boldsymbol{\delta b}_s(\mathbf{x},t) + \boldsymbol{\delta b}_{eff}(\mathbf{x},t)\right).$$

Interestingly, whenever a physical body source term appears, it is coupled with the analogous effective body source term. Substituting these expressions into equations (D2.1a and b) yields

$$\nabla^2 \boldsymbol{\delta e}(\mathbf{x},t) - \sigma\mu \frac{\partial\, \boldsymbol{\delta e}(\mathbf{x},t)}{\partial t} - \varepsilon\mu \frac{\partial^2\, \boldsymbol{\delta e}(\mathbf{x},t)}{\partial t^2}$$
$$= \mu \frac{\partial}{\partial t}\left(\boldsymbol{\delta j}_s(\mathbf{x},t) + \boldsymbol{\delta j}_{eff}(\mathbf{x},t)\right) + \mu \frac{\partial^2}{\partial t^2}\left(\boldsymbol{\delta d}_s(\mathbf{x},t) + \boldsymbol{\delta d}_{eff}(\mathbf{x},t)\right)$$
$$+ \frac{\partial}{\partial t}\left(\mathbf{curl}\, \boldsymbol{\delta b}_s(\mathbf{x},t) + \mathbf{curl}\, \boldsymbol{\delta b}_{eff}(\mathbf{x},t)\right),$$
$$- \frac{1}{\varepsilon} H(t) \exp\left(-\frac{\sigma}{\varepsilon} t\right) * \left\{ \mathbf{grad}\ \mathrm{div}\left(\boldsymbol{\delta j}_s(\mathbf{x},t) + \boldsymbol{\delta j}_{eff}(\mathbf{x},t)\right) \right.$$
$$\left. + \frac{\partial}{\partial t} \mathbf{grad}\ \mathrm{div}\left(\boldsymbol{\delta d}_s(\mathbf{x},t) + \boldsymbol{\delta d}_{eff}(\mathbf{x},t)\right) \right\}, \qquad \text{(D2.2a)}$$

and

$$\nabla^2\boldsymbol{\delta h}(\mathbf{x},t)-\sigma\mu\frac{\partial\,\boldsymbol{\delta h}(\mathbf{x},t)}{\partial t}-\varepsilon\mu\frac{\partial^2\,\boldsymbol{\delta h}(\mathbf{x},t)}{\partial t^2}$$
$$=-\mathbf{curl}\left(\boldsymbol{\delta j}_s(\mathbf{x},t)+\boldsymbol{\delta j}_{eff}(\mathbf{x},t)\right)-\frac{\partial}{\partial t}\left(\mathbf{curl}\,\boldsymbol{\delta d}_s(\mathbf{x},t)+\mathbf{curl}\,\boldsymbol{\delta d}_{eff}(\mathbf{x},t)\right)$$
$$+\sigma\frac{\partial}{\partial t}\left(\boldsymbol{\delta b}_s(\mathbf{x},t)+\boldsymbol{\delta b}_{eff}(\mathbf{x},t)\right)+\varepsilon\frac{\partial^2}{\partial t^2}\left(\boldsymbol{\delta b}_s(\mathbf{x},t)+\boldsymbol{\delta b}_{eff}(\mathbf{x},t)\right)$$
$$-\frac{1}{\mu}\mathbf{grad}\,\mathrm{div}\left(\boldsymbol{\delta b}_s(\mathbf{x},t)+\boldsymbol{\delta b}_{eff}(\mathbf{x},t)\right). \qquad \text{(D2.2b)}$$

These have the same mathematical forms as partial differential equations (A2.4a and b) in Appendix A for the primary electric and magnetic fields $\mathbf{e}(\mathbf{x},t)$ and $\mathbf{h}(\mathbf{x},t)$, respectively. In the common case where there are no additional body sources $\boldsymbol{\delta j}_s$, $\boldsymbol{\delta d}_s$, and $\boldsymbol{\delta b}_s$ active in the perturbed medium, then the secondary or scattered fields are governed by the simpler PDEs:

$$\nabla^2\boldsymbol{\delta e}(\mathbf{x},t)-\sigma\mu\frac{\partial\,\boldsymbol{\delta e}(\mathbf{x},t)}{\partial t}-\varepsilon\mu\frac{\partial^2\,\boldsymbol{\delta e}(\mathbf{x},t)}{\partial t^2}$$
$$=\mu\frac{\partial}{\partial t}\boldsymbol{\delta j}_{eff}(\mathbf{x},t)+\mu\frac{\partial^2}{\partial t^2}\boldsymbol{\delta d}_{eff}(\mathbf{x},t)+\frac{\partial}{\partial t}\mathbf{curl}\,\boldsymbol{\delta b}_{eff}(\mathbf{x},t)$$
$$-\frac{1}{\varepsilon}H(t)\exp\left(-\frac{\sigma}{\varepsilon}t\right)*\left\{\mathbf{grad}\,\mathrm{div}\,\boldsymbol{\delta j}_{eff}(\mathbf{x},t)+\frac{\partial}{\partial t}\mathbf{grad}\,\mathrm{div}\,\boldsymbol{\delta d}_{eff}(\mathbf{x},t)\right\}, \qquad \text{(D2.3a)}$$

and

$$\nabla^2\boldsymbol{\delta h}(\mathbf{x},t)-\sigma\mu\frac{\partial\,\boldsymbol{\delta h}(\mathbf{x},t)}{\partial t}-\varepsilon\mu\frac{\partial^2\,\boldsymbol{\delta h}(\mathbf{x},t)}{\partial t^2}$$
$$=-\mathbf{curl}\,\boldsymbol{\delta j}_{eff}(\mathbf{x},t)-\frac{\partial}{\partial t}\mathbf{curl}\,\boldsymbol{\delta d}_{eff}(\mathbf{x},t)+\sigma\frac{\partial}{\partial t}\boldsymbol{\delta b}_{eff}(\mathbf{x},t)+\varepsilon\frac{\partial^2}{\partial t^2}\boldsymbol{\delta b}_{eff}(\mathbf{x},t)$$
$$-\frac{1}{\mu}\mathbf{grad}\,\mathrm{div}\,\boldsymbol{\delta b}_{eff}(\mathbf{x},t). \qquad \text{(D2.3b)}$$

The scattered electromagnetic fields arise solely from spatially-dependent perturbations $\delta\varepsilon(\mathbf{x})$, $\delta\mu(\mathbf{x})$, and $\delta\sigma(\mathbf{x})$ in the medium properties. Often, the transition frequency $\omega_t = \sigma/\varepsilon$ is so large that the convolutional source term can be neglected.

D3.0 A Born Series

The focus of the present work is the *First* Born Approximation (FBA). However, there is some interest in the relationship of the FBA to *higher-order* Born Approximations (i.e., second, third,…and so on). We develop one such relationship in this sub-section. The mathematical approach is identical to that used by Snieder and Aldridge (1995) to develop higher-order perturbations to the eikonal equation for seismic wave propagation traveltimes.

The point of departure for the analysis is the first-order EH partial differential system (D1.1a,b) governing the electric vector $\mathbf{e}(\mathbf{x},t)$ and magnetic vector $\mathbf{h}(\mathbf{x},t)$. As before, perturb the medium supporting EM wave propagation/diffusion according to

$$\varepsilon(\mathbf{x}) = \varepsilon_0(\mathbf{x}) + \eta\delta\varepsilon(\mathbf{x}), \qquad \mu(\mathbf{x}) = \mu_0(\mathbf{x}) + \eta\delta\mu(\mathbf{x}), \qquad \sigma(\mathbf{x}) = \sigma_0(\mathbf{x}) + \eta\delta\sigma(\mathbf{x}), \qquad \text{(D3.1a,b,c)}$$

where η is a small dimensionless number ($0 < \eta < 1$) (basically, a bookkeeping parameter for the subsequent expansions). Then, we assume that the EM wavefields can be expressed via the infinite series

$$\mathbf{e}(\mathbf{x},t) = \mathbf{e}_0(\mathbf{x},t) + \sum_{n=1}^{\infty}\eta^n\mathbf{e}_n(\mathbf{x},t), \qquad \mathbf{h}(\mathbf{x},t) = \mathbf{h}_0(\mathbf{x},t) + \sum_{n=1}^{\infty}\eta^n\mathbf{h}_n(\mathbf{x},t). \qquad \text{(D3.2a,b)}$$

Subscript $n = 0,1,2,\ldots$ refers to the "order" of the EM wavefield perturbations. We tacitly assume that the series expansions exist, in the sense of converging to finite values. Proof of this proposition is well beyond the scope of this investigation; in fact, convergence is almost certainly situation (i.e., model) dependent.

Substitute the perturbations (D3.1a,b,c) and the series expansions (D3.2a,b) into EH system, and collect terms in powers of η. The Ampere-Maxwell Law (D1.1a) becomes.

$$\begin{aligned}
&\left\{\varepsilon_0(\mathbf{x})\frac{\partial\,\mathbf{e}_0(\mathbf{x},t)}{\partial t} + \sigma_0(\mathbf{x})\mathbf{e}_0(\mathbf{x},t) - \mathbf{curl}\,\mathbf{h}_0(\mathbf{x},t) + \mathbf{j}_s(\mathbf{x},t) + \frac{\partial\mathbf{d}_s(\mathbf{x},t)}{\partial t}\right\}\\
&+\eta\left\{\varepsilon_0(\mathbf{x})\frac{\partial\,\mathbf{e}_1(\mathbf{x},t)}{\partial t} + \sigma_0(\mathbf{x})\mathbf{e}_1(\mathbf{x},t) - \mathbf{curl}\,\mathbf{h}_1(\mathbf{x},t) + \delta\sigma(\mathbf{x})\mathbf{e}_0(\mathbf{x},t) + \delta\varepsilon(\mathbf{x})\frac{\partial\,\mathbf{e}_0(\mathbf{x},t)}{\partial t}\right\}\\
&+\eta^2\left\{\varepsilon_0(\mathbf{x})\frac{\partial\,\mathbf{e}_2(\mathbf{x},t)}{\partial t} + \sigma_0(\mathbf{x})\mathbf{e}_2(\mathbf{x},t) - \mathbf{curl}\,\mathbf{h}_2(\mathbf{x},t) + \delta\sigma(\mathbf{x})\mathbf{e}_1(\mathbf{x},t) + \delta\varepsilon(\mathbf{x})\frac{\partial\,\mathbf{e}_1(\mathbf{x},t)}{\partial t}\right\}\\
&+\cdots+\eta^n\left\{\varepsilon_0(\mathbf{x})\frac{\partial\,\mathbf{e}_n(\mathbf{x},t)}{\partial t} + \sigma_0(\mathbf{x})\mathbf{e}_n(\mathbf{x},t) - \mathbf{curl}\,\mathbf{h}_n(\mathbf{x},t) + \delta\sigma(\mathbf{x})\mathbf{e}_{n-1}(\mathbf{x},t) + \delta\varepsilon(\mathbf{x})\frac{\partial\,\mathbf{e}_{n-1}(\mathbf{x},t)}{\partial t}\right\} = 0.
\end{aligned} \qquad \text{(D3.3a)}$$

The Faraday Law (D1.1b) becomes

$$\begin{aligned}
&\left\{\mu_0(\mathbf{x})\frac{\partial\,\mathbf{h}_0(\mathbf{x},t)}{\partial t} + \mathbf{curl}\,\mathbf{e}_0(\mathbf{x},t) + \frac{\partial\mathbf{b}_s(\mathbf{x},t)}{\partial t}\right\}\\
&+\eta\left\{\mu_0(\mathbf{x})\frac{\partial\,\mathbf{h}_1(\mathbf{x},t)}{\partial t} + \mathbf{curl}\,\mathbf{e}_1(\mathbf{x},t) + \delta\mu(\mathbf{x})\frac{\partial\mathbf{h}_0(\mathbf{x},t)}{\partial t}\right\}\\
&+\eta^2\left\{\mu_0(\mathbf{x})\frac{\partial\,\mathbf{h}_2(\mathbf{x},t)}{\partial t} + \mathbf{curl}\,\mathbf{e}_2(\mathbf{x},t) + \delta\mu(\mathbf{x})\frac{\partial\mathbf{h}_1(\mathbf{x},t)}{\partial t}\right\}\\
&+\cdots+\eta^n\left\{\mu_0(\mathbf{x})\frac{\partial\,\mathbf{h}_n(\mathbf{x},t)}{\partial t} + \mathbf{curl}\,\mathbf{e}_n(\mathbf{x},t) + \delta\mu(\mathbf{x})\frac{\partial\mathbf{h}_{n-1}(\mathbf{x},t)}{\partial t}\right\} = 0.
\end{aligned} \qquad \text{(D3.3b)}$$

Both equations can be satisfied by equating terms in successive powers of parameter η to zero. This yields the following progression of EH PDE systems:

***Zeroth-order EH system*:**

$$\varepsilon_0(\mathbf{x})\frac{\partial \mathbf{e}_0(\mathbf{x},t)}{\partial t}+\sigma_0(\mathbf{x})\mathbf{e}_0(\mathbf{x},t)-\mathbf{curl}\,\mathbf{h}_0(\mathbf{x},t)=-\mathbf{j}_s(\mathbf{x},t)-\frac{\partial \mathbf{d}_s(\mathbf{x},t)}{\partial t}, \tag{D3.4a}$$

$$\mu_0(\mathbf{x})\frac{\partial \mathbf{h}_0(\mathbf{x},t)}{\partial t}+\mathbf{curl}\,\mathbf{e}_0(\mathbf{x},t)=-\frac{\partial \mathbf{b}_s(\mathbf{x},t)}{\partial t}. \tag{D3.4b}$$

***First-order EH system*:**

$$\varepsilon_0(\mathbf{x})\frac{\partial \mathbf{e}_1(\mathbf{x},t)}{\partial t}+\sigma_0(\mathbf{x})\mathbf{e}_1(\mathbf{x},t)-\mathbf{curl}\,\mathbf{h}_1(\mathbf{x},t)=-\delta\sigma(\mathbf{x})\mathbf{e}_0(\mathbf{x},t)-\delta\varepsilon(\mathbf{x})\frac{\partial \mathbf{e}_0(\mathbf{x},t)}{\partial t}, \tag{D3.5a}$$

$$\mu_0(\mathbf{x})\frac{\partial \mathbf{h}_1(\mathbf{x},t)}{\partial t}+\mathbf{curl}\,\mathbf{e}_1(\mathbf{x},t)=-\delta\mu(\mathbf{x})\frac{\partial \mathbf{h}_0(\mathbf{x},t)}{\partial t}. \tag{D3.5b}$$

***Second-order EH system*:**

$$\varepsilon_0(\mathbf{x})\frac{\partial \mathbf{e}_2(\mathbf{x},t)}{\partial t}+\sigma_0(\mathbf{x})\mathbf{e}_2(\mathbf{x},t)-\mathbf{curl}\,\mathbf{h}_2(\mathbf{x},t)=-\delta\sigma(\mathbf{x})\mathbf{e}_1(\mathbf{x},t)-\delta\varepsilon(\mathbf{x})\frac{\partial \mathbf{e}_1(\mathbf{x},t)}{\partial t}, \tag{D3.6a}$$

$$\mu_0(\mathbf{x})\frac{\partial \mathbf{h}_2(\mathbf{x},t)}{\partial t}+\mathbf{curl}\,\mathbf{e}_2(\mathbf{x},t)=-\delta\mu(\mathbf{x})\frac{\partial \mathbf{h}_1(\mathbf{x},t)}{\partial t}. \tag{D3.6b}$$

***nth-order EH system*:**

$$\varepsilon_0(\mathbf{x})\frac{\partial \mathbf{e}_n(\mathbf{x},t)}{\partial t}+\sigma_0(\mathbf{x})\mathbf{e}_n(\mathbf{x},t)-\mathbf{curl}\,\mathbf{h}_n(\mathbf{x},t)=-\delta\sigma(\mathbf{x})\mathbf{e}_{n-1}(\mathbf{x},t)-\delta\varepsilon(\mathbf{x})\frac{\partial \mathbf{e}_{n-1}(\mathbf{x},t)}{\partial t}, \tag{D3.7a}$$

$$\mu_0(\mathbf{x})\frac{\partial \mathbf{h}_n(\mathbf{x},t)}{\partial t}+\mathbf{curl}\,\mathbf{e}_n(\mathbf{x},t)=-\delta\mu(\mathbf{x})\frac{\partial \mathbf{h}_{n-1}(\mathbf{x},t)}{\partial t}. \tag{D3.7b}$$

Note that the coefficients on the left-hand-sides of all systems are the EM medium parameters of the "zeroth-order" or "background" or "reference" earth model. Hence, the *n*th-order perturbations are thought of as propagating within the zero-order earth model. Also, in developing the above PDE systems, we have not utilized any approximations, as in neglecting product terms in the previous derivation of the FBA. An obvious solution strategy for this recurrent system of PDEs is as follows:

Solve the zeroth-order EH system first, with physical body source terms on the right-hand-sides. Then solve the first-order EH system with effective body sources that depend on zeroth-order solution. This first-order solution is the classical "First Born Approximation". Then, solve the second-order EH system with effective body sources that depend on first-order solution. And so on… The same numerical algorithm can be used to solve for each perturbation order, because each of the above PDE systems is the same mathematical EH system. The approach is algorithmically achievable because the effective body sources for the n^{th}-order EH system depend on the previously-calculated $(n\text{-}1)^{\text{th}}$-order wavefield perturbations.

Finally, the total EM field propagating in the perturbed model (D3.1a,b,c) is constructed via the finite sums

$$\mathbf{e}(\mathbf{x},t) = \mathbf{e}_0(\mathbf{x},t) + \sum_{n=1}^{N} \eta^n \mathbf{e}_n(\mathbf{x},t), \qquad \mathbf{h}(\mathbf{x},t) = \mathbf{h}_0(\mathbf{x},t) + \sum_{n=1}^{N} \eta^n \mathbf{h}_n(\mathbf{x},t), \tag{D3.8a,b}$$

where the sums are truncated at N terms. An obvious question is "How is the numerical value of parameter η chosen?"; $\eta = 1$ is the logical choice. However, we remark that equations (D3.8a and b) present a very inefficient means for conducting forward modeling of an EM wavefield; a total of N+1 forward modeling runs is required to synthesize **e** and **h**! Rather, a modern modeler would simply substitute the perturbed model (D3.1a,b,c) into the EH system (D1.1a,b,c) and pull the trigger (once) on a favored numerical algorithm.

Perhaps the n^{th} Born Approximation $\mathbf{e}_n(\mathbf{x},t)$ and $\mathbf{h}_n(\mathbf{x},t)$ possesses theoretical or pedagogical utility.

For the case of a finite-thickness geologic layer with a conductivity contrast, the *First* Born Approximation wavefield *within* the layer $z_{top} < z < z_{bot}$ is given by equation (7.29) of the text, repeated here as:

$$E_B(z,\omega)\big|_{\Delta\sigma} = \frac{(\sigma_2 - \sigma_1)}{2} \frac{\mu_1(-i\omega)E_{inc}(z,\omega)}{K_1(\omega)^2} \times \frac{1}{2}\left\{ \left[1 - 2iK_1(\omega)\left(z - z_{mid} + \frac{h}{2} \right) \right] e^{+iK_1(\omega)(h/2)} - 1 \right\}. \tag{7.29 again}$$

In the notation of the present Appendix D, this is interpreted as the electric field solution $\mathbf{e}_1(\mathbf{x},t)$ of the *first*-order EH system (D3.5a,b) above (for the case when $\delta\varepsilon(\mathbf{x}) = \delta\mu(\mathbf{x}) = 0$). So, similar to equation (7.21a) of the text, the effective current density body source for the *second*-order EH system (D3.6a,b) is

$$j_{sx}^{2nd-B}(z,t) = (\sigma_2 - \sigma_1)\, e_1(z,\omega)\, \Pi\left(\frac{z - z_{mid}}{h} \right), \tag{D3.9a}$$

or, after Fourier transforming to the frequency-domain

$$J_{sx}^{2nd-B}(z,\omega) = (\sigma_2 - \sigma_1)\, E_1(z,\omega)\, \Pi\left(\frac{z - z_{mid}}{h} \right). \tag{D3.9b}$$

We could attempt to develop a solution for the *Second* Born Approximation (SBA) wavefield by Fourier transforming to the wavenumber (k) domain and following the analysis of the previous sub-section 7.3. However, all we do here is note that the SBA effective current density source is proportional to the *squared* conductivity contrast $(\sigma_2 - \sigma_1)^2$ and the incident wavefield $E_{inc}(z,\omega)$. Compare with the FBA source of equation (7.24). The detailed development of the SBA scattered field term is left for the future.

14.0 APPENDIX E: FREQUENCY SPECTRUM OF AN ALTERNATING POLARITY PULSE SEQUENCE

A common energy source signal used in electromagnetic (EM) geophysical prospecting consists of a periodic sequence of square pulses with alternating polarity. After transients associated with signal turn-on have decayed, the signal observed at a remote sensor will also be an alternating polarity pulse sequence with the same period. However, the pulse shape is no longer square due to attenuation and dispersion of the propagating/diffusing EM wave. In this Appendix, we develop formulae for the frequency spectrum of an alternating polarity pulse sequence. The formulae contain three parameters (fundamental period P, number of periods N_P, and in the duty cycle percentage d) that can be adjusted to optimize various aspects of the frequency spectrum.

E1.0 Transform of a Pulse Sequence

Let $w(t)$ be a time-domain wavelet (or pulse) with frequency-domain Fourier spectrum $W(\omega)$. Then, a finite sequence of N alternating-polarity pulses may be constructed via

$$s(t) = \sum_{n=0}^{N-1} (-1)^n \, w(t - nT) \,, \tag{E1.1}$$

where T is a fixed lag time (or delay time) between successive pulses. The Fourier transform of the pulse sequence $s(t)$ is easily calculated as

$$S(\omega) = W(\omega) \sum_{n=0}^{N-1} (-1)^n e^{+i\omega nT} = W(\omega) \sum_{n=0}^{N-1} \left(-e^{+i\omega T} \right)^n = W(\omega) \left[\frac{1 - \left(-e^{+i\omega T} \right)^N}{1 - \left(-e^{+i\omega T} \right)} \right] = W(\omega) \left[\frac{1 - (-1)^N e^{+iN\omega T}}{1 + e^{+i\omega T}} \right]. \tag{E1.2}$$

The finite sum has been evaluated via the famous geometric progression formula

$$\sum_{n=0}^{N-1} z^n = \frac{1 - z^N}{1 - z}, \tag{E1.3a}$$

where z is a complex number. Interestingly, if the modulus of z is less than unity, then the limit of equation (E1.3a) as N approaches infinity yields

$$\lim_{N \to \infty} \sum_{n=0}^{N-1} z^n = \sum_{n=0}^{\infty} z^n = \lim_{N \to \infty} \frac{1 - z^N}{1 - z} = \frac{1}{1 - z} \,. \tag{E1.3b}$$

However, we cannot take advantage of this result in the Fourier transform expression (E1.2) above, as the modulus of $z = -e^{+i\omega T}$ is exactly unity.

Equation (E1.2) indicates that the Fourier transform of a pulse sequence is obtained by multiplying the transform of the underlying pulse by a complex-valued factor (in square bracketes0. Our primary concern here is with the amplitude spectrum of the pulse sequence. This is easily calculated as

$$\left| S(\omega) \right| = \left| W(\omega) \right| \sqrt{\frac{1 - (-1)^N \cos(N\omega T)}{1 + \cos(\omega T)}} \,. \tag{E1.4}$$

Pulse sequence (E1.1) is parameterized in terms of 1) the lag time between successive pulses T, and 2) the total number of pulses N. However, from the vantage point of electromagnetic geophysics, perhaps a more useful parameterization involves the fundamental period P of the pulse sequence, and the total number of periods N_P. For an alternating-polarity sequence, the period is just

$$P = 2T \,. \tag{E1.5a}$$

That is, the period is twice the lag time. Furthermore, it is useful (and simple) to restrict consideration to an integer number of periods. The number of pulses is then

$$N = 2N_P \,. \tag{E1.5b}$$

That is, there are two pulses per period. [An obvious implication is that we do not consider sequences consisting of an odd number of pulses, which would have a non-zero dc spectral value equal to the area under a single pulse.] Amplitude spectrum (E1.4) becomes

$$\left|S(\omega)\right| = \left|W(\omega)\right| \sqrt{\frac{1-\cos(\omega P N_P)}{1+\cos(\omega P/2)}} \,. \tag{E1.6}$$

If waveform $w(t)$ is the Dirac delta function $\delta(t)$, then the amplitude spectrum $|W(\omega)| = 1$. Hence, the second factor in equation (E1.6) is just the amplitude spectrum of an alternating polarity "spike sequence". The following set of eight panels depicts the amplitude of this factor as a function of frequency over the range $f = 0$ Hz to $f = 6$ Hz. The fundamental period is fixed at $P = 1$ s, and the number of periods increases from $N_P = 1$ to $N_p = 128$ in powers of 2. Note that the logarithmic amplitude spectrum $\log_{10}\left(A(f)/A_{ref}\right)$ is plotted, with respect to reference value $A_{ref} = 1$ s = 1/Hz. Spectral peaks are located at odd integer multiples of the fundamental frequency $1/P = 1$ Hz (where the denominator in (E1.6) vanishes). These "primary peaks" increase in height and decrease in width as N_P increases. Additionally, numerous secondary peaks and zeros appear between the primary peaks. Since the interval between an adjacent secondary peak and zero diminishes as N_P increases, it is difficult to state just what value the spectrum assumes between primary peaks. However, the envelope of the spectrum $\left[1+\cos(\pi f P)\right]^{-1/2}$ is independent of N_P and remains invariant.

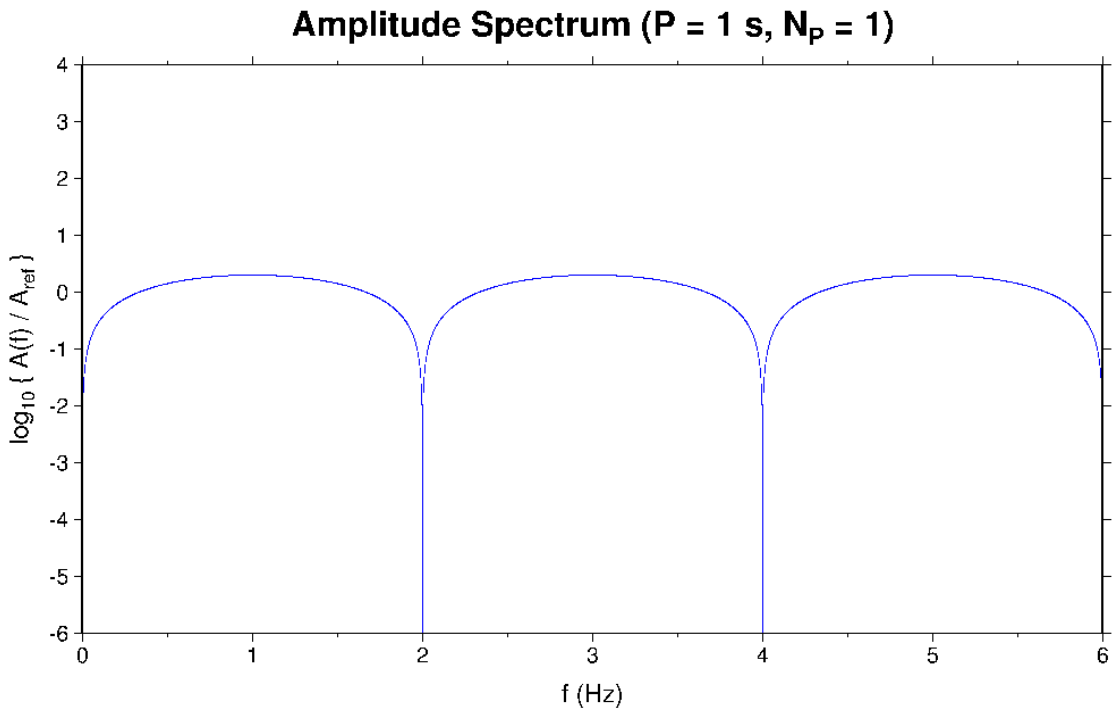

Figure E1a. Amplitude spectrum of an alternating polarity spike sequence with a single period $N_P = 1$.

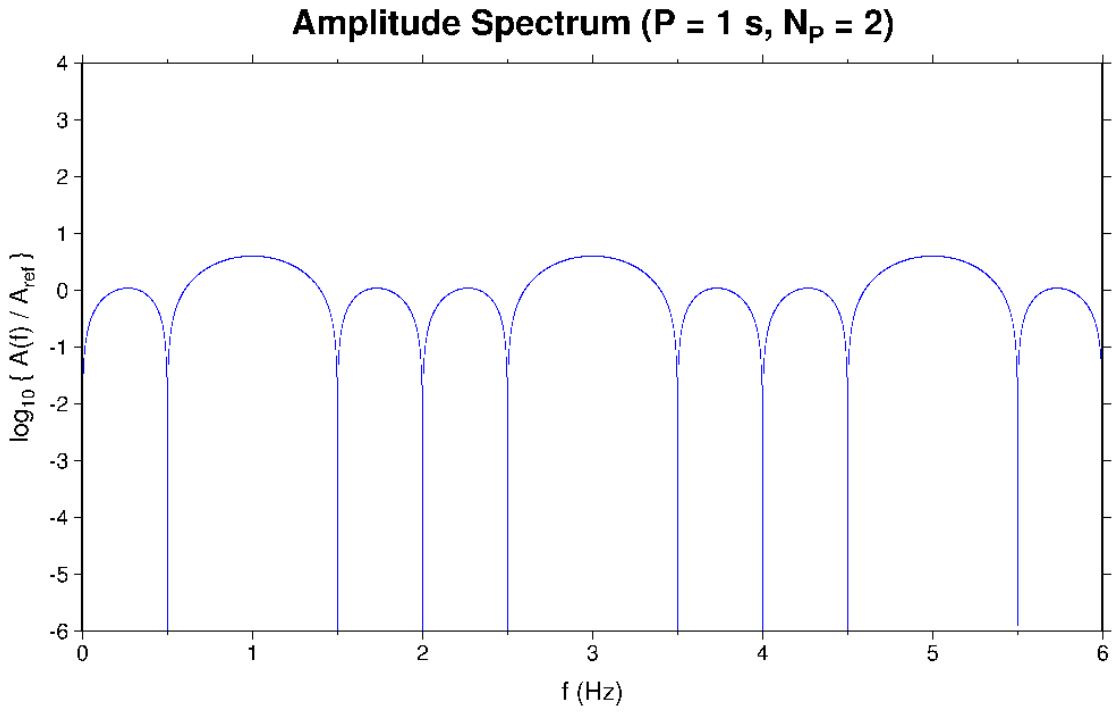

Figure E1b. $N_P = 2$.

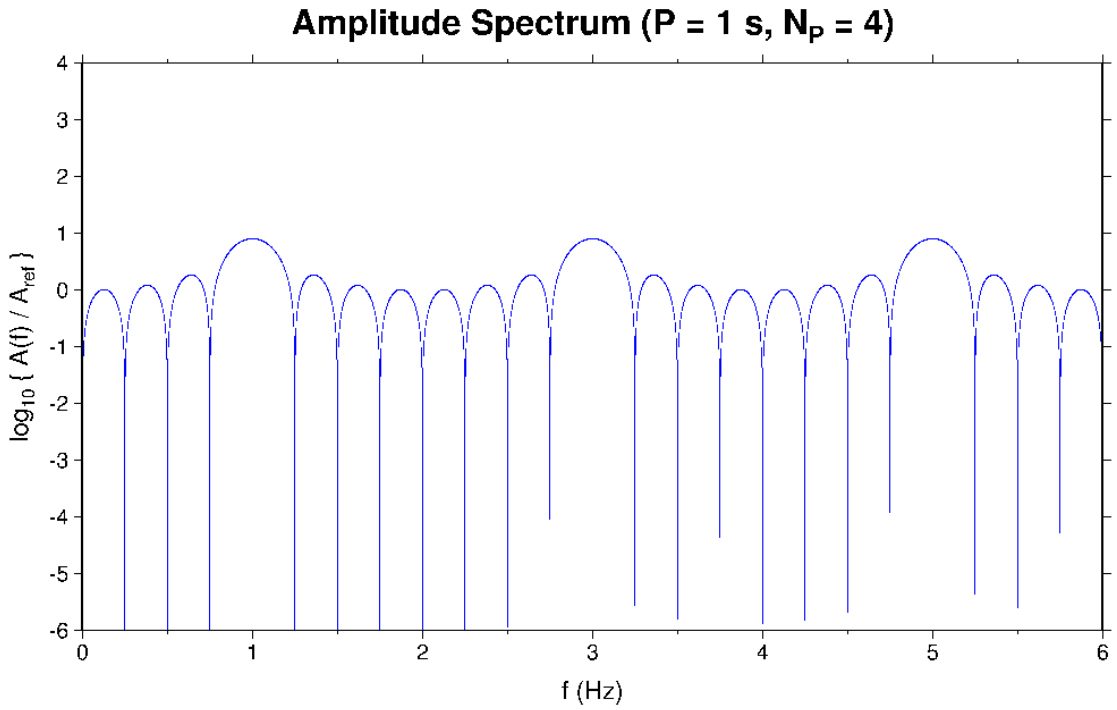

Figure E1c. $N_P = 4$.

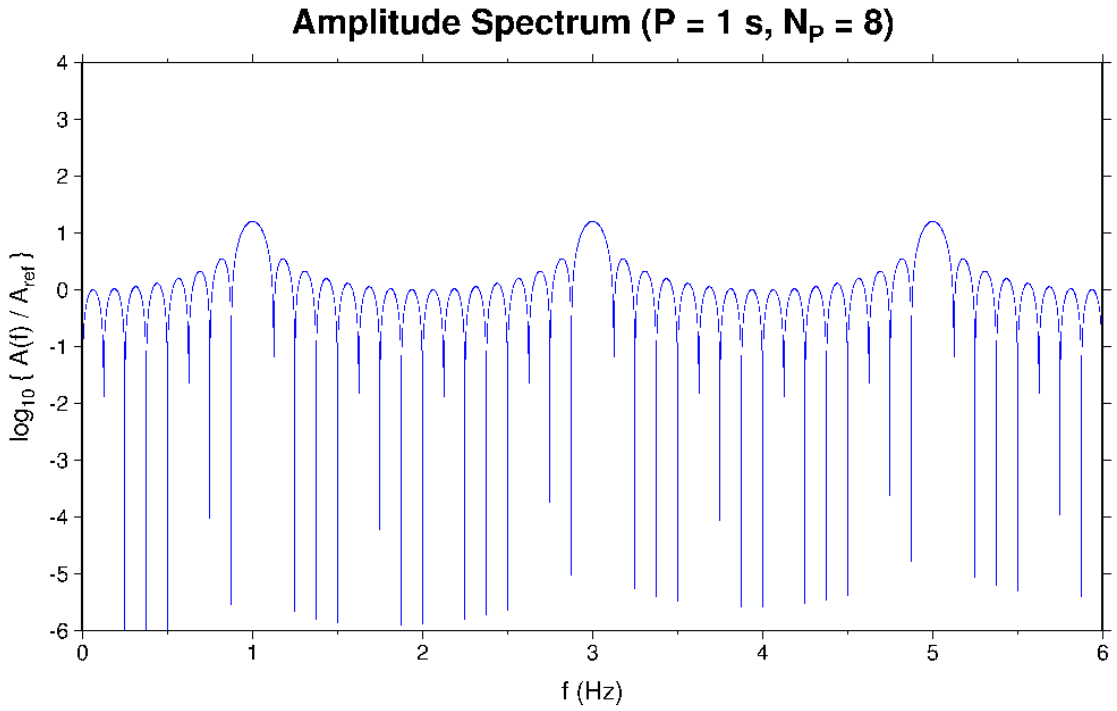

Figure E1d. $N_P = 8$.

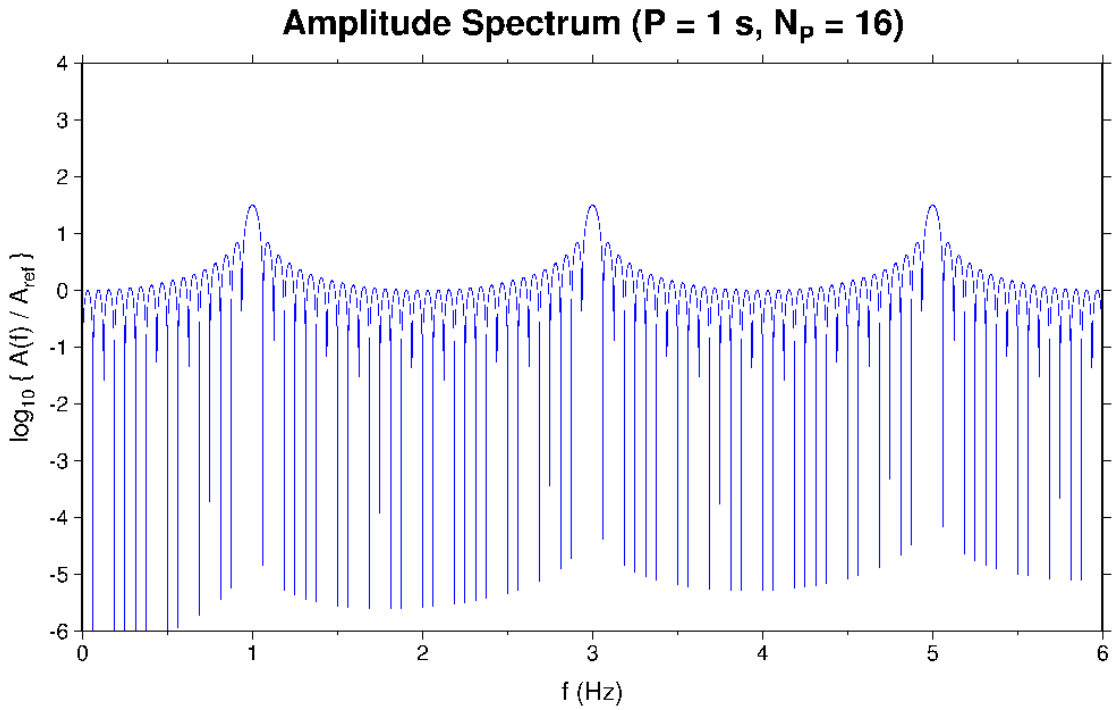

Figure E1e. $N_P = 16$.

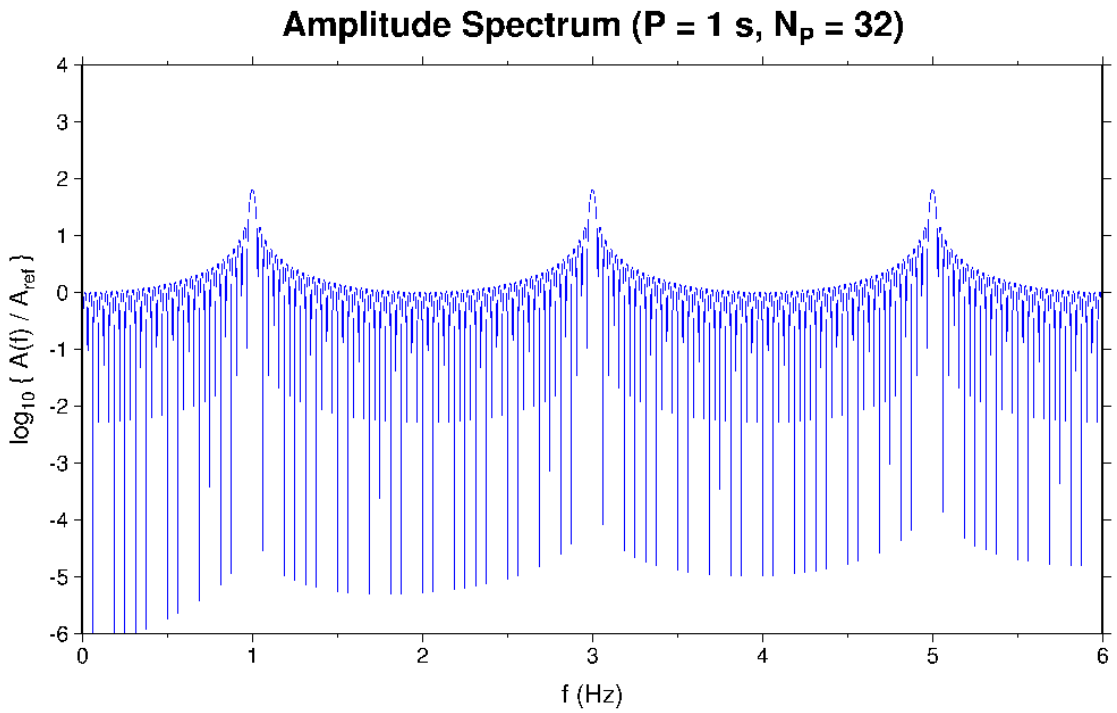

Figure E1f. $N_P = 32$.

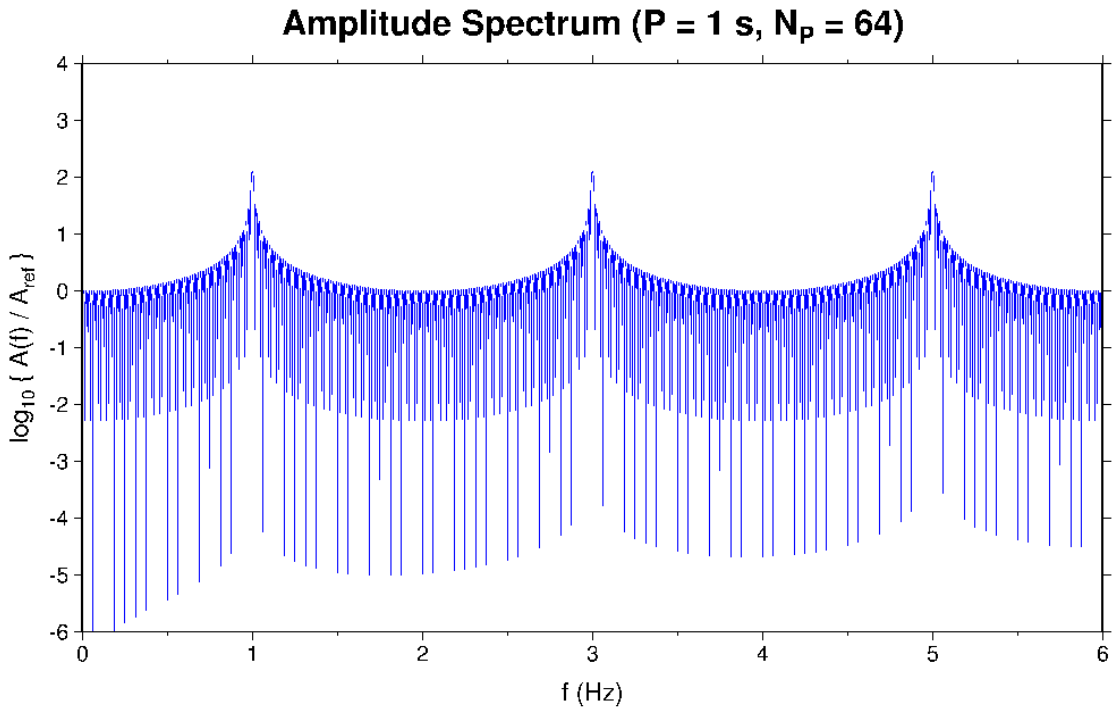

Figure E1g. $N_P = 64$.

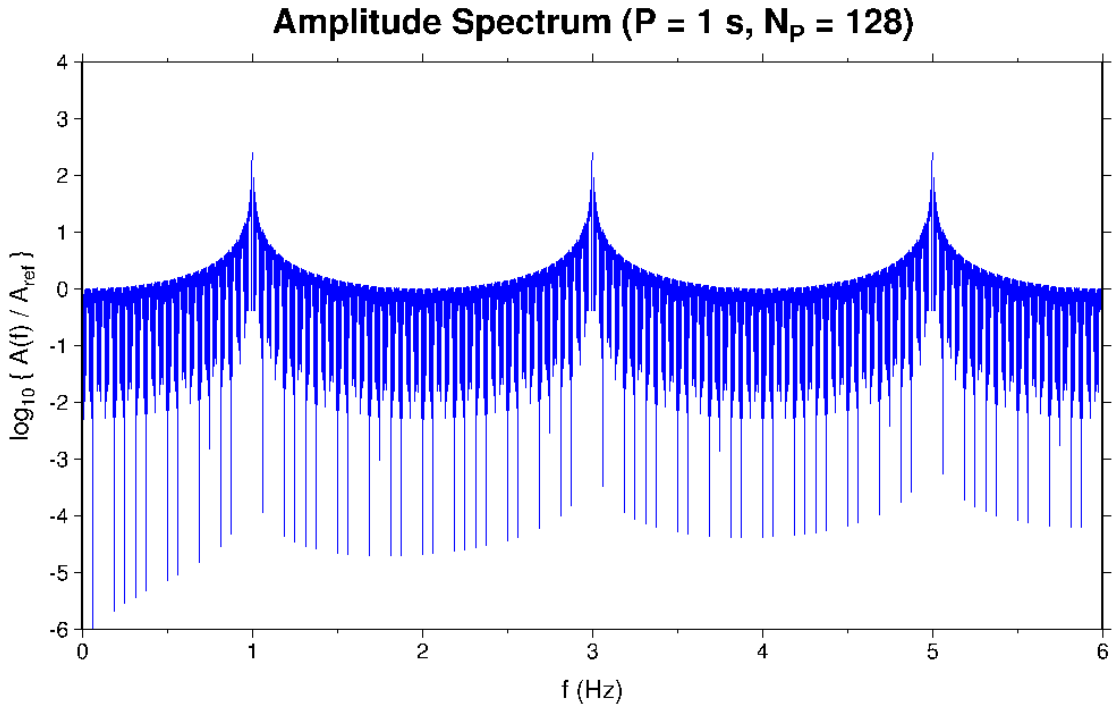

Figure E1h. $N_P = 128$.

E1.1 Peak Amplitude Analysis

The zeros of the denominator in the second factor (i.e., containing the square root) in equation (E1.4) occur at

$$f_l = \frac{2l-1}{P} \quad \text{for } l = 1,2,3,\ldots \tag{E1.7}$$

However, this factor is indeterminate (~0/0) at these frequencies, rather than infinite. Utilize L'Hopital's rule to determine the peak amplitude at these frequencies. Let $B(f)$ denote the argument of the square root in (E1.6):

$$B(f) = \frac{1-\cos(2\pi f P N_P)}{1+\cos(\pi f P)}.$$

Next, let the notation $\widehat{B}(f)$ refer to differentiating both the numerator and denominator, as required for application of L'Hopital's rule. Then

$$\widehat{B}(f) = -2N_P \frac{\sin(2\pi f P N_P)}{\sin(\pi f P)}, \qquad \text{and} \qquad \widehat{\widehat{B}}(f) = -4N_P^2 \frac{\cos(2\pi f P N_P)}{\cos(\pi f P)}.$$

It is straightforward to demonstrate that $\lim_{f \to (2l-1)/P} \widehat{\widehat{B}}(f) = 4N_P^2$. Hence, the peak spectral amplitude value at frequency f_l is given by

$$\left|S(f_l)\right| = 2N_P \left|W(f_l)\right|. \tag{E1.8}$$

The peak amplitude is directly proportional to the number of periods N_P; amplitude increases without bound as $N_P \rightarrow \infty$.

E2.0 Square Pulse

A commonly-used source pulse in electromagnetic geophysical prospecting is the square (or "boxcar") pulse

$$w(t) = \Pi\left(\frac{t - T_{box}/2}{T_{box}}\right), \tag{E2.1}$$

where $\Pi(x)$ is the rectangle function of unit height and area ($\Pi(x) = 1$ for $|x| \le 1/2$, zero otherwise). The square pulse duration time is T_{box}, so the onset time of the boxcar pulse (E2.1) is $t = 0$ s. The Fourier transform of this wavelet is

$$W(\omega) = T_{box}\,\mathrm{sinc}\left(\frac{\omega T_{box}}{2\pi}\right) e^{+i\omega T_{box}/2}, \tag{E2.2}$$

where $\mathrm{sinc}(x) = \sin(\pi x)/(\pi x)$ is the well-known "sinc" function (Bracewell, 1965). The complex exponential accounts for the time delay $T_{box}/2$ with respect to $t = 0$. Clearly, the modulus of (E2.2) is

$$|W(\omega)| = T_{box}\left|\mathrm{sinc}\left(\frac{\omega T_{box}}{2\pi}\right)\right|. \tag{E2.3}$$

The amplitude spectrum equals T_{box} at f = 0 Hz, and has zeros at $f = k/T_{box}$ with k = 1,2,3,… The boxcar duration time T_{box} can be taken to be a specified fraction (less than unity) of the lag time T:

$$T_{box} = \left(\frac{d}{100}\right)T = \left(\frac{d}{100}\right)\frac{P}{2}, \tag{E2.4}$$

where the positive number d, referred to herein as the "duty cycle percentage", ranges from 0 to 100 inclusive.

With this re-parameterization, equation (E1.6) above is re-written in the form

$$|S(f)| = \left\{\left(\frac{d}{100}\right)\left(\frac{P}{2}\right)\left|\mathrm{sinc}\left[\left(\frac{d}{100}\right)\left(\frac{fP}{2}\right)\right]\right|\right\}\ \sqrt{\frac{1-\cos(2\pi fPN_P)}{1+\cos(\pi fP)}}\,. \tag{E2.5}$$

The frequency amplitude spectrum of an alternating-polarity square pulse sequence depends on the three parameters i) period P, ii) number of periods N_P, and iii) duty cycle percentage d.

The first factor in (E2.5) (i.e., containing the sinc function) equals (d/100) (P/2) at zero frequency. However, multiplication by the second factor always annihilates the DC spectral component. Sinc function zeros occur at

$$f_k = \frac{2k}{P(d/100)} \quad \text{for } k = 1,2,3,\ldots \tag{E2.6}$$

So, the duty cycle percentage d influences the locations of these zeros. Peak values of the square pulse amplitude spectrum occur at $f_l = (2l-1)/P$ for l = 1,2,3… and equal

$$|S(f_l)| = PN_P\left\{\left(\frac{d}{100}\right)\left|\mathrm{sinc}\left[\left(\frac{d}{100}\right)\left(\frac{2l-1}{2}\right)\right]\right|\right\}. \tag{E2.7a}$$

The peak amplitude is directly proportional to the product of the period P and the number of periods N_P. The proportionality factor depends only on the duty cycle percentage d. An alternative way to write the spectral peak amplitude function is

$$|S(f_l)| = \left(\frac{2PN_P}{\pi}\right)\frac{\left|\sin\left[(2l-1)\frac{\pi}{2}\left(\frac{d}{100}\right)\right]\right|}{(2l-1)}. \tag{E2.7b}$$

For a 100% duty cycle, the peak amplitudes are given by

$$\left|S(f_l)\right|_{d=100\%} = \left(\frac{2PN_P}{\pi}\right)\frac{1}{(2l-1)} = \left(\frac{2PN_P}{\pi}\right)\left[\frac{1}{1},\frac{1}{3},\frac{1}{5},\frac{1}{7},\frac{1}{9},\ldots\right]. \tag{E2.8a}$$

For 50% duty cycle, we have

$$\left|S(f_l)\right|_{d=50\%} = \left(\frac{2PN_P}{\pi}\right)\frac{1/\sqrt{2}}{(2l-1)} = \left(\frac{2PN_P}{\pi}\right)\left(\frac{1}{\sqrt{2}}\right)\left[\frac{1}{1},\frac{1}{3},\frac{1}{5},\frac{1}{7},\frac{1}{9},\ldots\right], \tag{E2.8b}$$

implying $\left|S(f_l)\right|_{d=50\%} = \left(1/\sqrt{2}\right)\left|S(f_l)\right|_{d=100\%} \approx 0.707\left|S(f_l)\right|_{d=100\%}$. For these two cases, amplitudes of the higher harmonics diminish monotonically, and inversely proportional to the odd integers.

Figure E2 depicts normalized peak amplitude (i.e., $\left|S(f_l)\right|/\left(2PN_P/\pi\right)$) for the first four spectral lines (i.e., l = 1,2,3,4), plotted with respect to duty cycle percentage d.

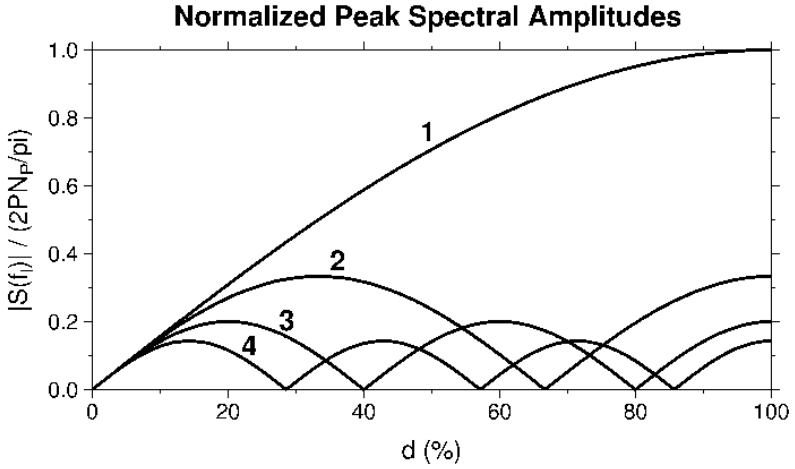

Figure E2. Normalized peak amplitude for spectral lines l = 1,2,3,4 as functions of duty cycle percentage.

Clearly, the amplitudes of all lines vanish for d = 0, as expected. The amplitude of the fundamental frequency line (l = 1) exceeds all of the harmonics (l = 2,3,4,…) and is indeed maximized for 100% duty cycle. Reading down the right edge of the plot yields the 1/(2l–1) amplitude decay at 100% duty cycle, as predicted by equation (E2.8a). But, the harmonics possess multiple maxima and zeros within the full range 0% < d < 100%! Harmonic l has l equal maxima and l – 1 zeros (not counting the common zero at d = 0%). Interestingly, over certain limited range of the duty cycle parameter, the amplitude of harmonic 3 exceeds that of 2. Similarly, there are ranges where harmonic 4 exceeds 3 (and even both 2 and 3). Finally, a harmonic is annihilated at a zero. For example, the line with frequency f_2 is removed from the spectrum if d/100 = 2/3.

The ratio of two successive peak amplitudes is

$$R_l(d) \equiv \frac{|S(f_{l+1})|}{|S(f_l)|} = \frac{\left|\operatorname{sinc}\left[\left(\frac{d}{100}\right)\left(\frac{2l+1}{2}\right)\right]\right|}{\left|\operatorname{sinc}\left[\left(\frac{d}{100}\right)\left(\frac{2l-1}{2}\right)\right]\right|} = \left(\frac{2l-1}{2l+1}\right)\left|\frac{\sin[(2l+1)(d/200)\pi]}{\sin[(2l-1)(d/200)\pi]}\right|, \qquad \text{(E2.9)}$$

(for l = 1,2,3,…) which is obviously independent of period P and number of periods N_P. Hence, a measurement of this amplitude ratio may serve to estimate an unknown duty cycle percentage d. The amplitude of the first harmonic (l = 2) to the fundamental (l = 1) is

$$R_1(d) = \frac{1}{3}\frac{|\sin[(3d/200)]\pi|}{|\sin[(d/200)]\pi|}. \qquad \text{(E2.10)}$$

This approaches unity for vanishing duty cycle d. Figure E3 depicts this amplitude ratio function. Note the vanishing spectral amplitude ratio $R_1(66.7)$.

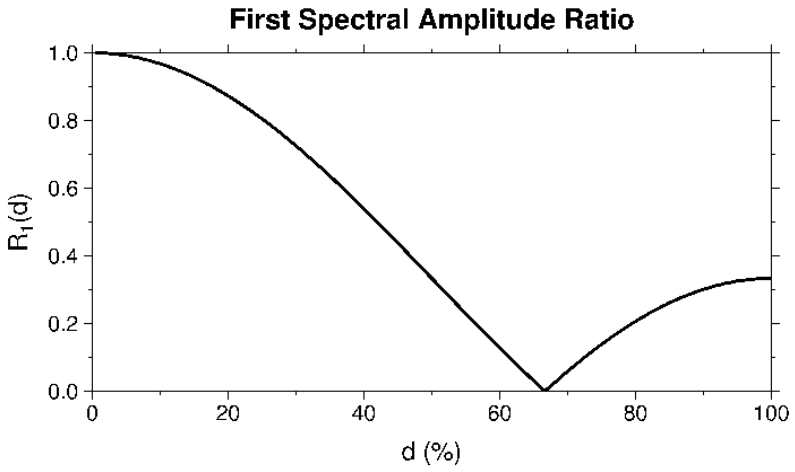

Figure E3. Ratio of spectral amplitude of first harmonic frequency (l = 2) to the fundamental frequency (l = 1) *vs*. duty cycle percentage.

E3.0 Examples

The following Figure E4 depicts six normalized source amplitude spectra $|S(f)|/|S(f_{Peak})|$ calculated with equation (E2.5) for a fixed fundamental period P = 1 s. The number of periods ranges from N_P = 1/2 in the top panel (implying a *single* square pulse) to N_P = 100 in the bottom panel. The duty cycle percentage is fixed at d = 50, which apparently corresponds to popular EM geophysical usage. The displayed frequency range is 0 to 50 Hz, although equation (E2.5) was evaluated from DC up to 300 Hz. The peak frequency f_{Peak} used for normalization is the fundamental frequency $f_1 = 1/P$ = 1 Hz. [Recall that Figure E2 indicates that the amplitude of the fundamental frequency spectral line is always the largest, for *any* duty cycle percentage.] The plotted results replicate those contained in Aldridge (2014).

The top panel plots $|\operatorname{sinc}(fP/4)|$, or the (normalized) first term in equation (E2.5). The sinc function has a maximum at zero frequency, and exhibits an overall $1/f$ amplitude decay as frequency increases. Zeros

occur at $f_k = 4k/P = 4k$ Hz for $k = 1,2,3,\ldots$, or 4, 8, 12, 16, 20,…Hz. Clearly, as the number of periods N_P increases, the source spectrum approaches a line spectrum, with lines located at frequencies $f_l = (2l-1)/P = (2l-1)$ Hz for $l = 1,2,3,\ldots$, or 1, 3, 5, 7, 9,… Hz. These spectral lines correspond to the zeros of the denominator of the second term in equation (E2.5). Note the diminishing amplitudes of the peak values as frequency increases. Also note that, as N_P increases from 1/2, the non-zero DC spectral value is annihilated. This reflects the simple fact that an alternating polarity pulse sequence with an integer number of periods has no net area, or no net DC value.

Although there is some non-zero fine structure to the amplitude spectra between the discrete spectral lines (as illustrated in Figure E1), this rapidly becomes invisible as the number of periods increases (and the normalization amplitude $|S(f_1)|$ increases). The linear (rather than logarithmic) vertical plot scale also suppresses the intra-line fine structure.

Various numerical values are tabulated below. Calculations include $N_P = 1000$, although that panel is not plotted because it appears identical to the $N_P = 100$ panel. Column two is the gain in signal-to-noise achieved by additive stacking of N_P periods of recorded data. [An assumption is that ambient EM noise is zero mean, fixed standard deviation, and uncorrelated between successive periods.]

N_P	G_{SNR}	Peak frequency (Hz)	Bandwidth (Hz)	Peak Amplitude (s)
1/2	---	0.00	0.00 to 126.17	0.250
1	1.00	0.92	0.01 to 106.86	0.454
2	1.41	0.98	0.01 to 101.10	0.902
3	1.73	0.99	0.01 to 99.01	1.352
10	3.16	1.00	0.01 to 99.00	4.471
100	10.0	1.00	0.99 to 99.00	45.016
1000	100	1.00	0.99 to 99.00	450.158

As the number of periods increases, the maximum frequency settles at 99.00 Hz, which is the point where the amplitude spectrum descends below 1% of its peak value at 1.00 Hz. However, $N_P = 3$ appears to yield virtually the same maximum frequency f_{max}! Of course, the major problem is that such a low stacking fold yields only a modest gain in the signal-to-noise ratio (recall that $G_{SNR} = \sqrt{N_{Periods}}$).

Note also that the peak spectral amplitude (which plots at 1.0 in the panels of Figure E4) increases with N_P. The values agree with those predicted by equation (E2.7a or b) above, for spectral line $l = 1$.

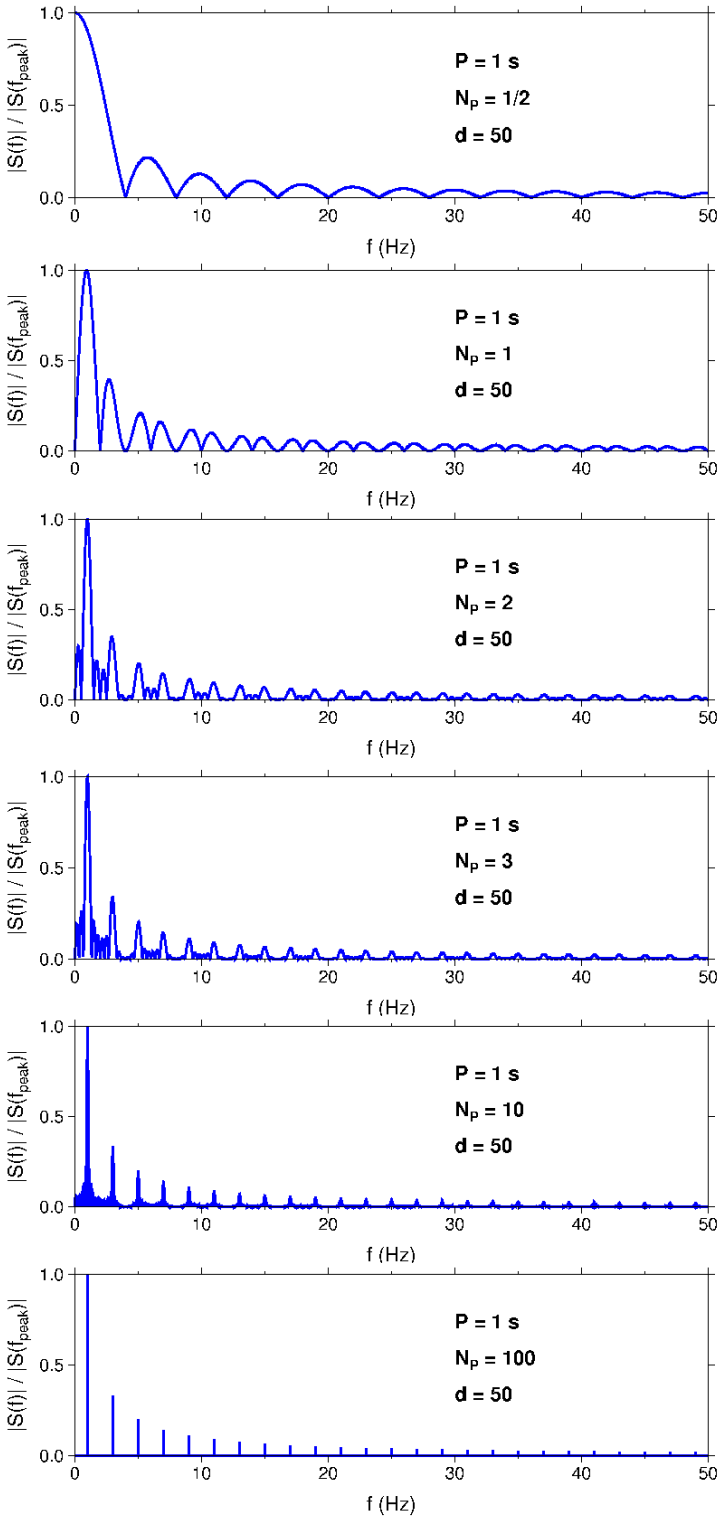

Figure E4. Effect of increasing number of periods N_P on frequency amplitude spectra, for fixed fundamental period P = 1 Hz and fixed duty cycle percentage d = 50%.

Figure E5 illustrates the effect of varying the duty cycle percentage *d*, while holding the fundamental period *P* (= 1 Hz) and number of periods N_P (= 100) fixed. Normalized amplitude spectra are again plotted. Clearly, increasing the duty cycle percentage changes the overall shape of these line spectra. The middle panel for *d* = 50% (which is the same as the bottom panel in the previous figure) appears identical to the bottom panel for *d* = 100%. This agrees with the conclusions of equations (E2.8a and b). However, peak amplitudes differ, as tabulated here:

d (%)	Peak frequency (Hz)	Bandwidth (Hz)	Peak Amplitude (s)
10	1.00	0.99 to 493.00	9.959
25	1.00	0.99 to 237.00	24.362
50	1.00	0.99 to 99.00	45.016
75	1.00	0.99 to 97.00	58.816
90	1.00	0.99 to 99.00	62.878
100	1.00	0.99 to 99.00	63.662

Recall that the positions of the spectral lines are independent of the duty cycle percentage, as indicated by expression (E1.7) above: $f_l = (2l-1)/P$ = 1, 3, 5, 7, 9, 11,… Hz for the present examples. However, the zeros of the multiplying sinc function *do* depend on the duty cycle parameter *d*, via equation (E2.6) above: $f_k = 2k/P(d/100)$ for *k* = 1,2,3,…The presence of the additional parameter *d* enables us to position these zeros to coincide with some of the discrete spectral lines f_l, and thus remove them from the amplitude spectrum.

Guided by the spectral line amplitude curves plotted in Figure E2, choose *d* = 66.67% which implies f_k = 3, 6, 9, 12, 15, 18, 21,…Hz. The top panel of Figure E6 indicates that the odd harmonics f_l = 3, 9, 15, 21, …Hz are removed. Choosing *d* = 40% as in the middle panel of Figure E6 implies sinc function zeros occur at frequencies f_k = 5, 10, 15, 20, 25, 30, 35,… Hz. The odd harmonics f_l = 5, 15, 25, 35,…Hz are then removed. However, Figure E2 indicates that the *same* harmonics may be removed by choosing *d* = 80%. The bottom panel of Figure E6 illustrates this situation. Moreover, the relative suppression of the non-zero harmonics at f_l = 3, 7, 9, 11, 13,…Hz appears superior. This is consistent with Figure E3. The geophysical advantages (or disadvantages) associated with modifying the source signal amplitude spectrum with this technique requires further study.

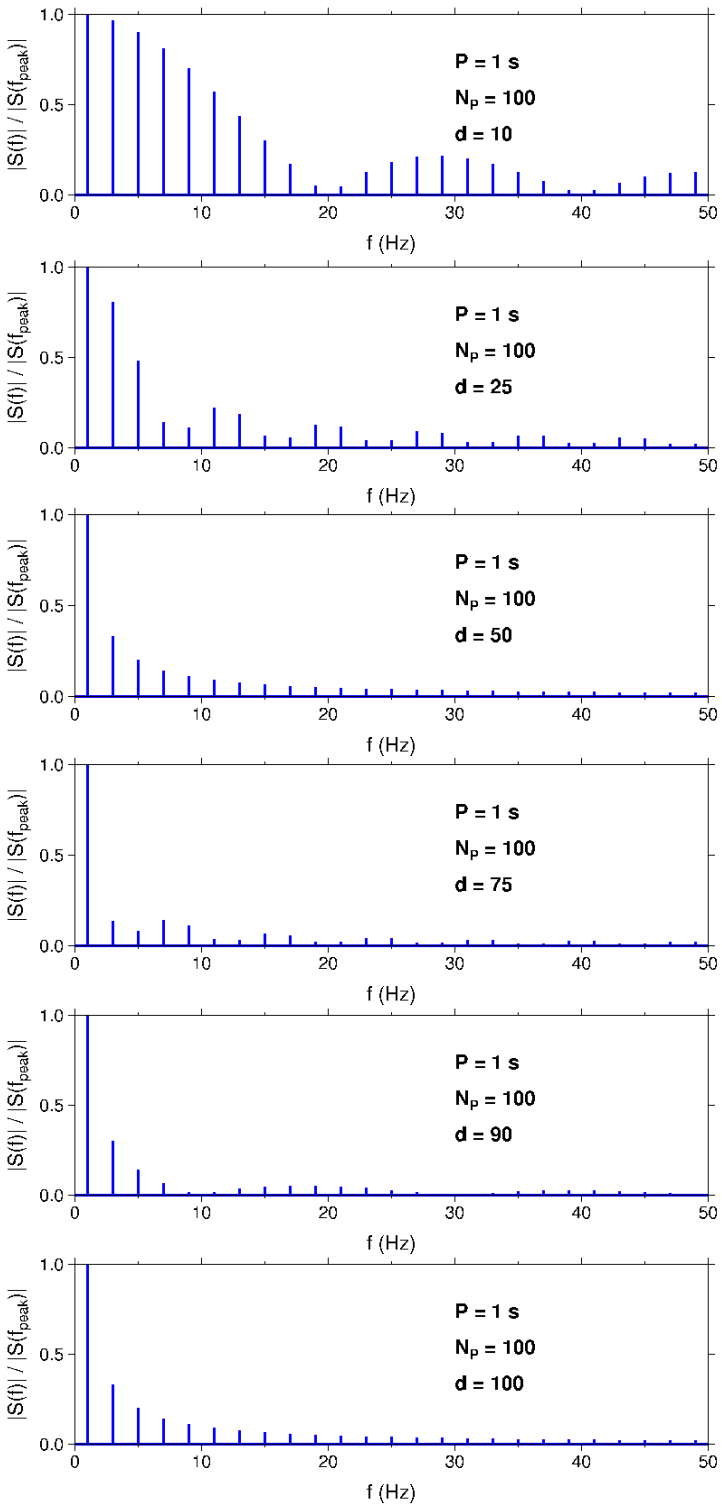

Figure E5. Effect of increasing duty cycle percentage *d* on frequency amplitude spectra, for fixed fundamental period P = 1 Hz and number of periods N_P = 100.

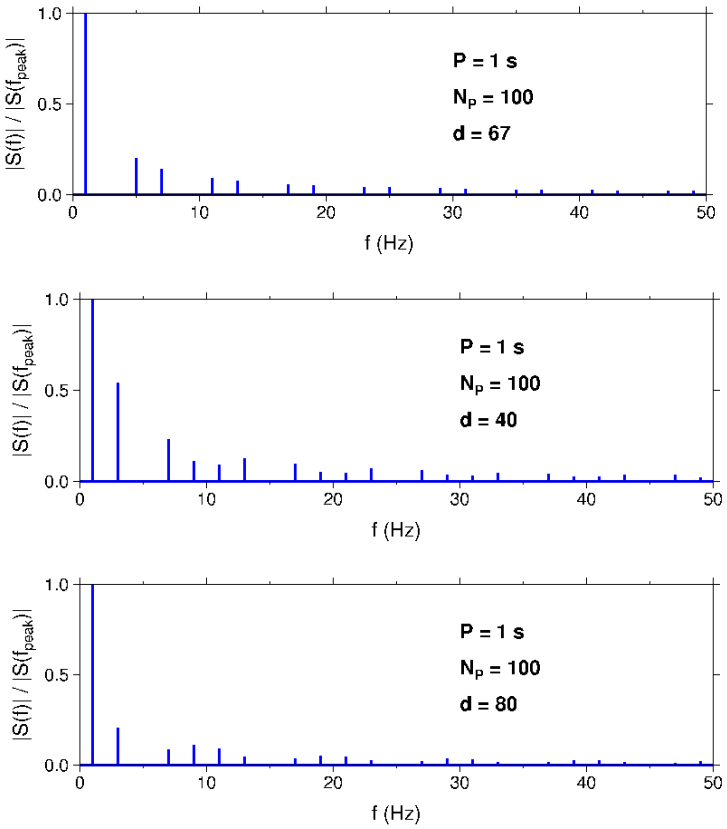

Figure E6. Annihilation of certain spectral lines via judicious choice of zero locations for the multiplying sinc function. Top panel: lines at 3, 9, 15, 21,… Hz are removed via a 67% duty cycle. Maximum amplitude = 55.133 s. Middle panel: lines at 5, 15, 25, 35,… Hz are removed via a 40% duty cycle. Maximum amplitude = 37.420 s. Bottom panel: the same lines at 5, 15, 25, 35,… Hz are removed by an 80% duty cycle. Maximum amplitude = 60.546 s.

Finally, Figure E7 depicts frequency spectra of horizontal electric field components observed at a Salton Sea, California geothermal site and at an undisclosed Saudi Arabian oil field (Marsala *et al.*, 2014). **Red** and **blue** curves show prominent spectral lines at f_l = 1, 3, 5, 7, 9, 11, 13, 15,… Hz, implying an EM source signal with a P = 1 s fundamental period. No information is given regarding the number of periods N_P, although the broad spectral peak at 1 Hz suggests a relatively low number (e.g., compare with Figure E4). Amplitude falloff between f_1 = 1 Hz and f_2 = 3 Hz crudely picked from the plot is about $R_1(d)$ = 0.20 (although the vertical plot scale, in units of V/√Hz is rather confusing). So, Figure E3 implies a duty cycle percentage of perhaps d ~ 55 or d ~ 80. Within the limits of accuracy of picking the Figure E7 curves, d ~ 50 (which we believe is common field practice) is perfectly acceptable.

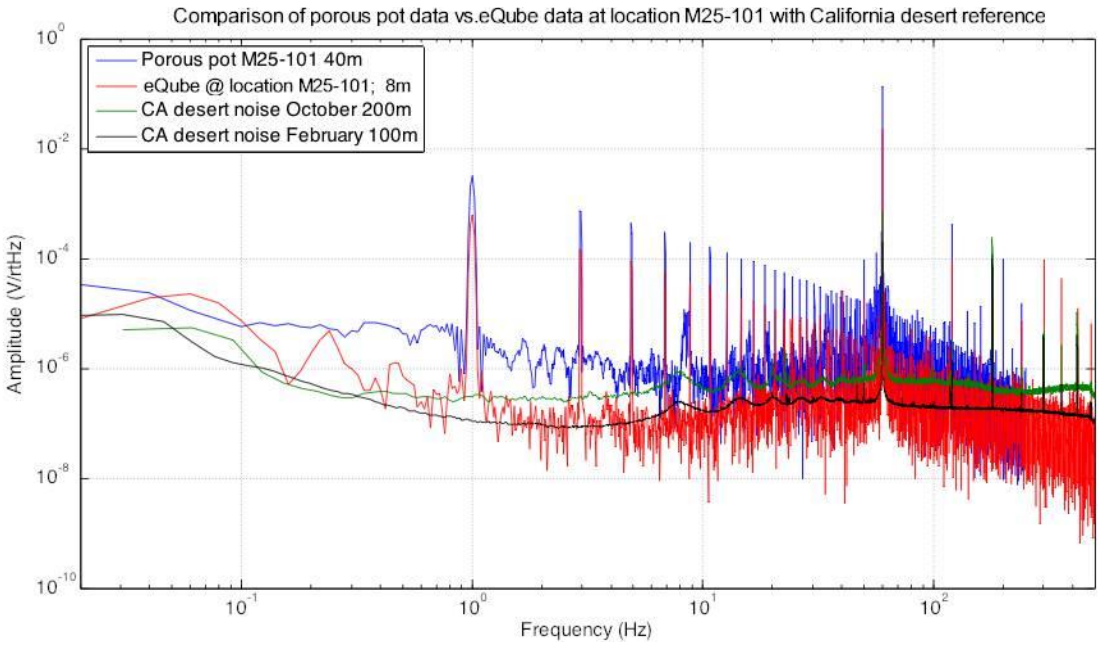

Figure E7. Frequency amplitude spectra of horizontal electric field measurements, from Marsala *et al.* (2014). **Red** and **blue** curves are spectra from active-source EM data recorded in an undisclosed Saudi Arabian oil field, using two different types of sensors (but note different sensor spacings). **Green** and **black** curves are ambient noise spectra (i.e., no active energy source) from EM data recorded at a Salton Sea geothermal site (also with different sensor spacings). Note the prominent noise peak at 60 Hz.

15.0 LIST OF FIGURES AND TABLES

Figure 6.3. Back-scattered E_x electric vector components (top panel) and B_y magnetic vector components (bottom panel) generated by a geologic bed with conductivity $\sigma_{bed} = 100\,\text{S/m}$ (5000 times larger than the background medium conductivity $\sigma_{bak} = 0.02\,\text{S/m}$). Bed permeability $\mu_{bed} = \mu_0$ and permittivity $\varepsilon_{bed} = 10\varepsilon_0$ are identical to background values. Bed thickness varies from h = 10 m (red curves) to h = 1 cm (brown curves).

Figure 6.4. For-scattered E_x electric vector components (top panel) and B_y magnetic vector components (bottom panel) generated by the same conductivity contrast geologic bed as in Figure 6.3.

Figure 6.5. Back-scattered EM field components generated by a geologic bed with fixed thickness $h_{bed} = 1\,\text{cm}$, and current conductivity σ_{bed} varying between 10^5 S/m (red curves) and 10^2 S/m (brown curves). Bed permeability $\mu_{bed} = \mu_0$ and permittivity $\varepsilon_{bed} = 10\varepsilon_0$ are identical to background.

Figure 6.6. For-scattered EM field components generated by the same conductivity contrast geologic bed as in Figure 6.5.

Figure 6.7. Back-scattered EM field components generated by a geologic bed with fixed thickness $h_{bed} = 10\,\text{m}$, and magnetic permeability μ_{bed} varying between $10^4\mu_0$ (red curves) and $10^1\mu_0$ (brown curves). Bed conductivity $\sigma_{bed} = 0.02\,\text{S/m}$ and permittivity $\varepsilon_{bed} = 10\varepsilon_0$ are identical to background.

Figure 6.8. For-scattered EM field components generated by the same permeability contrast geologic bed as in Figure 6.7.

Figure 6.9. Back-scattered EM field components generated by a geologic bed with fixed current conductivity $\sigma_{bed} = 100\,\text{S/m}$ and magnetic permeability $\mu_{bed} = 100\mu_0$, and with thickness varying between $h_{bed} = 10\,\text{m}$ (red curves) to $h_{bed} = 1\,\text{cm}$ (brown curves). Bed permittivity $\varepsilon_{bed} = 10\varepsilon_0$ is identical to background. These layers have strong conductivity contrast (×5000) and permeability contrast (×100) with the background medium.

Figure 6.10. For-scattered EM field components generated by the same joint conductivity/permeability contrast geologic bed as in Figure 6.9.

Figure 6.11. Back-scattered EM field components generated by a geologic bed with fixed conductance (i.e., conductivity × thickness product) equal to 100 S. Bed magnetic permeability $\mu_{bed} = \mu_0$ and electric permittivity $\varepsilon_{bed} = 10\varepsilon_0$ are identical to background values. All curves overplot at this plot scale.

Figure 6.12. For-scattered EM field components generated by a geologic bed with fixed inductance (i.e., permeability × thickness product) equal to 10^4 H. Bed current conductivity $\sigma_{bed} = 0.02\,\text{S/m}$ and electric permittivity $\varepsilon_{bed} = 10\varepsilon_0$ are identical to background values. All curves overplot at this plot scale.

Figure 6.13. For-scattered E_x field components generated by a thin geologic bed (h_{bed} = 5 mm) with strong permittivity contrasts with the background medium. Top / bottom panels correspond to layer relative permittivities of 4×10^6 and 10^{10}, respectively. Bed conductivity and permeability are the same as the homogenous background medium.

Figure 6.14. Reflection/Transmission modeling geometry. E_z-component electric field plane wave is incident from the left ($x < -h/2$) on a geologic layer of thickness h = 10 m. Both reflected ($x < -h/2$) and transmitted ($x > +h/2$) electromagnetic plane waves are generated.

Figure 6.15. Back-scattered and for-scattered E_z-component traces generated by proximal (top panel) and distal (bottom panel) plane wave sources positioned at the vertical **red** arrows. Maximum absolute amplitude within each panel is plotted at one trace spacing; positive lobes of the traces are shaded grey.

Figure 6.16. Logarithmic maximum relative E_z amplitude *vs*. receiver location for proximal (top) and distal (bottom) plane wave sources. Source amplitude level is indicated by the horizontal black dashed line at 0.0. Background medium conductivities are σ_2 =0.001 S/m (**red** curves), 0.01 S/m (**blue** curves), 0.1 S/m (**green** curves), and 1.0 S/m (**brown** curves). Solid and dashed amplitude profiles correspond to conductivity-only scattering, and joint conductivity and permeability scattering, respectively. The scattering zone is represented by the thin vertical brown strip.

Figure 6.17. Back-scattered and for-scattered B_y-component traces generated by proximal (top panel) and distal (bottom panel) plane wave electric field sources positioned at the vertical **red** arrows. Maximum absolute amplitude within each panel is plotted at one trace spacing; positive lobes of the traces are shaded grey.

Figure 6.18. Logarithmic maximum relative B_y amplitude *vs*. receiver location for proximal (top) and distal (bottom) plane wave sources. Reference amplitude level is B_{ref} = 1 T. Background medium conductivities are $\sigma_2 = 0.001\,\mathrm{S/m}$ (**red** curves), 0.01 S/m (**blue** curves), 0.1 S/m (**green** curves), and 1.0 S/m (**brown** curves). Solid and dashed amplitude profiles correspond to conductivity-only scattering, and joint conductivity and permeability scattering, respectively. The scattering zone is represented by the thin vertical brown strip.

Figure 7.1. Schematic depiction of First Born Approximation scattered wavefields (upward and downward propagating **red** plane wavefronts) for the case of a thin geologic layer possessing a contrast in current conductivity with respect to a homogeneous background. The material parameter contrast of the layer is replaced by a horizontally-directed electric current body source (**green** arrows) with the same vertical extent.

Figure 7.2. Exact (upper panel) and First Born Approximation (lower panel) back-scattered responses induced by a strong current conductivity contrast in a thin geologic layer with thickness h_{bed} = 1 cm. **Red**, **green**, **blue**, and **brown** curves correspond to $\sigma_{bed} = 10^3$, 10^4, 10^5, and 10^6 S/m, respectively. Blue and brown sinusoidal curves plot well off scale in bottom panel.

Figure 7.3. Exact (solid curves) and First Born Approximation (dashed curves) back-scattered responses induced by moderate current conductivity contrast in a thin geologic layer with thickness h_{bed} = 1 cm. **Brown**, **blue**, **green**, and **red** curves correspond to $\sigma_{bed} = 10^0$, 10^1, 10^2, and 10^3 S/m, respectively. Solid red curve is identical to previous Figure 7.2. Note expanded vertical scale of 10× compared with prior figures.

Figure 7.4. Backward-scattering (top panel) and forward-scattering (bottom panel) logarithmic amplitude ratios of First Born Approximation to exact scattered responses, calculated for a thin layer (h = 1 cm) and an incident EM sinusoidal signal with frequency f = 1 Hz. Background conductivity σ_1 = 0.1 S/m and permeability $\mu_1 = \mu_0$, implying the thickness-to-wavelength ratio is $h/\lambda_1 = 10^{-6}$. Paramagnetic/diamagnetic regions reside above/below the horizontal dashed lines.

Figure 7.5. Same as Figure 7.4, except for a thicker layer (h = 10 m) and a higher frequency incident signal (f = 10 Hz).

Figure 7.6. Same as Figure 7.5, except a larger magnetic permeability $\mu_1 = 10\mu_0$ is assigned to the background medium.

Figure 8.1. Non-normal incidence plane wave reflected and transmitted responses of a geologic layer.

Figure A1. Diagnostic frequency functions for electromagnetic wave propagation, plotted with respect to dimensionless frequency f / f_t. **Blue** curve is phase speed $c(f)$ and attenuation factor $\alpha(f)$, normalized by the respective infinite frequency values. **Red** curve is group speed $g(f)$, also normalized by the infinite frequency value. **Green** curve (linear with frequency) is quality factor $Q(f) = f / f_t$.

Figure A2. Diagnostic frequency functions for electromagnetic wave propagation, plotted with respect to physical frequency f in kilohertz. **Blue** curve is phase speed $c(f)$ and attenuation factor $\alpha(f)$, normalized by the respective infinite frequency values. **Red** curve is group speed $g(f)$, also normalized by the infinite frequency value. **Green** curve (linear with frequency) is quality factor $Q(f)$.

Figure B1. Geometric setup of the normal incidence plane wave reflection / transmission problem. Unit propagation direction vectors of the plane wavefronts are $\mathbf{n}_{inc} = \mathbf{n}_{trn} = +\mathbf{e}_z$ and $\mathbf{n}_{ref} = -\mathbf{e}_z$.

Figure B2. Reflected (top panel) and transmitted (bottom panel) electric vector x-components from an "invisible" or "transparent" geologic layer with thickness h = 10 m. Relative (i.e., dimensionless) permittivity $\hat{\varepsilon} = \varepsilon/\varepsilon_0$, permeability $\hat{\mu} = \mu/\mu_0$, and conductivity $\hat{\sigma} = \sigma/\sigma_{ref}$ (with $\sigma_{ref} = 1\,\mathrm{S/m}$) for the three media are: $(\hat{\varepsilon}_1, \hat{\mu}_1, \hat{\sigma}_1) = (1,1,1)$, $(\hat{\varepsilon}_2, \hat{\mu}_2, \hat{\sigma}_2) = (10,10,10)$, $(\hat{\varepsilon}_3, \hat{\mu}_3, \hat{\sigma}_3) = (1,1,1)$. The reflected response vanishes because both the top-bed and bottom-bed reflection coefficients numerically equal 0.0.

Figure B3. Reflected (top panel) and transmitted (bottom panel) electric vector x-components from a geologic layer with thickness h = 10 m. All medium parameters are the same as in Figure B2, except the relative (i.e., dimensionless) conductivity $\hat{\sigma}$ assigned to the layer (medium #2) is $\hat{\sigma}_3 = 15\,\mathrm{S/m}$. A weak reflected response is generated, and the transmitted response appears to be nearly unchanged (compare with Figure B2).

Figure E1a-h. Amplitude spectra of an alternating polarity spike sequence with N_P periods.

Figure E2. Normalized peak amplitude for spectral lines l = 1,2,3,4 as functions of duty cycle percentage.

Figure E3. Ratio of spectral amplitude of first harmonic frequency (l = 2) to the fundamental frequency (l = 1) *vs*. duty cycle percentage.

Figure E4. Effect of increasing number of periods N_P on frequency amplitude spectra, for fixed fundamental period P = 1 Hz and fixed duty cycle percentage d = 50%.

Figure E5. Effect of increasing duty cycle percentage d on frequency amplitude spectra, for fixed fundamental period P = 1 Hz and number of periods N_P = 100.

Figure E6. Annihilation of certain spectral lines via judicious choice of zero locations for the multiplying sinc function. Top panel: lines at 3, 9, 15, 21,… Hz are removed via a 67% duty cycle. Maximum amplitude = 55.133 s. Middle panel: lines at 5, 15, 25, 35,… Hz are removed via a 40% duty cycle.

Maximum amplitude = 37.420 s. Bottom panel: the same lines at 5, 15, 25, 35,… Hz are removed by an 80% duty cycle. Maximum amplitude = 60.546 s.

Figure E7. Frequency amplitude spectra of horizontal electric field measurements, from Marsala *et al.* (2014). **Red** and **blue** curves are spectra from active-source EM data recorded in an undisclosed Saudi Arabian oil field, using two different types of sensors (but note different sensor spacings). **Green** and **black** curves are ambient noise spectra (i.e., no active energy source) from EM data recorded at a Salton Sea geothermal site (also with different sensor spacings). Note the prominent noise peak at 60 Hz.

Table 5.1. Thin-bed time-domain scattering formulae.

Table 5.2. Thin-bed frequency-domain scattering formulae.

Table 7.1. Backward scattering formulae ($z_r < z_{top}$).

Table 7.2. Forward scattering formulae ($z_r > z_{bot}$).

16.0 DISTRIBUTION LIST

1	MS 0750	D.F. Aldridge, 06911
1	MS 0750	C.J. Weiss, 06911
1	MS 0750	S.R. Vigil, 06911
1	MS 0899	Technical Library, 9536 (electronic copy)
1		L.C. Bartel, Carbo Ceramics Corporation
1		S. Mukerhee, Carbo Caramics Corporation
1		T. Palisch, Carbo Ceramics Corporation
1		W. Al-Tailij, Carbo Ceramics Corporation
1		J. Zhang, Carbo Ceramics Corporation


Sandia National Laboratories